

CRANFIELD UNIVERSITY

**DEPARTMENT OF APPLIED SCIENCE AND
ENGINEERING**

Ph.D THESIS

Academic period 2009-2012

R. J. HUDSON

**Investigating the factors influencing RDX
shock sensitivity**

Supervisor: P. Gill

February 2012

BLANK PAGE

CRANFIELD UNIVERSITY

DEPARTMENT OF APPLIED SCIENCE AND ENGINEERING (DASE)

Ph.D Thesis

Keywords: Shock sensitivity, Defects, Morphology, Nanoindentation, Rheology

ABSTRACT

The shock sensitivity of RDX (cyclotrimethylenetrinitramine) is dependent upon factors including crystal size, morphology, internal defects, surface defects and HMX content. With the arrival of reduced sensitivity RDX (RS-RDX) and the drive towards insensitive munitions (IM), understanding what influences sensitivity has become a significant topic within energetic materials research. During the RS-RDX international Round Robin Study (R⁴) the parameters which influence sensitivity were investigated, however large discrepancies were seen between different laboratories so the results were inconclusive.

The objective of this work is to clarify how crystal properties and the manufacturing process affect RDX sensitivity. In this study the same RDX lots as those from the R⁴ were examined. Optical microscopy showed that internal defect content varied widely and was affected by the manufacturing process. A good correlation between sensitivity and defect quantity was seen for RDX lots produced by the same method. Likewise, microscopic examination also showed a large range of morphologies which was influenced by method of production. Scanning electron microscopy also showed that surface defects were approximately correlated to shock sensitivity, however general surface roughness agreed better with sensitivity than the number of specific defects such as cracks and holes. The mechanical properties of the RDX samples were investigated using nanoindentation. This showed a good correlation between the quantity of internal defects and modulus of elasticity, hardness and creep. There was also a good agreement between these parameters and sensitivity. Rheological analysis of RDX/polyethylene glycol suspensions indicated a good agreement between the rheological properties of the suspension and crystal morphology. This method could form a basis for a new testing method for RDX morphology. Differential scanning calorimetry demonstrated that crystal size influenced decomposition rate. The melting endotherm onset temperature and energy was correlated with HMX quantity.

Key results

- Internal crystal defects have been shown to influence the mechanical properties of RDX crystals. Crystals with many defects have lower elastic modulus and undergo more creep deformation than crystals with fewer defects when examined using nanoindentation. RDX crystal mechanical properties have a correlation with shock sensitivity.
- Crystal morphology is closely correlated with the rheological properties of RDX-polyethylene glycol suspensions. Angular/rough crystals produce suspensions that have a higher viscosity than suspensions of smoother crystals.
- Nanoindentation and rheological analysis have been demonstrated to provide more reliable results than the optical microscopy methods used in the Reduced sensitivity RDX Round Robin programme (R4). They could be used as a basis for new testing methods to discriminate between RS and non-RS RDX grades.

Thesis outline

This thesis addresses the factors influencing reduced sensitivity RDX (RS-RDX). It investigates the physico-chemical properties which influence RDX shock sensitivity such as internal crystal defects, crystal morphology, size, surface defects and HMX content. The main planned outcome is to provide new testing methods that can be used to characterise RS and non-RS RDX. This is relevant to the development of insensitive munitions (IM) that demonstrate a reduced sensitivity to unplanned stimuli.

This thesis consists of eight chapters and three appendices:

Chapter 1; Introduction to RDX, a brief overview of its properties and how it is synthesised. An overview of hot spot theory and how they are formed then follows.

Chapter 2; Literature review, a review of studies that examine how internal defects, crystal morphology, crystal size, HMX content and ageing affect RDX shock sensitivity. A short discussion on the gap tests used to measure shock sensitivity and a review of early studies into RS-RDX concludes the chapter.

Chapter 3; Theory of experimental techniques used. This chapter gives an outline of the theory of nanoindentation and rheology analysis, the two most significant techniques used.

Chapter 4; This chapter gives details of the experimental procedures used. Optical microscopy for internal defects and morphology, electron microscopy for surface defects, nanoindentation and rheology methods, DSC thermal analysis and small scale gap testing of loose packed RDX.

Chapter 5; This chapter gives the results from the internal crystal defect analysis using microscopy and nanoindentation experiments and discusses them.

Chapter 6; The results from the optical microscopy morphology assessment and rheology analysis of RDX-PEG suspensions are presented and discussed.

Chapter 7; Results from other experimental work investigating surface defects by scanning electron microscopy, thermal analysis by DSC and loose powder gap tests are given with discussion.

Chapter 8; Final conclusions and recommendations for future investigations. Summary conclusions from all the work undertaken and suggestions for further experimental work given.

Appendix A; Extra data from the small scale gap testing of loose RDX samples is presented.

Appendix B; Extra data from the nanoindentation experiments is presented.

Appendix C; Data from the angle of repose measurements.

Acknowledgements

My PhD student experience has been both an interesting and challenging one. During this time I have got to know many people who have been of vital help to me. Firstly I would like to thank my supervisors Dr. Philip Gill and Dr. John Bellerby for all their guidance, encouragement and patience. Thank you for being so dependable. I would also like to thank [dstl] (Adam Cumming, David Tucker and Peter Collins), Chemring Nobel and the other external organisations that were involved and of course their financial backing for this PhD project. Thanks to Dr. Peter Zioupos for all your help and guidance with the nanoindentation work and Adrian Mustey for casting the RDX-resin blocks. As for the rheology analysis I would like to mention Dr's John Rock and Monir Moniruzznan for their assistance as well. Other people who I would like to thank are Dr. Natalie Mai, Richard Hall and Rodger Cox, Dr's. James Padfield and Alex Contini for their interest and advice on many occasions. A big thank you goes to everyone who took part in the multi-person crystal morphology exercise. Thanks for spending time to do it and the data that you produced. I should also include Chris Ransom for setting up the on-line version of this assessment. I need to also include the guys at the ERDA; Paul Walker for helping with the gap tests, Graham Creighton, and Jim Clements. I must not forget all my friends here including my fellow office mates James Tucker and Chris Peel. I am indebted to my family for all their support for me. Finally I also thank my friends back in Hertfordshire and elsewhere, you know who you are!

In memory of my mother
Marianne Carol Hudson
September 1945- January 1997

Publications and conferences attended

Conferences:

Proceedings of the 41st International Annual Conference of ICT, Karlsruhe, Germany. 29 June- 2 July 2010.

R. J. Hudson, P. P. Gill, P. Q. Flower, A. S. Cumming.

Paper 1; Assessment of RDX crystal morphology and defects, p. 73/1-73/15

Paper 2; Thermal analysis of RDX using Differential Scanning Calorimetry, p. 74/1-74/13

Proceedings of the 14th International seminar, New Trends in Research of Energetic Materials. 13-15th April 2011, University of Pardubice, Czech Republic.

Paper and presentation:

R. J. Hudson, P. P. Gill.

Multi-person assessment of RDX crystal morphology using the RS-RDX round robin method, vol. I, p. 237-245.

Journal paper:

R. J. Hudson, P. Zioupos, P. P. Gill, *Investigating the mechanical properties of RDX crystals using nano-indentation*, Propellants, Explosives, Pyrotechnics, **(2012)**, vol. 37(2), p. 191-197.

Contents

Abstract	i
Key results	ii
Thesis outline	ii
Acknowledgements	iv
Publications and conferences attended	v
Contents	vi
Lists of figures, tables and equations	xi
Abbreviations and symbols	xxii

Chapter 1 Introduction	1
1.1 General introduction to RDX	1
1.2 Synthesis and production of RDX	2
1.2.1 Overview of the process used today	2
1.2.2 Possible reaction mechanism for the synthesis of RDX	4
1.2.3 Recrystallisation methods used in RDX manufacture	7
1.3 Hot spot theory of initiation	7
1.3.1 Initiation by rapid collapse of gas filled bubbles and spaces	8
1.3.2 Initiation by friction	12
1.3.3 Initiation by localised adiabatic shear	14
1.3.4 Hot spot formation at crack tips and dislocations	16
1.4 Overview of the processes of deflagration and detonation.	18
1.4.1 Deflagration	18
1.4.2 Detonation	20
a) General description and theory	20

b) Burn to detonation	22
c) Shock to detonation	22
1.5 Summary	23
Chapter 2 Literature review	24
2.1 The influence of internal crystal defects, voids and inclusions	24
2.1.1 The formation of internal crystal defects	24
2.1.2 Investigating the influence of internal defects on shock sensitivity	27
2.2 The influence of particle morphology on shock sensitivity	43
2.2.1 The influence of impurities and solvent on morphology during RDX crystallisation.	49
2.3 The influence of crystal size on shock sensitivity	52
2.4 The influence of HMX content on RDX shock sensitivity	62
2.5 The effect of RDX ageing on shock sensitivity	68
2.6 Characterisation of RS-RDX by shock sensitivity testing	72
2.6.1 The gap test	72
2.7 Review of early studies of RS-RDX	75
2.8 Introduction to the RS-RDX inter-laboratory round robin (R ⁴) program	77
Chapter 3 Theory of experimental techniques used	79
3.1 Micromechanical property analysis using nanoindentation	79

3.2	Assessment of crystal morphology by rheological analysis of RDX suspensions	82
Chapter 4	Experimental methods	85
4.1	Samples studied and sampling techniques used	85
4.2	Internal defects assessment and nanoindentation methods	86
4.2.1	Internal defects assessment	86
4.2.2	Nanoindentation methods	87
4.3	Morphology assessment, rheology methods and surface defects assessment using SEM	90
4.3.1	Matching refractive index microscopy	90
a)	Morphology assessment performed by the author	90
b)	Multi-person RDX crystal morphology assessment exercise	91
4.3.2	Rheology experimental methods	92
a)	Samples tested and instrument used	92
b)	Viscosity/shear rate verses controlled shear stress	92
4.3.3	Surface defect assessment method using SEM	93
4.4	Thermal analysis method using DSC	95
4.4.1	Initial DSC investigations, raw RDX samples	95
4.4.2	DSC analysis of RDX in a pseudo-PBX formulation	96
4.4.3	The effect of HMX on DSC analysis of raw RDX and RDX in pseudo-PBX formulation	97
4.4.4	The effect of RDX crystal size on decomposition exotherm of pseudo-PBX formulation	97

4.5	Shock sensitivity measurements using the small scale gap test	97
Chapter 5	Results and discussion; Internal defect assessment and nanoindentation	100
5.1	Internal defect assessment results	100
5.2	Results from nanoindentation analysis of RDX crystals	104
5.2.1	Measurements from 150-500 μm crystal size range	104
a)	The effect of increasing load on the elasticity and stiffness of RDX	104
b)	The effect of internal defects on mechanical properties of RDX	106
c)	The relation between RDX mechanical properties and shock sensitivity	108
5.2.2	Nanoindentation experiments comparing the mechanical properties of small and large RDX crystals	110
a)	The effect of increasing load on elastic modulus and creep	110
b)	Elasticity <i>vs.</i> hardness, elasticity <i>vs.</i> creep and hardness <i>vs.</i> creep	111
5.3	Discussion of results	113
5.3.1	Discussion of results from internal defect assessment	113
5.3.2	Discussion of nanoindentation results	115
a)	Discussion of results from 150-500 μm size fraction	115
b)	Discussion of results comparing crystal size	116
5.4	Conclusions	119

Chapter 6	Results and discussion; Morphology assessments and rheology	120
6.1	Morphology assessment results	120
6.1.1	Rheology analysis results and discussion	120
6.2	Results and discussion of initial morphology assessment by the author and the Cranfield multi-person assessment	125
6.2.1	Simplification of assessment by reducing the number of morphology bins	131
6.3	Conclusions	132
Chapter 7	Results and discussion; Other results	134
7.1	Surface defect assessment results	134
7.1.2	Discussion of results from surface defect assessment	137
7.1.3	Conclusions	139
7.2	Thermal analysis of the R ⁴ RDX lots using DSC	140
7.2.1	Initial analysis of raw RDX	140
7.2.2	Raw RDX spiked with HMX	143
7.2.3	Results from the initial analysis of RDX in pseudo-HTPB PBX formulation	145
7.2.4	The effect of RDX Particle size upon pseudo-PBX decomposition	147
7.2.5	RDX spiked with HMX in pseudo-PBX formulation	148
7.2.6	Discussion of results from DSC analysis	149
7.2.7	Conclusions	151
7.3	Shock sensitivity testing of loose RDX	152
7.3.1	Results	152
7.3.2	Discussion	153
7.3.3	Conclusions	155

Chapter 8	Final Conclusions and recommendations	156
8.1	Final conclusions	156
8.2	Future investigations	159
Appendix A	Extra data from loose powder gap tests	161
Appendix B	Extra data from nanoindentation experiments	163
Appendix C	Angle of repose measurements	167
References		170

List of figures, tables and equations

Figures:

Chapter 1

Fig. 1.1	a) molecular structure for RDX.	1
	b) 3D model depicting the molecular conformation of RDX under ambient conditions.	1
Fig. 1.2	molecular structure for HMX.	3
Fig. 1.3	Reaction schemes showing the formation of RDX by the action of nitric acid on hexamine dinitrate.	5
Fig. 1.4	Reaction scheme showing the formation of RDX via the influence of the nitracidic ion.	6
Fig. 1.5	Photographs showing a bubble in an inert gel being collapsed by a shock wave.	9
Fig. 1.6	Series of high speed photographs showing the collapse of a bubble and production of lobes of trapped gas.	11
Fig. 1.7	Series of high speed photographs showing the progressive collapse of voids in an inert gel.	12

Fig. 1.8	Illustration showing the formation of hot spots caused by frictional forces between rubbing surfaces.	13
Fig. 1.9	Diagram showing the formation of shear bands within a material during impact by a penetrating body.	15
Fig. 1.10	Photo showing shear banding produced during impact of HMX.	16
Fig. 1.11	Schematic diagram of a detonation wave passing through an explosive.	20
Fig. 1.12	A series of high speed photographs showing a detonation wave passing through a steel cylindrical charge.	21

Chapter 2

Fig. 2.1	Schematic diagram illustrating the formation of an internal defect caused by the adsorption of an impurity molecule into the growing crystal.	25
Fig. 2.2	The reaction of RDX by-product, TAX with cyclohexanone to produce two compounds that can promote the formation of internal defects.	26
Fig. 2.3	Plot of amount of neutron scattering against LSGT sensitivity obtained by Stoltz <i>et al.</i>	39
Fig. 2.4	Photograph and schematic of the BIC used by Bouma <i>et al.</i>	41
Fig. 2.5	Micrograph of RDX crystal grown in cyclohexanone.	49
Fig. 2.6	Micrograph of RDX crystal grown in γ -butyrolactone.	49
Fig. 2.7	Micrograph of RDX crystal grown in acetone.	50
Fig. 2.8	Schematic diagram illustrating how adsorption of an impurity affects crystal morphology.	51
Fig. 2.9	Shock sensitivity results obtained by Stepanov <i>et al.</i>	60

Fig. 2.10	Illustration showing the passage of a shock wave of short duration through large crystals and a long shock passing through small crystals.	61
Fig. 2.11	Schematic illustrating the changes in crystal size and proportion of small to large crystals in a bimodal composition that increase sensitivity.	62
Fig. 2.12	Plot of RDX crystal microstrain verses proportion of co-crystallised HMX for the RDX lots tested by Herrmann <i>et al.</i>	67
Fig. 2.13	Diagram showing the arrangement of the large scale gap test.	74
 Chapter 3		
Fig. 3.1	Schematic diagram of a typical nanoindentation instrument.	79
Fig. 3.2	Diagram of a typical nanoindenter with a Berkovich tip.	80
Fig. 3.3	SEM image of a Berkovich tip.	80
Fig. 3.4	An example of an indentation versus applied load curve obtained from a BAE-RO RDX crystal using a maximum load of 200 mN.	81
Fig. 3.5	Schematic showing the basic principle of a rheometer.	83
 Chapter 4		
Fig. 4.1	A resin block with an RDX sample embedded in it.	88
Fig. 4.2	Micrograph of an RDX crystal with indentations produced at each maximum load.	89
Fig. 4.3	The CSM Nanohardness tester used in this work.	89
Fig. 4.4	Photo of the C-VOR 150 (Bohlin Instruments Ltd.) used to measure the rheological properties of the RDX-PEG suspensions.	92

Fig. 4.5	The Mettler DSC-30 instrument used for thermal analysis of RDX.	95
Fig. 4.6	Close-up view of the DSC sample chamber.	95
Fig. 4.7	Schematic of the small scale gap test used in this study.	99

Chapter 5

Fig. 5.1	Micrograph showing typical internal defect structure of Eurenco MI-RDX crystals.	101
Fig. 5.2	Micrograph showing typical internal defect structure of BAE-Royal Ordnance crystals.	101
Fig. 5.3	Micrograph showing typical internal defect structure of Dyno type II RDX.	102
Fig. 5.4	Micrograph showing typical internal defect structure of BAE Holston RDX.	102
Fig. 5.5	Mean number of small, medium and large sized internal defects per crystal for each RDX lot.	102
Fig. 5.6	Number of crystals from each lot that were dark or cloudy.	103
Fig. 5.7	Mean internal defect scores of the R ⁴ RDX lots obtained from micrograph images plotted against shock sensitivity data obtained during the R ⁴ study.	104
Fig. 5.8	Plot of mean elastic modulus versus applied load for high defect and low defect RDX lot groups.	105
Fig. 5.9	Plots of the mean stiffness against applied load for “high defect” and “low defect” RDX lot groups.	106
Fig. 5.10	Mean internal defect score for each RDX lot versus mean modulus of elasticity measured at 200 mN.	107
Fig. 5.11	Mean internal defect score per crystal versus mean indentation creep (C_{IT}) measured at 200 mN.	107

Fig. 5.12	Mean internal defect score per crystal versus mean η_{IT} measured at 200 mN.	108
Fig. 5.13	Plot of mean elastic modulus at 200 mN load against large scale gap test results from R ⁴ study.	109
Fig. 5.14	Plot of mean η_{IT} at 200 mN load against large scale gap test results from R ⁴ study.	109
Fig. 5.15	Plot of mean elastic modulus versus maximum applied load for high and low defect/small and large RDX crystals.	110
Fig. 5.16	Plot of mean creep versus maximum applied load for high and low defect/small and large RDX crystals.	111
Fig. 5.17	Plot of mean hardness vs. mean elastic modulus at 200 mN.	112
Fig. 5.18	Plot of mean hardness vs. mean creep at 200 mN.	112
Fig. 5.19	A series of photomicrographs of the same RDX crystal showing how the appearance of internal defects can change with different depths of focus.	114
Fig. 5.20	Plot of mean internal defect score per crystal against minimum load for pop-in.	117

Chapter 6

Fig. 6.1	Plots of mean viscosity verses applied shear stress for the RDX-PEG suspensions.	121
Fig. 6.2	Plots of mean shear rate verses applied shear stress for the RDX-PEG suspensions.	122
Fig. 6.3	Plots of mean shear rate verses mean viscosity for each RDX-PEG suspension.	123
Fig. 6.4	Plots of maximum shear rate and maximum viscosity against the mean morphology score of the RDX lots.	124

Fig. 6.5	Plots of maximum shear rate and maximum viscosity verses the shock sensitivity results from the R ⁴	124
Fig. 6.6	Morphology distributions for the RDX lots examined plotted as an accumulative percentage of crystals assigned to each morphology bin.	126
Fig. 6.7	Mean morphology scores of the R ⁴ RDX lots plotted against shock sensitivity.	127
Fig. 6.8	Plot showing the agreement between the mean morphology scores from the author's assessment and the multi-person assessment.	129
Fig. 6.9	Morphology distributions of the RDX lots from the multi-person assessment.	129
Fig. 6.10	Plot of total morphology scores from the original and combined bins assessment.	131

Chapter 7

Fig. 7.1	SEM micrograph showing typical surface features of a Dyno RS-RDX crystal.	134
Fig. 7.2	SEM micrograph showing typical surface features of a Dyno Type II RDX crystal.	134
Fig. 7.3	SEM micrograph showing typical surface features of an ADI RDX crystal.	135
Fig. 7.4	SEM micrograph showing typical surface features of a Holston RDX crystal.	135
Fig. 7.5	Mean surface defect scores of the R ⁴ RDX lots obtained from SEM micrograph images plotted against shock sensitivity data obtained during the R ⁴ study.	135
Fig. 7.6	The number of crystals from each RDX lot having either rough, medium rough or smooth surface.	136
Fig. 7.7	Mean number of cracks, holes, depressions and knobs per crystal from each RDX lot.	137

Fig. 7.8	Plot of shock sensitivity results from R^4 against the average standard deviation of the surface roughness calculated by Bellitto et al	138
Fig. 7.9	Typical DSC scan of a Woolwich RDX sample, showing the melting endotherm and decomposition exotherm peaks.	141
Fig. 7.10	Typical DSC scan for an unrefined Bachmann RDX sample, showing the additional endothermic peak arising from the HMX/RDX eutectic.	142
Fig. 7.11	Relationship between wt% HMX in Dyno-RS-RDX and melting endotherm onset temperature.	144
Fig. 7.12	Relationship between wt% HMX in Dyno RS-RDX and the melting endotherm energy.	144
Fig. 7.13	DSC thermograms of BAE-RO (type I) and Holston RDX (type II) in a pseudo-PBX formulation with no nitrogen purge.	146
Fig. 7.14	DSC thermograms of BAE-RO (type I) and Holston RDX (type II) in a pseudo-PBX formulation with a nitrogen purge.	146
Fig. 7.15	DSC scans of Dyno type II RDX pseudo-PBX analysed without any purge, a nitrogen purge and an air purge.	147
Fig. 7.16	Optical micrograph of RDX crystals from the 45 - 125 μm size fraction of Dyno RS-RDX.	148
Fig. 7.17	Optical micrograph of RDX crystals from the 500 – 1000 μm size fraction of Dyno RS-RDX.	148
Fig. 7.18	Shock sensitivity results from the small scale gap tests.	152
Fig. 7.19	Plot of mean packing density vs. shock sensitivity results from the small scale gap tests.	153

Appendix A

Fig. A1	Plot of mean morphology score per crystal vs. shock sensitivity results from the small scale gap tests.	161
---------	---	-----

Fig. A2	Plot of mean internal defect score per crystal vs. shock sensitivity results from the small scale gap tests.	161
Fig. A3	Plot of mean surface defect score per crystal vs. shock sensitivity results from the small scale gap tests.	162

Appendix B

Fig. B1	Plot of minimum load required for pop-in to occur versus the shock sensitivity (LSGT) results from the R ⁴ study.	163
Fig. B2	Plot of fraction of dark/cloudy crystals versus minimum load for pop-in.	164
Fig. B3	Plot of mean number of internal defects less than 10 μm in size per crystal versus minimum load for pop-in.	164
Fig. B4	Plot of mean number of internal defects greater than 100 μm per crystal versus minimum load for pop-in.	165
Fig. B5	Plot of mean elasticity of the RDX samples against the mean minimum load required for pop-in.	165
Fig. B6	Plot of proportion of elastic work against the mean minimum load required for pop-in.	166

Appendix C

Fig. C1	Measurement of the angle of repose, θ of a conical pile of RDX.	167
Fig. C2	Plot of mean morphology score against mean angle of repose.	168
Fig. C3	Plot of mean surface defect score against mean angle of repose.	168
Fig. C4	Plot of angle of repose against the shock sensitivity from the loose powder gap tests.	169

Tables

Chapter 1

Table 1.1	Some properties of RDX at RDX density of 1.70 g cm ⁻³ at 1 bar and 0 °C.	2
Table 1.2	RDX types based upon synthesis process and HMX content of final product.	4

Chapter 2

Table 2.1	Characteristics of RDX batches examined by Balliou <i>et al.</i>	30
Table 2.2	Characteristics of HMX batches examined by Borne.	32
Table 2.3	RDX lot characteristics and projectile impact test data from Borne and Beaucamp.	34
Table 2.4	RDX lot characteristics examined by Borne <i>et al.</i>	35
Table 2.5	Results from projectile impact tests from Borne <i>et al.</i>	36
Table 2.6	NQR line widths and shock sensitivities of formulations tested by Caulder <i>et al.</i>	37
Table 2.7	Particle characteristics of the RDX lots used by Van der Steen.	44
Table 2.8	RDX crystal morphology and LSGT results obtained by Matsuzaki <i>et al.</i>	46
Table 2.9	Shock sensitivity, crystal size and HMX content of the batches tested by Min-Jun <i>et al.</i>	48
Table 2.10	Characteristics of the formulations produced by Qiu <i>et al.</i>	59
Table 2.11	Mean HMX content and shock sensitivity results from the R ⁴ program.	63
Table 2.12	Crystal characteristics, HMX content and shock sensitivity of the RDX lots examined by Borne and Ritter.	64
Table 2.13	HMX content and shock sensitivity of low HMX Bachmann RDX prepared by Spyckerelle <i>et al.</i>	65

Table 2.14	HMX content and shock sensitivity results of RDX lots investigated by Oxley <i>et al.</i>	66
Table 2.15	Results obtained by Herrmann <i>et al</i> giving the mean crystal size, microstrain, total HMX content, proportions of freely crystallised HMX and HMX co-crystallised within RDX crystals.	67
Table 2.16	Some characteristics of the NOL-LSGT, IMADGT, IHEGT and water gap tests.	74
Table 2.17	Gap test results for shock sensitivity assessment performed on ARX-2020 PBX formulations by DSTO.	77

Chapter 4

Table 4.1	RDX lots used in this analysis.	85
Table 4.2	Micrographs showing RDX crystals containing small, medium and large internal defects.	87
Table 4.3	Measurement parameters used for nanoindentation experiment.	89
Table 4.4	Examples of crystals from each morphology bin with scores given for each crystal.	90
Table 4.5	Scanning electron micrographs showing examples of each of the surface defect criteria used in the surface defect assessment.	94
Table 4.6	Composition of the pseudo-PBX composition used for DSC analysis.	96
Table 4.7	Experimental parameters used for the DSC analysis.	96
Table 4.8	Amounts of RDX and HMX mixed for each spiked sample.	97
Table 4.9	RDX samples tested for shock sensitivity.	98
Table 4.10	Mean packing densities for the RDX samples.	98

Chapter 6

Table 6.1	General description of the morphology of each RDX lot.	126
Table 6.2	The combined morphology bins and their associated scores.	131

Chapter 7

Table 7.1	DSC thermogram data for raw Eurenco I-RDX.	142
Table 7.2	DSC thermogram data for raw Dyno Nobel type II RDX.	143
Table 7.3	The effect of RDX type and nitrogen purge on the thermal behaviour.	145
Table 7.4	Summary of particle size results, mean peak widths and onset temperatures are shown.	148
Table 7.5	Melting endotherm data from HMX spiked RDX samples in the pseudo-PBX composition.	149

Equations**Chapter 1**

1.1	Power index of an explosive.	1
1.2	Chemical equation for the direct nitration of hexamine to generate RDX (Woolwich process).	3
1.3	Chemical equation for the synthesis of RDX by the Bachmann process.	3
1.4	Temperature attained by compression of a gas filled void.	9
1.5	Temperature attained by two surfaces rubbing together.	13
1.6	Temperature rise in a shear band.	15
1.7	Vielle's Law.	19
1.8	Mass burning rate.	19
1.9	Chapman-Jouget relationship.	

Chapter 3

3.1	Equation for calculating indentation hardness.	75
3.2	Equation for calculating indentation modulus.	75
3.3	Equation for calculating reduced modulus.	75
3.4	Equation for calculating indentation creep.	75
3.5	Equation for calculating proportion of elastic work to total work during indentation.	76
3.6	Equation for shear stress.	76
3.7	Shear rate.	77
3.8	Viscosity.	77

Abbreviations and symbols used**Abbreviations**

ADI	Australian Defence Industries
AFM	Atomic force microscope
BAE	British Aerospace
BAE-RO	British Aerospace-Royal Ordnance
BIC	ballistic impact chamber
DMSO	dimethyl sulphoxide
DOA	dioctyl adipate
DSC	differential scanning calorimetry
DSTO	Defence Science Technology Organisation (Australia)
GBL	γ -butyrolactone
HMX	cyclotetramethylenetetranitramine, octogen
HNS	hexanitrostilbene
HPLC	high performance/pressure liquid chromatography
HTPB	hydroxyl terminated polybutadiene
IHEGT	insensitive high explosive gap test
IM	insensitive munition(s)
IMADGT	insensitive munitions advanced development gap test

IPA	isopropyl alcohol
I-RDX®	insensitive RDX, (produced by Eurenco, France)
ISL	Institute Saint Louis, France
LSGT	large scale gap test
MI-RDX	medium insensitive RDX, (produced by Eurenco, France)
MSIAC	Munitions Safety Information Analysis Centre
NATO	North Atlantic Treaty Organisation
NIMIC	NATO Insensitive Munitions Information Centre
NOL	Naval Ordnance Laboratory
NQR	nuclear quadrupole resonance
PBX	polymer/plastic bonded explosive
PEG	polyethylene glycol
PETN	pentaerythritol tetranitrate
PI	power index
PMMA	polymethylmethacrylate
PVA	polyvinyl acetate
R ⁴	reduced sensitivity RDX round robin program
RDX	cyclotrimethylenetrinitramine, hexogen, cyclonite
RESS	rapid expansion of supercritical solution
RS	reduced sensitivity
sd	standard deviation
SANS	small angle neutron scattering
SDT	shock to detonation transition
SEM	scanning electron microscopy
SNPE	<i>Societe Nationale des Poudres et Explosifs, France</i>
SSGT	small scale gap test
STANAG	standardised NATO agreement
TMD	theoretical maximum density
TNO	<i>Nederlandse Organisatie voor Toegepast Natuurwetenschappelijk Onderzoek (Netherlands Organisation for Applied Scientific Research)</i>
TNT	trinitrotoluene
XRD	x-ray diffraction
µm	micrometers

Symbols

A	surface area of energetic material
A_p	contact area of indentation
a	radius of circular surface contact area
c	speed of sound, specific heat capacity
C_{IT}	indentation creep
E_i	elastic modulus of indenter
E_{IT}	indentation (elastic) modulus
E_r	reduced elastic modulus
H_{IT}	universal instrumented hardness
J	mechanical equivalent of heat
k	thermal conductivity
m	mass rate of burning
n	refractive index
P	pressure
P_{50}	shock pressure for 50% probability of initiation
P_{max}	maximum applied load
Q_{exp}	heat of explosion
R^2	correlation coefficient
r	regression rate
T	temperature
U	velocity of reaction product particles
V	steady state velocity of shock front
V_{exp}	volume of explosion
W	load between contacting surfaces
$W_{elastic}$	elastic work performed during indentation
$W_{plastic}$	plastic work performed during indentation
α	burning rate index
β	burning rate coefficient
γ	ratio of specific heats, fracture surface energy, shear strain
γ^*	shear strain rate
ΔH_f	specific heat of formation
ΔT	temperature rise between contacting surfaces

η_{IT}	proportion of elastic work to total work during indentation
μ	coefficient of friction
ν	Poisson's ratio
ρ	energetic material density
σ	shear stress rate

BLANK PAGE

CHAPTER 1

Introduction

1.1 General Introduction to RDX

RDX, also known as cyclonite or hexogen, is an explosive of major importance. Its chemical name is cyclotrimethylenetrinitramine or 1,3,5-trinitro-1,3,5-triazacyclohexane. It has an explosive power greatly exceeding that of TNT, having a power index of 159 compared to 117 for TNT*. The velocity of detonation of RDX is also much larger being 8440 ms⁻¹ compared to only 6950 ms⁻¹ for TNT [1]. The enhanced explosive power of RDX is partially due to the fact that its energy of formation is endothermic, $\Delta H_f^\circ = +89.6 \text{ kJ mol}^{-1}$ [2]. RDX belongs to a class of compounds called cyclic nitramines and it has the molecular structure shown in figure 1.1.

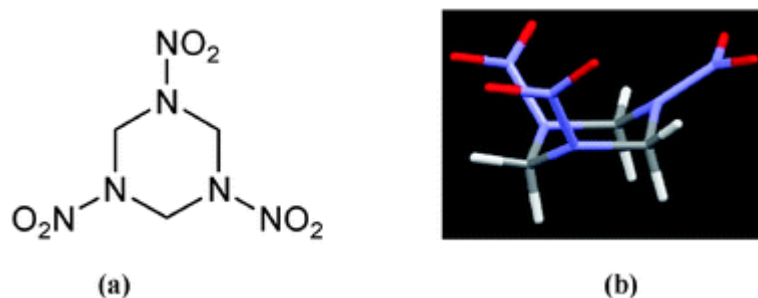


Fig. 1.1 (a) molecular structure for RDX, (b) 3D model depicting the molecular conformation under ambient conditions. Red oxygen atoms, blue nitrogen atoms, grey carbon atoms, white hydrogen atoms. From reference 3.

Under ambient conditions RDX is a white crystalline solid with a melting point of 204°C. Pure RDX crystals are shock and friction sensitive, having a figure of insensitiveness of 80 (Rotter impact machine) and a figure of friction

* The power index (P.I.) of any given explosive is calculated using the formula;

$$\text{P.I.} = 100 \left(\frac{Q_{\text{exp}} V_{\text{exp}}}{Q_{\text{pa}} V_{\text{pa}}} \right) \quad (1.1)$$

Here Q_{exp} and V_{exp} are the heat of explosion in J g⁻¹ and the volume of gaseous products produced in cm³ g⁻¹ for the explosive during detonation. Q_{oa} and V_{pa} are the same parameters for picric acid. Since the power index is a ratio then it has no units.

of 3.0 (rotary friction machine) [4]. For RDX to be used safely, it is mixed with waxes, oils, polymeric materials and plasticisers [5]. Table 1.1 gives some more physical and chemical properties of RDX.

Table 1.1 Some properties of RDX. at RDX density of 1.70 g cm^{-3} ^a, at 1 bar and 0°C ^b.

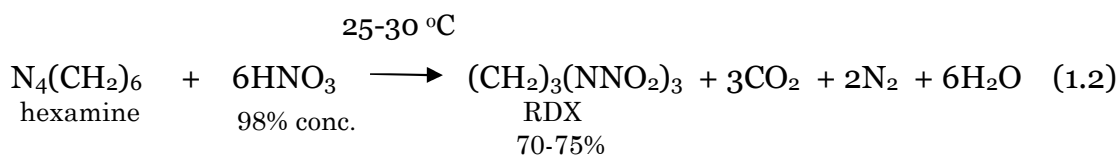
RDX characteristic		RDX characteristic	
Molecular weight, (g mol^{-1})	222.1 ^[5]	Velocity of detonation ^a , (ms^{-1})	8440 ^[1]
Melting point, ($^\circ\text{C}$)	204 ^[5]	Heat of detonation, (J g^{-1})	5130 ^[6]
Decomposition temperature, ($^\circ\text{C}$)	213 ^[5]	Pressure of detonation ^a , (kbar)	300 ^[1]
Thermal ignition temperature, ($^\circ\text{C}$)	260 ^[5]	Gas volume of det. ^b ($\text{cm}^3 \text{g}^{-1}$)	908 ^[7]
Crystal density at 20°C , (g cm^{-3})	1.82 ^[5]		
Enthalpy of formation, (kJ kg^{-1})	+318 ^[5]		

The German chemist Georg Friedrich Henning first prepared RDX in 1899 by the nitration of hexamethylenetetramine nitrate. In his patent he promoted its use for medicinal purposes [8]. He later suggested its use in smokeless propellants since it produced less smoke during decomposition than other propellants used at the time. The explosive properties of RDX were first acknowledged by Herz around 1920 who prepared RDX by nitrating hexamine directly [9], however the yields were low and the process was expensive. This was because during the reaction the hexamine molecule is not completely converted to RDX. By 1925 Hale based at the Picatinny Arsenal, U.S.A. produced a method that yielded 68% RDX. No further improvements of the synthesis of RDX were forthcoming until 1940 with the development of a continuous method devised by Meissner [10].

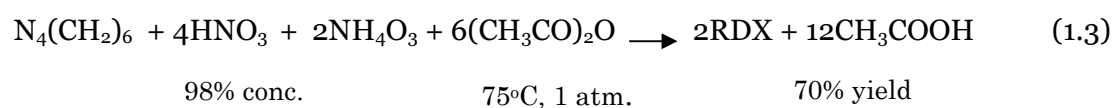
1.2 Synthesis and production of RDX

1.2.1 Overview of the processes used today

The manufacture of RDX on a large scale is usually performed by one of two synthetic routes, the Woolwich or Bachmann processes. The Woolwich process was developed at the British Armament Research Department at Woolwich in the 1920's and 30's [10]. This process is also known as the direct nitrolysis process where hexamine is directly nitrated with nitric acid to produce RDX as shown in equation 1.2.



This process produces a yield of RDX of between 70 and 75% with only traces of impurities [11]. In the U.S during the 1940's Werner Emmanuel Bachmann developed the process named after him. This process takes hexamine and reacts it with a mixture of ammonium nitrate and nitric acid in the presence of acetic anhydride at 75°C, as shown in equation 1.3 [12].



This process was adopted by the USA for large scale production of RDX. The yield is about 70% RDX with an impurity of around 8 to 12% HMX or octogen (cyclotetramethylenetetranitramine) which is an even more powerful explosive than RDX. The presence of HMX in the RDX product increases its shock sensitivity. HMX is also a cyclic nitramine consisting of an eight membered ring instead of the six membered ring structure of RDX. The molecular structure of HMX is shown in figure 1.2.

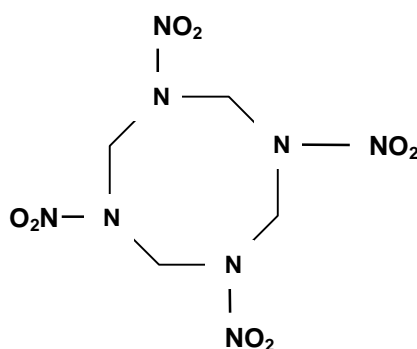


Fig. 1.2 The molecular structure of HMX.

Compared to the Bachmann process the Woolwich method produces very little HMX as an impurity. The method of manufacture and HMX content are used to classify RDX types [13]. Table 1.2 shows the classifications of RDX based upon the synthesis process (type A or B) and HMX content (type I or II) of the

final product. Type A, (Woolwich RDX) is usually type I and type B (Bachmann) is normally type II. However HMX can be removed from type B RDX by recrystallisation to create a type I RDX.

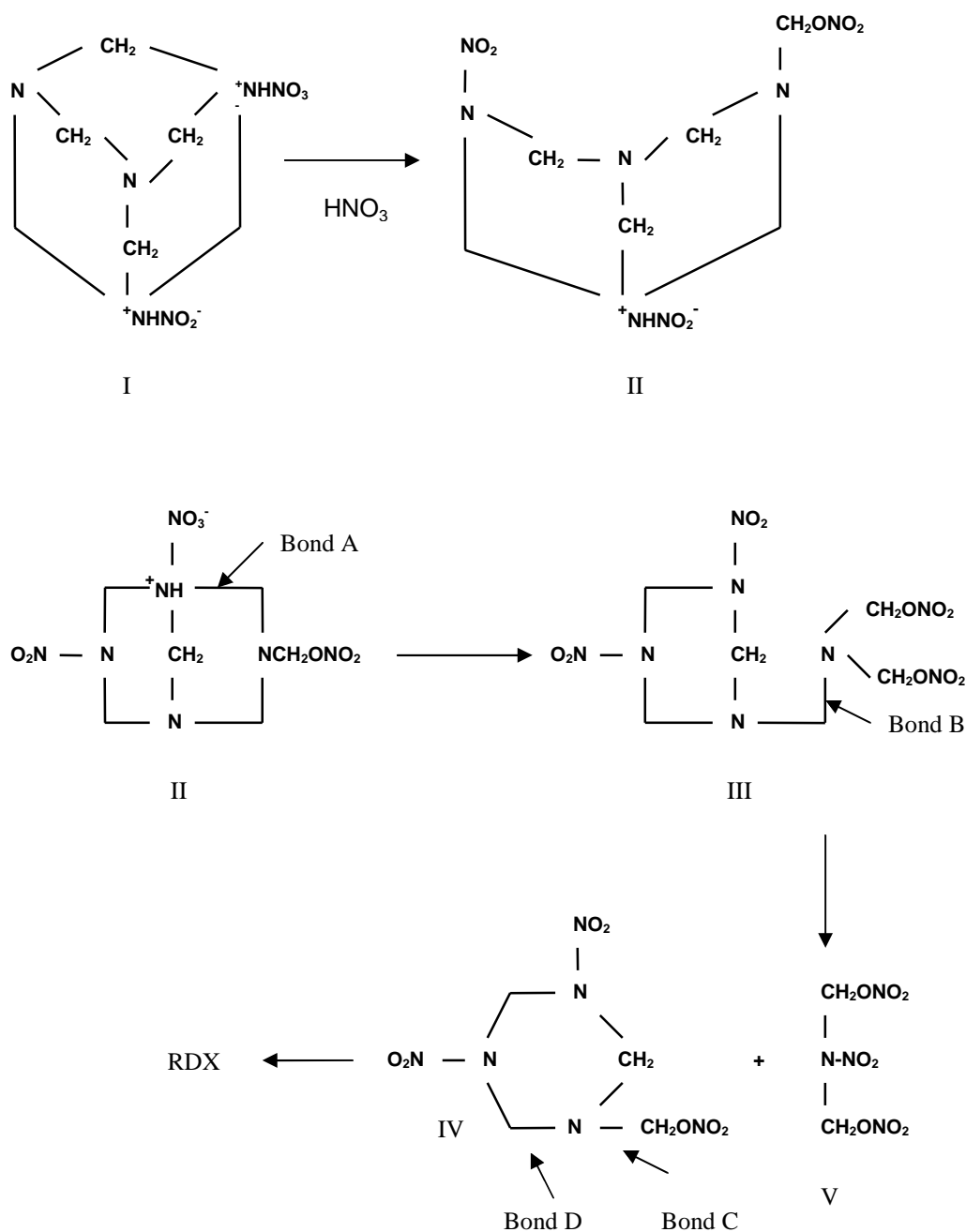
Table 1.2 RDX types based upon synthesis process and HMX content of final product.

RDX type	Synthesis method / HMX content
Type A	Produced by the Woolwich process (direct nitration) ^[13]
Type B	Produced by the Bachmann Process ^[13]
Type I	< 5% HMX ^[14]
Type II	4 - 17% HMX ^[14]

1.2.2 Possible reaction mechanisms for the synthesis of RDX

The nitration of hexamine with nitric acid can be regarded as proceeding in a stepwise nitrolysis reaction. During the nitration of the amine the bonds between the nitrogen and carbon atoms are broken ^[15]. A proposed reaction pathway is shown in figure 1.3.

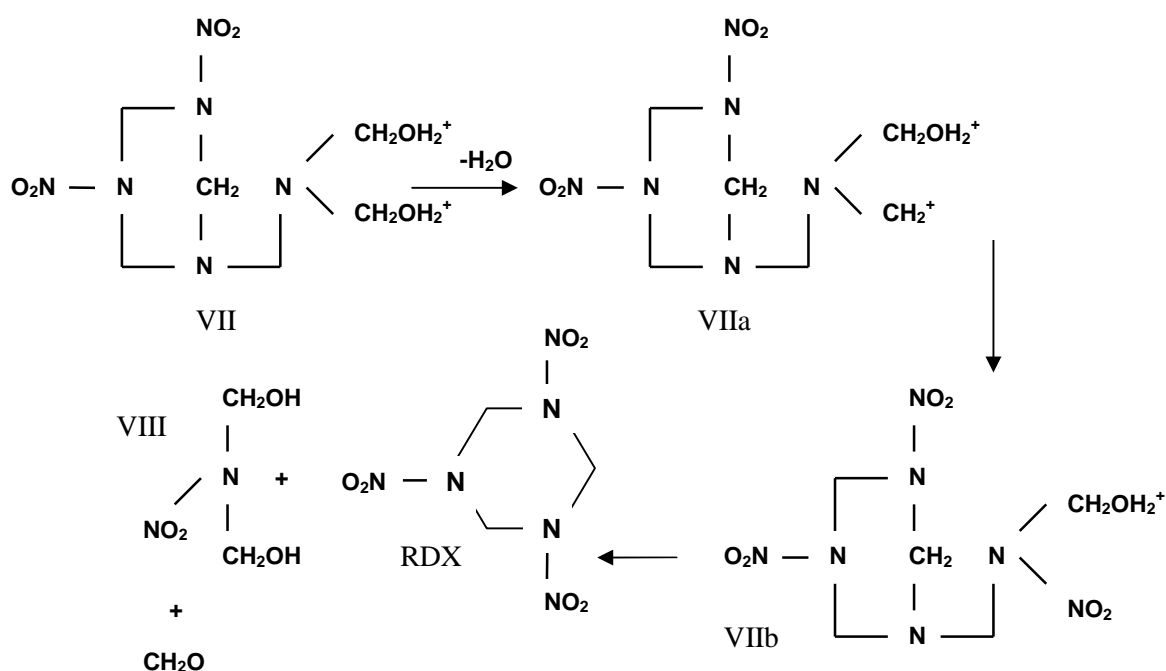
Fig. 1.3 Reaction schemes showing the formation of RDX by the action of nitric acid on hexamine dinitrate (adapted from reference 15).



Starting with the nitrolysis of hexamine dinitrate (compound I) by nitric acid the intermediate (compound II) is formed [16]. The reaction proceeds via further cleavage of N-C bonds, experimental data indicating that bond A breaks making a hypothetical intermediate III [15]. This intermediate undergoes further nitrolysis at bond B to form another hypothetical

intermediate, IV and compound V [17,18,19,20]. The nitrolysis of bond C on intermediate IV gives RDX, (VI). An open chain impurity product can also form if bond D is nitrolysed [15]. Another mechanism, shown in figure 1.4, involves the nitracidic ion (H_2NO_3^+) [21]. Hexamethylenetetramine is first hydrolysed to form III as shown in figure 1.3 then hydrolysis of III forms the ionic intermediate VII. This intermediate can be hydrolysed further to form VIIa and then VIIb. Nitrolysis of VIIb produces RDX, methylnitramine (VIII) and formaldehyde. Nitrolysis of compound II can also produce HMX.

Fig. 1.4 Reaction scheme showing the formation of RDX via the influence of the nitracidic ion, ref. 15.



1.2.3 Recrystallisation methods used in RDX manufacture

After the crude RDX product is produced it is purified to remove undesirable contaminants that are formed during its synthesis. For instance the by-product produced by nitrolysis of bond D in figure 1.3 can sensitise the RDX product [15]. This is done by recrystallisation usually by cooling or evaporating RDX saturated acetone or cyclohexanone solutions [22]. The recrystallisation process is of fundamental importance to the quality of the final product [23]. It has been observed that poorer crystal quality caused by internal voids, inclusions and other crystal defects leads to increased sensitivity [24]. Recrystallisation is often carried out on a large scale. One method described uses a 110 kg RDX batch dissolved in 900 litres of acetone at 50°C. This solution is filtered and drained into a second tank where cold water is added. The RDX crystals precipitate out of the acetone-water solution and are separated on a vacuum filter. Approximately 90% of the crystals produced by this method are 0.1 mm or longer [25].

Recrystallisation can also be carried out on smaller scale batches using crystalliser vessels of a few litres capacity. This technique uses cooling crystallisation where the temperature of the solution is gradually reduced at a steady and carefully controlled rate. The solubility of the RDX decreases with decreasing temperature, leading to supersaturation of the solvent which is the driving force behind crystal nucleation and growth [26]. Stirring the solution to maintain suspension of the RDX particles has been reported to reduce crystal quality compared to crystals grown in stagnant solution. Crystals grown in a stirred solution have more inclusions probably containing the solvent solution. This is thought to be due to collisions between crystals in the turbulent solution [27] leading to damage and defects on their growing surfaces. These surface defects could develop into internal defects as the crystal grows.

1.3 Hot spot theory of initiation

The detonation of an explosive is now generally considered to be a thermal process [28,29]. However, it was known for many years that the energy supplied to an explosive material by impact was not sufficient to raise its temperature high enough for deflagration or detonation to occur. Therefore it was

concluded that localisation and concentration of energy in discrete regions of the bulk of the explosive must be occurring [28,29 30]. Research carried out to find the causes of initiation in solid explosives by friction produced the concept of “hot spots” in 1952 by Bowden and Yoffe. They proposed that hot spots are produced by; adiabatic compression of gas bubbles trapped in the energetic material, friction between the explosive confinement surfaces or between individual explosive crystals/grit particles and finally viscous heating due to rapid flow of explosive between impacting surfaces [31]. The formation of shear bands, caused by a non-uniform stress distribution within a crystal, has subsequently become a recognised mechanism. The energy released by shear banding can significantly raise the temperature of the surrounding material. Other mechanisms have additionally been suggested, such as heating at crack tips and dislocation pileups [28], however these processes have been shown to be insufficient on their own to form hot spots. It appears that the formation of hotspots occurs by a variety of processes none of which is singularly dominant. An overall description of a hot spot can be given as:

- 1) a region where mechanical energy is highly localised and concentrated
- 2) existence of a thermal mass surrounding this localisation
- 3) creation or existence of a region occupied by gas
- 4) heat flow between these regions
- 5) reaction chemistry occurring in the gas and or gas/solid interface [32]

It has been calculated that for a hot spot to be able to cause an initiation of an explosive it has to reach a temperature of at least 500°C, last between 10 μ s and 1 ms and have a size between 0.1 and 10 μ m [31]. With a larger hot spot the temperature produced is lower as the thermal energy is dissipated more rapidly. Therefore, initiation in energetic materials may also occur at much lower temperatures if the initiation temperature of the explosive is low enough.

1.3.1 Initiation by rapid collapse of gas filled bubbles and spaces

In both solid explosives such as RDX and liquid explosives like nitroglycerine there are very tiny gas bubbles and voids which sensitise these materials to shock and impact. These gas bubbles and spaces become hot spots during their compression by an applied shock. The compression raises the

temperature of the trapped gas to a point where the surrounding material can reach its decomposition temperature. Figure 1.5 illustrates the collapse of a bubble by a shock wave, the trapped gas inside reaching a temperature high enough for light to be emitted.

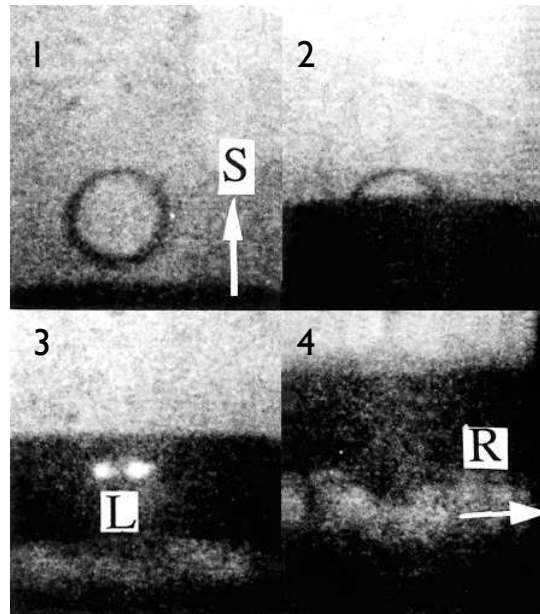


Fig. 1.5 Photographs showing a bubble in an inert gel being collapsed by a shock wave, S of 2.0 GPa strength. In frame 3 glowing lobes of trapped gas within the bubble L , are formed due to the high temperature reached during its compression. Frame 4, reaction products are being dissipated, R . From reference 33.

The temperature attained by an ideal gas in a compressing bubble depends upon its initial pressure before compression and its final pressure. This is expressed in equation 1.4.

$$T_2 = T_1 \left(\frac{P_2}{P_1} \right)^{\gamma-1/\gamma} \quad (1.4)$$

Here T_1 and T_2 are the initial and final temperatures of the gas bubble and P_1 and P_2 are the initial and final pressures within the bubble, and γ is the ratio of the specific heats. It can be seen from this relationship that the final temperature reached by the gas bubble is dependent upon the initial pressure inside. A higher initial gas pressure will result in a lower final temperature.

This has implications for how the explosive will behave when subjected to a shock. For example, if nitroglycerine is subjected to an impact energy of 5000 g cm at an initial pressure of one atmosphere an explosion will occur but if the initial bubble pressure is raised to 20-30 atmospheres no detonations are observed at the same impact energy [31]. Chaudhri and Field's work indicated that gas filled bubbles ranging in diameter from one millimetre to 50 μm , when compressed by a relatively weak shock of 0.1 GPa, were able to initiate explosives including PETN. They also observed the formation of a jet within the bubble during its collapse travelling in the same direction as the shock front, but they concluded that jet formation did not cause initiation of the explosive. To investigate the importance of thermal transfer from the collapsing bubble to the explosive an explosive crystal (lead azide) was coated with a 300 nm thick film of gold or silver. It was found that this greatly reduced the chance of initiation in the explosive when the bubble was shocked. They concluded that adiabatic heating of the gas bubble during its collapse and thermal transfer were the major causes of hot spot formation and initiation of explosive [34]. In a later study Field and Bourne used slabs of an explosive emulsion made of ammonium nitrate/sodium nitrate with cylindrical cavities formed into them. These slabs were subjected to shocks ranging from 0.3 to 10 GPa. On impact of the shock wave a jet was formed that travelled in the same direction. The jet crossed the cavity and struck the opposite side of the cavity sending a shock into the surrounding material. The trapped gas within the cavity was compressed rapidly and heated to a temperature high enough to cause luminescence, suggesting that the trapped gas attains temperatures of at least 800 K. The duration of these high temperatures was under 1 μs . When the jet penetrated the opposite wall a pair of vortices was generated which then travelled forward with the advancing shock front. When the cavity collapsed in the explosive material a reaction was observed in the vapour in the cavity and in the surrounding material. In contrast to Field's earlier work the principle mechanism of ignition was considered to be caused by jet formation and jet impact in the collapsing cavity [35]. Using high speed photography work has also been undertaken investigating the collapse of 2D cavity arrays in inert gels. 3 mm diameter cavities were arranged in a 3 x 3 array and subjected them to a shock of 0.26

GPa from one side. It was observed that during collapse of the cavities a high speed jet was produced which compressed trapped gas into two lobes. The gas in these lobes became hot enough to glow. The glowing was attributed to free radical recombination and radiative recombination. This indicates a possible hot spot formation mechanism in energetic materials. The cavities collapsed layer by layer, the second row only being compressed after the shock collapsed the first layer [36,37]. In figure 1.6 bubble collapse and lobe formation during compression by a shock wave is demonstrated and in figure 1.7 a series of high speed photographs show the progressive collapse of three voids in an inert gel matrix after the application of a shock.

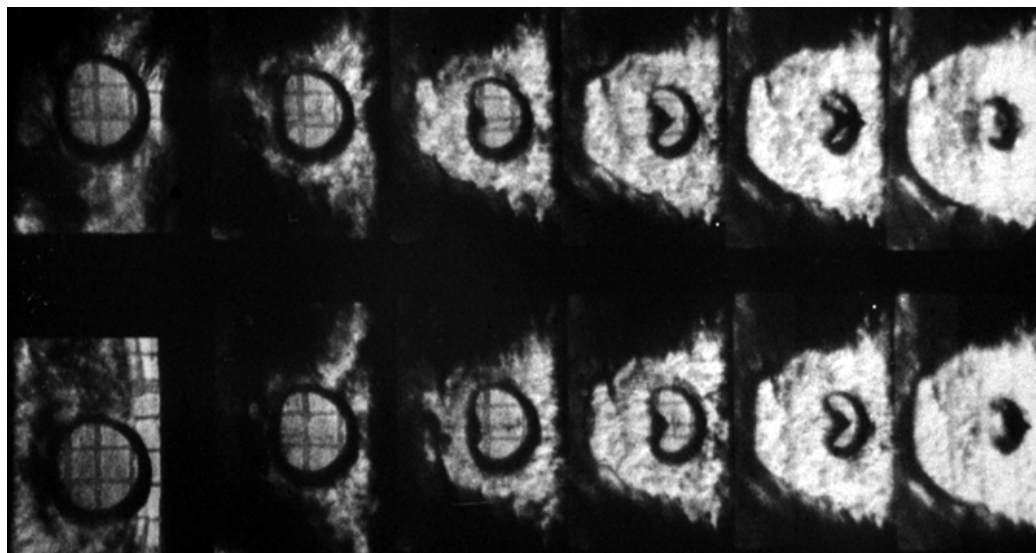


Fig. 1.6 Series of high speed photographs showing the collapse of a bubble and the production of lobes of trapped gas. From reference 33.

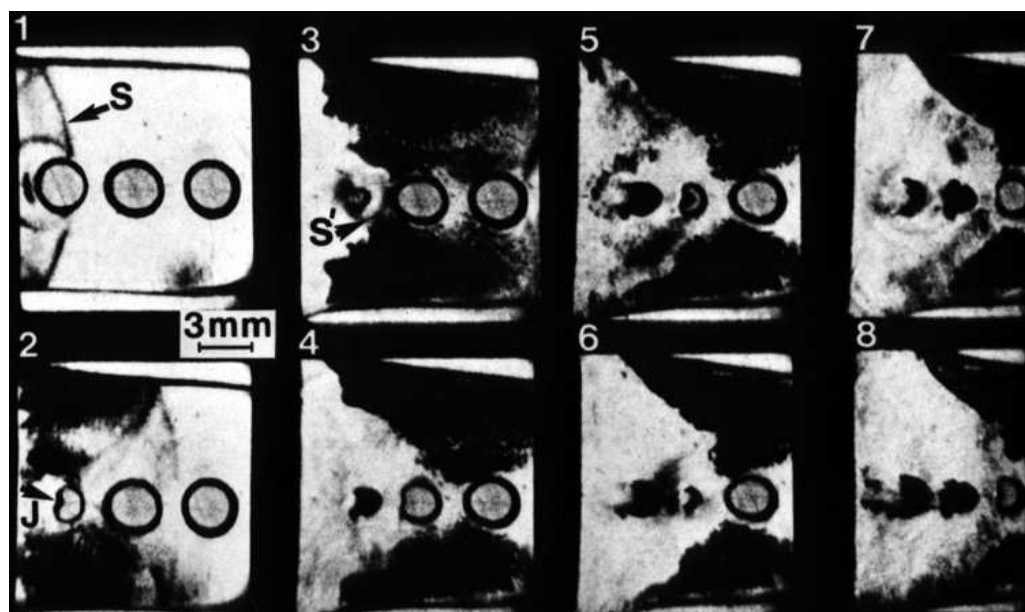


Fig. 1.7 Series of high speed photographs showing the progressive collapse of voids in an inert gel. The shock front is shown in frame 1 labelled S. From reference 33.

In conclusion, when a larger cavity is collapsed relatively slowly the adiabatic heating of the trapped gas is the major process behind hot spot formation. At high shock pressures, the formation of a jet and subsequent jet impact becomes more important. It can be generalised that bubbles and gas filled spaces have a significant role in the initiation of energetic materials. Voids that are filled with solvent are less able to form hot spots since they cannot reach high enough temperatures because liquids are less compressible than air or other gases.

1.3.2 Initiation by friction

Hot spot formation by friction is another important source of initiation of explosives. When two surfaces are rubbed together, unless they are perfectly smooth contact will occur at the highest surface features. Therefore the actual area of contact between the surfaces is small. During rubbing heat will build up in these areas leading to high temperatures and hot spot formation. This principle is shown in figure 1.8 which depicts the movement of two rough surfaces against each other producing regions of high temperature where the frictional stress builds up.

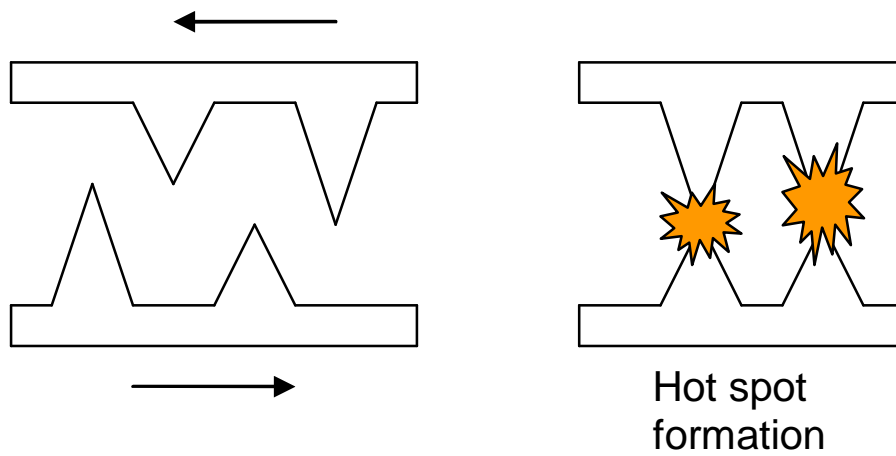


Fig. 1.8 Illustration showing the formation of hot spots caused by frictional forces between rubbing surfaces.

The maximum temperature reached by these localised regions is dependent on the material with the lowest melting point. When this temperature is reached and melting occurs, any hot spots that are formed are extinguished. When the material starts to melt, frictional forces are reduced, leading to lower localised stresses and heat dissipation is faster through the liquidified material. These effects act to inhibit hot spot development. However if the decomposition temperature of the energetic material is lower than its melting point, then melting will not have much effect. This is the case with primary explosives such as lead azide which decompose before melting. The thermal conductivity, hardness, coefficient of friction and how quickly the contacting surfaces are moving are also important in the generation of hot spots. The temperature rise, ΔT between the contacting surfaces can be found using equation 1.5 If this temperature rise is great enough initiation of the explosive will occur.

$$\Delta T = \frac{\mu W V}{4aJ} \frac{1}{k_1 + k_2} \quad (1.5)$$

Here μ is the coefficient of friction, W is the load between the contacting surfaces, V is the velocity of the surfaces, a is the radius of circular contact

area, J is the mechanical equivalent of heat and k_1 and k_2 are the thermal conductivities of the contacting materials. It can be seen from this relationship that a combination of a lower thermal conductivity, higher rubbing velocity and higher applied load gives a larger increase in surface temperature. The addition of grit particles to a solid explosive is a well known method of increasing its sensitiveness. The melting point of the grit material is an important factor. When grits of different melting points were added to PETN and subjected to a friction test, initiation was only observed when the grit had a melting point greater than 430°C. The same minimum melting temperature was seen for experiments with RDX. Again the reasons for this are due to the reduction of friction between the particle and explosive as a particle melts and increased heat conduction, leading to inhibition of hot spot formation. The size and hardness of grit particles also have an effect. Particles larger than 100 μm are more effective in initiating explosives than smaller ones. For many smaller particles the impact and frictional energy is dissipated over many contact points over a larger area indicating that hot spot generation is not as efficient. Harder particles are also more efficient as they are less likely to break and deform and so are better at localising thermal energy. The duration of hot spots formed by friction is generally between 1 ms and 10 μs [31]. Stab initiation is used in some explosive applications and is essentially a frictional process. As the needle enters the explosive it picks up a layer of explosive crystals which rub against the crystals of the bulk material. This leads to generation of hot spots and initiation of the explosive charge [38].

1.3.3 Initiation by localised adiabatic shear

When a material is subject to a shock event it will be deformed by the shock front. The deformation will not generally be uniform through the material but is localised in bands running through the material produced by adiabatic shearing. Adiabatic shear bands can be formed if two conditions are met. Firstly the rate of heat production by plastic flow is greater than that lost by conduction leading to a rise in temperature. Secondly the rate of thermal softening in the shear band is greater than the rate of work hardening. The increase in temperature at these shear bands can be large enough to form hot spots. This temperature rise, ΔT can be calculated if the conditions for

adiabatic shear are present. If the rate of heat production at a shear band is σV , where σ is the shear stress and V is the velocity of the shear, the temperature rise after time t is given by equation 1.6.

$$\Delta T = \sigma V \left(\frac{t}{\pi k \rho c} \right)^{\frac{1}{2}} \quad (1.6)$$

Here k , ρ and c are the thermal conductivity, density and specific heat capacity of the material. Figure 1.9 shows how shear bands are formed during impaction.

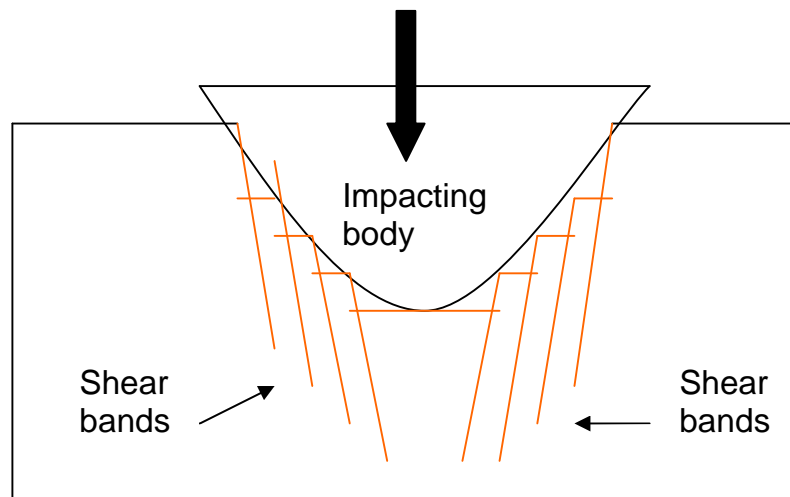


Fig. 1.9 Diagram illustrating the formation of shear bands within a material during impaction by a penetrating body.

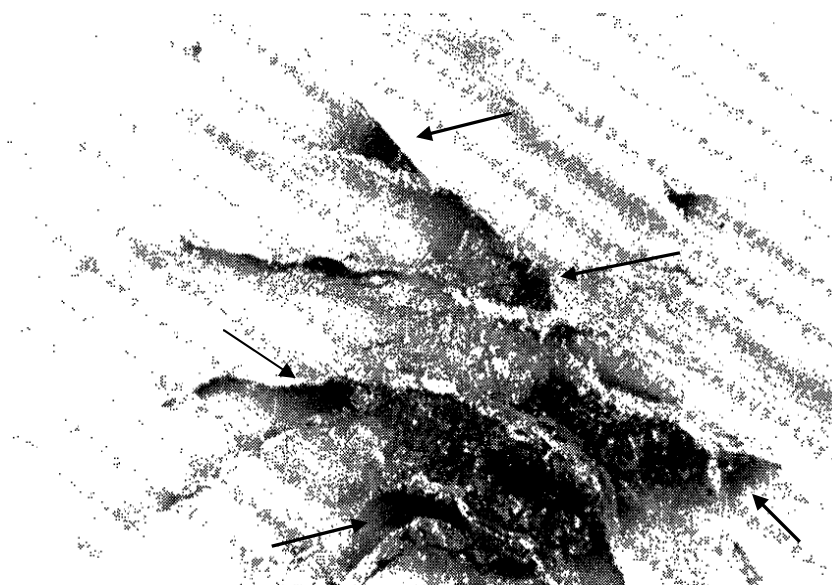


Fig. 1.10 Photo showing shear banding produced during impact of HMX. Note the darker areas at the branches of the bands where the highest temperatures were reached (indicated by arrows). Taken from reference 29.

Winter and Field have shown that when lead and silver azide single crystals are impacted by small aluminium and glass spheres, initiation by the formation of adiabatic shear bands can occur [39]. Drop weight impact experiments on small quantities of PETN and HMX placed on a heat sensitive film also indicate the formation of shear bands during initiation of the explosive. Bands were burned into the film where the highest temperatures were reached. Some of the bands were seen to split, the highest temperatures were reached at these points [29,40]. Figure 1.10 shows the shear banding produced after impact of HMX placed on heat sensitive film.

1.3.4 Hot spot formation at crack tips and dislocations

When an explosive material is impacted by a strong shock cracks may appear at weak points within the explosive crystals or if in a PBX, in the crystals and binder matrix. High stresses can be produced at the tips of these cracks leading to localised increases in temperature. The development of high temperatures at crack tips in plastically deforming materials like metals and polymers is well known. For example a temperature rise of 500 K has been reported at the crack tips in deforming polymethylmethacrylate [41]. Fox and

Soria-Ruiz have reported that temperatures of at least 850 K are generated at the crack tips in lead azide suggesting that this is a possible initiation method in energetic materials [42]. However, there is also evidence that shows that the temperatures generated at crack tips are not sufficient to cause initiation in energetic materials. Chaudhri subjected individual lead azide crystals to impacts. For impact velocities less than 75 ms^{-1} fragmentation but no initiation of the crystal was observed. A high speed crack was seen but with no evidence of ignition at the crack tip [43]. Further experimental evidence showing that propagation of cracks through energetic materials without causing initiation has also been reported by Chaudhri [44]. The most probable reason why viable hot spots are not formed by crack tip heating in energetic materials is that the energy release is too small to give the required hot spot size and temperature. This is possibly due to the low fracture surface energies γ , of many explosives, RDX, HMX and PETN for example have γ values of approximately 0.1 J m^{-2} . Therefore, in a pure homogeneous explosive, initiation by crack tip heating is unlikely but if a polymer or metallic particles are added to the explosive as in a PBX, then this is a possible mechanism of initiation. In comparison to explosives, polymers like PMMA and steels have high γ values, typically several hundred joules per square metre, PMMA having a γ of between 200 and 350 J m^{-2} [45]. Since these materials release greater energy during crack tip formation, fracturing in embedded particles produces rapid heating of the surrounding explosive leading to detonation [46]. So far, all the hot spot mechanisms discussed occur at a macroscopic scale. The formation of hot spots at dislocations within the crystalline lattice is of course at a much smaller level. A dislocation site gives rise to a weak point within the crystal lattice structure, however just a single dislocation is insufficient to cause a hot spot to form. It is thought that several dislocations close together create pile ups which can then form hot spots, the energy being localised along the slip planes of the crystal lattice [47]. The main objection here is that for a hot spot to be effective in causing initiation, it has to be at least $1 \text{ }\mu\text{m}$ therefore this raises the question; can a dislocation pile up create a hot spot large enough. Studies of HMX samples impacted in a drop weight apparatus, showed ignition only occurred after compaction and compression. Dislocation formation and movement would occur during the

early stages of impact and cause ignition in the initial moments of compression. However, no evidence of this was seen. Therefore, it was concluded that initiation was by a macroscopic process such as shear banding and not due to dislocations within the crystal lattice [29]. Single crystals of PETN and RDX when impacted with 100 μm particles at velocities between 105 and 200 ms^{-1} , were observed to form linear arrays of dislocations, but no initiation of the sample occurred [48]. In summary, crack tips and dislocations can create hot spots but they are unlikely to form “critical” hot spots of sufficient size and temperature to cause initiation of an explosive.

1.4 Overview of the processes of deflagration and detonation

This section will give a basic explanation how deflagration and detonation events proceed and the factors that influence them. During deflagration or detonation the energetic material is consumed and converted into stable low energy products by thermal decomposition. The major difference between the processes is the kinetics of the chemical reactions driving them, the reaction rate of a detonation being orders of magnitude faster than a deflagration. These processes will be described in the following sections [49,50].

1.4.1 Deflagration

Deflagration is the term for the process of rapid burning of an energetic substance. It is faster and more sudden compared to most combustible materials. In some cases the reaction may stop if energy loss to the surroundings is greater than that produced by the reaction. The rate of the reaction will increase if it is confined. When the material is enclosed within a sealed metal container, or under self confinement, then the gaseous reaction products cannot escape leading to a pressure build up. The increased pressure increases the burning rate and subsequently the temperature also increases. This situation is self-propagating and can lead to a detonation if the pressure becomes high enough. The deflagration process is considered to be a surface process where the reaction takes place in the combustion zone in the vicinity of the surface of the energetic material. It can also be viewed as a layer by layer process where the unreacted material just behind the reaction zone is heated by thermal conduction until it ignites. The burning zone recedes through the

material being consumed in a direction perpendicular to the materials surface. This concept is expressed as Piobert's Law (1839). The burning or regression rate is dependent upon instantaneous pressure (P) at the energetic materials surface and can be obtained using the relationship known as Vieille's Law (1893), equation 1.7.

$$r = \beta P^\alpha \quad (1.7)$$

The regression rate, r is given as mm s^{-1} , β is the burning rate coefficient and is dependent upon the units of r and P , α is the burning rate index and is determined experimentally by plotting the burning rate against pressure. Another way of expressing the rate of deflagration is the mass rate of burning, m . This is the mass of energetic material that is consumed per unit time. The mass burning rate can be calculated using equation 1.8.

$$m = rA\rho \quad (1.8)$$

The mass burning rate is dependent on the surface area of the energetic material A and its density ρ . From this relationship it can be seen that the deflagration rate of an energetic material will increase with higher density and/or larger surface area. Gun propellants are therefore produced as materials with a large surface area. When ignited, they burn rapidly to produce large volumes of gaseous combustion products and consequently a high pressure within the breach which propels the projectile. Compared to detonation, deflagration proceeds at a relatively slow rate. A strand of typical gun propellant burns at approximately 5 mm s^{-1} when unconfined (when confined in a gun the velocity is about 400 mm s^{-1}). The speed of the reaction zone through the material is always subsonic and is dependent upon the rate of heat transfer to the unreacted material.

1.4.2 Detonation

a) General description and theory

Energetic materials that detonate exhibit a more rapid decomposition than deflagration. Instead of the decomposition zone being propagated by thermal energy transfer at subsonic speed, the reaction zone is driven by a supersonic shock wave travelling at between 1500 and 9000 ms^{-1} . The decomposition rate of the energetic material is controlled by the velocity of the shock wave which is in turn dependent upon the density of the explosive. Therefore the density of the explosive is a major limiting factor in the rate of decomposition in a detonative event. Like deflagration, a detonation can be considered to be a layer by layer process. Consider a cylindrical length of explosive as shown schematically in figure 1.11. As the shock wave passes through the explosive, unreacted material is decomposed in the reaction zone directly behind the shock wave front. Behind the reaction zone the decomposition products that have been formed flow away from the wave front.

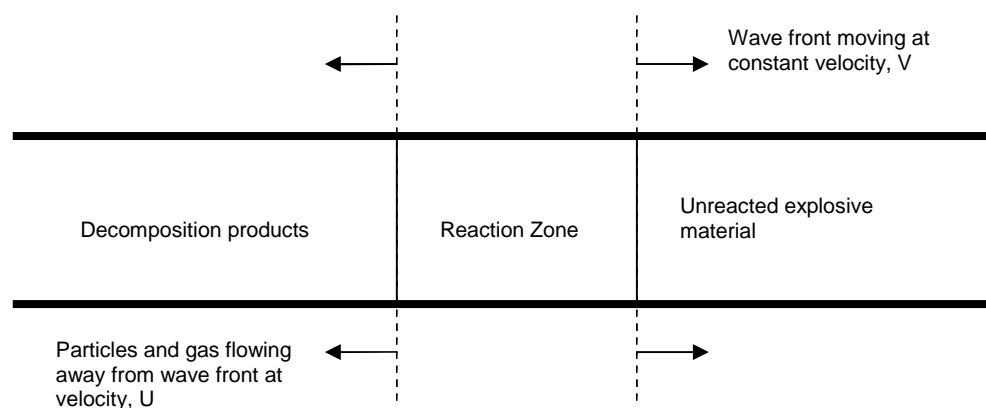


Fig. 1.11 Schematic diagram of a detonation wave passing through an explosive, reproduced from reference 49.

The shock wave compresses the explosive material so that its temperature increases above its decomposition temperature, an exothermic reaction then takes place within the explosive. The gaseous products generated raise the pressure just behind the wave front driving it forward. The shock wave accelerates through the explosive material and increases in strength until it reaches a steady state velocity, V . The steady state is reached when the rate of

energy release from the detonation equals the rate at which it is lost to the surrounding medium and equals the energy used to compress and displace the explosive material. At the steady state velocity the shock wave will be supersonic. The shock wave will move forward through the explosive as long as its velocity is the sum of the speed of sound, c and the velocity of the reaction product particles, U as expressed by the Chapman-Jouguet relationship:

$$V = U + c \quad (1.9)$$

When the velocity of the decomposition products is less than the speed of sound then detonation will not occur. Figure 1.12 shows a series of high speed photographs of a detonation wave passing through a steel cylindrical charge. The detonation starts from the top of the charge and can be clearly seen to travel down its length leaving behind a cloud of detonation products. The photos also illustrate the concept of “run to detonation” where the shock wave accelerates through the charge for a distance of a few millimetres before reaching supersonic (detonation) velocity.

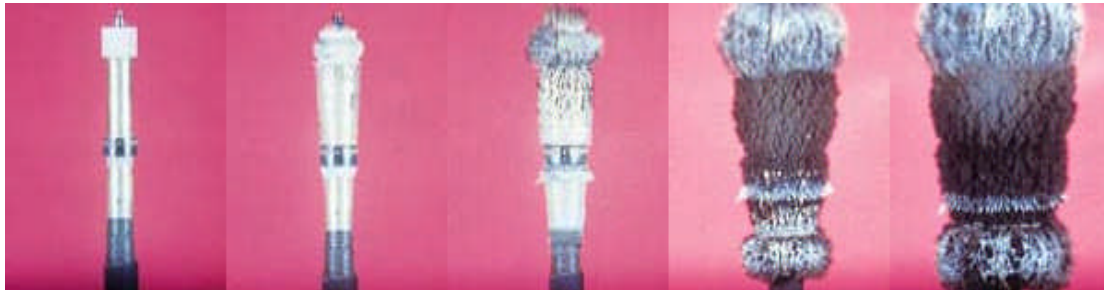


Fig. 1.12 A series of high speed photographs showing a detonation wave passing through a steel cylindrical charge. Taken from reference 51.

Another factor that is important to the propagation of a detonation shock wave is the diameter of the explosive charge. If the diameter is too small the energy of the shock wave will be attenuated to the surrounding medium and lost, therefore a critical diameter is needed for the shock wave to be able to sustain the detonation. This critical diameter varies depending upon the

energetic material and its composition. Initiation of a detonation can occur by two possible processes, burning to detonation or shock to detonation.

b) Burning to detonation

Initiation of a detonation by this method starts by burning of the energetic material. After initial ignition of the material, the speed of the reaction zone rapidly increases to become a supersonic shock wave, the burn to detonation transition is reached. This situation is best visualised as an explosive burning in a confined tube from one end. As the pressure builds up, the reaction rate increases until a sonic shock wave is formed. The burning rate index, α provides the indication that an energetic material will burn to detonation. If it is greater than unity or increases with increasing pressure, then the material will burn to detonation, on the other hand if it is less than unity the material will only deflagrate. There is a delay between the start of burning and the eventual detonation in this situation. The duration of this period depends upon the explosive material, its particle size, density and degree of confinement. An example of an application of a burn to detonation event is in a blasting detonator. The detonator contains lead azide which is ignited and rapidly burns to detonation, initiating the explosive charge.

c) Shock to detonation

Shock to detonation requires the application of a high velocity shock wave from another detonating charge in close proximity (called the donor charge) to the charge being detonated, the receptor charge. Ideally both charges should be in contact to minimise attenuation of the shock wave from the donor. The shock wave on entering the receptor charge compresses the explosive and causes adiabatic heating. Up to this point the shock from the donor charge has been decelerating as it is doing work on the receptor explosive. However, the heating caused by the shock wave raises the temperature of the receptor explosive beyond its decomposition temperature, initiating a decomposition reaction. This release of thermal energy and pressure re-accelerates the shockwave to supersonic velocity leading to a detonation in the receptor charge. The shock to detonation transition is much faster than the burn to detonation transition. The burn to detonation transition may take several

seconds to complete but the shock to detonation transition is measured in microseconds. The shock to detonation method of initiation is the most reliable way of initiating a charge of high explosive as long as the shock wave from the donor is strong enough and the diameter of the acceptor charge is equal to or exceeds the critical diameter of the explosive material.

1.5 Summary

The hot spot theory offers a good explanation for the processes behind initiation of energetic materials. It appears that there are several key methods of hot spot formation which probably occur together, but no single mechanism seems to dominate the process. The different formation mechanisms appear to act additively. For instance frictional processes may occur alongside adiabatic heating of gas filled spaces within the material. Heating at crack tips and dislocation pile ups generally seems unable to cause initiation due to the small amounts of energy released by these methods. The energy released is between two and three orders of magnitude too low for initiation to occur. Crack tips forming in polymer particles within a PBX could possibly be a mechanism for hot spot formation.

CHAPTER 2

Literature review

This chapter will investigate the literature that addresses the issues affecting RDX sensitivity. Areas to be investigated include crystal size and size distribution, crystal morphology, internal and surface crystal defects, impurities and HMX content and the interaction between energetic crystals and binder particles.

2.1 The influence of internal crystal defects, voids and inclusions

During the crystallisation process void defects within the crystal often form ranging in size from less than a micrometre to over a hundred micrometers. These defects are a potential site for hot spot formation when they are collapsed by shock compression. This section will firstly explain their formation and then cover literature that has investigated the effect of internal defects on shock sensitivity.

2.1.1 The formation of internal crystal defects

Impurities in the solvent and in the energetic material are involved in the formation of internal defects during the crystallisation process. An impurity that can build into a growing crystal has to have a molecular structure that is similar to the molecules forming the crystal. If the impurity molecule has a large moiety which is very different in structure to the crystal molecules then crystal growth is disrupted by steric hindrance. Other molecules joining the growing crystal lattice cannot pack correctly around the impurity molecule. This leads to the formation of an internal crystal defect as depicted in figure 2.1. A possible mechanism of impurity formation has been suggested by Ter Horst *et al* [52]. They propose that by-products from the synthesis of RDX react with cyclohexanone to produce molecular species that promote the formation of internal defects.

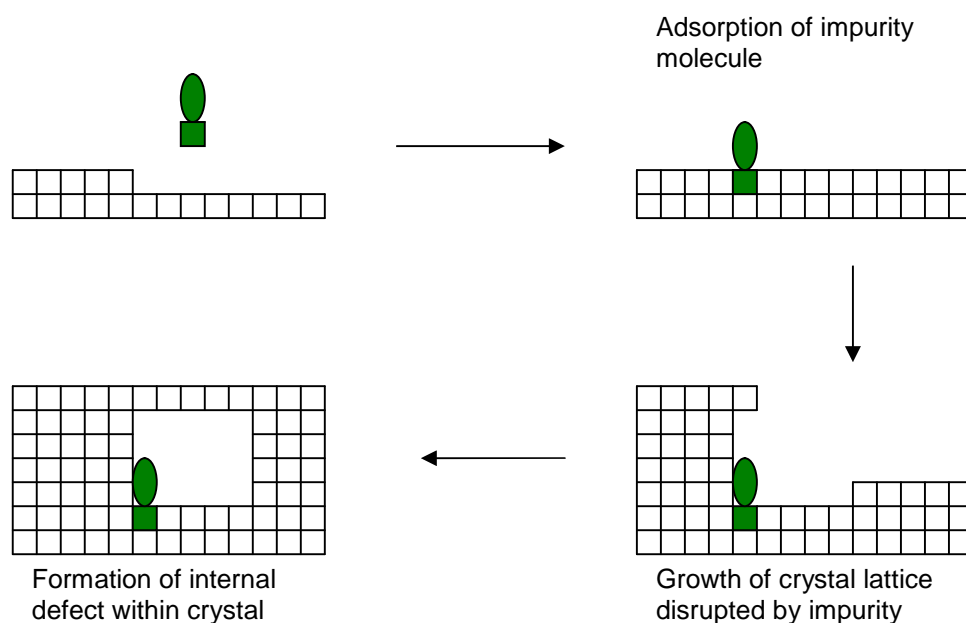


Fig. 2.1 Schematic diagram illustrating the formation of an internal defect caused by the adsorption of an impurity molecule into the growing crystal. Reproduced from reference 52.

One such by-product is the N-acetyl derivative, TAX[†]. The TAX molecule can react with cyclohexanone via condensation reaction to produce two compounds which are capable of blocking growth by steric hindrance. This reaction is shown in figure 2.2.

[†] The definition of TAX was not given in the paper.

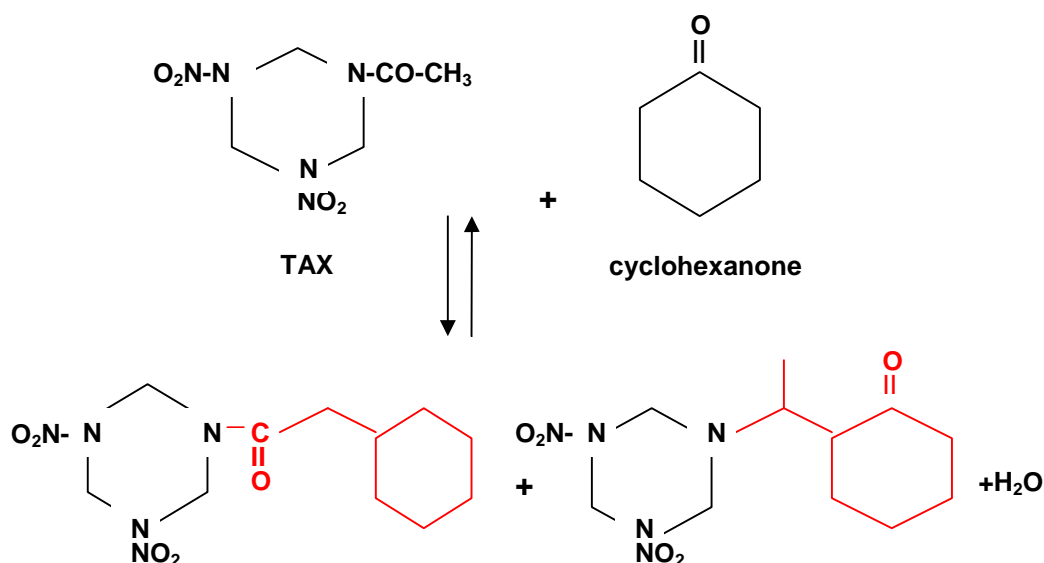


Fig. 2.2 The reaction of RDX by-product, TAX with cyclohexanone to produce two compounds that can promote the formation of internal defects. The moieties in red disrupt growth of the crystal lattice by steric hindrance. Reproduced from reference 52.

As this is an equilibrium reaction, addition of water to the RDX/cyclohexanone solution would shift the reaction back to the unreacted cyclohexanone and water. This would then prevent the formation of the impurity and subsequent internal defects. It has in fact been observed that when RDX is recrystallised from cyclohexanone containing 3 wt.% water, hardly any internal defects are seen within the crystals compared to recrystallisation from cyclohexanone only [27,52].

Internal defects are also produced by other processes. Collisions constantly occur between individual crystals and crystals impacting against the walls of the crystalliser vessel and the stirrer. This causes damage to crystal surfaces and disruption of the lattice structure which generate internal defects. The formation of internal defects by surface impacts has been observed during the crystallisation of magnesium sulphate and aluminium-potassium sulphate from saturated solutions. Internal defects were produced with very low impact energies [53]. The agglomeration of crystals can also form internal defects. As separate crystals combine voids form where the crystal surfaces do not touch completely, often trapping the crystallisation solvent. This has been observed during the crystallisation of potassium dihydrogen phosphate. A direct correlation between the amount of agglomeration and number of internal defects was reported [54]. The growth rate and crystal size

also seem to influence the quantity of internal defects. Saito *et al* found that as crystal size increased the proportion of internal defects also increased. This is possibly because larger crystals experience more collisions than smaller ones since they have a greater surface area [55]. This might also help to explain why larger energetic crystals are more sensitive as they possibly contain more internal defects which would provide sites for hot spot formation. The formation of internal voids within RDX crystals was briefly described by Gross [56]. It was noted that the defects were filled with a fluid which was assumed to be trapped crystallisation solvent. Defects were also observed to occur along lattice dislocation lines. Partial photolytic decomposition of the trapped solvent within the defects was observed leading to gas formation. Accumulation of defects along dislocations is probably due to an interaction between the stress fields of the dislocation and the internal voids [57]. Kim *et al* [58] used a technique known as internal seeding crystallisation to successfully improve internal crystal quality. Commercial RDX produced by the Woolwich process was dissolved in γ -butyrolactone at an initial temperature of 70°C and the solution was then cooled at a rate of 0.5 °C/min to around 62°C to allow primary nucleation of crystals. This temperature was then held for 30 minutes, then the temperature was raised to 63.5°C to dissolve finer crystals which would prevent the growth of larger crystals. This temperature was held for 30 minutes and the solution was cooled down to 50°C at a rate of 0.5°C/min. During this time the larger crystals would grow. Throughout the crystallisation process, the solution was stirred. This method significantly reduced the number of solvent inclusions in the crystals.

2.1.2 Investigating the influence of internal defects on shock sensitivity

Probably the first investigation into the relationship between internal defects and shock sensitivity of RDX was reported by Mishra and Vande-Kieft based at the U.S. Army ballistic research laboratory [59]. They recognised that crystals which had more internal defects had a higher sensitivity and so the elimination of these defects would produce a safer explosive. All of the commercial RDX products that they examined contained internal defects and the size of the defects increased as the crystal size became larger. To

investigate the effect of elimination of internal defects, a commercial grade RDX (source not specified) was recrystallised. The method used a hot, RDX saturated, mixed alkyl phosphine oxide solvent that was cooled rapidly to precipitate RDX crystals. Optical microscopy revealed that the recrystallised RDX was free from internal defects, whereas the as-received RDX contained defects. To determine shock sensitivity a dropweight impact test was used (the exact details of the method were not stated in the paper). The results showed an obvious reduction of sensitivity for the recrystallised RDX, a drop height of 53 cm for a 50% probability of initiation was recorded. In contrast the as-received RDX was initiated at only a 30 cm drop height. These tests did not consider the effect of crystal size and morphology on sensitivity or the effect of intergranular pores which could also be a site for hot spot formation. The recrystallisation process may have changed particle morphology which might have contributed to the decrease in shock sensitivity. This was also not addressed in the report. If shock sensitivity tests were performed on PBX formulations of these RDX samples, any sensitisation effects due to intergranular pores would have been significantly reduced. The effect of defect size was discussed briefly. Larger defects require lower shock pressures to form hot spots so RDX crystals that contain bigger defects will be more sensitive. Therefore reducing internal defect size will improve shock sensitivity. Interestingly, it was also noted that larger crystals had larger defects, which helps to explain why larger crystals seem to be more sensitive. A more extensive study of internal defects was undertaken at SNPE (Eurengo) by Baillou *et al* [60]. They investigated seven different batches of RDX, six recrystallised and one that had not been reprocessed. In comparison with Mishra's study, HTPB-PBX formulations of each of the RDX batches were tested rather than just the RDX crystals alone. This was an improvement as it eliminated intergranular voids. Table 2.1 lists the characteristics of each RDX batch used. Wedge tests were performed on each PBX to determine shock sensitivity and run distance to detonation. To observe internal defects, RDX crystals were suspended in a matching refractive fluid medium and examined under an optical microscope. The shock sensitivity tests indicated that the most sensitive RDX was the raw batch which had the largest internal defects (batch B). Batch A2 which had the next largest internal defects was less

sensitive than batch B but was still more sensitive than the other RDX samples which had similar shock sensitivities. In this study, particle size does not seem to have much effect on sensitivity. For instance, batches A1 and A2 have similar particle size but the sensitivity of A2 was greater than that of A1. RDX crystals from A2 had larger and more internal defects than those from batch A1. Furthermore, crystals from batch C1 were much larger compared to crystals from batches B and A2. The largest crystals were less sensitive than those from either B or A2, they also had much smaller internal defects. This shows that the quantity and size of internal defects has a strong influence on shock sensitivity, perhaps greater than crystal size. There is a direct relationship between the solvent content and the total volume of internal defects. In one experiment a dye was added to the solvent prior to crystallisation. Examination of the crystals formed showed colouration within the defects, which indicates that the internal defects contained trapped solvent. This study also suggests that the solvent used for recrystallisation has little effect on the number and size of internal defects. Batches A1 and A2 were both recrystallised from acetone but had different amounts/size of internal defects, whereas C3 and M used different solvents but had similar quantities of inclusions.

Table 2.1 Characteristics of RDX batches examined by Balliou *et al.* From reference 60.

RDX batch	Median particle Size, μm	Reprocessing characteristics	Internal defects and morphology	Solvent content wt. %
A1	194	Recrystallised from Acetone, sieved.	Most crystals, no internal defects, some with voids $< 5 \mu\text{m}$.	0.005
A2	174	Recrystallised from Acetone, sieved.	Lots of internal defects, some have bubbles inside. Max. size $60 \times 30 \mu\text{m}^2$.	0.12
B	175	Raw RDX product.	Many cavities, max. size $100 \times 20 \mu\text{m}^2$.	-
C1	475	Recrystallised from Cyclohexanone.	Crystals have surface defects. Lots of internal defects between $15\text{-}50 \mu\text{m}$.	0.06
C2	165	Recrystallised from Cyclohexanone, ground.	Irregular shaped crystals. Internal defects between $15\text{-}20 \mu\text{m}$. Some have bubbles.	0.04
C3	130	Recrystallised from Cyclohexanone, sieved	Few internal defects between $15\text{-}30 \mu\text{m}$, some have bubbles	0.04
M	189	Recrystallised from methyl ethyl ketone, sieved	Similar to C3.	0.02

Lionel Borne working at the Institute Saint-Louis (ISL), France, presented a report in 1993 investigating internal defects in RDX crystals [61]. Two different commercial RDX batches with the same particle size distribution were investigated, therefore preventing crystal size influencing the results. Batch 2 had more internal defects than batch 1, but it also had more surface defects. Therefore batch 2 had surface and internal defects both of which would possibly contribute to shock sensitivity. To determine the influence of internal defects only, two sub-batches were prepared from batch 1. A density floatation method was used that separated crystals into a high density, low defect (batch -1) and a low density, high defect (batch +1). Microscopy of the sub-batches showed that batch +1 had defects between 50 and $100 \mu\text{m}$ and batch -1 had an average defect size of only $10 \mu\text{m}$. This allowed the effect of internal defect size as well as quantity of internal defects on shock sensitivity to be investigated. Cast monomodal compositions of each batch were prepared using 70% RDX

and 30% wax. The final density was 99.5% of TMD showing that the presence of voids within the formulation bulk has been reduced to a minimum. The SDT behaviour of each batch formulation was investigated using a high velocity projectile impact test. This allowed the transit time of the applied shock wave through the sample to be measured. Formulations from batches 1 and 2 were subjected to shocks of 4.7, 5.7, 6.7 and 8.2 GPa. At 4.7 and 5.7 GPa batch 2 (more defects) had a fastest SDT. When shocks of 8.2 GPa were applied batch 1 (fewer defects) showed the fastest SDT. For batches +1 (larger/more numerous defects) and -1 (smaller/fewer defects) similar results were seen. At 4.7 GPa batch +1 has the fastest SDT, but at higher shock pressures batch -1 became more sensitive. The difference between RDX shock sensitivities/SDT behaviour was larger between batches 1 and 2. It was suggested that this was because batch 2 RDX crystals also had more surface defects which increased its sensitivity further. These results were ascribed to the two stage initiation theory. At lower shock pressures, larger internal defects form hot spots easier than smaller ones as they require lower pressures to be collapsed. Smaller internal defects require higher pressures to compress them enough to become hot spots. This paper shows clearly that shock sensitivity is not only controlled by the number of defects but defect size as well.

Another report, published also by Borne in 1998, examined internal defects in HMX [62]. The experiments used the same monomodal formulation as described in his previous report [61]. Again a high density (>99.5% of TMD) was achieved with good homogeneity. The monomodal particle size distribution for each of the three HMX batches tested was very narrow, (200-300 μm) so crystal size effects would not be an influence. The crystal morphology and internal defects were examined using SEM and optical microscopy in matching refractive index fluid, (see table 2.2). The volume of the surface defects for each batch was determined by mercury intrusion porosimetry. This showed that there were small differences between each batch, batch 1 having the most and batch 3 having the fewest surface defects.

Table 2.2 Characteristics of HMX batches examined by Borne, from reference 62.

HMX batch	Morphology and internal defects	Median density (g cm⁻³)	Mean internal defect volume	Surface defects (cm³ g)	Shock initiation pressure (GPa)
1	Faceted crystals, large isolated defects in centre.	1.9000	0.10%	≈ 0.35	5.6
2	Faceted crystals, large central defects with small defects.	1.8965	0.30%	≈ 0.33	4.0
3	Rounded crystals, more small defects than batch 1 or 2.	1.8953	0.45%	≈ 0.30	3.6

Again Borne used high velocity projectile impact tests to measure the shock sensitivity of each HMX batch. The results obtained clearly showed that more internal defects led to increased shock sensitivity. The presence of smaller defects seems to drastically reduce the shock initiation pressure. This is possibly because smaller defects are better in propagating the reaction front during detonation. With batch 1 there are hardly any small defects, whereas in batch 2 and 3 there were many. Therefore batch 1 crystals needed a greater shock to sustain a reaction front. This is rather interesting considering the findings from Borne's previous report [61], where larger voids gave increased sensitivity. This apparent contradiction may be explained by considering the interplay between small and large internal defects. Large defects require lower shock pressures to form efficient hot spots, but without smaller defects present to propagate the reaction they might not be sufficient to sustain a deflagration. A Large internal defect releases more energy when compressed but at a slower rate than a small defect. Also, larger defects require longer duration shocks as the shock wave has to transverse a larger distance to completely collapse the defect compared to smaller defects. Therefore, many smaller defects could reduce the shock pressure required since their combined high surface area would make it easier to build up and spread a detonation wave. Finally, crystal morphology seems also to have little effect. The most sensitive crystals were rounded compared to the more angular crystals of batch 1. This also contradicts studies that suggest rounded crystals are less sensitive. Probably, in this study, internal defects had a more dominant effect than particle shape. A deficiency of this investigation was that extragranular

porosity was not considered since very high loading densities were achieved for the HMX/wax compositions. In a further report by Borne and Beaucamp, supplementary data was provided on the extragranular void volumes for the three HMX batches [63]. The most sensitive, batch 3 had a much lower extragranular void volume fraction (0.001%) than batches 1 and 2, (0.3 and 0.6%). This was likely because the rounder crystals of batch 3 were coated more efficiently than the angular crystals of batch 1 and 2, leaving fewer spaces between the crystals and the wax. Despite this very low volume of intergranular voids, batch 3 was the most sensitive. Compared to internal defects, intergranular voids seem to have little effect on composition shock sensitivity. Experimental data was presented that investigated internal defects in various RDX batches cast into the same wax composition used in Borne's previous work. Voids between RDX particles in the cast compositions were also considered. Borne and Beaucamp investigated eight commercial RDX lots, lots 1 to 8 and three RDX lots processed by ISL. Commercial lots 1 to 5 had the same particle size distribution but differing quantities of internal/external defects and morphology. Lot 7 was recrystallised from lot 6 to give more spherical crystals. The three ISL lots had faceted crystals with much lower internal and external defects than the commercial lots. The ISL batches were hardest to cast because the angular crystals made wax coating more difficult. Projectile impact experiments were performed to test the shock sensitivity of each lot formulation. Table 2.3 gives the impact energy required to detonate each lot formulation along with percentage of internal and surface defects and the particle size range.

Table 2.3 RDX lot characteristics and projectile impact test data from Borne and Beaucamp, ref. 63.

RDX lot	Particle size range (µm)	Internal defect volume, %	Intergranular void volume, %	Impact energy threshold, (kJ)
1	100-315	0.20	0.38	30
2	100-315	0.53	0.06	29
3	100-315	0.44	0.80	21
4	100-315	0.12	1.95	28
5	100-315	0.24	0.36	28
6	100-200	0.14	2.29	27
7	100-200	0.14	1.11	32
8	315-800	0.10	0.23	35
ISL 1	100-315	0.06	1.63	35
ISL 2	315-630	0.06	0.80	35
ISL 3	100-630	0.06	1.22	35

The results clearly showed that shock sensitivity increased with larger internal defect populations. Least sensitive were the ISL lots and commercial lot 8, each having 0.1% or less internal defect volume. Intergranular voids seem to have a minimal effect on sensitivity. Lots 1,4,5,6 and 7 have a similar particle size range, similar internal defect volumes and similar impact energy thresholds for detonation but have quite different intergranular void volumes. The ISL lot results demonstrate that crystal size range also had no influence on shock sensitivity. The three ISL lots had different size ranges but identical impact energy thresholds. There are some deviations from the trends observed though. For instance, lot 2 has the highest volume of internal defects but only an intermediate sensitivity. This could be due to internal defect size, lot 2 could possibly have more large internal voids and fewer small internal defects. This situation could give an overall higher defect volume, but reduce its sensitivity as discussed earlier. This investigation did not look at the sizes of internal defects though so this explanation cannot be proven. Crystal surface defects were also not examined and this too could possibly have been a contributory factor. In summary this paper shows that internal defects could have a dominant role in determining RDX shock sensitivity. By using gas chromatography Borne *et al* showed that internal defects contain the solvent/water solution used during the crystallisation process [64]. RDX crystals were dissolved in N-methylpyrrolidone and this solution was then analysed using an internal standard method to find the amount of trapped

solvent within the internal defects. A strong correlation was found between the concentration of solvent and the RDX crystal density.

A recent study was conducted by Borne *et al* in 2008 which took into consideration the effects of pressing and casting wax coated RDX [65]. The role of voids within the bulk of the wax binder, voids between binder and RDX crystals and internal RDX crystal defects were assessed. Three RDX lots were analysed and their characteristics are shown in table 2.4.

Table 2.4 RDX lot characteristics examined by Borne *et al*, reference 65.

RDX lot	Source	Crystal morphology	Amount of internal defects
A	Commercial RS-RDX	Smooth, rounded	Medium amount
B	ISL laboratory	Sharp angular, faceted	Very few/none
C	Commercial non RS-RDX	Smooth rounded	High amount

There was a variation of particle size between each lot but this was considered to be irrelevant by the authors. Particle sizes for all lots were greater than 100 μm . Each RDX lot was coated with 30 wt.% of wax. Three pressed formulations and one cast was prepared from lot A, two cast from lot B (one under gravity and one under vacuum) and one formulation cast with lot C. Lot A formulations allowed a comparison to be made between casting, pressing and the intergranular pores/voids within the bulk of the composition. It also would indicate if pressing reduces RS-RDX characteristics. Because of the angular morphology of lot B crystals it was expected that formulations made with this lot would contain a higher number of voids between crystals and wax binder. This was in fact the case. So lot B provided data regarding the effect of these voids on shock sensitivity and lot C was a control. This study also used the 20 mm high velocity projectile impact test to ascertain shock sensitivity of the formulations. Table 2.5 gives the minimum impact velocity to induce detonation for each formulation and the volume fraction of extragranular voids.

Table 2.5 Results from projectile impact tests from Borne *et al*, reference 65.

Formulation	Minimum impact velocity (ms ⁻¹)	Extragranular voids (volume fraction %)
Lot A, pressed 5%	~1120	≈ 4.3
Lot A, pressed 2.5%	~1140	≈ 2.2
Lot A, pressed 0%	~1150	< 0.1
Lot A, cast	~1140	≈ 0.4
Lot B, vacuum cast	~1140	≈ 0.2
Lot B gravity cast	~1160	≈ 1.2
Lot C gravity cast	~900	≈ 0.5

The results from the pressed lot A samples showed that there was only a slight reduction of sensitivity when the extragranular void volume was reduced, furthermore pressing had no affect either. RS-RDX did not lose its RS-properties as a result of the pressing process. Voids located between RDX crystals and the binder also seem to have little influence on sensitivity. Elimination of these interface pores by vacuum casting lot B did not produce a significant change in sensitivity as compared to lot B cast under gravity. It was thought that these interface pores were smaller than the pores in the binder and so would be less efficient in forming critical hot spots at the relatively low shock pressures generated in these experiments. Lot C, however, did show a significant increase in shock sensitivity. Despite having a rounded particle shape like crystals from lot A, lot C was much more sensitive. This increase in sensitivity was probably due to the very high internal defect population of lot C crystals. Particle morphology seems to be insignificant. Lot B which had angular faceted crystals would be expected to have a high sensitivity due to increased frictional and compressive forces at the facet tips and sharp crystal edges. In this report though, there is no difference between angular and rounded crystals. Perhaps the wax binder acts as a “cushion” around the angular crystals reducing stress build up on their tips and edges. In conclusion Borne *et al* in this paper have provided useful information about how shock sensitivity is dependent on different pore and void types. Pores within the bulk of the formulation and at the binder/crystal interface were less sensitising then internal crystal defects. Crystal morphology seemed also to have a minimal effect. Borne *et al* suggested that further experiments should be undertaken using a different binder, perhaps a HTPB based binder as used in investigations into crystal morphology by TNO [66,67]. The TNO studies

indicated that angular crystals were more sensitive when in a HTPB PBX. Possibly hot spot formation is more efficient with the HTPB binder than with wax because the viscosity and density of HTPB is more favourable for hot spot formation. Repeating these experiments with an HTPB binder could yield interesting information about the effects of binder properties on shock sensitivity. Gap testing would also provide sensitivity data on the behaviour of these compositions at higher shock pressures than those produced by the projectile impact test.

Nuclear quadrupole resonance (NQR) has been used as a quantitative method to determine the quantity of internal defects within RDX crystals [68,69,70]. The electric field gradient of nitrogen nuclei in RDX molecules is strongly influenced by crystal defects such as voids and dislocations. These imperfections can lead to broadening of the NQR absorption line compared to crystals with fewer defects. Erofeev *et al* [68] were probably the first to use NQR to quantify internal defects within RDX crystals, finding that crystals with more defects produced wider NQR lines. Following on, Caulder *et al* [70] undertook NQR experiments on insensitive RDX from SNPE (SIRDX), raw Holston RDX (HRDX) and Holston RDX recrystallised by SNPE (HIRDX) and compared the NQR results with shock sensitivity data. The amine N¹⁴ NQR absorption line was measured as this line is least affected by variation of temperature. The shock sensitivity of each formulation was determined using the large scale gap test (LSGT). A correlation was found between the shock sensitivity results and the NQR line widths. Unprocessed Holston RDX had the widest line width and was the most sensitive, whereas the insensitive RDX has the narrowest line width and had the lowest shock sensitivity. Table 2.6 gives the results obtained, (a lower LSGT result indicates increased sensitivity).

Table 2.6 NQR line widths and shock sensitivities of formulations tested by Caulder *et al*, * mean line widths from two measurements. Taken from ref. 70.

RDX type in formulation	NQR line width (Hz)	LSGT result (kbar)
Insensitive SNPE RDX	140	50.4
Holston RDX reprocessed	280 *	48.5
Holston RDX unprocessed	370 *	29.5

The process of formulating a PBX does not appear to change the NQR line width compared to raw RDX [69]. These results show that shock sensitivity is influenced by internal defects and that NQR can potentially be used to determine these parameters for different RDX samples.

Small angle neutron scattering (SANS) experiments of loose HMX crystals were performed by Mang *et al* [71] to determine the internal defect volume and defect size distribution. They clearly showed that fine HMX crystals contained smaller voids than coarser crystals. Their SANS experiments were also able to accurately measure mean particle size. Following on from this successful demonstration of neutron scattering, Stoltz *et al* [72] used small angle neutron scattering and ultra-small angle neutron scattering (USANS) to investigate the relationship between internal defects and shock sensitivity. RDX crystals were wetted in a solution that had the same neutron scattering characteristic as RDX (deuterated cyclohexanone) so only scattering caused by internal defects was observed. Five RDX samples were studied, Eurenco I and MI-RDX, Dyno Nobel RS-RDX, Holston RDX and ADI RDX. The RDX samples were also subjected to the large scale gap test (LSGT) to determine their shock sensitivities using a HTPB formulation. Prior to formulation, samples were sieved to eliminate particle size effects. There was a good agreement between the shock sensitivity of the samples tested and how much scattering they produced. RDX samples that showed greater scattering due to more defects were also more shock sensitive. Figure 2.3 shows the correlation that was observed.

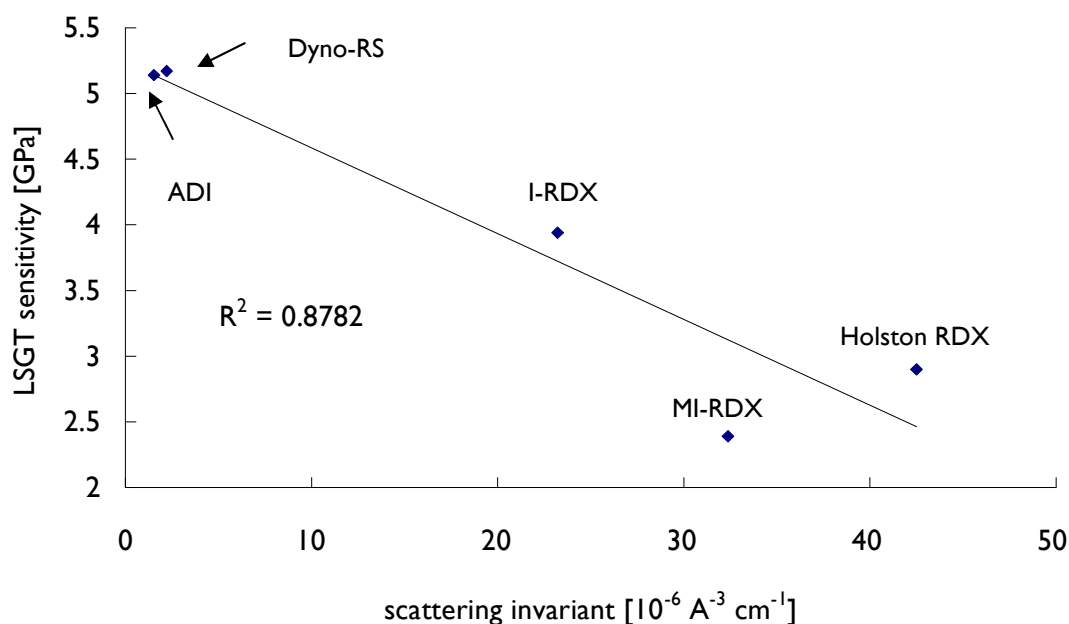


Fig. 2.3 Plot of amount of neutron scattering against LSGT sensitivity obtained by Stoltz *et al*, taken from ref. 72.

The main shortcoming of this work was that the method used was not able to detect scatter resulting from defects larger than 20 μm . Therefore only an estimate of the total combined defect volume was obtained. However, the results do indicate that the quantity of defects present within the crystals has a strong influence on shock sensitivity.

Quantitative methods for assessing the volume of internal defects in RDX crystals and optimisation of recrystallisation techniques to reduce them were reported by Koo *et al* [73]. The first part of their paper dealt with assessing the internal defects of standard sensitivity Hanwha-RDX, Korea, (produced by the Woolwich process) and Eurenco (SNPE) I-RDX[®]. Matching fluid microscopy and digital image analysis were used to measure the total defect area for each crystal. This gave a quantitative assessment rather than just a qualitative description of defects. By this method it was found that the mean internal defect area for Hanwha-RDX was 9.3 +/- 0.4% and for Eurenco I-RDX[®] it was 5.0 +/- 0.3%. Solvent content by GC analysis was also performed. A direct and linear correlation between solvent content and volume of internal defects was observed. This reinforces the proposal by Bourne that internal defects are filled with crystallisation solvent [64]. X-ray diffraction rocking curves indicated that I-RDX[®] had a higher crystal lattice

order than the Hanwha-RDX. The second part of the Koo *et al* paper investigated the effects of cooling recrystallisation methods on the number of internal voids. Recrystallisation was performed using either uncontrolled or controlled cooling from different initial temperatures. After recrystallisation, the amount of trapped solvent was determined by gas chromatography. The results indicated that temperature controlled cooling and a lower initial crystallisation temperature reduced the number of solvent inclusions. It was also shown that using a slower cooling rate improved crystal quality. Most internal defects were observed to form at the initial stages of crystal growth when growth was most rapid. Therefore it was suggested that a low supersaturation would slow the initial crystal growth and reduce the number of internal defects, since the degree of supersaturation determines crystal growth rate. It was seen that larger crystals were formed at higher initial crystallisation temperatures and these larger crystals contained more trapped solvent and so had more internal defects. This might explain why larger crystals are more shock sensitive in monomodal compositions. In summary Koo has shown quantitatively that I-RDX® has fewer internal defects than standard RDX products. It also provides a useful insight for optimising crystallisation conditions to reduce solvent inclusions and therefore reduce shock sensitivity.

A similar series of cooling crystallisation experiments were undertaken by Kim and Kim [74]. They carried out batch recrystallisation of Hanwha-RDX using controlled cooling rates of 12, 2, 1 and 0.2°C min⁻¹ from 65°C to 10°C. They also investigated the effect of changing the ratio of solvent (γ -butyrolactone) to anti-solvent (water). The quantity of internal defects within the recrystallised crystals was examined using optical microscopy with matching contrast medium and SEM for surface and morphology analysis. Gas chromatography was used to determine the quantity of trapped solvent in the crystals. In agreement with Koo *et al* [73] it was found that increasing the cooling rate produced crystals with more internal defects. Morphology was influenced by the cooling rate, at 12°C min⁻¹ plate shaped crystals were formed with irregular surfaces and many large pores. Slower cooling rates produced smoother polygonal crystals. Crystal size also decreased with faster cooling. Increasing the proportion of water to GBL reduced the number of internal

defects. Above 80% water content however, this effect was reversed. Crystal morphology was also affected by the water/GBL ratio. With increasing proportion of water the morphology changed from smooth/polygonal to rough/porous. Roberts *et al* [75] have reported the preparation of RDX crystals having a smooth uniform morphology and reduced internal defect content by means of controlled evaporation and ultrasonic agitation. Ultrasonic agitation produced cavitation within the solution which created localised regions of supersaturation where crystal nucleation occurred. This allowed a much lower overall supersaturation which promoted the formation of smoother crystals. The controlled evaporation reduced the defect content.

Impact testing using a ballistic impact chamber (BIC) was used by Bouma *et al* to distinguish between raw RDX samples with different numbers of internal defects [76,77]. The sample is initiated by a drop-weight impacting on the striker. A pressure gauge records the pressure produced by the initiation and a photodiode captures the initiation of the sample. A photo and schematic diagram of the BIC used are shown in figure 2.4.

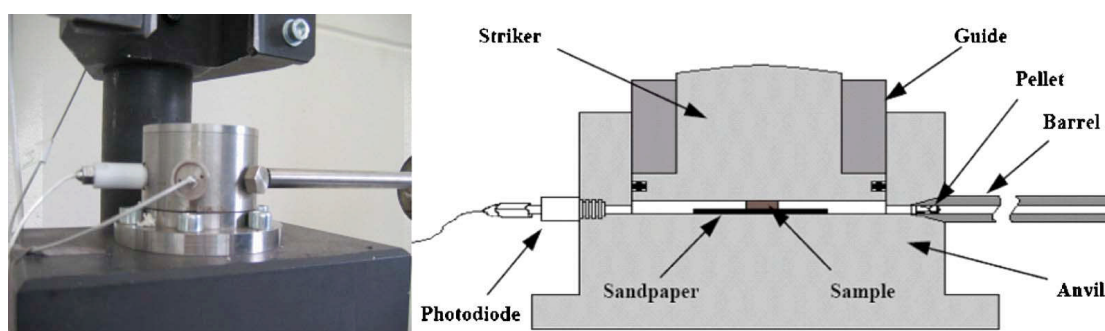


Fig. 2.4 Photograph and schematic of the ballistic impact chamber used by Bouma *et al*, taken from reference 76.

The RDX samples used were those from the R⁴ programme. Prior to actual testing, computer based simulations were performed, in order to optimise the experimental design. For each test, 40 and 60 mg quantities of each RDX sample were placed in the BIC and subjected to the same impact (0.047 GPa). Pressure-time response curves were obtained to investigate the reaction of the samples to the applied impact. Optical micrographs and SEM images showed that there was a large variation in crystal quality between the samples. From the pressure-time curves it was possible to distinguish between less sensitive and more sensitive RDX samples. Samples that were less sensitive showed

relatively slow and smooth pressure build up with a lower peak pressure after impact. More sensitive RDX samples produced a fast build up with multiple high pressure “spikes”. Comparison with the optical micrographs showed that the samples which produced the rapid and sharp pressure curves had more internal defects than the less sensitive samples, they also had large quantities of very small internal voids. This again highlights the possibility that defect size is important in determining shock sensitivity and that large numbers of small defects enhance susceptibility to initiation. The main shortcoming of Bouma’s work was that intergranular voids between the crystals were not really considered and they could have been influencing the results as well. This may be important as the samples studied had different morphologies and so could pack in different ways, producing variation in quantity and size of intergranular spaces.

Internal defects have also been found to affect the bulk mechanical properties of RDX crystals as investigated by Ming using a compressive stiffness test [78]. This experiment involved placing 2 g samples into a steel press and slowly compressing the sample with a piston at a constant rate. Five RDX lots were tested, two as-received commercial lots, two recrystallised lots and one lot that had been recrystallised and processed further to give a smoother spherical morphology. It was observed that the reprocessed samples were much “stiffer” than the as-received RDX lots which seemed “softer”. Although the mean packing density of the as-received samples was slightly less (0.930 g/cm^3), compared to that of the re-processed samples (1.133 g/cm^3), this difference was considered not to be influential. The as-received and processed samples achieved the same density, (1.250 g/cm^3) at a loading stress of 3.5 MPa. No significant differences in the mechanical properties between the as-received and reprocessed samples were seen until much higher loading pressures were reached. Optical micrographs of the samples showed that the reprocessed samples had very few internal defects compared to the as-received lots. It was concluded that internal defects had a dominant effect on RDX bulk mechanical properties and surface defects had only a limited influence. This investigation only considered raw RDX crystals. If they were in a PBX how would they behave? Repeating the experiment with the lots in a PBX formulation could have provided useful information as to the effects of

pressing. Molecular dynamics simulations performed by Yang *et al* showed that the presence of voids within a crystal lattice affected the elastic modulus of the bulk material. Increasing the size of the voids and the total void volume within the crystal reduced the elasticity [79]. Indentation methods such as micro and nanoindentation have also been used to investigate the mechanical properties of energetic materials. Hagan and Choudhri [80] were the first to use microindentation to study the mechanical properties of RDX. Using this technique they were able to determine the fracture surface energy of RDX and PETN by measuring the extent of fracture formation in crystals subjected to increasing applied loads. From knowing the fracture surface energy of an energetic material an indication of its mechanical integrity and sensitivity can be deduced. More recently Li *et al* used nanoindentation to measure the elastic modulus of single crystals of HMX [81].

All of the findings discussed so far are in agreement that internal defects cause an increase in shock sensitivity. However, Czerski and Proud [82,83] report that RDX crystals with more internal defects show *reduced* sensitivity compared to RDX crystals with few internal voids. Their results indicated that an angular crystal morphology and increased surface roughness were more important characteristics than the number of internal defects. Because they examined raw RDX crystals in the gap tests and not a PBX formulation perhaps intergranular voids were affecting the results as well. This illustrates how shock sensitivity is dependent upon not just one factor but many working together. In some circumstances one type of crystal characteristic may have more of an influence than in another situation.

2.2 The influence of particle morphology on shock sensitivity

The influence of crystal shape on the shock sensitivity of energetic materials has also been studied and shown to be significant. The first extensive research programme to investigate particle morphology was conducted at the TNO Prins Maurits Laboratory, in the Netherlands by van der Steen *et al* [66]. They prepared 85 wt.% RDX in HTPB PBX formulations, with vacuum casting to minimise voids so reducing hot spot formation. Bimodal RDX formulations were tested using three coarse (samples A, B and C) and two fine RDX lots (samples D and E) each of a different morphology as described in table 2.7.

PBXs containing bimodal mixtures of A/D, B/D, and C/E were prepared and studied. The coarse to fine ratio was 64/36 for all PBX formulations.

Table 2.7 Particle characteristics of the RDX lots used by Van der Steen, from reference 66.

Batch	Crystal morphology	Average particle size, μm
A	Very irregular shaped.	285
B	Rounded particles, broken With sharp edges	460
C	Reprocessed, spherical and oval shaped.	370
D	Small regularly shaped crystals.	17
E	Processed same as sample C, same shape.	52

The NOL-LSGT was used to determine the shock sensitivity of each PBX. The most sensitive was formulation A/D with a shock pressure of 3.2 GPa for 50% probability of initiation. PBXs made with bimodal formulations containing regular more rounded RDX particles (C/E and B/D) were less sensitive with 50% initiation pressures of 3.7 and 3.9 GPa respectively. Run distance to detonation was also tested using unconfined PBX samples. Again the most sensitive was formulation A/D and the least B/D, the run distance to detonation for composition B/D was twice that of A/D. Although the particle size distribution of batch A and B was not identical it was thought that the size difference was not enough to cause the difference in sensitivity that was seen. Instead the reduced sensitivity of PBXs made with B/D and C/E was attributed to the RDX particles being more regular and rounded. It was suggested that formation of microscopic voids during casting was more likely on the rougher crystals of batch A than the more regular crystals from batch B, making PBXs containing batch A RDX more sensitive. This work has clearly shown that there is a link between particle shape and sensitivity. Perhaps better control over size distribution by sieving would have reduced the possibility of particle size affecting sensitivity. Another issue that could have influenced the results is that batches A and B were from different sources, the origin and production method were not specified in the paper. They could have contained different amounts of HMX or other impurities which would

have influenced the shock sensitivities but this matter of HMX content was not addressed.

Another study was conducted at the TNO laboratory which also investigated the role of particle size distribution on sensitivity [67]. They tested bimodal 85 wt.% RDX HTPB formulations. The investigation used as-received RDX and also RDX that had undergone recrystallisation to produce smoother particles. This process involved the partial dissolution of the as-received RDX in RDX saturated acetone to round off the irregular shaped crystals. All the RDX used was from the same source and produced by the Bachmann process (the manufacturer was not stated). This therefore removes the possible influence of different production methods, *i.e.* HMX content on sensitivity. A coarse-to-fine ratio of 64/36 was used in each PBX of either as-received (coarse/fine) or spheroidised (coarse/fine) RDX. Particle size analysis indicated that there was a large difference in size distribution between the fine as-received RDX and fine spheroidised RDX, but there was only a small difference between the coarse RDX batches. Any effects on shock sensitivity due to this difference of particle size for the processed RDX samples was assessed by also preparing a PBX with spheroidised coarse and as-received fine RDX. This is an improvement on their previous report [66] which did not consider size distribution effects. The initiation pressure and run distance to detonation results were in good agreement with their earlier report. The PBX made with the irregular and angular as-received RDX was the most sensitive. In the gap tests performed[‡] it had the shortest run to detonation distance and lowest initiation pressure (3.3 GPa) of the three PBXs. The PBX with the rounded re-processed crystals was the least sensitive (3.9 GPa). The PBX made with coarse spheroidised and fine as-received RDX had a shock sensitivity just below that of the PBX made with spheroidised crystals. This suggests that particle morphology is a more dominant factor for influencing sensitivity than particle size distribution. Again it was thought that the increased sensitivity of the irregular particles was due to the formation of microscopic voids on the particle surfaces. Also HMX contamination was considered. During the recrystallisation process HMX is dissolved producing a lower amount of HMX in the final spheroidised crystals compared to the as-

[‡] A modified NOL gap test was used using bare 50 mm diameter test charges.

received RDX. This reduced HMX content could also have been contributing to the reduced sensitivity of the rounder crystals. This is possibly a flaw of this study, perhaps a RDX product which was known to have a low HMX content before recrystallisation should have been used. This would have removed the issue of sensitisation by HMX, making the results more meaningful.

A more recent study into the effect of crystal morphology was conducted by Matsuzaki *et al* [84] at the Nippon Koki company. They were developing a RS-RDX product by recrystallising their standard RDX product made by the Woolwich process. Shock sensitivity tests were performed using a LSGT on PBXN-109 formulations containing their standard RDX, RS-RDX and RS-RDX that had undergone a further recrystallisation to produce almost spherical crystals. Table 2.8 shows the crystal morphologies of the RDX samples used and the shock pressure results for the LSGTs.

Table 2.8 RDX crystal morphology and LSGT results obtained by Matsuzaki *et al*. Ref 84.

RDX sample	Crystal morphology	Shock pressure for 50% detonation (GPa)
Standard RDX	Rounded, irregular with many pores and cracks.	2.2
RS-RDX	Faceted, polyhedral with very few surface defects.	5.0
RS-RDX spheroidised	Spherical, very smooth very few surface defects.	5.6

These results clearly show that crystal morphology has a strong effect on shock sensitivity. Interestingly there is a much smaller reduction in sensitivity between the faceted RS-RDX and the spheroidised RS-RDX crystals, compared to the much greater decrease from the standard RDX to RS-RDX. In the previous papers discussed [66,67] it was concluded that angular shaped crystals had a higher sensitivity. In this set of results a significant reduction of sensitivity was obtained with the angular crystals, this seems to be contradictory. However, when considering surface defects, this conflict is resolved. From these results it seems that as well as crystal shape, surface defects have a significant effect on sensitivity. Despite the reduction in sensitivity due to spheroidisation, a greater reduction was obtained by producing crystals with fewer cracks and pores. The findings from this study

show again that shock sensitivity is not controlled by just one crystal characteristic. This work also has an advantage over the TNO studies in that RDX from one manufacturer was examined and also that it was a type I material, so it would probably have a very low HMX impurity. An earlier investigation by Lecume *et al* [85] clearly shows that sensitivity is influenced by surface defects. They used atomic force microscopy to determine the number of pores on three different lots of RDX. Then they performed LSGTs on PBXN-109 formulations containing each of the RDX lots. It was found that the shock sensitivity increased in a linear relationship with increasing number of surface pores.

Surface defects on RDX crystals have also been studied using atomic force microscopy (AFM) by Bellitto *et al* [86,87]. From the AFM data the mean surface roughness was obtained and statistical analysis was used to obtain the standard deviation of the roughness for each crystal. They plotted these results against shock the shock sensitivity data for the RDX lots from an earlier report [24]. Only a weak correlation was seen between the mean crystal roughness and shock sensitivity (rougher crystals being more sensitive). A better correlation was observed with the standard deviation of the mean roughness, i.e. how constant the crystal roughness was. This suggests shock sensitivity is not influenced so strongly by the mean roughness but rather by how much the roughness varies across the crystal surface.

Song *et al* [88] investigated the relationship between surface roughness/morphology of RDX crystals and their impact and friction sensitivity. Surface roughness was quantified by calculating the surface fractal dimension, D_s from SEM images of RDX crystals using fractal image processing software (FIPS). Higher values of D_s indicate a rougher crystal surface. They reported that RDX samples consisting of crystals having a higher D_s had increased friction sensitivity. As D_s increases the number of contacting points between crystals becomes larger leading to increased shearing, deformation and friction.

The effects of recrystallisation and surface etching on the morphology and shock sensitivity of RDX were investigated by Min-Jun *et al* [89]. They used RDX produced by the Woolwich process, (origin was unspecified). Two separate batches were produced using a cooling-recrystallisation process, one

batch recrystallised using dimethylsulphoxide, DMSO (batch 1) and the other with γ -butyrolactone, GBL (batch 2). Samples from each of these batches were then etched with ethyl acetate to produce a smoother crystal morphology which was demonstrated by SEM (batches 1.1, 2.1). Each batch was formulated into a PBXN-109 composition, cast-cured and subsequently tested for shock sensitivity using the large scale gap test (LSGT). Table 2.9 gives the shock sensitivities of each RDX batch along with mean particle size and HMX content.

Table 2.9 Shock sensitivity, crystal size and HMX content of the batches tested by Min-Jun *et al.* Taken from ref. 89.

RDX batch	Mean crystal size (mm)	HMX content (wt.%)	Initiation pressure (kbar)
Batch 1 (DMSO recrystallised)	326.66	0.7	43.8
Batch 2 (GBL recrystallised)	342.46	0.5	41.37
Batch 1.1 (etched with ethyl acetate)	307.44	0.7	49.54
Batch 2.1 (etched with ethyl acetate)	327.93	0.5	47.68

These results clearly show that a reduction in shock sensitivity is obtained by making the RDX crystals smoother. There is also a slight reduction in mean crystal size during the etching process, but this was not discussed by the authors. This small reduction in size is probably not having a significant effect on sensitivity compared to the change in morphology that has occurred. The consistent and small amount of HMX present would probably also have had a minimal, (if any) influence on the results obtained. The authors concluded that recrystallisation of RDX is required to reduce shock sensitivity.

To understand what makes energetic crystals that have faceted and angular morphologies more shock sensitive than smooth spherical crystals a series of molecular dynamics simulations was devised by Shi and Brenner [90]. They developed a computational model using a nanometre scale nitrogen cubane (N_8) crystal. Shocks were simulated by displacement of the binder molecules towards the binder-crystal interface. It was concluded that the

facets of the crystals form regions of compression around the facet tips that generate hot spots due to shock focusing and facet compression. As the shock wave impacts the facet tip it is refracted. The amount of refraction increases for sharper facets, and this leads to greater energy focusing in the crystal. Therefore sharper crystals are more sensitive than smoother crystals.

From these reports it can be concluded that crystals that have a rounder morphology are significantly less sensitive than angular crystals. Surface defects such as cracks and pores appear to have a sensitising effect. Again it is demonstrated that shock sensitivity is not determined by a single crystal characteristic but several acting together.

2.2.1 The influence of impurities and solvent on morphology during RDX crystallisation.

The choice of solvent can have an effect on the crystal morphology. When RDX crystals are grown in cyclohexanone (without added water) the crystals become narrow and plate shaped. When grown from γ -butyrolactone the crystals acquire a needle type appearance. When grown from acetone RDX crystals show a wide plate structure [26,27,52]. Micrographs of RDX crystals grown in these solvents are shown in figures 2.5 to 2.7 together with the Miller indices of the crystal faces [26].

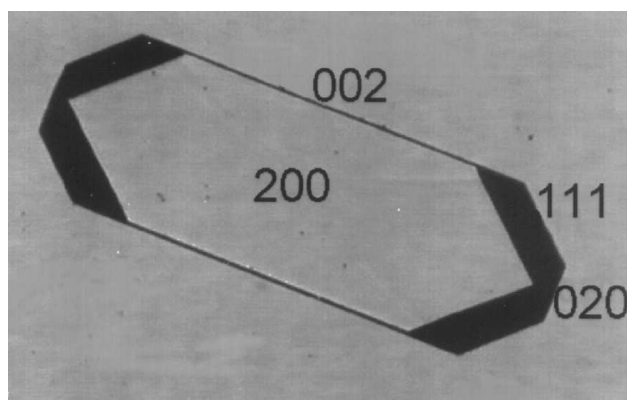


Fig. 2.5 Micrograph of RDX crystal grown in cyclohexanone, from ref. 26.

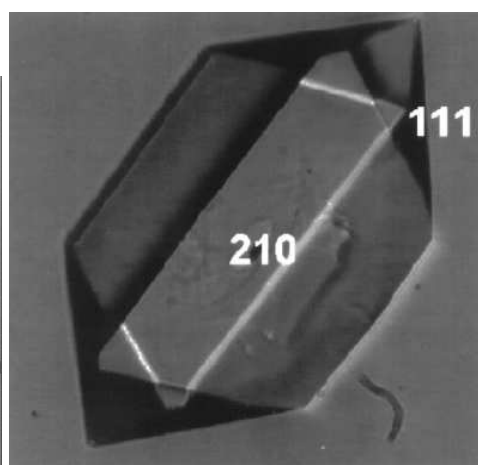


Fig. 2.6 Micrograph of RDX crystal grown in γ -butyrolactone from ref. 26.

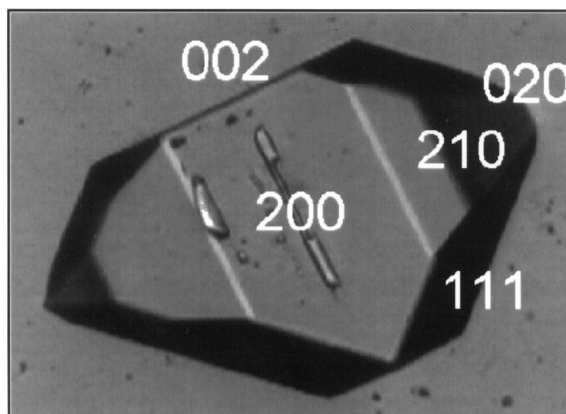


Fig. 2.7 Micrograph of RDX crystal grown in acetone from ref. 26.

The overall morphology is determined by the growth rates of different crystallographic (hkl) planes of the crystal. Planes that are growing faster will be further away from the site of crystal nucleation and will be smaller than those growing at a slower rate. The morphology is determined by the slowest growing faces. This is shown in diagram A of figure 2.8. An impurity that can adsorb onto a specific crystal face will inhibit further growth by blocking adsorption of RDX molecules and slow the rate of growth in that crystallographic plane, this plane will then define the morphology (diagram B, figure 2.8). An impurity is defined as any species that is not a constituent of the crystal, which includes the solvent. Since the solvent has the highest concentration in the crystallisation system it will have a dominating role in determining morphology, as it will be the strongest competitor for adsorption on to the crystal [52].

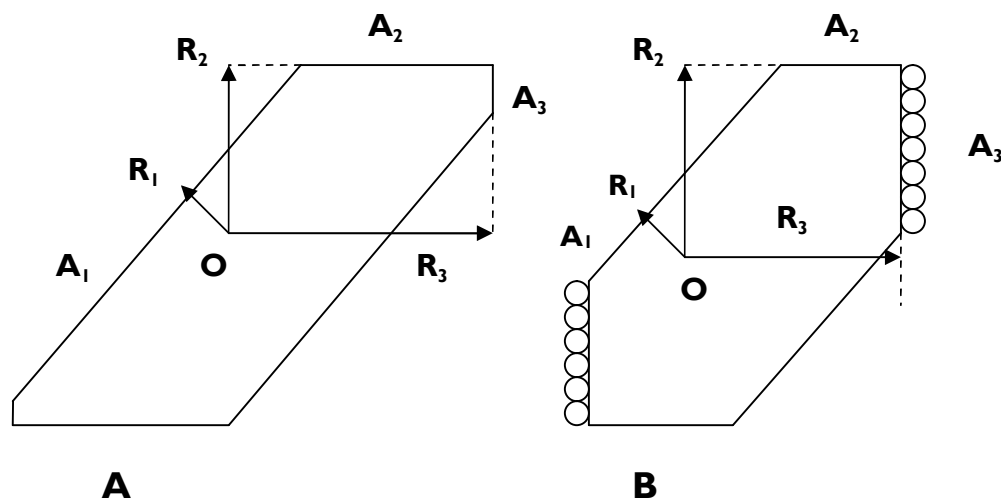


Fig. 2.8 In diagram 'A' rate of growth is fastest in direction R_3 and slowest in R_1 . Therefore surface area A_3 is smallest and surface area A_1 is largest. Surface A_1 determines the crystal morphology. In diagram B, preferential adsorption of impurity/solvent molecules (circles) on surface A_3 occurs. A_3 is now the slowest growing crystal plane and determines morphology. Point O is the nucleation site of the crystal. Reproduced from reference 52.

The adsorption of an impurity/solvent molecule onto a growing crystal face requires a specific adsorption energy. To remove the impurity molecule so that a RDX molecule can be adsorbed requires the same amount of energy. If the adsorption energy is very high the RDX molecules cannot be adsorbed into the crystal lattice and growth of the plane is blocked or very slow. Therefore the morphology determining crystal planes are the ones which require the highest adsorption energies.

The binding energies for the adsorption of acetone, cyclohexanone and γ -butyrolactone on RDX crystal lattice planes was calculated using a molecular modelling method by Horst *et al* [26]. The technique used a Monte Carlo energy minimisation simulation to obtain the binding energies for each solvent. By determining the adsorption energies for each lattice plane, the RDX crystal morphology most likely to form in a given solvent was predicted. To see how accurate the predicted morphologies for each solvent were, small scale cooling crystallisation experiments were performed. RDX was recrystallised from saturated solutions of the same solvents modelled in the simulation. Cooling was carefully controlled at a steady rate from 50°C to 20°C. The morphology of the crystals grown in cyclohexanone (figure 1.5) was in good agreement with the predicted morphology. The simulation suggested

that the (200), (002), (020) and (111) planes had the highest absorption energies and these were indeed the preferred lattice planes for growth. Unfortunately, for crystals grown from acetone and γ -butyrolactone the predicted morphologies were not seen so clearly. This is possibly due to the simulation being too simplistic. The model ignored the interactions between adsorbed molecules and molecules in solution or interactions between adsorbed molecules. This method could be a useful tool to predict what crystal morphologies would be seen from a specific solvent. However, further refinements would need to be carried out before the model can provide more accurate and reliable predictions of crystal morphology.

2.3 The influence of crystal size on shock sensitivity

An investigation into RDX particle size on shock sensitivity was conducted by Moulard *et al* [91]. In their work they used two monomodal [§]cast PBX formulations, one containing fine RDX particles with a median size of 6 μm and the other coarse particles with 134 μm median size. Both contained 70% by weight RDX with a polyurethane binder. The shock to detonation (SDT) behaviour for the compositions was tested using flyer plate impact, projectile impact and wedge test. It was found that the PBX made with the fine RDX particles had a much lower shock sensitivity than the coarse RDX composition in the flyer plate experiment. The wedge test again showed that the finer RDX composition was less sensitive, showing a longer SDT period. In the projectile impact tests small steel cylinders were fired at 40 mm thick PBX samples from a powder gun. It was also seen that the PBX with the smaller RDX particles had a lower shock sensitivity, requiring a minimum projectile impact velocity of 1350 ms^{-1} . The coarse RDX PBX had a minimum impact velocity of 1133 ms^{-1} . The amounts of RDX ignited and the reaction growth rate was also calculated using a computer model based on the experimental data for input shock pressures ranging from 4 to 9 GPa. For all shock pressures only 0.2% of the fine RDX formulation was consumed. For the coarse RDX 5% was ignited at 4 GPa and at 9 GPa 13%. This suggests that there are more ignition sites in the coarse RDX. The reaction growth rates were the same for both fine and

[§] Monomodal, consisting of RDX crystals belonging to one size distribution.

coarse RDX PBX up to 6 GPa shock, above 6 GPa the reaction rate for the coarse RDX increased but the fine RDX showed no change. These results strongly suggest that smaller RDX particles have a reduced shock sensitivity as compared to larger ones. One shortcoming of this study was that only two particle sizes were examined, no intermediate crystal size was included, or data on bimodal compositions.

Belanger *et al* did look at a bimodal composition [92], PBX (CX-84). This PBX contains 84 wt.% RDX and 16 wt.% of an HTPB/DOA binder. PBX formulations were produced containing either a coarse-to-fine ratio of 70/30 or 75/25. The PBX samples were subjected to impacts over a range of shock energies by an explosively propelled flyer plate. It was found that the PBX containing the larger proportion of coarse RDX had a lower shock sensitivity. These results are contradictory to those obtained by Moulard previously described. However in this study two surfactants (Danatol DHE and HDBA**) were also used in the compositions. When only one surfactant was used in a formulation, the shock sensitivity of the PBX was reduced compared to when both were added. This is probably because when used alone it is more effective in coating the RDX crystals. This raises the question of how much of an effect the surfactant is having on the sensitivity. Would there be a difference if no surfactants were used? Perhaps experiments should have been included where this was the case so only the effect of changing the ratio of coarse to fine particles could clearly be seen

These apparently contradictory results were addressed by a second investigation by Moulard [93]. Three monomodal PBX formulations each containing 70 wt.% RDX and 30 wt.% polyurethane binder were prepared using either fine (6 μm), coarse (134 μm) or very coarse (428 μm) RDX crystals. The PBX formulations were subjected to wedge tests using an aluminium alloy flyer plate impacting between 1100 and 2300 ms^{-1} . It was reported that the shock sensitivity of each PBX was dependent upon the median particle size and the applied shock pressure. At low shock pressures (4.4 GPa) the PBX made with very coarse RDX was most sensitive. At high shock pressure (12 GPa) the very coarse RDX composition was the least

** Danatol DHE, 2-hydroxymethyl dimethylhydantoin
HDBA, 4-hydroxy-N,N-dimethylbulbularamide

sensitive and the fine RDX composition was the most sensitive, the coarse PBX had intermediate sensitivity. They explained that this reversal of shock sensitivity was due to the two stage process of shock to detonation transition as described by Lee and Tarver [94]. The first stage being ignition of hot spots by the shock wave and the second, growth of the reaction by coalescence of the burning fronts started at the hot spots. At lower shock pressures larger crystals are more sensitive, as the SDT is controlled by hotspot formation and larger particles are more efficient at producing hot spots than finer ones. This is because larger crystals localise the shock energy, whereas small crystals would dissipate the energy preventing hot spot formation. At high shock pressures smaller particles become more sensitive as they can support the growth of the reaction front since they are more efficient in energy transfer. It should be noted that the very coarse and fine RDX batches were produced by recrystallising from acetone and cyclohexanone respectively but the coarse RDX was produced by milling the very coarse RDX and sieving. This produced different crystal shapes, sharp crystals for the milled batch and smooth crystals for the fine and very coarse RDX. These differences in particle morphology could possibly have an effect on the sensitivity although the author [93] did not consider this to be significant and suggested that more work would be done to investigate any effects that particle processing might have.

The effect of particle size on the shock sensitivity of PBX compositions containing HMX was also investigated by Schledbauer and Kretschmer [95]. They produced monomodal and bimodal HMX compositions. The PBX compositions contained either 15 or 20% HTPB/IDPI binder. To maintain consistent mechanical properties, the Youngs modulus was kept constant by adjusting the proportion of plasticiser present. Large scale gap tests and steel projectile impact tests were performed on the compositions. Those formulated with 20% binder had a lower shock sensitivity than those made with 15% binder. It was found that compositions made with the coarse HMX crystals had a higher shock sensitivity than the fine HMX formulations. The bimodal PBX compositions had an intermediate shock sensitivity. In the projectile impact tests coarse HMX compositions were also the most shock sensitive. This investigation only looked at one bimodal composition, 80% coarse 20%

fine HMX. It would have been interesting to see what results would have obtained from another bimodal composition perhaps a 70/30 coarse to fine ratio. This would provide a comparison with the results from Moulard, who showed an increase in shock sensitivity when the proportion of fine particles was increased in a bimodal PBX. Would the same have been seen for the HMX PBXs?

The shock sensitivity of HTPB based PBXs with monomodal and bimodal RDX was investigated by Van der Steen using a gap test (the type of gap test was not specified in the paper) [96]. Monomodal PBXs containing 65 wt.% RDX showed that again PBXs formulated with the larger crystals were the most shock sensitive. In the same study PBX samples were subjected to high pressure (>10 GPa), short duration impacts from thin kapton flyers. This time the fine RDX compositions had the greater shock sensitivity. Two sets of results were presented for bimodal PBXs. The first kept the coarse to fine ratio the same (64/36) with coarse particles of 370 μm average size. The fine particle size was either 55 μm or 20 μm for each PBX sample. The results clearly showed that the PBX with the smaller fine RDX crystals was the most sensitive. For the second set of bimodal experiments the proportion of fine RDX particles was increased. The shock sensitivity increased when the coarse to fine ratio was changed from 76/24 (least sensitive) to 59/41 (most sensitive). These results are in good agreement with those obtained by Moulard [93]. In fact similar conclusions are made in this paper [96] that coarse crystals are more sensitive at lower shock pressures and at higher pressures finer particles have higher sensitiveness because they have a larger surface area allowing faster shock energy transfer.

Bouma *et al* [97] investigated PBX formulations using RDX particles of 300, 150 and 50 μm size. The crystals were pre-treated to produce a rounded and smooth morphology to eliminate any shape effect on sensitivity. PBXs were either cast or extruded using 70 or 85 wt.% RDX content. Initial impact sensitivity testing of the raw RDX lots was performed using a BAM fallhammer apparatus showed a significant decrease of sensitivity with decreasing particle size. Shock sensitivity was determined using the small scale gap test and the TNO PMMA gap test. In conflict with the results discussed in the previous papers [93,95,96] both the cast and extruded PBX

formulations containing the largest (300 μm) crystals were the least sensitive. Interestingly for the cast PBXs the most sensitive formulation was the one containing the medium (150 μm) crystals. These crystals were found to have the lowest density of the three batches. This implies a large number of internal defects, in fact optical microscopy showed that this was the case. The results from the extruded PBXs were not conclusive, voids were present in the binder and at the binder-RDX interface producing further sensitisation of the PBX and invalidating the results. In conclusion, these results do not provide much evidence for the effect of particle size on shock sensitivity. It does show that internal crystal defects can also have a strong sensitising effect. Also it should be noted that despite efforts to keep the crystal morphology the same for each RDX crystal size there were still some differences. The crystals with the most internal defects (150 μm) also were the most irregular in shape. Morphology therefore could also have affected the results obtained in this study.

Wang *et al* investigated the effect of RDX particle size on the shock sensitivity of a PBX composition using a “fluorine rubber F2641”^{††} [98]. RDX was sieved to produce fractions of particle sizes from 124 μm to 1.5 μm . Monomodal PBX formulations were produced with pressing to give final densities of 80, 90 and 95% of TMD. Shock sensitivity was determined by the small scale gap test (SSGT). For PBXs pressed to 80% of TMD the shock sensitivity increased with increasing particle size. The initiation pressure was lower for the PBXs made with larger RDX crystals. The same trends were seen for PBX formulations pressed to 90% of TMD although for each particle size the shock sensitivity was lower and the initiation pressure was higher than that at 80% TMD. For PBX compositions pressed to 95% of the TMD the trends were reversed with increasing shock sensitivity with PBXs made with smaller particles. Wang ascribed these results to the two stage theory of hot spot formation and subsequent reaction propagation as proposed by references; [93,96]. Unfortunately this paper did not include any work on bimodal compositions so no comparison to shock sensitivity results from the bimodal PBXs discussed earlier can be made. Another point that could be of significance is the effect of pressing at high densities when crystal fracture or

^{††} The exact nature of this binder was not given in this paper.

damage might occur (especially with larger crystals) which would lead to increased sensitivity. This was not considered by the authors.

The relationship between RDX shock sensitivity and crystal size was examined during a study by Czerski and Proud [82,83]. The shock sensitivity of raw RDX from three manufacturers was tested as-supplied using the SSGT using unpressed charges of 5 mm diameter and 25 mm length. Two class sizes were tested; “class 1” (three samples) 100-300 μm and “class 5” (four samples) 10-30 μm . Between samples of the same size class there were significant differences in shock sensitivity. This was attributed to differences in temperature distribution through the material after the shock was applied. There was no significant difference in sensitivity between the smaller and larger size classes. It appears in this case that other factors are influencing the differences seen for shock sensitivity such as crystal morphology. Within the two size classes there was a range of particle shapes. For the class 1 samples there were rounded (least sensitive), angular (most shock sensitive) and intermediate morphologies having a medium level of sensitivity suggesting that in this size range particle shape had a major influence on sensitivity. With the class 5 samples there was less variation in shape both the most and least sensitive crystals were rounded. Surface roughness (measured by mercury porosimetry) had a greater effect on sensitivity than size or morphology for the class 5 samples, however no correlation was seen between surface defects and sensitivity for the class 1 samples. From results of this paper the effect of particle size cannot be deduced since there was a great variation of morphology and surface defects within a size class. Instead it lends insight to the fact that shock sensitivity is also influenced by other crystal characteristics.

A better indication of the influence of particle size was reported by Caulder *et al* [99]. They tested monomodal PBX formulations containing I-RDX[®] that had been sieved into fractions ranging from 300 μm to <45 μm . Each PBX contained 77 wt.% of a specific particle size (300-212 μm , 212-125 μm , 90-45 μm , 45 μm) with 23 wt.% HTPB binder. Shock sensitivity of the PBXs was tested using the IHEGT. This showed that the shock sensitivity for PBXs containing smaller I-RDX[®] crystals was lower than that of PBXs containing the larger ones. In agreement with Czerski and Proud this report

also shows that other factors are involved in sensitivity other than just particle size. Scanning electron microscopy (SEM) of the different fractions of the I-RDX® indicated that the larger particles had more surface defects than the smaller crystals. The study also included shock sensitivity of a PBX made with Eurenco MI-RDX, this had a higher sensitivity than the I-RDX® PBX. SEM analysis of the MI-RDX revealed that it had more surface defects and wider range of crystal morphology than the I-RDX®. The results obtained here are more useful than those obtained by Czerski and Proud because this time RDX from the same manufacture (Eurenco/SNPE) was used, allowing a better comparison to be made between different particle sizes.

X-ray powder diffraction was used by Herrmann *et al* to investigate the effect of crystal size and crystal microstructure [100,101]. They examined standard RDX, I-RDX and RS-RDX grades (the origin of the samples was not specified). To overcome low sample absorbance and poor orientation statistics that often occur with powder diffraction measurements, a rocking curve technique was used. During a rocking curve measurement the sample is tilted through a reflection condition angle, this allows the evaluation of reflections separately crystal by crystal. From measuring the diffraction peak width they calculated the mean crystal size of each RDX sample, (the peak width at half of the maximum peak height is inversely proportional to the mean crystal size). They found that I-RDX crystals had the largest and standard RDX the smallest crystals, RS-RDX crystals were of intermediate size. This therefore also supports the theory that larger crystals confer reduced shock sensitivity.

Nanocomposite micro-particles of RDX were produced by Qiu *et al* using a novel spray drying method [102]. They took RDX recrystallised from acetone and 4 µm milled RDX crystals. Two nanocomposite formulations were prepared using polyvinyl acetate binder (PVA) and a vinyl resin VMCC[Ⓜ]. The formulations were dissolved into acetone then spray dried, producing micro-particles. A third conventional formulation made by slurry coating the RDX crystals with the VMCC binder was prepared as a comparison. SEM analysis showed that the micro-particles contained RDX crystals between 100 nm and 1 µm. The shock sensitivity of the three formulations was examined using a

[Ⓜ] VMCC contains vinyl chloride, vinyl acetate and maleic acid [102].

small scale gap test. Table 2.10 gives the shock sensitivities for the formulations.

Table 2.10 Characteristics of the formulations produced by Qiu et al, from reference 102.

Composition	Shock sensitivity (GPa)	RDX crystal size (μm)	Density (g/cm^3)	HMX (%)
RDX/PVA (spray dried)	4.0	0.1 - 1	1.58	4
RDX/VMCC (spray dried)	3.3	0.1 - 1	1.62	9
Milled RDX/VMCC (slurry coated)	2.5	4	1.64	9

The reduced shock sensitivity of the spray dried formulations compared to the slurry coated formulation was attributed to them containing much finer RDX crystals. SEM examination of the micro-particle formulations after pressing revealed that only very small intergranular voids of about 250 μm were present. The reduction in intergranular void size could also contribute to the reduction in shock sensitivity. Uniform mixing of the RDX and binder and the small RDX crystal size was given as probable causes for the much smaller void size observed. Qiu's work not only gives further evidence that particle size effects shock sensitivity but also provides a new method to produce explosive formulations of reduced sensitivity. Balzer *et al* [103] during their drop weight impact experiments of RDX and PETN also reported that ultra-fine PETN particles were less sensitive than conventional sized PETN. They stated that the smaller air/gas filled voids present are less efficient in forming hot spots during compression leading to reduced sensitivity.

In another study, Stepanov *et al* also investigated nano-crystalline RDX based compositions and found a significant reduction in shock sensitivity [104]. They produced nano-crystalline RDX by the rapid expansion of supercritical solutions (RESS) method using carbon dioxide as the solvent. This method allows the formation of powders with a narrow particle size distribution. Powders of mean particle size of 200 and 500 nm were prepared. As references, 4 μm RDX and class 1 RDX were also included. Shock sensitivity tests were performed using the NOL-small scale gap test (SSGT) on uncoated crystals and crystals coated with 12 wt.% wax binder. Figure 2.9 gives the SSGT results that were obtained.

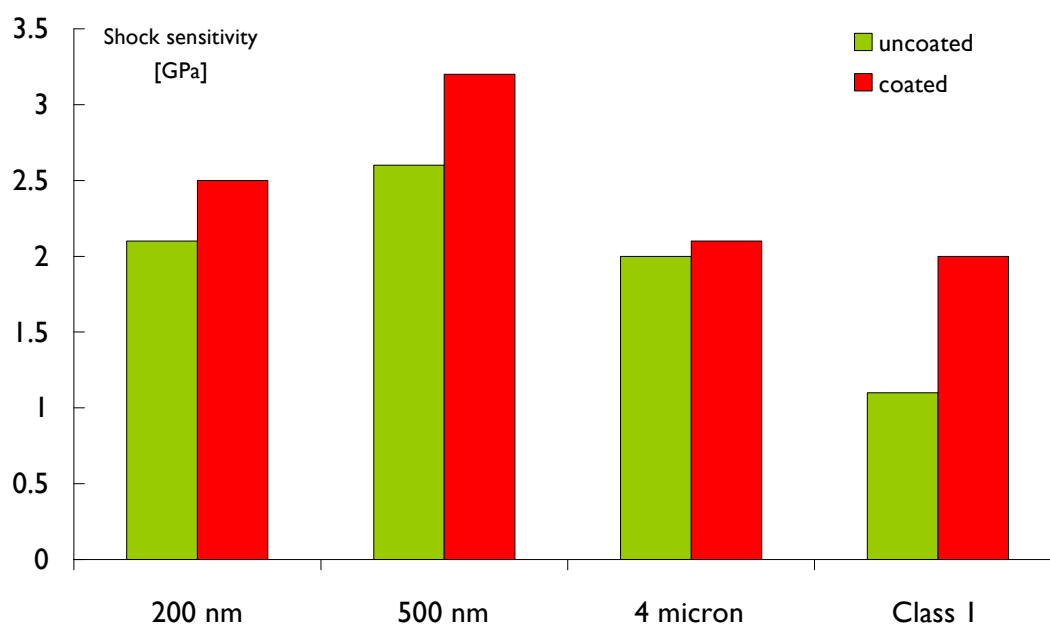


Fig 2.9 Shock sensitivity results obtained by Stepanov *et al* [104].

The nano-crystalline RDX products were found to have a lower shock sensitivity compared to the coarse reference samples. All the coated samples had a reduced sensitivity due to their higher densities (reduced void volume). Interestingly there was a reversal in shock sensitivity from 500 to 200 nm crystal size. This was thought to be due to a change in initiation mechanism. For formulations containing larger crystal sizes initiation is dominated by void collapse. At much smaller sizes, below around 500 nm, the overall specific surface area becomes very large allowing increased efficiency of the reaction front development, leading to increased sensitivity.

The duration of a shock wave also influences the sensitivity of energetic crystals of different sizes. With shocks of longer duration (a few microseconds), larger crystals are more sensitive, smaller particles become sensitive when shorter shocks are applied. Gap test experiments on packed PETN columns were undertaken by Chakravaty *et al* [105] to investigate the effect of shocks of relatively long duration, particle sizes tested were 180 μm and <1 μm . At a packing density of 90% TMD the large crystals had a critical initiation pressure of approximately 2.1 GPa whereas the sub-micron crystals required twice the initiation pressure (4.1 GPa) at the same packing density.

Shock initiation of hexanitrostilbene (HNS) using a laser driven flyer was done by Greenaway *et al* [106]. The flyer plate impact provided a shock of much shorter duration (approximately 1 ns) than the that in the gap tests. HNS particle sizes of 25 μm and <1 μm were packed to a TMD of 65-78%. Initiations were only observed for the sub-micron sized HNS, the coarse grain HNS was not initiated. The dependency of shock wave duration and crystal size on sensitivity can be explained by how effective hot spots are formed within the crystals. Shocks of short duration can easily cross the length of smaller crystals and generate hot spots within them. Shorter shocks however are less able to pass through larger crystals before weakening, so hot spot formation in larger crystals is less efficient. Therefore, when subjected to shocks of short duration, smaller crystals have higher sensitivity. Larger crystals have increased sensitivity to shocks of long duration as the shock wave is more likely to transverse the crystal and generate sufficient number of hot spots. Figure 2.10 illustrates these concepts.

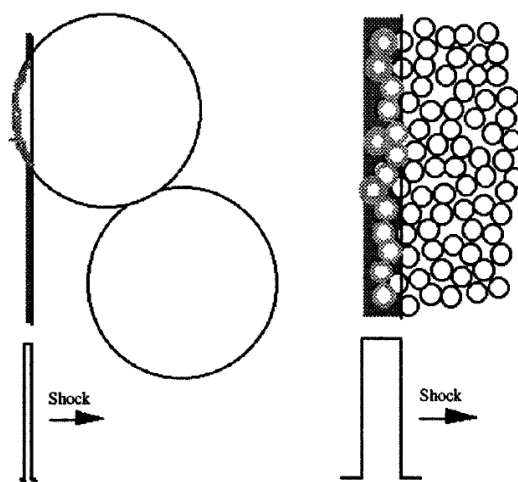


Fig. 2.10 Illustration showing the passage of a shock wave of short duration through large crystals (left) and a long shock passing through small crystals (right). Taken from reference 106.

In conclusion, it can be seen that particle size probably has a significant effect on the shock sensitivity of energetic materials. In monomodal formulations larger crystals are more sensitive at low shock pressures and smaller particles have a greater sensitivity at higher pressures. In bimodal compositions the situation is more complex. Increasing the ratio of fine to coarse crystals (while keeping the size of the fine crystals constant) or a reduction in the size of the fine crystals (while keeping the fine to coarse ratio constant) seems to increase

shock sensitivity. This is due to the greater efficiency of smaller particles in reaction propagation. Figure 2.11 illustrates this point. It is also apparent that shock sensitivity is also controlled by other parameters such as crystal morphology, internal defects and crystal surface roughness.

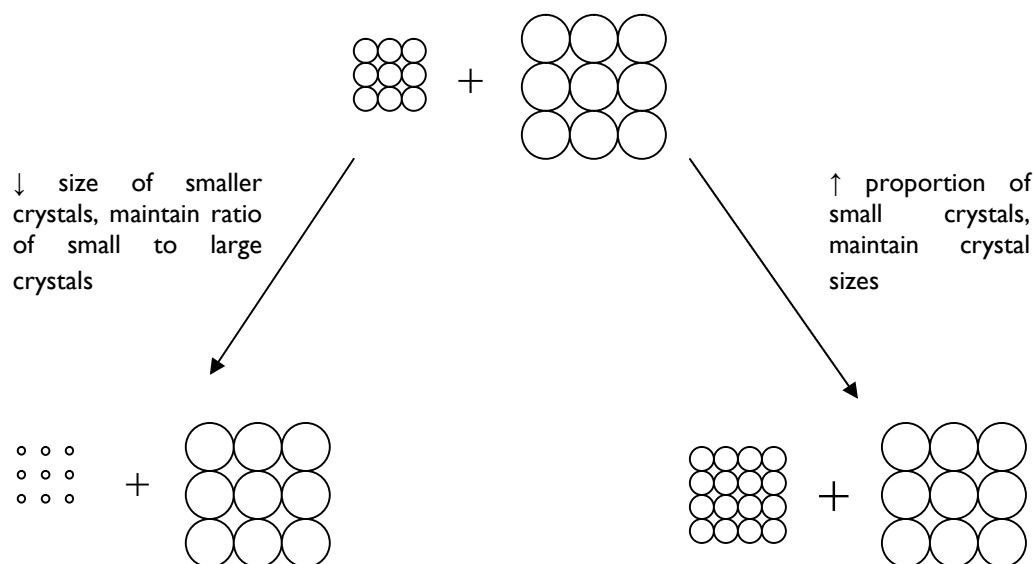


Fig. 2.11 Schematic illustrating the changes in crystal size and proportion of small to large crystals in a bimodal composition that increase sensitivity.

2.4 The influence of HMX content on RDX shock sensitivity

As highlighted in chapter 1, depending upon the synthesis method used RDX can contain different amounts of HMX formed as a by-product. Since it is more sensitive than RDX, (its figure of insensitiveness is only 56 compared to 80 for RDX [107]) its presence could increase shock sensitivity. This section will give an overview of some reports that have investigated this issue.

Gerber *et al* reported a correlation between HMX content and shock sensitivity with RDX formulated in bimodal PBXN-109 [108]. RS-RDX and conventional RDX from Dyno Nobel (Norway) and Eurenco I-RDX were used in the formulations and subjected to 50 mm gap tests. HMX content of each of the RDX lots was determined by HPLC. The results showed that there was a direct relationship between HMX content of the bimodal composition and its shock sensitivity. The RS-RDX formulation had the lowest amount of HMX and required the highest initiation pressure, (approximately 53 kbar) whereas standard RDX was initiated at around 12 kbar.

The contribution of HMX to shock sensitivity was investigated during the R⁴ program. The amount of HMX in each of the seven RDX lots was assessed by the participating laboratories using HPLC. Shock sensitivity was determined using the LSGT on the RDX lots formulated into PBXN-109. Table 2.11 gives the RDX lots studied and their mean HMX content and LSGT P_{50} results (shock pressure for 50% probability of detonation).

Table 2.11 Mean HMX content and shock sensitivity results from the R⁴ program. From reference 24.

RDX lot	Type	Mean %HMX (s.d.)	LSGT, P_{50} (GPa)
Eurengo MI-RDX	I	0.03 (0.02)	2.22
Eurengo I-RDX®	I	0.02 (0.08)	4.66
ADI	I	0.02 (0.01)	5.21
BAE RO	I	0.19 (0.13)	5.06
Dyno RS-RDX	II	0.82 (0.10)	5.24
Dyno Type II	II	8.55 (2.28)	3.86
BAE Holston	II	7.36 (0.92)	4.20

Dyno RS-RDX, Eurengo I-RDX®, ADI and BAE Royal Ordnance lots, all had relatively low shock sensitivities and contained less than 1% HMX, while Dyno type II and BAE Holston had much higher HMX content and showed a higher shock sensitivity. However, Eurengo MI-RDX also had a high sensitivity and also had a very low amount of HMX. These results therefore cannot suggest a definitive link between HMX content and sensitivity. For Eurengo MI-RDX perhaps another crystal characteristic was causing the increased sensitivity, such as surface or internal defects. For the high HMX lots there was a greater spread of results from the HMX analysis. This was possibly due to poor sampling technique. In RDX lots containing a larger amount of HMX, HMX tends to be present as small discreet crystals which settle out to the bottom of the container. Inadequate mixing prior to sampling may have been the reason for the higher standard deviations for these samples. The HPLC analysis method used was not consistent across the laboratories in the study. Different labs used different HPLC equipment and methodologies, although they did abide by the general procedure given by the munitions safety information and analysis centre (MSIAC) [24]. This may raise some reservations regarding the reliability of the results from this study.

Borne and Ritter published a report that investigated the link between HMX content of three RDX lots and their shock sensitivity when cast using 30 wt.% wax as a binder [109]. HPLC analysis was used to determine the HMX content of each RDX lot, while matching fluid optical microscopy and SEM were also performed to study internal and surface defects. In common with the other studies by Bourne [61,62,63,65] a high velocity projectile impact test was the method for assessing shock sensitivity. For statistical reliability, eight cast samples of each lot were tested. Table 2.12 gives details of the morphology, defects, HMX content and shock sensitivity test results of the three lots.

Table 2.12 Crystal characteristics, HMX content and shock sensitivity of the RDX lots examined by Borne and Ritter. From reference 109.

RDX lot	Crystal morphology	Defects	HMX %	Shock sensitivity (GPa)
1	angular and faceted	Very few internal or surface defects	0	≈ 6.05
2	rounded and irregular	Many internal voids	0.035	≈ 4.40
3	angular and faceted	Many internal voids, rough surface with HMX crystals embedded.	2.30	≈ 4.37
4	No details given	No details given	0.10	≈ 5.55
5	No details given	No details given	0.13	≈ 5.40

From these results it is difficult to find a relationship between HMX content and shock sensitivity. Lot 1 does have the lowest shock sensitivity and zero HMX, lots 2 and 3 however have similar sensitivities but lot 3 has much more HMX than lot 2. Furthermore, lots 4 and 5 both have much lower sensitivities than lot 2 despite containing more HMX than lot 2. It was concluded by the authors that HMX levels greater than 1% produce increased sensitivity but at amounts less than 0.15%, there was no correlation. In this study, shock sensitivity is probably being influenced more by internal defects than HMX content or any other crystal parameter. Lot 1 has very few defects and the lowest sensitivity whereas lots 2 and 3 have many defects and are more sensitive. Crystal morphology seems to have little influence, lot 2 has rounded crystals while lot 3 has faceted crystals with sharp edges and both showed

similar shock sensitivity. Interestingly, lot 1 consisted of sharp angular crystals but was the least sensitive, which runs against the theory that this type of morphology leads to increased sensitivity. Perhaps this study could be improved by controlling the number of internal defects and morphology between the lots that were examined. In agreement with the R⁴ results this report does not suggest a clear link between HMX content and shock sensitivity.

The removal of HMX from RDX lots produced by the Bachmann process was undertaken by Spyckerelle *et al* [110]. Two batches were recrystallised using a propriety method to produce low HMX Bachmann RDX having mean crystal diameters of 323 and 313 μm respectively. A third batch was also prepared by recrystallisation of low HMX Bachmann RDX to produce a smaller mean particle size (242 μm). These batches were cast into PBXN-109 formulations and shock sensitivity was measured using the LSGT. The results were compared to a PBXN-109 formulated with conventional type II RDX. Table 2.13 gives the HMX content and LSGT results for the three batches compared to the standard type II PBX.

Table 2.13 HMX content and shock sensitivity of low HMX Bachmann RDX prepared by Spyckerelle *et al*, from reference 110.

RDX Batch	HMX %	Shock sensitivity in PBXN-109 (GPa)
1	0.2	5.37
2	0.4	5.64
3	0.2	5.12
Standard type II RDX	> 4	2.63

These results clearly show that removal of HMX from type II RDX significantly reduces its shock sensitivity when in a PBX formulation. This study therefore provides good evidence that HMX content has a sensitising effect. It also shows that it is possible to improve the shock sensitivity of RDX produced by the Bachmann process. However the recrystallisation process can also reduce the quantity of internal defects and reduce surface roughness which would also lead to a reduction in shock sensitivity. Therefore the reduction in sensitivity obtained here may also be due to these effects.

The effect of the removal of HMX from commercially prepared type II RDX was investigated by Oxley *et al* [111]. Five RDX lots were studied, Eurenco

I-RDX[®], Dyno Nobel RS-RDX, one unprocessed BAE Holston (type II) and two BAE Holston lots that had been reprocessed by Eurenco to reduce their HMX content. The amount of HMX present in each lot was assessed by HPLC. Each RDX lot was formulated into a PBX (the composition was not specified) and tested for shock sensitivity using a LSGT. Table 2.14 gives the HMX content of each lot and its shock sensitivity.

Table 2.14 HMX content and shock sensitivity results of RDX lots investigated by Oxley *et al*, from reference 111.

RDX lot	HMX %	Shock sensitivity of PBX formulation (kbar)
I-RDX [®]	0	46.3
Dyno RS-RDX	0.1	44.3
Holston, reprocessed 1	2.9	43.1
Holston, reprocessed 2	1.9	41.6
Holston, unprocessed	15.5	35.6

There is an obvious correlation between the amount of HMX present in each RDX lot and its shock sensitivity when formulated into the PBX. The unprocessed Holston RDX lot contained the most HMX and was significantly more sensitive than the other lots. This study again indicates that reduced sensitivity can be achieved by reprocessing. The paper gave no information about crystal morphology and defects, and so it is not possible to determine if these factors could also have contributed to the observed results.

Herrmann *et al* [112] demonstrated that the way HMX recrystallises with RDX has an effect on overall crystal quality and shock sensitivity. They examined four RDX lots, Dyno RS-RDX, Eurenco I-RDX, a second Dyno RDX lot (referred to as RDX 2) and a sample processed by ICT referred to as RDX 1). They used X-ray diffraction (XRD) to determine mean crystal size and microstrain by measuring diffraction peak width. The total amount of HMX present was determined by HPLC. XRD was also used to determine the proportion of free crystallised HMX not co-crystallised in RDX crystals. Table 2.15 gives the results from their work. The final column gives the proportion of HMX that is co-crystallised within RDX crystals. Plotting the proportion of co-crystallised HMX against microstrain (fig. 2.12) gives a very good correlation. From this finding it was suggested by the authors that co-crystallised HMX has the greatest influence upon RDX microstrain and sensitivity rather than

the total HMX content. Incorporation of the larger HMX molecules within the RDX crystal lattice probably produces the increased microstrain that is observed.

Table 2.15 Results obtained by Herrmann *et al* giving the mean crystal size, microstrain, total HMX content, proportions of freely crystallised HMX and HMX co-crystallised within RDX crystals, ref. 112.

RDX lot	Mean crystal Size (μm)	Strain	Total HMX % by HPLC	Free crystallised HMX % by XRD	Co-crystallised HMX %
RDX 1	0.244	0.045	6.5	4.7	1.8
RDX 2	> 3	0.029	0.52	0.44	0.08
RS-RDX	> 3	0.021	2.6	2.6	0
I-RDX	> 3	0.023	0.01	0	0.01

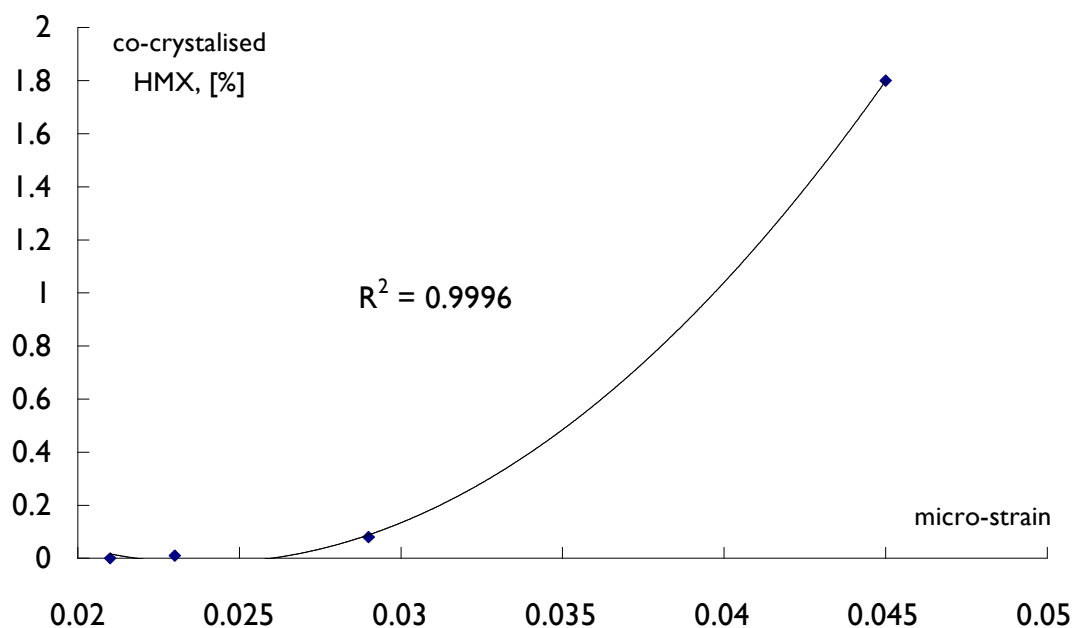


Fig 2.12 Plot of RDX crystal microstrain verses proportion of co-crystallised HMX for the RDX lots tested by Herrmann *et al*. Reproduced from reference 112.

The different solubilities of RDX and HMX in acetonitrile and water have been used by Boddu *et al* to separate HMX from crude type II RDX, leading to a less sensitive RDX product [113]. A solution of crude RDX containing 8.6% HMX was prepared by dissolving 40 g of RDX in one litre of acetonitrile at ambient temperature. A set of 50 ml aliquots were taken and each one had a

different volume of deionised water added, ranging from 25 to 250 ml. These were stirred at ambient temperature for two hours. The precipitate that formed was filtered and dried before weighing. It was found that when water was added up to a volume of 50 ml, a precipitate was produced which was greater than 99% RDX by weight. This method therefore could be a promising way of improving the quality of the final RDX product and reducing its sensitivity.

In summary, the amount of HMX in a given RDX lot can influence its shock sensitivity, but only when present in larger quantities as observed for type II RDX lots. HMX that crystallises within the RDX crystal has a greater influence than freely crystallised HMX. With smaller amounts, under about 4 wt.% HMX does not seem to have a significant effect on shock sensitivity. At these levels other factors such as internal defects appear to have a more dominant influence.

2.5 The effect of RDX ageing on shock sensitivity

Munitions are often stored for long periods and sometimes at high or very low temperatures. Ageing and severe environmental conditions could potentially alter IM characteristics, leading to an increased risk of initiation during storage, transportation or handling. Research has been carried out to see if reduced sensitivity grades of RDX suffer any loss of RS-characteristics over time and under environmental stress.

The first study was conducted by Eurenco on their I-RDX[®] product, ageing experiments being performed on both raw I-RDX[®] and I-RDX[®] in PBXN-109 formulation [114]. The first part investigated how the binder (wax), solvent (isopropyl alcohol), and phlegmatising agent dioctyl adipate (DOA) affected the chemical and crystal properties of five different RDX lots. Ageing was performed at room temperature for six months and at 60°C for one month. Results from IR-spectroscopy, HPLC and differential scanning calorimetry (DSC) showed no significant chemical changes for any of the RDX samples after room temperature or elevated temperature ageing. I-RDX[®] aged dry for 8 months or in IPA/water for three months, suffered no reduction in shock sensitivity when cast in PBXN-109. Ageing of PBX formulations containing either fresh or aged I-RDX[®] for up to six months at 60°C also

resulted in no reduction of shock sensitivity. However, for Holston RDX reprocessed by Eurenco to improve its sensitivity, the reduced sensitivity was lost after ageing. Oxley *et al* [111], provide a possible explanation for the loss of RS-property in reprocessed type II RDX. Ageing experiments on I-RDX® and reprocessed Holston type II RDX were conducted and a reversal to non-RS characteristic for the reprocessed RDX was found. Differential scanning calorimetry was used to study the thermal behaviour of the RDX samples. For the unprocessed and reprocessed Holston RDX samples an endotherm peak was observed on the DSC trace at 190°C which was absent for the I-RDX® sample. This endotherm is due to the formation of an HMX/RDX eutectic [115]. It was observed that the size of this eutectic peak increased during thermal cycling and ageing of samples that contained HMX. It was theorised that the binders and plasticisers present in a PBX formulation might enhance the formation of the HMX/RDX eutectic at ambient temperatures. In fact, unformulated Dyno Nobel RDX did not produce a eutectic after one year of ageing at 60°C, but a HMX/RDX eutectic was seen after ageing in a PBX formulation at room temperature. Therefore the loss of RS-behaviour in reprocessed type II RDX is probably caused by the formation of the HMX/RDX eutectic rather than HMX content. Thermal analysis by DSC was also undertaken during the Reduced Sensitivity Round Robin study (R4). The method used was specified by STANAG 4022 [13]. Unfortunately this method was unable to discriminate between RS and standard RDX samples. The melting points reported for type I RDX samples (Woolwich synthesis) were reproduced well but there was considerable variation in the melting points for the type II (Bachmann synthesis) samples. There was also difficulty in determining the decomposition energy [116]. Doherty and Watt suggest that DSC was only indicating the presence of HMX rather than any actual reduced sensitivity characteristics and that sample selection can have an influence on the result especially if the sample contains a high proportion of HMX [24]. Proper mixing and representative sampling before analysis would reduce the likelihood of unreliable results. Results obtained from DSC analysis have shown that the addition of only 2% HMX can cause sensitisation of RDX due to the formation of an RDX/HMX eutectic [111]. Therefore, it seems that there is some doubt that DSC is actually detecting RS-RDX quality. In RDX lots that

have large amounts of HMX, thorough mixing of the bulk sample before analysis is important, since HMX can settle out. Coning and quartering of lots prior to sampling should give an improved representative sample. Spyckerelle reported a modified DSC method that he claimed could distinguish between RS and non-RS RDX [110,117]. For non-RS RDX the DSC thermogram showed a broad exothermic decomposition peak whereas an RS-RDX sample showed a sharp exotherm peak. Spyckerelle applied this method to the R⁴ RDX batches with mixed success, assigning the correct sensitivity to only four of the seven RDX lots. Eurenco highlighted the fact that the sample has to be correctly sampled and prepared in accordance with their new method [118]. Since this method is being patented, little is known about its exact details [119]. Therefore, until this procedure can be fully assessed, there will be significant doubt about its ability to discriminate between RS and non RS-RDX. Research has also been carried out by Chemring Nobel into the effects of ageing on their RS-RDX product [120,121]. The first part of their paper presented data from shock sensitivity tests of RS-RDX formulated in pressed and cast-cured compositions. Pressed compositions were made using 10% binder (identity not specified) and 90% RS-RDX, standard Chemring Nobel type II and RDX type I. Formulations were subjected to a water gap test to determine their sensitivities. The RS-RDX showed a 50% reduction in shock sensitivity as compared to the standard type II RDX. PBXN-109 cast cured compositions of the same RDX lots were tested using the Intermediate Small scale Gap Test (ISGT). In agreement with the pressed composition result, RS-RDX had approximately half the sensitivity of the cast-cured standard type II RDX. This showed that the production method (pressed or cast-cured) used during formulation had no effect on sensitivity. RS-RDX crystals were aged at 60°C for 6 and 12 months and RS-RDX formulated into PBXN-109 were also aged at 60°C for 3, 6, 12 and 18 months. Both the pure crystals and the cast formulations showed no change in shock sensitivity, even after 18 months of ageing. This is an interesting result, Dyno RS-RDX is a type II RDX as is the reprocessed Holston RDX which showed a loss of RS-properties after ageing. A possible explanation for this conflict is that different PBX formulations were used for the reprocessed Holston and Dyno RS-RDX lots. It is possible that the HMX/RDX eutectic did not form as easily in the PBXN-109 formulation

used in this study so no loss of sensitivity was observed. Also, different gap tests were used, here the ISGT was chosen but the Eurenco study used the LSGT. Perhaps ageing and shock sensitivity tests should be done again with the same PBX formulation and gap test format to allow a better comparison between RS-RDX and I-RDX[®]. Finally, the I-RDX[®] and RS-RDX evaluations were carried out by their manufacturers, Eurenco and Chemring Nobel respectively. Because of this there may have been some degree of subconscious bias in their results. Perhaps these experiments should be repeated by an independent organisation to remove any doubt.

Spyckerelle *et al* at Eurenco undertook a series of experiments to investigate the loss of RS-properties after aging of I-RDX[®] mixed with HMX [117]. For their first experiment they added 2% HMX to pure I-RDX[®] and used this in a PBXN-109 formulation. This was subjected to LSGT before and after three months ageing at 60°C. The shock initiation pressures for the un-aged and aged formulations were 53.7 and 51.2 kbar with no significant reduction of RS characteristic due to ageing, was concluded. The second experiment involved HMX being present during recrystallisation of Woolwich RDX. Two batches were recrystallised, one with 0.5% HMX the other with 5% HMX. These were then formulated into PBXN-109 and subjected to LSGT before and after three months ageing at 60°C. It was found that the RDX co-crystallised with 5% HMX was more sensitive initially and after ageing. Physico-chemical analysis was performed on the three RDX batches. Melting point, density, particle size and solvent content were assessed and there was little variation in size distribution and internal defects between the three batches. HMX was found to be mostly in the fine fraction, which was believed to be because of its lower solubility so that HMX crystals form later and are smaller than RDX crystals. When there is a higher proportion of HMX, HMX crystallisation will occur earlier. DSC analysis of raw crystals from the three batches indicated that formation of an HMX/RDX eutectic was occurring during recrystallisation, which supports the findings and conclusions of Oxley *et al*.

To conclude, it seems that ageing of RS-type RDX does not cause any change in its RS characteristics. A loss of shock sensitivity is observed after ageing with reprocessed type II (Bachmann) RDX, possibly due to formation

of an HMX/RDX eutectic during the ageing process and/or recrystallisation which leads to an increase in shock sensitivity.

2.6 Characterisation of RS-RDX by shock sensitivity testing

RS-RDX grade products can only be distinguished from standard RDX by shock sensitivity testing using PBX formulations. The following section describes in more detail the various versions of the gap test and the initial findings from investigations into RS-RDX.

2.6.1 The gap test

Gap tests can be performed in a number of different ways but in essence they all share the same features. The gap test is used to determine the amount of shock that needs to be supplied to the test explosive to cause it to detonate. The gap test consists of the test explosive (the acceptor charge) which can either be unconfined or confined in a tube. The shock is supplied by a detonator and a booster charge (called the donor) which is placed above the test explosive. Between the donor and the acceptor there is a gap of variable thickness which acts to attenuate the shock wave from the donor. This gap can be made of a variety of materials depending upon the type of gap test being used. Many gap tests use an attenuator made from the plastic, polymethylmethacrylate (PMMA) while another version uses water as the gap material. To determine the result of a test a steel witness plate or block is positioned against the acceptor charge and usually there is a small air gap between the acceptor and the witness. A detonation (or a GO response) is considered to have occurred if a hole or depression is made in the witness plate/block. For a given explosive, a series of tests is performed to find the thickness of the gap at which there is a 50% probability of the test explosive detonating. The gap thickness indicates the shock sensitivity of the test explosive, a smaller gap at which a detonation occurs means a lower shock sensitivity. By knowing the size of the gap, the gap material and donor charge system used, the shock pressure delivered to the test explosive can be obtained using standard calibration curves [122]. The dimensions of the test charge are critical, if the diameter is less than its critical diameter then detonation will not occur. This is why there is a range of gap tests available. The critical

diameter of the explosive under examination is a key characteristic that has to be considered when choosing the gap test required. For explosives with critical diameters of less than 20 mm the small scale gap test (SSGT) is used. The intermediate scale gap test is selected for testing explosives with critical diameters between 20 and 40 mm. For larger critical diameters the extended large scale gap test and super large scale gap tests are available [48]. The most commonly used test for main charge explosives is the Naval Ordnance Laboratory large scale gap test (NOL-LSGT)^{**} [99], which has been used extensively for the shock sensitivity assessment of RS-RDX [123]. Figure 2.13 is a diagram showing the configuration for the LSGT. There is also an Insensitive Munitions Advanced Development Gap Test (IMADGT) which uses a larger diameter test charge than that used in the LSGT. It has an advantage over the LSGT because it uses a dent block instead of a witness plate to determine the strength of detonation, the deeper the dent the more powerful the reaction. This allows a correlation between the applied shock pressure or gap thickness and the depth of the dent produced [24]. The Insensitive High Explosive Gap Test (IHEGT) was developed as a smaller scale alternative to the NOL-LSGT for testing insensitive high explosives. The volume of the acceptor charge used in the IHEGT is only 4.4% of the acceptor charge volume used in the LSGT [124]. The water gap test uses a water gap instead of PMMA. It is essentially a small scale gap test used for explosives with critical diameters under 20 mm [125]. Table 2.16 lists some characteristics of the LSGT, IMADGT, IHEGT and the small scale water gap test. Because of the large range of gap-test formats in use, the NATO Insensitive Munitions Information Centre (NIMIC) has set up a software data-base providing information on the most commonly used gap tests, the NIMIC Excel Worksheets on Gap Tests (NEWGATES). Information regarding test design, scope, and testing principles is given. Also pressure and time calibration curves and gap test results are included [126].

^{**} The NOL-LSGT is not performed in the UK

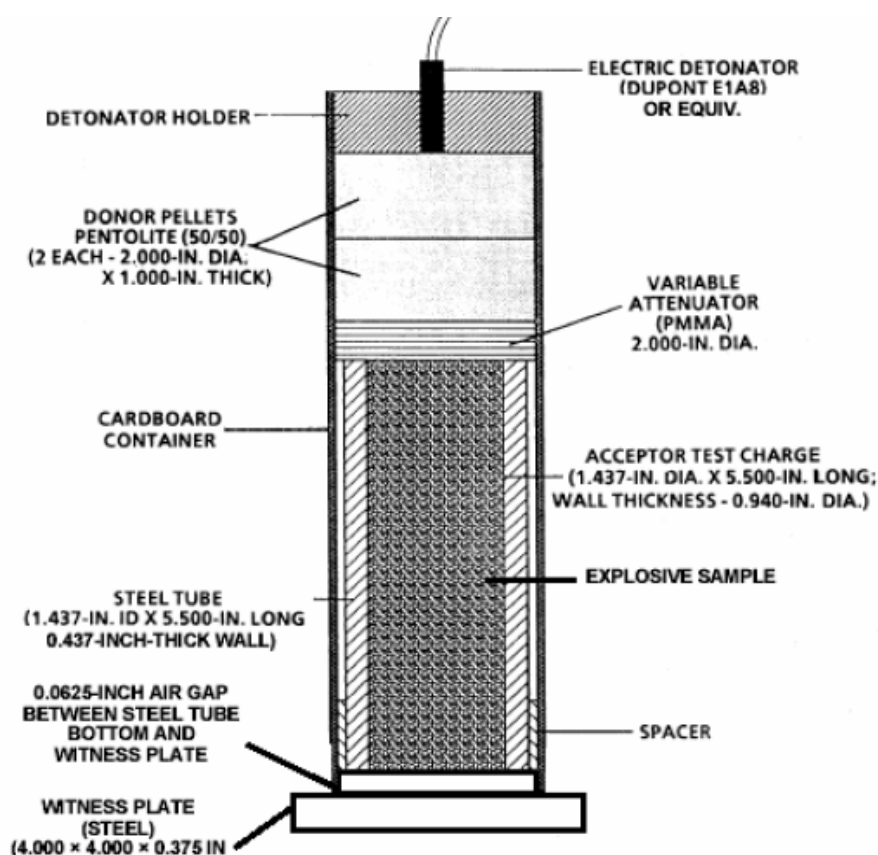


Fig. 2.13 Diagram showing the arrangement of the large scale gap test. From reference 99.

Table 2.16 Some characteristics of the NOL-LSGT, IMADGT, IHEGT and water gap tests.

Characteristic	IMADGT	NOL-LSGT	Water gap test	IHEGT
Charge diameter (mm)	73.2 ^[24]	36.5 ^[24]	21 ^[122]	12 ^[99]
Charge height (mm)	101.6 ^[24]	139.7 ^[24]	40 ^[122]	50.8 ^[96]
Confinement	Mild steel tube ^[24]	Mild steel tube ^[24]	Plexiglass tube ^[122]	PMMA tube ^[96]
Donor charge	Pressed pentolite pellets (x2), ρ 1.56 g cm ⁻³ ^[24]	Pressed pentolite pellets (x2), ρ 1.56 g cm ⁻³ ^[24]	95% RDX 5% wax, ρ 1.6 g cm ⁻³ ^[122]	Pressed pentolite pellets (x2), ρ 1.56 g cm ⁻³ ^[96]
Gap material	PMMA ^[24]	PMMA ^[24]	Water ^[122]	PMMA ^[96]
Witness	Mild steel dent block ^[24]	Mild steel witness plate ^[24]	Detonating cord and aluminium/lead witness plate ^[122]	Mild steel dent block ^[96]

Table 2.16 continued.

Characteristic	IMADGT	NOL-LSGT	Water gap test	IHEGT
GO/NO-GO metric	Depth of dent in dent block ^[24]	Presence or absence of clean hole in witness plate ^[24]	Dent/hole in witness plate ^[122]	Depth of dent in dent block

2.7 Review of early studies of RS-RDX

The first shock sensitivity test results were presented by Freche *et al* ^[124]. They performed LSGTs and ELSGTs on PBX formulations (PBXN-109/111 and PBXW-115)^{§§} using SNPE I-RDX, MI-RDX and standard RDX from other sources. For PBXN-109 formulations using SNPE I-RDX a shock pressure of approximately 56 kbar was required to produce detonation whereas for MI-RDX a shock of 37 kbar was needed. This shows a reduction in shock sensitivity of about 30%. A similar result was achieved for a PBX composition of I-RDX[®] (95 kbar) compared to MI-RDX (65 kbar) but from the data presented it was not possible to tell which composition was used (PBXN-111 or PBXW-115). The shock sensitivity for the PBXW-115 formulation using RDX from an Australian supplier was also incorrectly reported by Freche as being about 55 kbar. In fact it is less sensitive, requiring a shock of 62 kbar (6.3 GPa) for 50% probability of initiation ^[127]. Data were also supplied by Freche indicating a reduction in sensitivity of munitions filled with a PBXN-109 composition with I-RDX[®] when subjected to a heavy fragment impact and sympathetic detonation. For the heavy fragment impact test, detonation occurred with impact velocities above 1400 ms⁻¹ for munitions filled with MI-RDX PBX but when filled with I-RDX[®] PBX, detonation occurred at impact velocities above 1900 ms⁻¹. In the sympathetic detonation test, munitions filled with an I-RDX[®] PBX also performed better. No response was seen for munitions filled with I-RDX[®] PBX with a diameter of up to 130 mm, for munitions filled with MI-RDX the maximum diameter was only 75 mm before sympathetic detonation took place ^[124]. The Australian research group, Defence Science and Technology Organisation (DSTO) has also found a

^{§§} PBXN-109 is 64% RDX, 24% aluminium, 7.3% HTPB polymer and 7.3% plasticiser.

PBXW-115 is 20% RDX 43% ammonium perchlorate, 25% aluminium, 6% HTPB and 6% IDP plasticiser

PBXW-111 is 20% RDX, 25% aluminium, 43% ammonium perchlorate, 5.7% HTPB and 5.7% IDP plasticiser.

reduction in shock sensitivity in sympathetic detonation tests with munitions filled with RS-RDX PBXs. With a RS-RDX filling the test is passed (a type II response or better) at a stand off distance of 240 – 300 mm. With a conventional RDX based PBX filling the test was passed at a separation distance of 360 mm or greater [128]. An insensitive RDX-PBX (FOXIT) has also been produced by NEXPLO Bofors AB by a proprietary recrystallisation process. The critical diameter of FOXIT is in excess of 110 mm^{***}. The same test was carried out on a PBX containing a standard RDX (FPX 7) which gave a critical diameter of only 50 mm. Gap tests on the same PBXs showed the same reduced shock sensitivity for FOXIT over FPX 7 [129]. These results are supported by data from SNPE reporting that the critical diameter of PBXN-109 is increased from 7 to 14 mm when I-RDX[®] is used instead of MI-RDX [130]. Comparisons between two RDX grades produced by ADI Ltd (Australia), called Grade A and B, when used in pressed PBX formulations indicate a loss of reduced sensitivity after pressing. When a composition based on Grade A RDX (which has RS-RDX properties) was pressed it was shown to have the same sensitivity as that of Grade B, (a non-RS-RDX). Pressing of the RS-RDX possibly causes fracture of the crystals negating their RS quality [131]. DSTO carried out shock sensitivity tests using a LSGT on SNPE I-RDX, Dyno Nobel type II, two ADI grade A batches and an ADI grade B batch. The tests were performed using a PBX formulation (ARX-2020) of 78% RDX to 22% of a binder based on HTPB polymer and dioctyl adipate plasticiser. To allow direct comparison of shock sensitivities the PBX mixing and curing processes were carried out under the same conditions. Table 2.17 shows the gap test results for each RDX lot.

^{***} FOXIT has identical composition to FPX 7 developed as an underwater charge. Its composition is 20% RDX, 25% aluminium, 40% ammonium perchlorate, 15% HTPB binder (MSIAC energetic materials compendium).

Table 2.17 Gap test results for shock sensitivity assessment performed on ARX-2020 PBX formulations by DSTO, from reference [131].

RDX Source	Initiation pressure (50% gap) GPa
Dyno Nobel Type II	3.01
ADI (Grade B)	2.92
SNPE I-RDX	4.46
ADI (Grade A, Mulwala plant)	4.62
ADI (Grade A, Albion plant)	4.68

Both the I-RDX® and the ADI grade A RDX show a significant decrease in shock sensitivity, requiring a greater applied shock wave pressure to cause initiation, compared to the standard RDX products, (Dyno Nobel and ADI grade B). The small variations seen between the ADI grade A RDX and I-RDX® were attributed to minor differences in particle size distribution or morphology. The shock sensitivities of Dyno-Nobel RS-RDX, Eurenco I-RDX and conventional Dyno-RS-RDX were compared using a LSGT of these products cast into a PBXN-109 formulation. The initiation pressure for the standard RDX was approximately 40 kbar lower than that of the RS-RDX and the I-RDX formulations [132].

2.8 Introduction to the RS-RDX inter-laboratory round robin (R4) program

Following the investigations carried out to distinguish between RS-RDX and conventional RDX, it became apparent that STANAG 4022 [13] (which gives specifications and characteristics for RDX) did not cover appropriate analytical procedures to achieve this aim. Also the standardised sensitivity testing of pure RDX and RDX PBX compositions was not successful in differentiating between RS-RDX and standard RDX [133]. A technical meeting was jointly organised by NATO AC/326 sub-group 1 and NIMIC (NATO Insensitive Munitions Information Centre^{†††}) during the period of 17 – 20 November 2003 in Meppen, Germany to discuss the RS-RDX issue [134]. During this meeting available data were reviewed to define the designation of RS-RDX and to find analytical procedures that might be able to identify between RS and standard RDX. These methods investigated crystal properties

^{†††} Now known as the Munitions Safety Information and Analysis Centre, (MSIAC)

that were considered to influence RDX sensitivity, such as internal crystal defects, surface defects and lattice dislocations. The most significant outcome of the meeting was the proposal of an inter-laboratory RS-RDX Round Robin program (R⁴). This programme was to perform a suite of tests on RS-RDX and standard RDX batches supplied by various manufacturers. Each laboratory was supplied with a sample of every RDX batch to be analysed. The samples were identified only with a code number so that participating laboratories were “blinded” to the source of each sample. The principle aim of the R⁴ program was to find test methods capable of determining RS-RDX that could be included in an updated version of STANAG 4020 [123]

CHAPTER 3

Theory of experimental techniques used

3.1 Micromechanical property analysis using nanoindentation

Nanoindentation as the name suggests, involves indenting the material being analysed at very small scales. The main advantage of the technique is that it allows a direct measurement of the mechanical properties of a material from the load/displacement data that is obtained. This obviates the need to image and measure the indentation impression that other indentation methods require [135]. Figure 3.1 is a schematic diagram of a typical nanoindentation instrument.

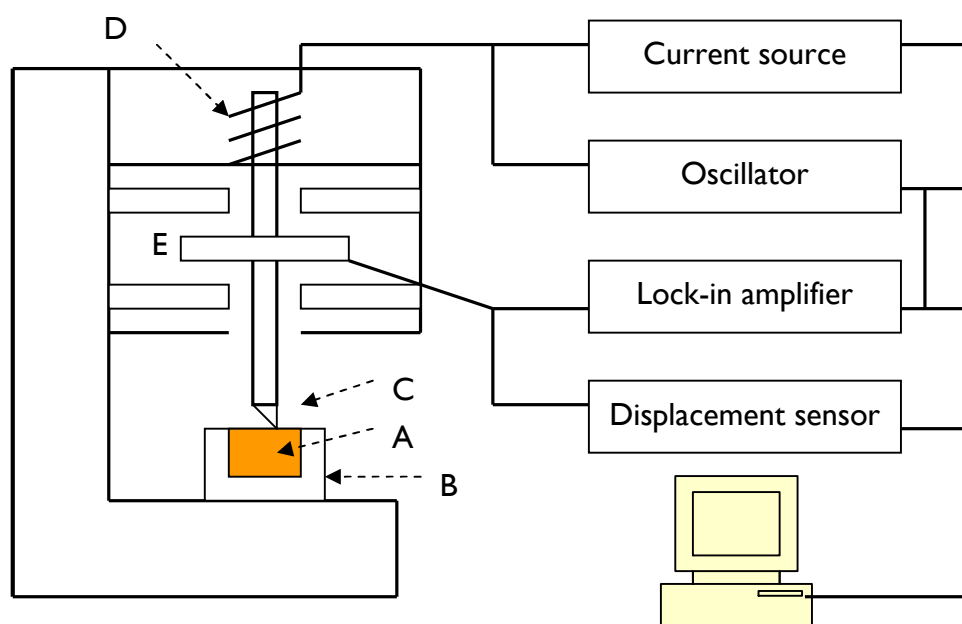


Fig. 3.1 Schematic diagram of a typical nanoindentation instrument. (A) sample, (B) resin block, (C) indenter, (D) load application coil, (E) displacement sensor system. Taken from reference 135.

During a nanoindentation measurement, the indenter is lowered until it touches the sample surface, then the tip is pressed into the sample until a predetermined maximum load is reached. The tip of the indenter is usually made from diamond. In the work described here, a Berkovich indenter is used which has a triangular pyramid shape. Figure 3.2 is a diagram of a typical nanoindenter with a Berkovich tip, figure 3.3 is an SEM image of a Berkovich tip.

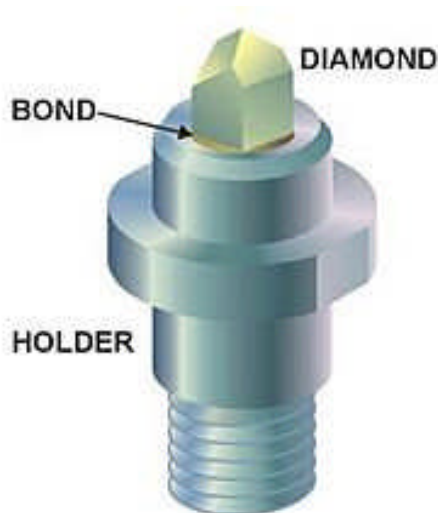


Fig. 3.2 Diagram of a typical nanoindenter with a Berkovich tip. From reference 136.

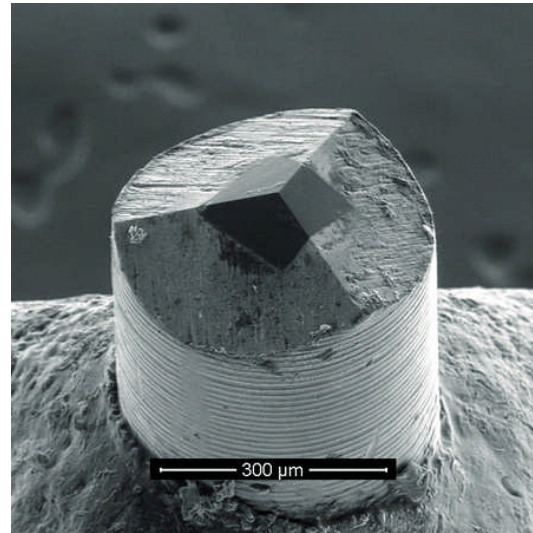


Fig. 3.3 SEM image of a Berkovich tip. Taken from reference 137.

The load applied to the indenter is controlled by the indentation software via the load application coil. The rate at which the load is applied can also be selected. Once the maximum load is reached, the indenter is retracted (also at a preselected rate), this is known as the unloading phase. The maximum load may also be held for a period of time prior to unloading, if required. The response of the material to the applied load is measured by the displacement sensor system. Whilst the measurement is running the software can display a real-time plot of the load-displacement data, an example of a load-displacement curve is figure 3.4. From the curve three fundamental quantities are obtained, the maximum load P_{\max} , maximum displacement or penetration depth h_{\max} and the elastic unloading stiffness or contact stiffness S . The stiffness of the sample is given by the gradient of the initial section of the unloading curve dP/dh . The accuracy of the hardness and elastic modulus measurements is dependent upon how well these basic values are obtained. The final depth of the indenter after the load is completely released, (the permanent indentation depth) h_f , is also an important measurement that is provided [135]. On the loading curve, steps are sometimes observed, that are known as “pop-ins”. Figure 3.4 give such an example. Pop-ins occur when the indenter suddenly moves deeper into the sample due to plastic deformation such as fracturing or cracking. Crystals that are less elastic would be expected to exhibit plastic deformation (pop-ins) at a lower applied load.

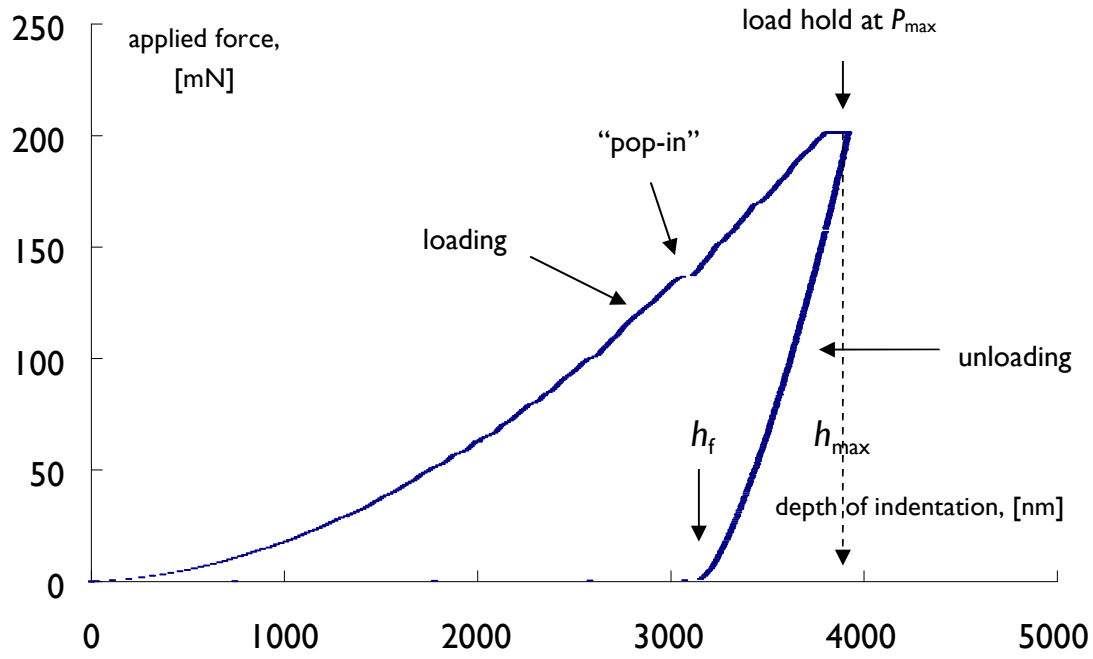


Fig. 3.4 An example of an indentation versus applied load curve obtained from a BAE-RO RDX crystal using a maximum load of 200 mN.

From the curves produced, the mean values for the indentation hardness, H_{IT} and indentation modulus E_{IT} (in GPa) were calculated for each RDX sample. The indentation hardness (expressed as MPa) was calculated using equation 3.1 [138], it is a measure of the resistance of the RDX crystal to permanent deformation.

$$H_{IT} = \frac{P_{\max}}{A_p} \quad 3.1$$

Here, A_p is the projected contact area of the applied load. The indentation modulus, E_{IT} was found using formula 3.2 [138,139].

$$E_{IT} = \frac{1 - \nu_s^2}{\frac{1}{E_r} - \frac{1 - \nu_i^2}{E_i}} \quad 3.2$$

Where, ν_s and ν_i are the Poissons ratios for the sample and the indenter; E_i is the elastic modulus of the indenter and E_r is the reduced modulus. The

Poisson's ratio is the ratio of expansion (lateral strain) to compression (axial strain) [140], E_r is calculated from equation 3.3 [138]. Therefore E_{IT} takes into account that elastic deformations occur in both the specimen and the indenter co-currently.

$$E_r = \frac{S \sqrt{\pi}}{2 \beta \sqrt{A_p}} \quad 3.3$$

Here, S is the stiffness of the sample and β is a geometric factor that depends upon the indenter profile. For a Berkovich tip this has a value of 1.034. The units for E_{IT} and E_r are in Pa. The indentation creep, C_{IT} and the proportion of elastic work to total work during indentation, η_{IT} was also determined. C_{IT} is a measure of how much the material permanently deforms whilst the maximum load is applied. It is given by formula 3.4:

$$C_{IT} = \frac{h_2 - h_1}{h_1} \times 100 \quad (3.4)$$

Here, h_1 is the indentation depth when maximum load is reached and h_2 is the depth at the end of the load holding period. η_{IT} is calculated using formula 3.5:

$$\eta_{IT} = \frac{W_{elastic}}{W_{elastic} + W_{plastic}} \times 100 \quad (3.5)$$

Here $W_{elastic}$ and $W_{plastic}$ are the elastic and plastic work performed during the indentation.

3.2 Assessment of crystal morphology by rheological analysis of RDX suspensions

Rheology is the study of the deformation and flow of materials either as single substances or of mixtures and suspensions [141]. The flow behaviour of

particles is strongly influenced by particle shape [142] and this has been reported for a wide range of materials [143,144,145]. In view of this rheological analysis was used to characterise RDX particle morphology.

A rheometer is an instrument that measures rheological properties of a material. A typical rheometer consists of a stationary lower plate where the sample is placed and an upper plate of area A , which rotates at a defined angular velocity, ω . The material between the plates undergoes shear deformation. At the surface of the upper plate the material has the same velocity, at the surface of the stationary plate its velocity is zero, (figure 3.5). The shear stress, σ experienced by the material is simply the applied tangential force F , divided by the area A and is measured in Pascals (Pa). (Equation 3.6)

$$\sigma = \frac{F}{A} \quad (3.6)$$

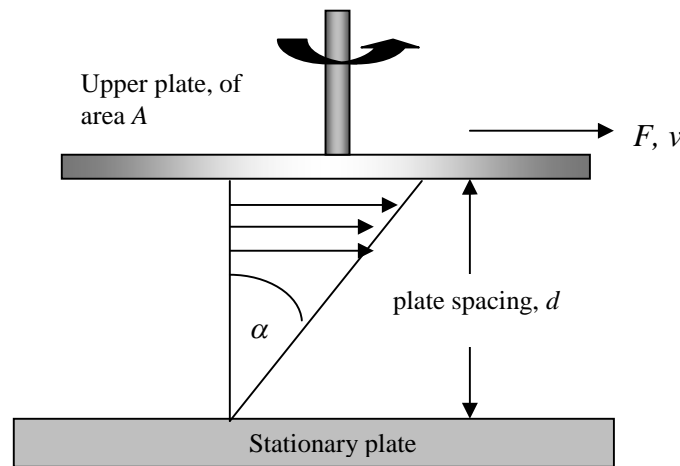


Fig. 3.5 Schematic showing the basic principle of a rheometer.

The deformation that is produced by the shear stress, (shown by angle α) is the shear strain, γ . The rate at which γ changes with time is constant across the spacing between the plates, d this is known as the shear rate, $\dot{\gamma}$ its units are s^{-1} , (equation 3.7).

$$\gamma^* = \frac{d\gamma}{dt} \quad (3.7)$$

The shear stress σ , is proportional to the shear rate γ^* , the constant is the viscosity, η of the material given in Pascal-seconds (Pa.s) it is a measure of how resistant the material is to deformation [146], (equation 3.8).

$$\eta = \frac{\sigma}{\gamma^*} \quad (3.8)$$

CHAPTER 4

Experimental methods

4.1 Samples studied and sampling techniques used

The RDX samples studied throughout this work are listed in table 4.1 ^[147].

Table 4.1 RDX lots used in this analysis [** Now Chemring Nobel † plant no longer in operation*].

Ref. #	RDX Source	Production Method	Mean HMX content (Wt.%) ¹⁴⁷
1	Eureco MI-RDX	Woolwich	0.03
2	†BAE-RO Bridgwater	Woolwich	0.19
3	ADI	Woolwich	0.02
4	*Dyno Nobel Type II	Bachmann Process	8.55
5	*Dyno Nobel RS-RDX	Bachmann, (<i>reprocessed</i>)	0.82
6	Eureco I-RDX	Woolwich	0.02
7	BAE Holston	Bachmann Process	7.36
8	Chemring Type II	Bachmann Process	4-17 (expected)
9	Chemring F-RDX	Bachmann Process (<i>reprocessed</i>)	<5 (expected)
10	Chemring RS-RDX	Bachman Process (<i>reprocessed</i>)	<5 (expected)

Representative samples of each RDX lot (>100 g) were obtained using the coning and quartering method. During the coning and quartering method the bulk material to be sampled is poured into a cone shaped pile on a flat surface. The pile is then flattened into a “cake” which is then divided into four quarters. One pair of diagonally opposing quarters are taken and collected together for re-sampling and the other two quarters are placed back in the container for storage. The material for re-sampling is coned and quartered again and the process is repeated until the required amount of sample is left. Samples were then dried, in a vacuum oven at 100°C for approximately two hours. Further sampling using a riffle splitter was also used when sampling RDX for the rheology experiments.

4.2 Internal defects assessment and nanoindentation methods



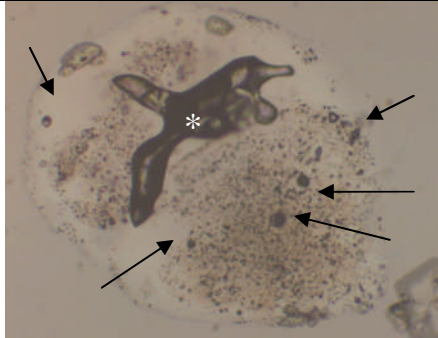
4.2.1 Internal defects assessment by optical microscopy

This study used the method prescribed for the NATO R⁴ program [148], the samples examined being those listed in table 4.1. Approximately 5 g of each RDX sample was dried in a vacuum oven at 100°C for approximately two hours if no dry sample was available. A small quantity (< 1 mg) was sprinkled over a glass microscope slide and approximately five drops of matching refractive index fluid, $n = 1.590$ (Cargille, USA) were added. The crystals were dispersed through the fluid by gentle stirring, whilst trying to avoid breaking any crystals. A cover slip was placed on top of the crystal suspension.

Microscopy was performed using an optical microscope (Polyvar MET) and images of selected crystals were captured using a digital camera (Polaroid, Cybertek) linked to the microscope. Fifty crystals were selected from each sample and the images captured using the digital camera. Since it was often hard to see the edges of a crystal it was important that a crystal was not in contact with another.

For each selected crystal an internal defect score was awarded. This was done by counting the number of each size of defect within the crystal. Larger defects scored higher than smaller defects, also crystal clarity was included. Defects were assessed as being either large ($> 100\ \mu\text{m}$), medium ($10\text{--}100\ \mu\text{m}$) or small ($< 10\ \mu\text{m}$). Points were also given if the crystal had any dark or cloudy areas. In the original R⁴ study 400 points were awarded to a cloudy crystal, in this study a score of 4000 per cloudy crystal was given. This modification gave a slight improvement on the correlation between the internal defect scores and shock sensitivity. Table 4.2 shows examples of crystals containing small, medium and large defects and cloudy crystals. The points awarded for each defect are also given. The scores for each sample of 50 crystals were obtained using a scoring system to assign a total internal defect score for a particular RDX lot. A mean score per crystal was obtained and the standard deviation and 95% confidence limits were calculated. This gave an indication of the consistency and reliability of the data. The mean internal defect score for each RDX lot was plotted against its shock sensitivity obtained during the R⁴ program to find if there is a correlation between the two characteristics.

Table 4.2 Micrographs showing RDX crystals containing small, medium and large internal defects. The defect scores awarded to each crystal are given.

	Large defects x 100	Medium defects x 50 (←)	Small defects x 10 ()	Dark/ cloudy 4000	Total score 410
	0	4	21	Not cloudy	
	0	200	210	0	
	Large defects x 100	Medium defects x 50 (←)	Small defects x 10 ()	Dark/ cloudy 4000	Total score 290
	0	1	24	Not cloudy	
	0	50	240	0	
	Large defects x 100 (*)	Medium defects x 50 (←)	Small defects x 10	Dark/ cloudy 4000	Total score 8990
	1	7	454	Cloudy	
	100	350	4540	4000	

4.2.2 Nanoindentation methods

The samples analysed were 1 to 7 in table 4.1. RDX lots were categorised into two groups, high defect content (Dyno Type II, BAE Holston and Eurenco MI-RDX) and low defect content (BAE-RO, ADI, Eurenco I-RDX and Dyno RS-RDX). Representative samples were obtained using the coning and quartering procedure. Each RDX sample was then sieved into 150-500 μm and 45-150 μm size fractions and dried in a vacuum oven at 100°C. The sieved and dried crystals were then collected into a small vial which was rolled and tipped to ensure complete mixing. Approximately 0.5 g of each fraction was taken from the vial for mounting into resin blocks. Each sample was placed into an empty pharmaceutical tablet blister, resin (Kleer Set type FF, Metprep UK) was then poured into the blister and allowed to set. After setting the resin-sample tablet was extracted from the blister and placed into a mould. Resin (10 ml), was

poured into the moulds and allowed to cure. Another 25 ml of resin was then added and left to cure for up to 12 hours at room temperature. After solidification, the surface containing embedded crystals was ground using 800 and 4000 grit sandpaper to expose the crystals and provide a smooth surface. Further polishing with 0.5 μm alumina paste provided a mirror finish. Figure 4.1 shows a resin block with an RDX sample embedded in it.

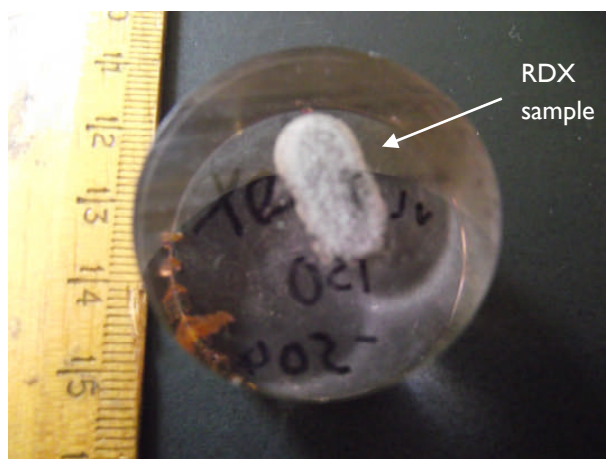


Fig. 4.1 A resin block with an RDX sample embedded in it.

Nanohardness testing was undertaken with a Nanohardness tester (CSM instruments, Switzerland) using a Berkovich indenter, see figure 4.3. Approximately 25 crystals were examined from each sample. For each crystal, six indentations, using loads of 10, 20, 50, 100, 150 and 200 mN were performed. Further measurements were also carried out at 200 mN load. Table 4.3 shows the loading/unloading rates and pause duration at maximum applied load at each load level. A linear loading and unloading rate was used throughout. Figure 4.2 shows an RDX crystal with indentations made at each maximum load level.

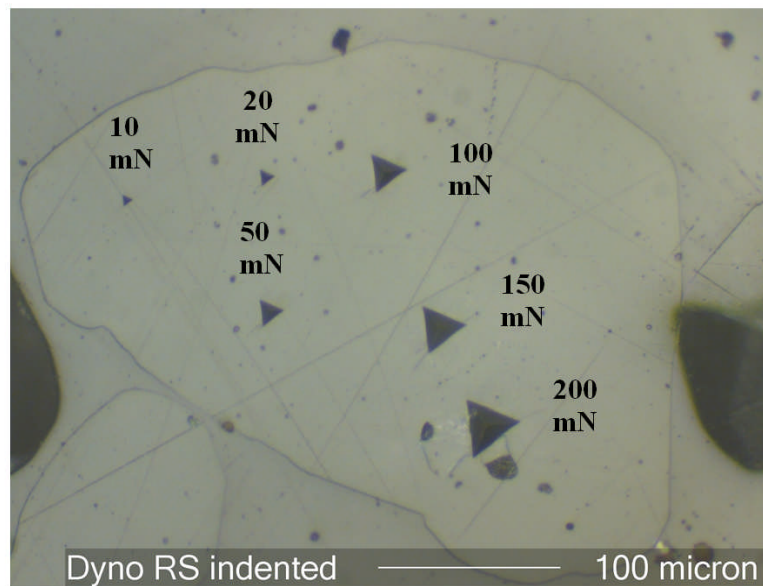


Fig. 4.2 Micrograph of an RDX crystal with indentations produced at each maximum load.

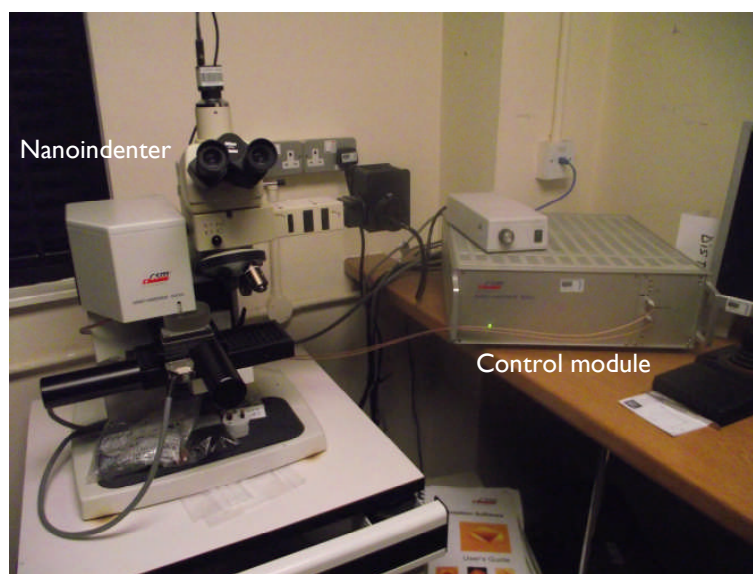


Fig. 4.3 The CSM Nanohardness tester used in this work.

Table 4.3 Measurement parameters used for nanoindentation experiment.

Maximum applied load (mN)	Loading/unloading rate (mN/min)	Pause duration at maximum load (s)
10	20	30
20	40	30
50	100	30
100	200	30
150	300	30
200	400	30

4.3 Morphology assessment, rheology methods and surface defects assessment using SEM

4.3.1 Matching refractive index microscopy

4.3.1 a) Morphology assessment performed by the author

RDX samples analysed were #1-7 listed in table 4.1. The sample preparation was exactly the same as that for the internal defect assessment method, except contrasting refractive index media was used $n = 1.512$ (Cargille, USA). For each RDX sample fifty crystals were selected. A crystal was selected if it was not in contact with another crystal. Crystals were selected according to the following guidelines [148]:

1. Very small crystals were not selected.
(possibly fragments or HMX crystals)
2. Crystal edges clearly defined and in focus.
3. Crystal fills at least 50% of field of view.

Each of the fifty crystals was assigned to a “morphology bin” and scored depending upon its shape. Table 4.4 shows examples of crystals from each morphology bin and their assigned scores.

Table. 4.4 Examples of crystals from each morphology bin with scores given for each crystal.

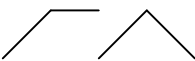




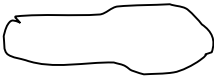
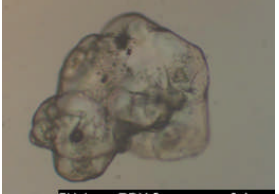

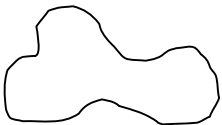














Bin	Description	Points	Examples	
A	Sharp edges and/or corners 	100		
B	Elongated, rounded	40		
C	Irregular, rough 	35		

Table 4.4 continued.

D	Irregular, smooth 	30		
E	Much geometry 	20		
F	Some geometry 	15		
G	Elliptical 	10		
H	Circular/spherical 	5		

4.3.1 b) Multi-person RDX crystal morphology assessment exercise

The morphology assessment described in the previous section is highly subjective, crystal shapes can be ambiguous and do not always fit into a particular morphology class, and often a best guess or estimation is needed. Therefore to investigate how reproducible the morphology assessment technique was a multi-person assessment exercise was undertaken. This involved collating all the photo-micrographs taken into a single document. This document was then given to members of staff and students at Cranfield University who were asked to assess each crystal in the same way as the original assessment. An improvement upon the original assessment was to give the assessors a crib sheet which had photomicrographs of crystals that exemplified each morphology bin (table 4.4). In the original R⁴ assessment only hand drawn outlines were given as a guideline for assigning morphology.

The completed assessment forms were then scored using the same scoring system as the original assessment.

4.3.2 Rheology experimental methods

4.3.2 a) Samples tested and instrument used

Five of the R⁴ samples were examined. Samples chosen were ones which showed the extremes of morphology (Dyno Type II and Dyno RS) and RDX lots having intermediate morphology characteristics, (BAE-Holston, BAE-RO and Eurenco I-RDX). All measurements were performed using a CVOR-150 (Bohlin instruments Ltd.) rheometer with a parallel plate geometry (40 mm diameter plate), see figure 4.4. A Peltier temperature control system was used to keep a constant temperature of 25°C for all measurements.



Fig. 4.4 Photo of the C-VOR 150 (Bohlin Instruments Ltd.) used to measure the rheological properties of the RDX-PEG suspensions.

4.3.2 b) Viscosity/shear rate versus controlled shear stress

Viscometry measurements were performed to determine how/if RDX crystal morphology affects the viscosity, η and shear rate, $\dot{\gamma}^*$ of RDX suspensions with increasing applied shear stress, σ . RDX suspensions were made using polyethylene glycol (polyethylene glycol-200, BDH, UK) as the suspending medium. PEG was chosen as the matrix fluid as it has Newtonian rheological

properties, its viscosity does not change with changes in applied shear stress. PEG therefore does not mask any rheological effects that may be due to the different RDX crystal morphologies. A total solid load of 60 wt% RDX was prepared for each RDX lot, 5 wt% of teepol surfactant was also added to ensure good dispersion of the crystals. For each test 75 measurements were taken ranging from a minimum applied shear stress of 5 Pa to a maximum of 200 Pa, with the stress levels increasing logarithmically. For each measurement, an equilibration period of 15 seconds was taken before measurement commenced (the measurement period was set at a maximum of 30 seconds at each stress level). A 1 mm gap was used for Dyno Type II, BAE-RO and Eurenco I-RDX. For Dyno-RS and Holston samples a 2 mm gap was used. This was because the Dyno-RS and Holston RDX suspensions could not flow smoothly with only a 1 mm gap, so to obtain reliable results a wider gap of 2 mm was used. This however does not invalidate comparisons to the samples measured with a 1 mm gap as the software recalculates the viscosity with the wider gap size using the relationship:

$$\eta = \frac{d\sigma}{U} \quad (4.1)$$

Where η is the viscosity, σ the applied shear stress, U the rotation velocity and d the gap size [149].

4.3.3 Surface defect assessment method using SEM

An external defect score was also given to each of the R⁴ RDX lots. For each lot a small number of crystals were evenly distributed on a sticky carbon pad affixed to an SEM stub. Five stubs were prepared for each lot. The stubs were splutter coated with a thin film of gold to increase the conductivity of the RDX crystals. This was to improve SEM image quality and resolution. SEM images were obtained using a LEO 435-VP scanning electron microscope, an acceleration potential of 2 kV was used for image generation. From each stub ten crystals were selected for assessment. In a similar way to the morphology and internal defect assessments, points were awarded to each crystal

depending on the degree of roughness, the number of cracks, holes, depressions and “knobs”. A “knob” is defined as a smaller projecting portion of a crystal. They possibly arise from the fusion of a smaller particle with a larger crystal and can appear as convex protrusions. A mean surface defect score per crystal was calculated for each RDX sample. Table 4.5 gives examples of each defect type, roughness and scores awarded for each defect type.

Table 4.5 Scanning electron micrographs showing examples of each of the surface defect criteria used in the surface defect assessment.

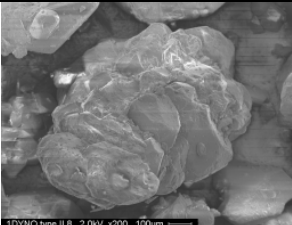
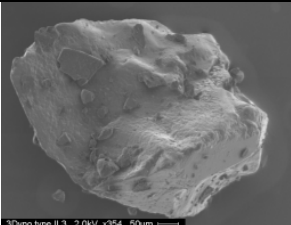
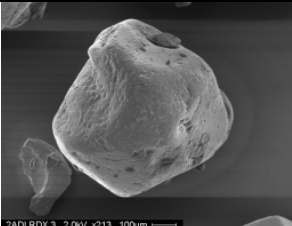
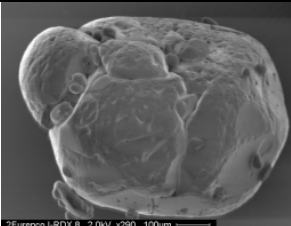
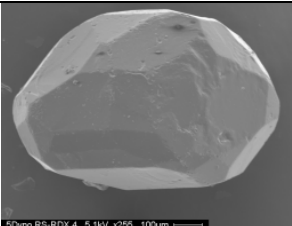
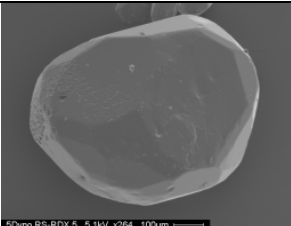
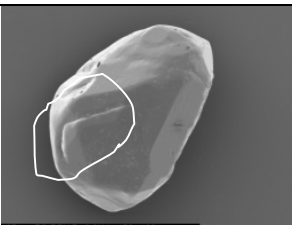
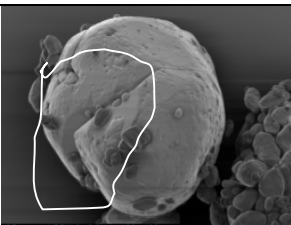
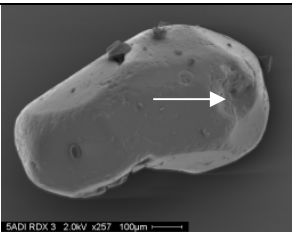
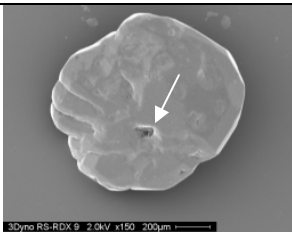

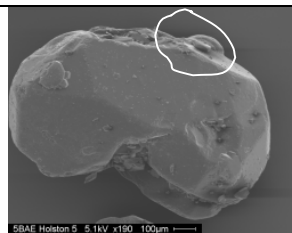
Defect criteria	Examples	
Very rough surface: Majority of the visible surfaces are rough and irregular. 100 points		
Medium rough surface: Majority of visible surfaces are covered with small pits and indentations. Some roughness may be present 50 points		
Slightly rough/smooth surface: Majority of visible surfaces are free of pits or indentations. Some localised groupings of these features may be present. 10 Points		
Cracks: Long fissures, some deep others shallow. Sometimes may be circular. Bifurcated cracks are counted separately. 50 points per crack		

Table 4.5 continued.

Defect criteria	Examples
Holes, depressions: Small black points with sharp edges. Depressions are concave features that usually cover a larger area, sometimes containing a hole(s). 5 points /hole/ depression	 
Knobs: Protrusions from the main body of a crystal. Often convex. Maybe attached to the crystal by a thin neck. Unattached particles on the surface are not knobs. 5 points per knob	 

4.4 Thermal analysis method using DSC

DSC analysis was performed using a Mettler DSC-30 instrument, shown in figure 4.5. Figure 4.6 is a close up view of the sample chamber, the sample crucible being placed on the left and the empty reference crucible on the right.

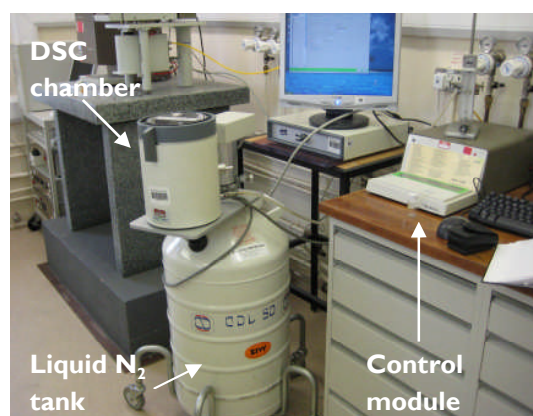


Fig. 4.5 The Mettler DSC-30 instrument used for thermal analysis of RDX.

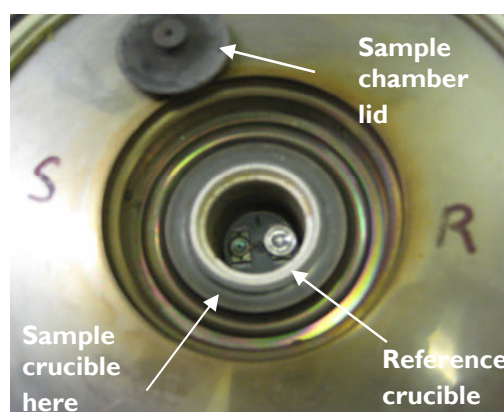


Fig. 4.6 Close-up view of the DSC sample chamber.

4.4.1 Initial DSC investigations, raw RDX samples

The R⁴ lots were analysed in sealed aluminium crucibles. Crucibles were pierced to allow decomposition gases to escape. Samples were analysed with and without a nitrogen purge. The experimental parameters used are listed in table 4.7.

4.4.2 DSC analysis of RDX in a pseudo-PBX formulation

Differential scanning calorimetry was carried out on each of the seven RDX batches to determine the thermal behaviour of the RDX material when mixed with a pre-polymeric binder. TENAX (a porous polymer) was added to absorb any volatile organic compounds that might be released during analysis and affect the results. The composition used is detailed in table 4.6. This formulation was based on that used by Spyckerelle [119]. The materials were thoroughly mixed together in a weighing boat, which created a PBX mixture with a dough type consistency.

Table 4.6 Composition of the pseudo-PBX composition used for DSC analysis.

Material	Description	Source	Quantity
RDX	energetic	various	50 mg
TENAX 30/60 mesh	volatile organic compound absorbent	Analytical Columns UK	10 mg
HTPB 2-3 kDa	pre-polymeric binder R45-HTLO	Sartomer	35 mg

Approximately 2 mg of the pseudo-PBX material was weighed into an aluminium DSC pan and sealed with an aluminium lid. The lid was pierced to allow evolved gases to escape during DSC analysis. Three replicates were analysed with nitrogen and three without nitrogen. Table 4.7 lists the experimental conditions used for the analysis.

Table 4.7 Experimental parameters used for the DSC analysis.

Experimental parameter	
Sample size	2.0 – 2.6 mg
Format	Al pans pierced
Heating rate	5 °C min ⁻¹
Temperature range	180 – 250 °C
Nitrogen flow rate	0/50 ml min ⁻¹
Replicates	3
Standard	Empty Al pan
DSC Instrument	Mettler Toledo DSC-30 with N ₂ cooling

4.4.3 The effect of HMX on DSC analysis of raw RDX and RDX in pseudo-PBX formulation

In a second set of experiments, the effect of adding known amounts of HMX to an RDX lot with low HMX content was investigated. HMX was added to the Dyno RS-RDX lot^{†††}. Table 4.8 shows the amounts used to make each mix. To ensure that the HMX and RDX were well mixed the vials were placed on a roller mixer for a minimum of two hours. For each sample four replicate DSC measurements were taken. All samples were analysed using a nitrogen gas purge. The experimental parameters used are shown in table 4.7.

Table 4.8 Amounts of RDX and HMX mixed for each spiked sample.

	Amount of RDX (mg)	Amount of HMX (mg)
4 wt% HMX	137.0	5.7
8 wt% HMX	184.3	16.0
12 wt% HMX	176.1	24.0
16 wt% HMX	167.6	32.7

DSC analysis was also performed on HMX spiked RDX samples made into PBX composition. The composition was the same as the unspiked RDX samples. All samples were analysed with a nitrogen gas purge.

4.4.4 The effect of RDX crystal size on the shape of the decomposition exotherm of pseudo-PBX formulation

Dyno Nobel RS-RDX (51.3 g) was sieved and DSC analysis was carried out on the material collected in the 500-1000 μm and 45-125 μm particle size fractions. Two pseudo-PBX compositions were made using the method described in section 4.4.2, one containing the smaller fraction and the other containing the larger fraction. Ten replicate samples of each pseudo-PBX were carried out without nitrogen purging, using the parameters listed in table 4.7.

4.5 Shock sensitivity measurements using the small scale gap test

The shock sensitivity of five RDX samples was tested using a small scale gap test. The RDX samples were tested as loosely packed powders and not in a

^{†††} Pure, raw Dyno-Nobel RS-RDX contains 0.82% HMX (average) ^[3].

formulation. Table 4.9 lists the RDX samples tested. The samples were contained in PMMA tubing.

Table 4.9 RDX samples tested for shock sensitivity.

RDX sample	Source	Notes
Dyno Type II	Dyno Nobel	sample from R ⁴
Dyno RS-RDX	Dyno Nobel	sample from R ⁴
Chemring Type II	Chemring	Class I, batch CH739/09 V87
Chemring F-RDX	Chemring	Class I, batch I326/08 V22
Chemring RS-RDX	Chemring	Class I, batch 3404/05

For each RDX sample 25 shots were performed. RDX was placed into PMMA tubes of 25 mm length and 12 mm internal diameter. Electrical tape was placed at the bottom end to contain the sample. Each tube was filled completely so that the level of the RDX crystals was flush with the top of the PMMA tube. The mean maximum packing densities obtained for each sample are shown in table 4.10. The top end of the PMMA tube was sealed with electrical tape.

Fig. 4.10 Mean packing densities for the RDX samples.

RDX sample	Mean packing density (g/cm³)	95% confidence interval
Dyno Type II	1.197	+/- 0.004
Dyno RS-RDX	1.240	+/- 0.004
Chemring Type II	0.971	+/- 0.004
Chemring F-RDX	1.174	+/- 0.003
Chemring RS-RDX	1.176	+/- 0.002

Donor charges were prepared using PMMA tubes, length 12.5 mm and internal diameter of 12.0 mm completely filled with PE4 explosive. The mean packing density of the PE4 was 1.60 g/cm³ (95% confidence interval +/- 0.004 g/cm³). The tubes were filled so that the PE4 was flush with both ends of the tube. An L2A1 electric detonator was used to initiate each shot, brass shims were placed between the donor and acceptor charges as the attenuator. The acceptor charge was placed on top of a mild steel witness block, size 25 x 25 x

25 mm. The presence or absence of a dent in the witness block was used to determine if each shot was a “Go” or “No-Go” respectively. The whole assembly was held together by electrical tape. Figure 4.7 shows a schematic of the small scale gap test set up.

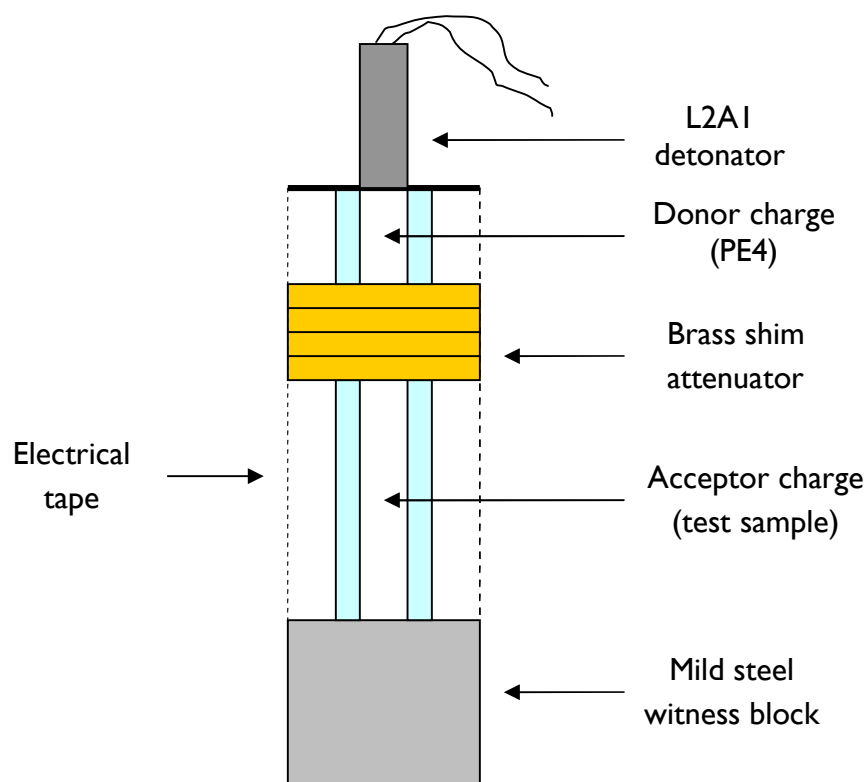


Fig. 4.7 schematic of the small scale gap test used in this study.

After each “shot” the witness block was examined, if a dent was present then the gap for the next shot was increased by 0.25 mm. If the shot was a “No-Go” then the gap was reduced by 0.25 mm. This procedure was continued until all the shots for each RDX sample were fired. The mean gap size for a “Go” and a “No-Go” response was then calculated.

CHAPTER 5

Results and discussion; internal defects analysis and nanoindentation

5.1 Internal defect assessment results

Figures 5.1 to 5.4 show the typical internal defect population of each RDX lot when viewed using a matching refractive index medium. BAE-RO, ADI, Dyno RS-RDX and Eurenco I-RDX have a similar appearance. The crystals were mostly clear with no dark or cloudy areas. There were very few large internal defects, they were mostly small ($< 10\ \mu\text{m}$) with medium sized defects scattered amongst them, within the $0.1\text{-}10\ \mu\text{m}$ size range proposed for hot spot formation [31]. The defects tended to be evenly distributed throughout the crystals. The only significant difference between these lots was that Dyno RS-RDX had, on average, just over twice as many small internal defects (see figure 5.5). This did not have any effect on RS-RDX sensitivity, the lack of large defects in RS-RDX prevented increased sensitisation due to the greater number of small defects that they contained. Frey [150] has shown that as defect size increases the temperature of the hot spot it produces also increases. Therefore the presence of large defects makes initiation more likely due to the higher hot spot temperature they produce during their compression. Many small defects alone don't have as great a sensitising effect.

Eurenco MI-RDX has a similar internal defect population to that of Dyno RS-RDX, in terms of average number of small, medium and large defects (figure 5.5). However, Eurenco MI-RDX had a high proportion of crystals (72%) that contained extensive cloudy/dark areas whereas Dyno RS-RDX did not have any crystals with cloudy regions, (figure 5.6). These dark regions have been attributed to the presence of micrometer sized internal defects [76]. Some cloudy areas can also be attributed to internal defects that are out of focus

The morphology of BAE Holston crystals is similar to Eurenco MI-RDX crystals. Of all of the RDX lots, BAE Holston has by far the highest number of large defects (see figure 5.5). Most crystals contained at least one large defect. These defects were often elongated or irregular shaped and located near the

centre of the crystal, (figure 5.4). Often the large defects contained trapped air bubbles, this could possibly enhance shock sensitivity since air bubbles are easily compressed and form hot spots. Trapped air bubbles have also been observed by Baillou [60] and Bourne [64].

BAE Holston crystals contained the highest number of small defects. These small defects were usually tightly clustered together in clearly defined areas, leaving parts of the crystal clear. The areas containing the small defects usually appeared dark, with a sharp boundary between the clear regions of the crystal. Dyno type II crystals had a very different internal defect population. These crystals mostly contained large numbers of small defects, but few large defects. Unlike the BAE Holston crystals the small defects were usually distributed evenly throughout the crystal. The crystal usually appeared dark/cloudy, with occasional clear regions but there was no sharply defined boundary between these areas. These differences in defect distribution may be because BAE Holston and Dyno Type II were crystallised under different conditions. Faster crystallisation and a higher supersaturation of the solvent tends to lead to more internal defects being formed and increased angular or rough morphology [73,74]. The high concentration of defects towards the centre of BAE Holston crystals surrounded by defect free regions may indicate an initial fast crystallisation rate, when more defects form, followed by slower crystallisation, when few defects form. The high defect content throughout Dyno Type II crystals can be attributed to a rapid crystallisation at a high supersaturation without a slower crystallisation phase. This would also account for the more angular/rough crystal morphology typical of Dyno Type II crystals.



Fig. 5.1 Micrograph showing typical internal defect structure of Eurengo MI-RDX crystals.



Fig. 5.2 Micrograph showing typical internal defect structure of BAE-Royal Ordnance crystals.

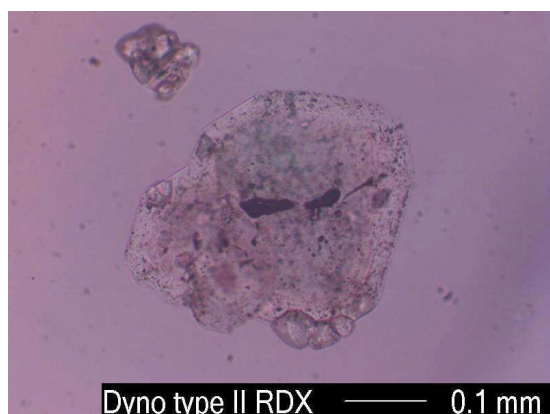


Fig. 5.3 Micrograph showing typical internal defect structure of Dyno type II RDX.



Fig. 5.4 Micrograph showing typical internal defect structure of BAE Holston RDX.

The mean number of large defects in all RDX lots is low and consistent except for the BAE Holston material. The mean number of medium sized defects does not vary significantly between any of the lots. The number of small internal defects is significantly higher in Dyno type II and BAE Holston crystals than any other lot. Eurenco MI-RDX and Dyno RS-RDX had about twice as many as BAE-RO, ADI and Eurenco I-RDX, (see figure 5.5). Large numbers of cloudy/dark crystals were only found in Eurenco MI-RDX, Dyno type II and BAE Holston lots, (see figure 5.6).

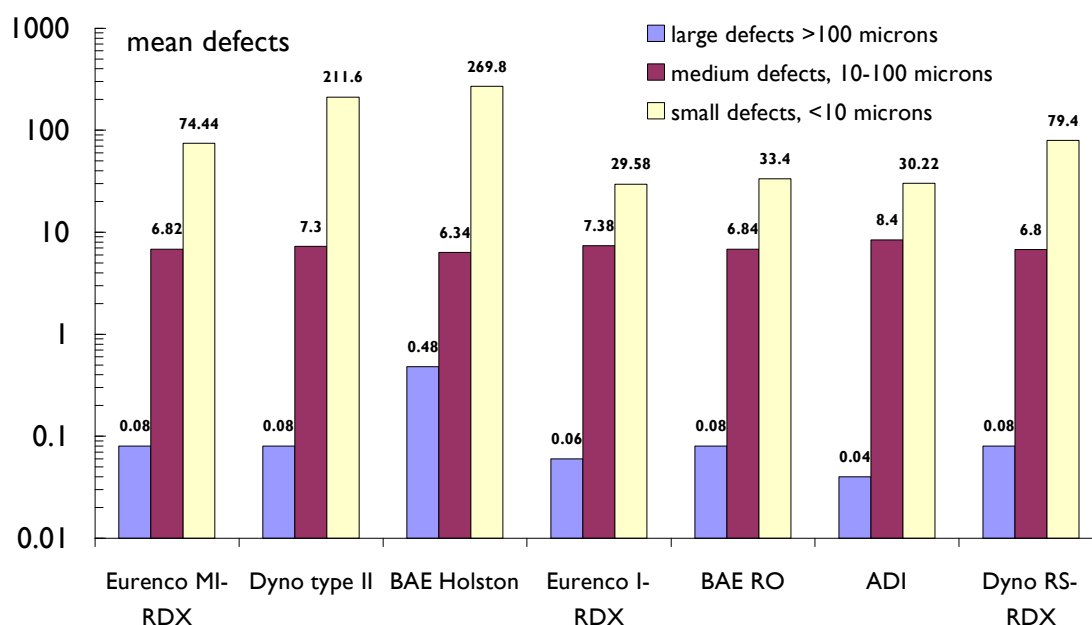


Fig. 5.5 Mean number of small, medium and large sized internal defects per crystal for each RDX lot. Lots are listed in order of shock sensitivity as obtained from the R^4 program. Most sensitive lot is on the left.

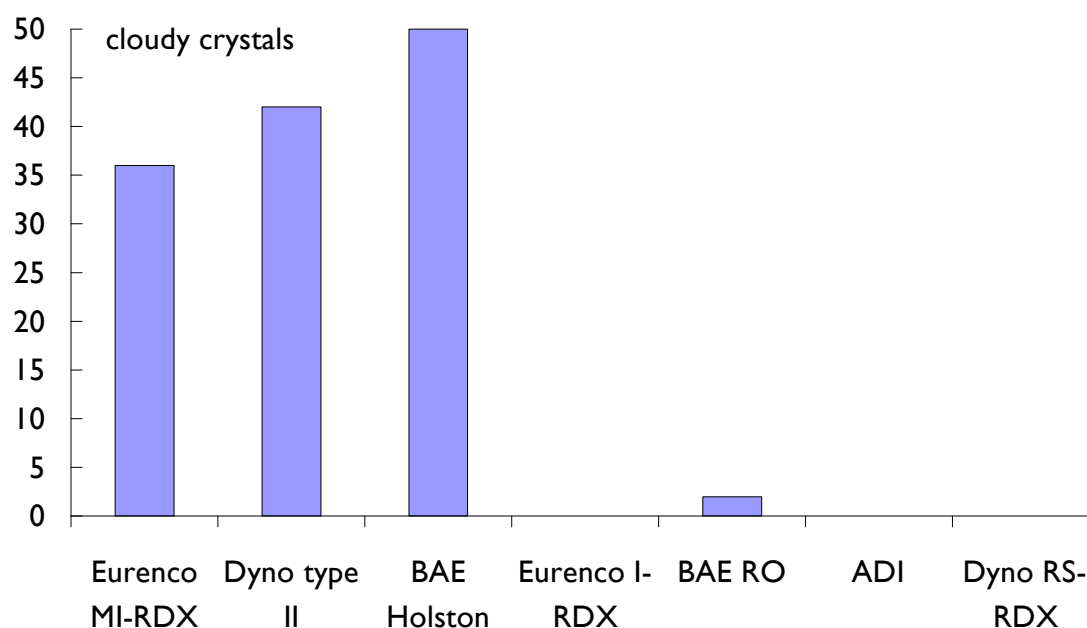


Fig. 5.6 Number of crystals from each lot that were dark or cloudy (50 crystals assessed for each lot).

It can be clearly seen from figure 5.6, that the most sensitive RDX samples were those which contained many dark or cloudy crystals. Apart from a few crystals from BAE-RO, less sensitive crystals had no cloudy crystals. Figure 5.7 shows the mean internal defect scores for each of the R⁴ RDX lots plotted against their shock sensitivities obtained during the R⁴ study [24]. Both Dyno type II and BAE Holston have much higher scores than the type I RDX lots and Dyno RS-RDX. This is not surprising as both BAE Holston and Dyno type II contain a much higher number of small defects than the other lots and BAE Holston crystals contain many large defects. Given the large amount of evidence in the literature that links shock sensitivity with internal defects, an initial inspection of figure 5.7 suggests very little correlation. However, when the data is grouped according to the method of production, a clearer trend between defect score and sensitivity is seen. RDX lots that are produced by the same method, show an increase in sensitivity with increasing internal defect content. The reduction in shock sensitivity that is gained by recrystallisation is also clearly demonstrated. Dyno RS-RDX is produced by the Bachmann process but has been recrystallised. Compared to Dyno Type II and BAE-Holston, it has a much lower defect score, and the least shock sensitive. HMX content could also be having an effect, Dyno RS having a much lower amount (0.82% [147]) than the other type II samples (8.55% and 7.36% for Dyno Type

II and BAE Holston respectively [147]). This could also contribute to its low sensitivity.

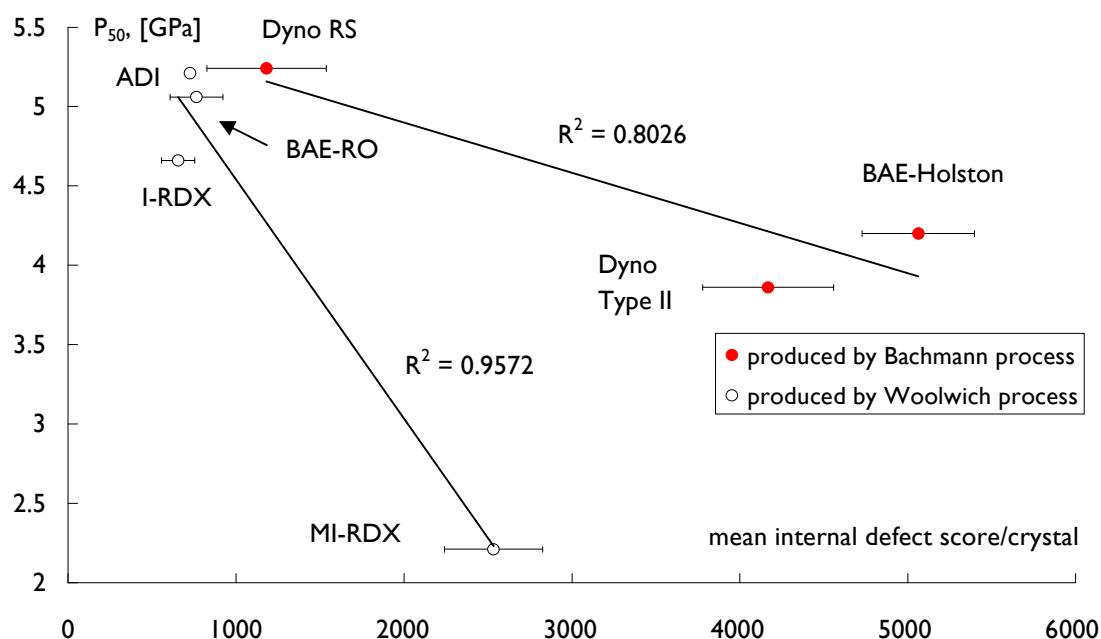


Fig. 5.7 Mean internal defect scores per crystal of the R⁴ RDX lots obtained from micrograph images plotted against shock sensitivity data obtained during the R⁴ study. The trend lines illustrate the correlations between internal defect scores and sensitivity for samples produced by the Woolwich and Bachmann processes. Error bars give 95% confidence intervals of the mean values.

5.2 Results from nanoindentation analysis of RDX crystals

The first part of this section (5.3.1) will present the results from the first set of nanoindentation experiments which looked at one particle size range (150-500 μm). The second part (5.3.2) describes the results obtained from the experimental work comparing the two particle size ranges (45-150 μm and 150-500 μm).

5.2.1 Measurements from 150-500 μm crystal size range

5.2.1 a) The effect of increasing load on the elasticity and stiffness of RDX

Nanoindentation measurements using a range of applied loads from 10 to 200 mN, showed consistent behaviour for all samples examined. With increasing applied load the modulus of elasticity decreased (figure 5.8). The quality of the RDX lots was observed to influence mechanical behaviour. RDX lots with few internal defects (RS/I-RDX and reprocessed type II grades) showed a higher modulus of elasticity at all applied loads compared to RDX lots which had

many internal defects (type II lots and MI-RDX). These results are plotted in figure 5.8, which shows that crystals with fewer defects have a significantly higher modulus of elasticity by about 10-15% compared to crystals that had many internal defects.

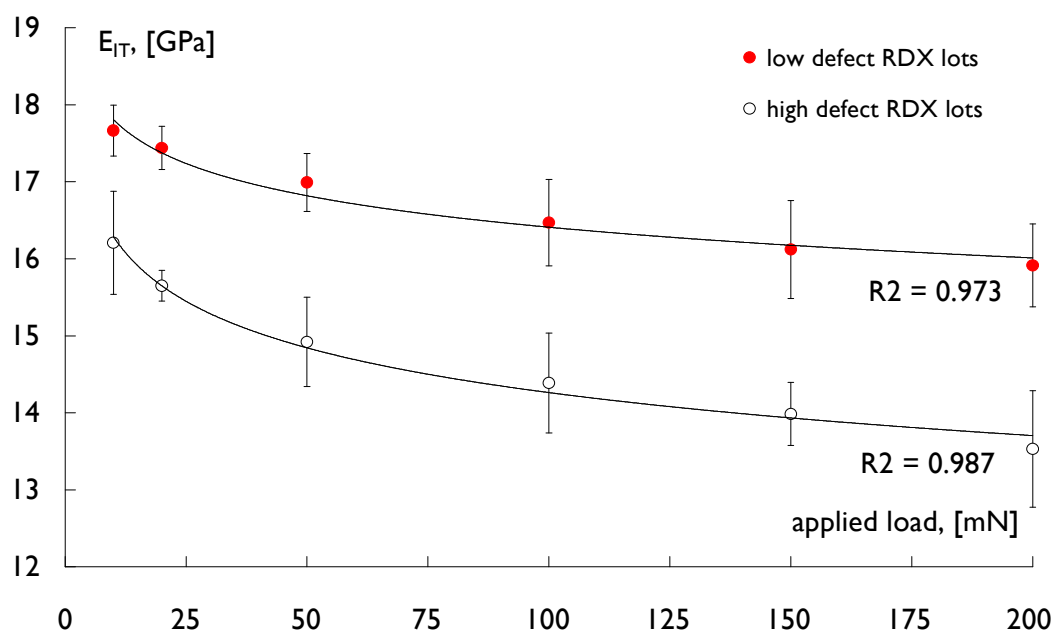


Fig. 5.8 Plot of mean elastic modulus versus applied load for high defect and low defect RDX lot groups. Error bars indicate the 95% confidence intervals of the mean values.

The stiffness of the RDX lots at each load level was also determined. As the applied load was increased the stiffness also increased. Agreeing with the elasticity results, RDX lots with more internal defects had a reduced stiffness compared to RDX lots fewer defects at all applied load levels. Figure 5.9 is a plot of the mean stiffness data, showing the difference in stiffness between the low purity RDX and high purity RDX lots.

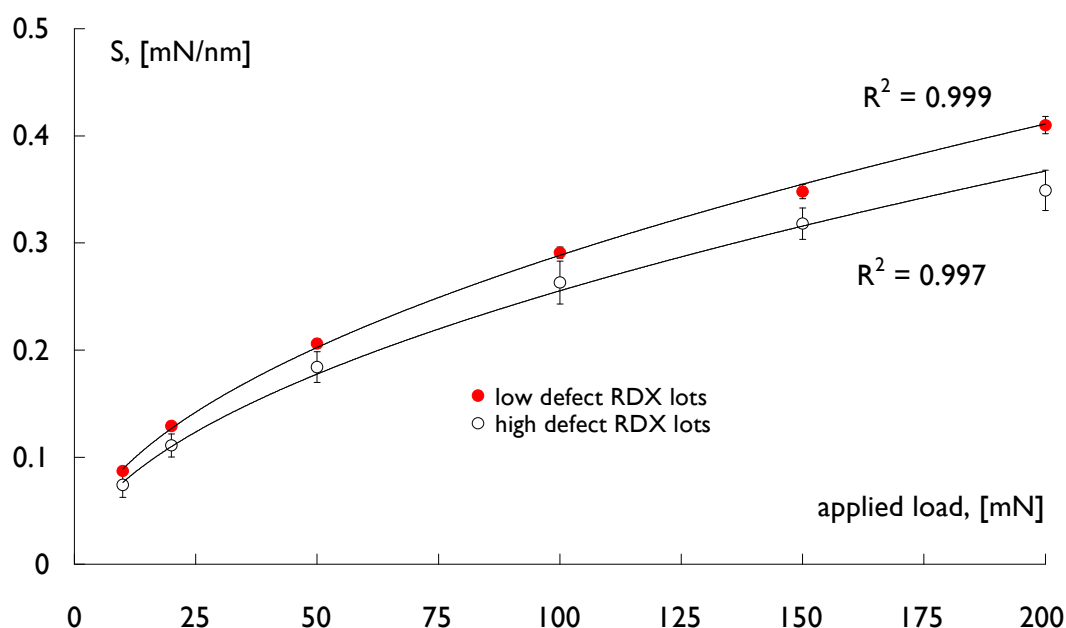


Fig. 5.9 Plots of the mean stiffness against applied load for “high defect” and “low defect” RDX lot groups. Error bars indicate the 95% confidence intervals of the mean values.

5.2.1 b) The effect of internal defects on mechanical properties of RDX

Using data obtained from the previous assessment of RDX crystal internal defects, the mean internal defect scores for each RDX lot was plotted against the mean elastic modulus (E), creep (C_{IT}), and mean elastic work of indentation (η_{IT}) at 200 mN load (figures 5.10-5.12). The 200 mN maximum load was selected as the samples showed the greatest variation when that force was applied. On average poorer quality RDX crystals with more internal defects have a lower modulus of elasticity, exhibit more creep and elastic work compared to RDX crystals that have fewer internal defects.

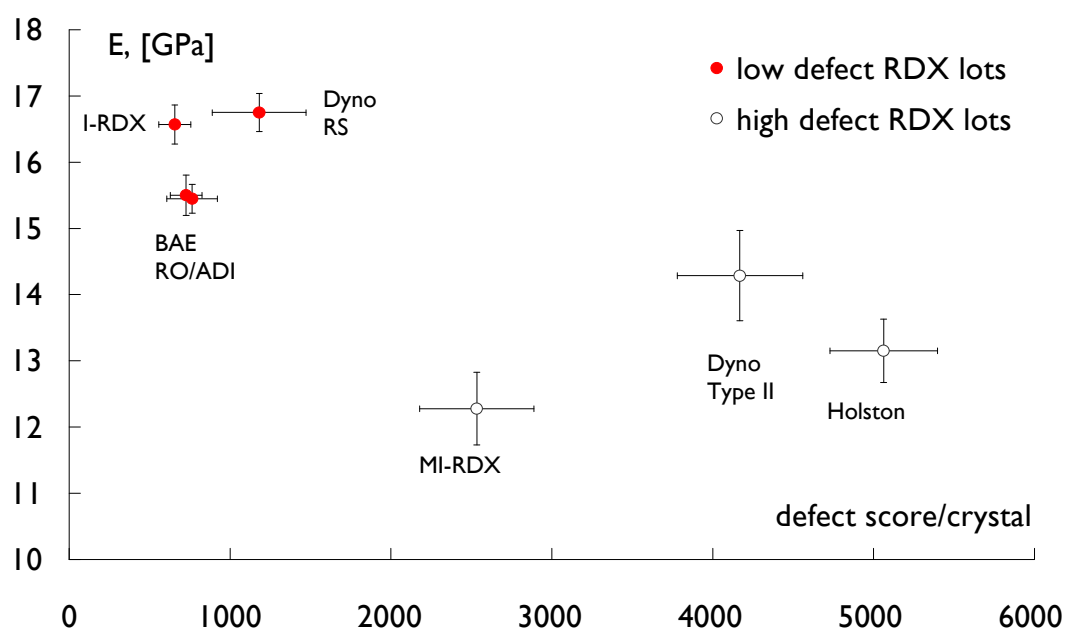


Fig. 5.10 Mean internal defect score for each RDX lot versus mean modulus of elasticity measured at 200 mN. Error bars indicate 95% confidence intervals of the mean values.

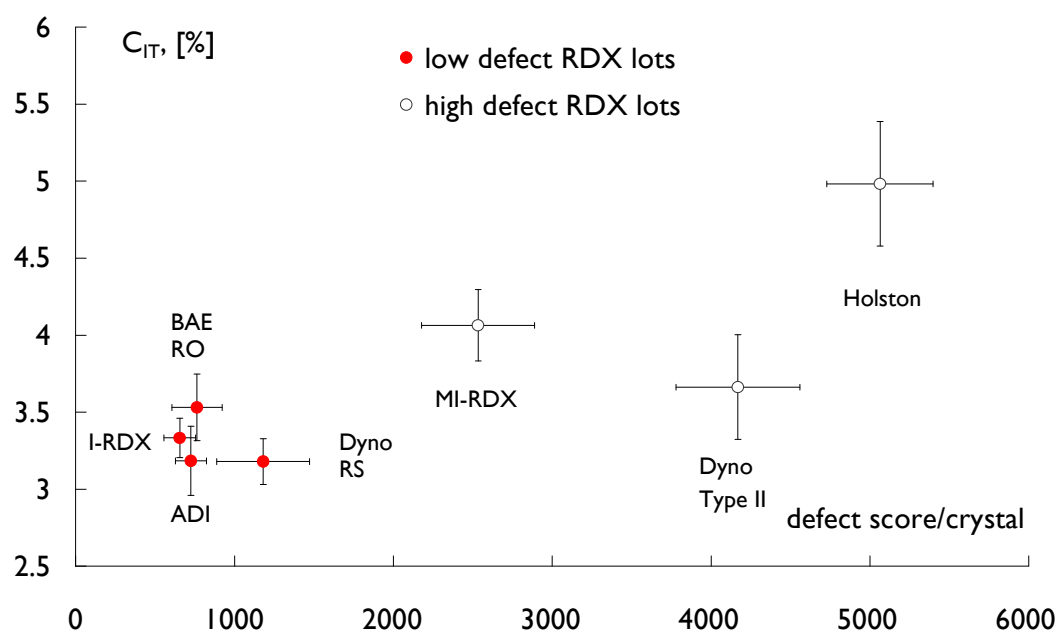


Fig. 5.11 Mean internal defect score per crystal versus mean indentation creep (C_{IT}) measured at 200 mN. Error bars indicate 95% confidence intervals of the mean values.

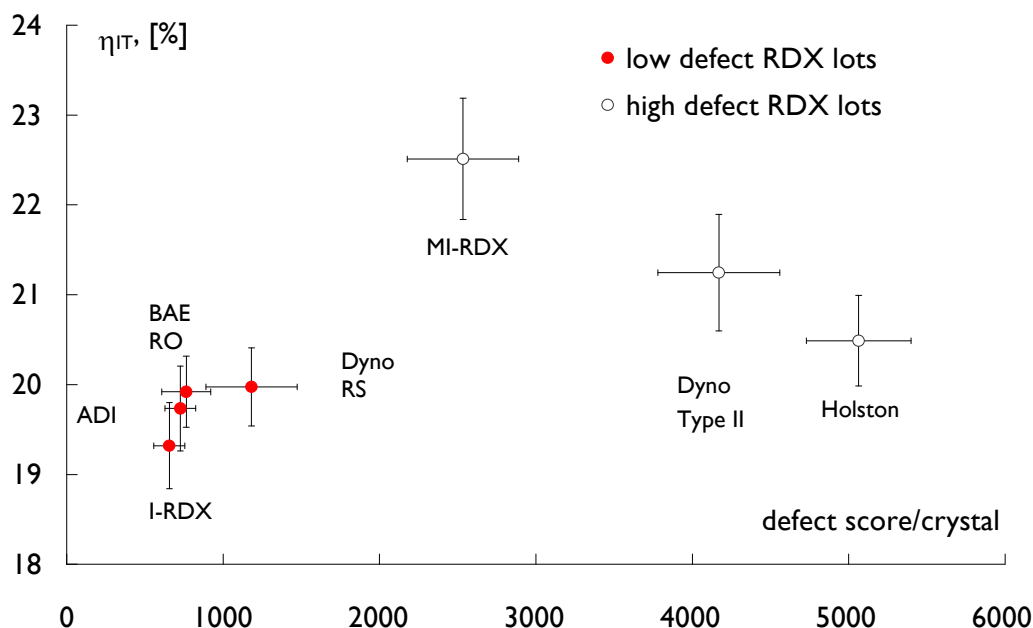


Fig. 5.12 Mean internal defect score per crystal versus mean η_{IT} measured at 200 mN. Error bars indicate 95% confidence intervals of the mean values.

5.2.1 c) The relationship between RDX mechanical properties and shock sensitivity

Figures 5.13 and 5.14 are plots of the mean elastic modulus (E_{IT}) and proportion of elastic work (η_{IT}) at 200 mN applied load for each RDX lot, against their formulated PBXN-109 shock sensitivity results (large scale gap test) from the R4 study [24]. There is a good correlation to the shock sensitivity for elastic modulus and elastic work. RDX lots with lower shock sensitivities (higher critical shock pressure) have a higher elastic modulus and undergo less elastic work.

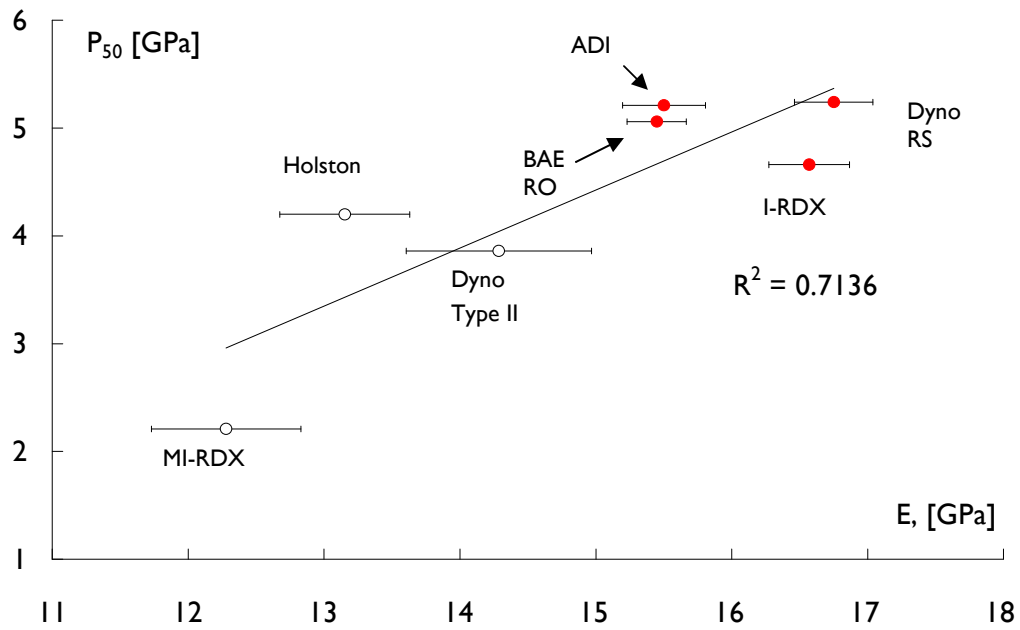


Fig. 5.13 Plot of mean elastic modulus at 200 mN load against large scale gap test results from R^4 study. Error bars give 95% confidence intervals of the mean. Red circles, low defect RDX lots. empty circles high defect RDX lots.

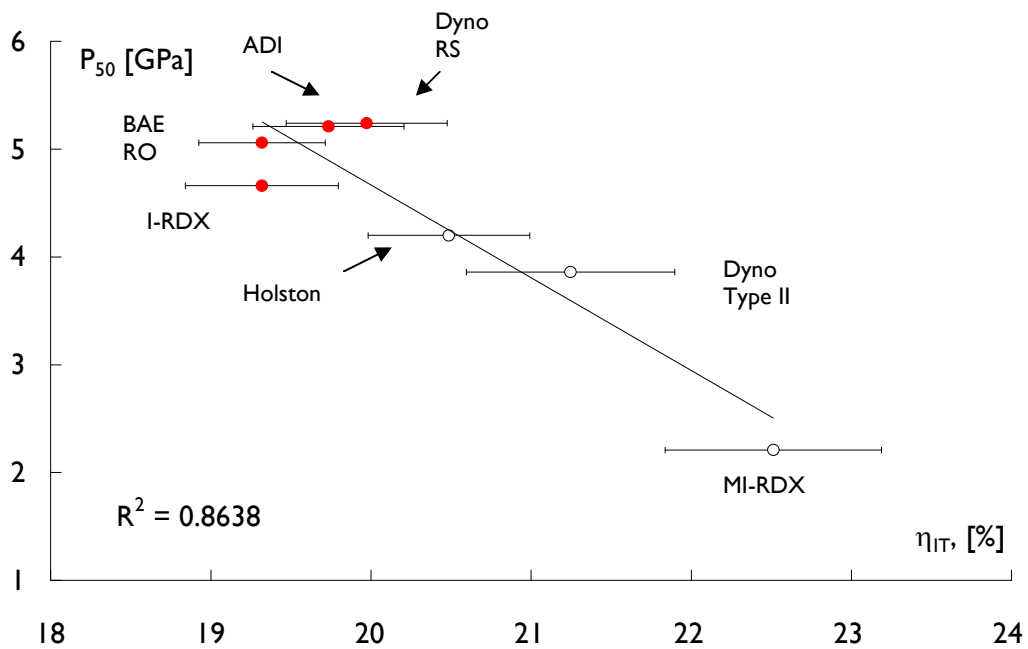


Fig. 5.14 Plot of mean η_{IT} at 200 mN load against large scale gap test results from R^4 study. Error bars give 95% confidence intervals of the mean. Red circles, low defect RDX lots. empty circles high defect RDX lots.

5.2.2 The effect of crystal size on mechanical properties

5.2.2 a) The effect of increasing load on elastic modulus and creep

The following graphs (figures 5.15 and 5.16) show how the elastic modulus and creep change with increasing maximum applied load. For each graph, data points are given for the mean result for small crystals with many defects (small grey triangle), large crystals with many defects (large black triangle), small crystals with few defects (small grey circle), and large crystals with few defects (large black circle) at each load level. The plots show that irrespective of the number of crystal defects present, smaller crystals have lower elasticity than larger crystals. Small crystals with more defects do however show a greater reduction of elasticity with increasing load compared to small RDX crystals with fewer defects. The elasticity of crystals with fewer defects is higher at all load levels, for both large and small crystal size. For both high defect and low defect crystals, smaller crystals undergo more creep during maximum applied load than larger crystals. Above 100 mN RDX crystals containing many defects (irrespective of size) show more creep than RDX crystals with few defects.

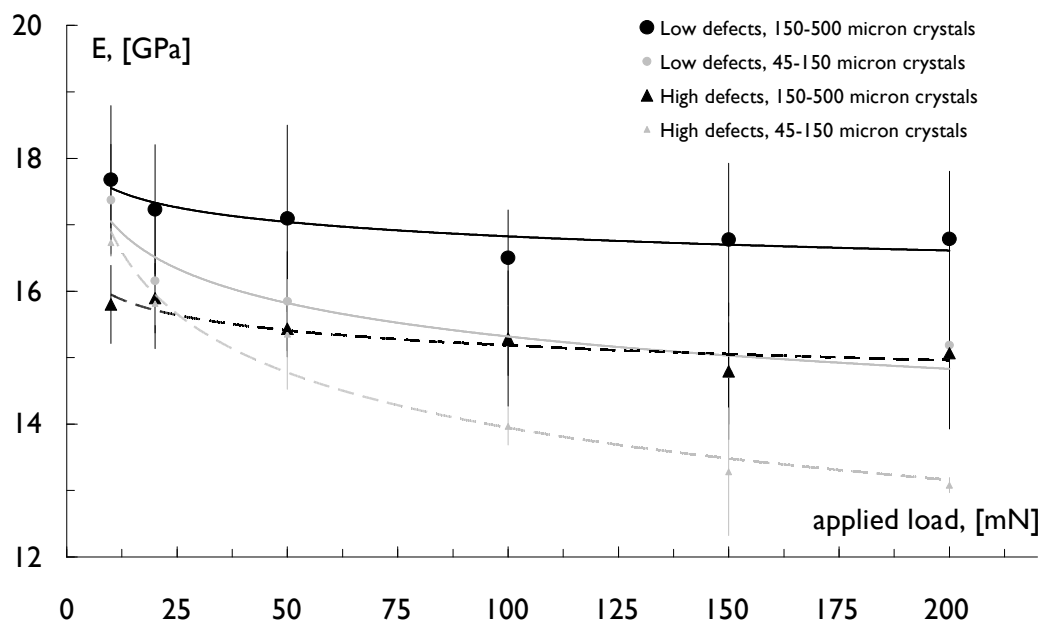


Fig 5.15 Plot of mean elastic modulus versus maximum applied load for high and low defect/small and large RDX crystals. Error bars indicate 95% confidence intervals.

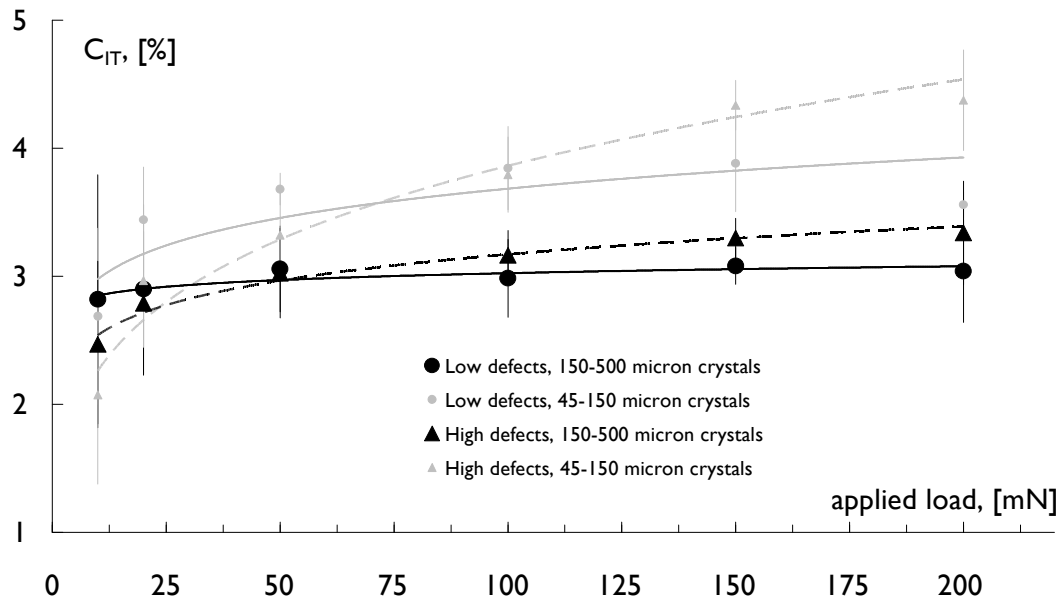


Fig. 5.16 Plot of mean creep versus maximum applied load for high and low defect/small and large RDX crystals. Error bars indicate 95% confidence intervals.

5.2.2 b) Elasticity vs. hardness, elasticity vs. creep and hardness vs. creep

Figures 5.17 and 5.18 are plots of the indentation hardness (H_{IT}) against elastic modulus and amount of creep against each other for the small/large crystals high defect/low defect containing samples.

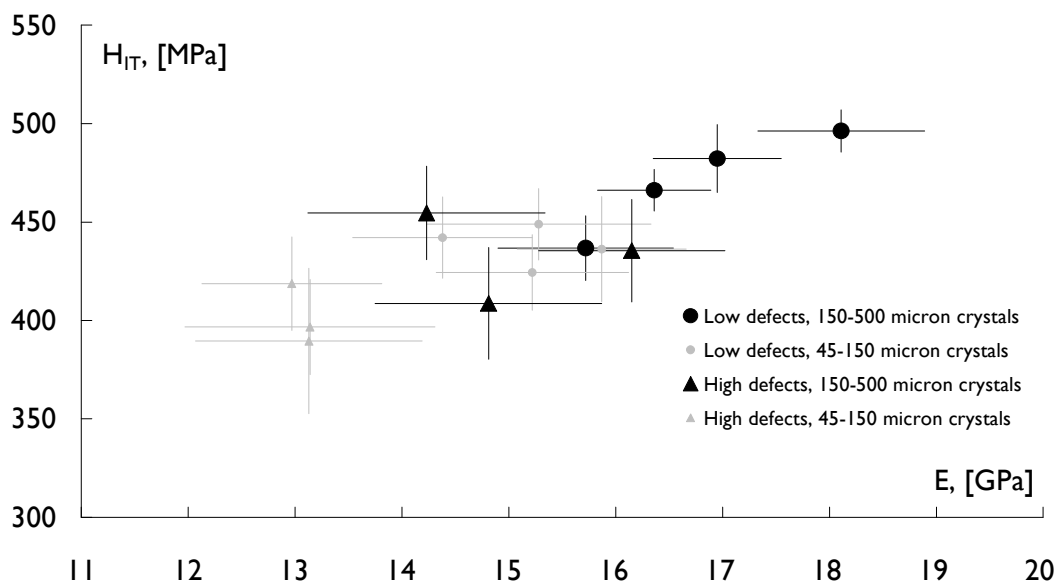


Fig. 5.17 Plot of mean hardness vs. mean elastic modulus at 200 mN. Error bars give the 95% confidence intervals.

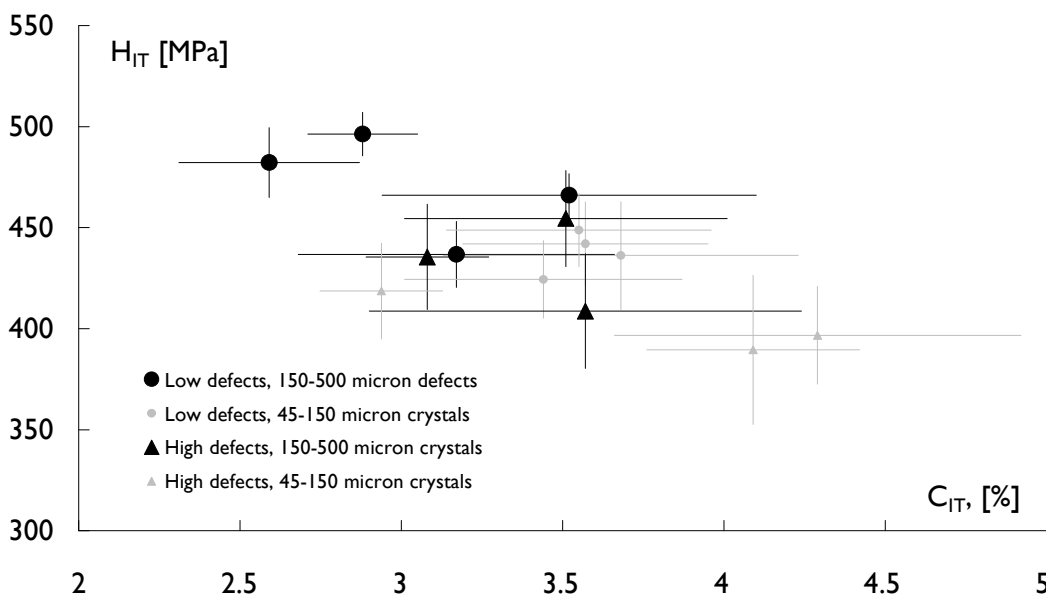


Fig. 5.18 Plot of mean hardness vs. mean creep at 200 mN. Error bars give the 95% confidence intervals.

The plot of mean hardness against elastic modulus shows a direct correlation (figure 5.17). Larger crystals with few defects have the highest elastic modulus and are the hardest crystals. On the other hand, small crystals with many defects have, on average, the lowest elasticity and hardness. Smaller crystals

with few internal defects and larger crystals with many demonstrate intermediate values of hardness and elasticity.

Plotting mean hardness against mean creep gives an inverse correlation (fig. 5.18). Crystals that have reduced hardness exhibit increased creep deformation as would be expected. The hardest crystals that show the least creep are also the largest and have few defects. The softest crystals that also undergo the most creep are small and have many internal defects. Again, intermediate hardness and amount of creep is seen for small crystals with few defects and large crystals with many defects.

5.3 Discussion of results

5.3.1 Discussion of results from internal defect assessment

The internal defect characteristics of the RDX lots studied appear to be influenced by the method of production. RDX produced by the Woolwich process has fewer impurities such as HMX inclusions which promote formation of voids compared to Bachmann produced RDX. The controlled recrystallisation of crude Bachmann RDX removes the crystallographic defects and impurities leading to a reduced amount of internal voids.

Figure 5.7 suggests that the relationship of shock sensitivity to quantity/volume of internal defects is best when RDX samples produced by the same method are compared alone rather than when all RDX types are considered together. For instance, MI-RDX has a relatively low defect score (compared to Dyno type II and Holston) although it is the most sensitive. MI-RDX is produced by the Woolwich process which would explain its lower defect content compared to the Bachmann RDX lots. The higher score for MI-RDX, in contrast to the other Woolwich RDX lots, is due to it having a large proportion of crystals that contain submicron sized defects which can enhance sensitivity (see figure 5.6). It seems that a large number of both large *and* small internal defects significantly increases shock sensitivity. Large defects are easily compressed to form hot spots and the many small defects are proficient in propagating the subsequent reaction front through the crystal [61]. Large defects alone are not as efficient in propagation of the reaction front. The microscopy method is subjective, selection bias can easily occur, crystals

that have fewer defects could be chosen rather than crystals with many defects to make counting quicker and easier. The crystal clarity assessment (assessing if the crystal has large dark or cloudy areas), could also be used to reduce counting. A crystal with a very large number of small defects could simply be judged as being cloudy/dark, reducing a score that would otherwise be much higher. This could explain the wide discrepancies observed in the R⁴ results. Another issue with microscopy is that only a single two dimensional cross section of the crystal being viewed is in focus at any time. This means that other defects may also be present but are not visible without adjusting the microscope focal settings. Some defects may also be poorly resolved and out of focus, leading to a lower defect count than is actually the case. Figure 5.19 illustrates how the appearance of defects within a crystal changes with different focal settings. The procedure is very time consuming and tedious. The guidelines given are too vague, especially regarding designation for cloudy/dark crystals. A way of improving this assessment is using digital imaging to measure the total amount of defects as used by Koo *et al.* [73].

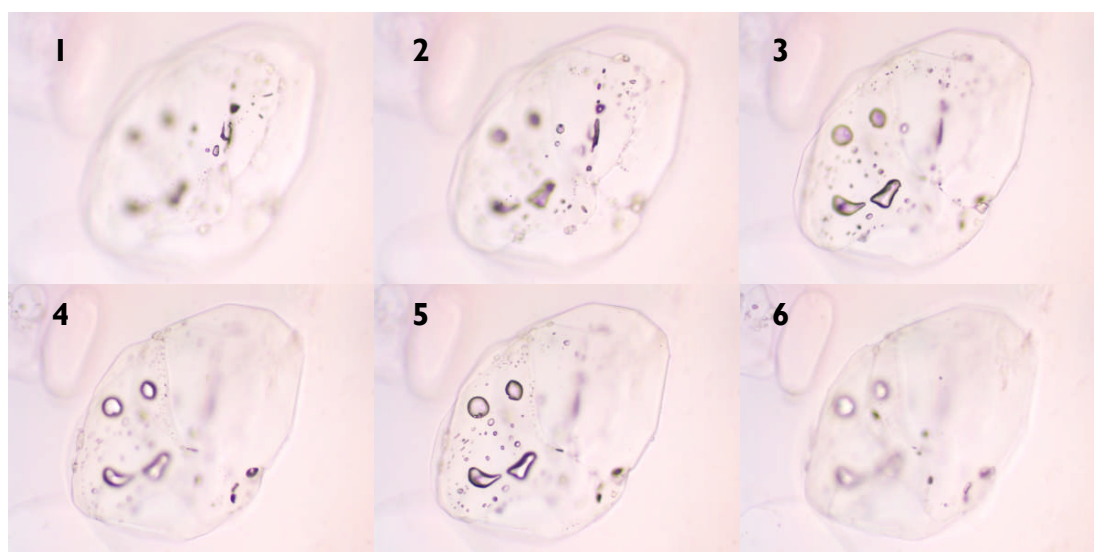


Fig. 5.19 A series of photomicrographs of the same RDX crystal showing how the appearance of internal defects can change with different depths of focus.

5.3.2 Discussion of nanoindentation results

5.3.2 a) Discussion of results from 150-500 μm size fraction

In this study, three sets of variables are considered and compared. Firstly, the micro-mechanical data obtained from the nanoindentation experiments. Secondly, the internal defect assessment scores that were described in section 5.1 for each of the RDX lots. Thirdly, the shock sensitivity data of the same samples from the large scale gap tests performed during the R⁴ programme.

Comparing how the elasticity and stiffness changes with increasing maximum load for RDX lots with many and few internal defects (figures 5.8 and 5.9) reveals that internal defects have a significant effect on the mechanical properties of RDX. This conclusion is supported by Ming *et al* [78]. As highlighted in section 2.1.2, they showed that increased internal void volume had a detrimental effect on the mechanical properties of RDX crystals. Larger number of voids/defects reduces the ability of the bulk material to dissipate stress and recover elastically, as shown by [78,79]. This makes an RDX crystal containing more internal defects, less elastic and reduces its stiffness, (see figures 5.8 and 5.9). RDX lots with lower mean internal defect scores (i.e. ADI, Dyno RS-RDX, Eurenco I-RDX and BAE-RO) all showed significantly higher elastic moduli, less creep and less elastic work. Voids within a crystal make it less able to return to the pre-loaded crystal state because they disrupt the crystalline structure. Internal defects increase the amount of creep deformation because the crystallographic dislocations they produce allow deformation to occur during load application. Ramos *et al* [151], performed nanoindentation measurements to measure the mechanical properties of RDX crystals. They reported a correlation between number of crystal defects (dislocations) and mechanical properties. Crystals containing a larger defect density had a lower yield stress.

The modulus of elasticity of crystals with more defects reduces faster with increasing applied load compared to crystals with few defects. This is because with increasing applied load a larger volume of crystal was indented. At low loads any defects present deep within the crystal would not effect the measurement since the indentation will not reach them. As loading increases a greater volume is indented and so deeper defects will have a measurable effect

on elasticity and other mechanical properties. Therefore to obtain reliable information about mechanical properties higher maximum loads are required. RDX crystals that have lower elasticity and stiffness have higher shock sensitivities. Stresses that accumulate within less elastic/stiff crystals are not dissipated as efficiently leading to greater probability of crystal fracture and hot spot formation. In fact molecular dynamics experiments [152,153,154] have shown this to be the case. Localised strain energy centred at crystal lattice defects creates hot spots and the presence of defects reduces the mechanical strength of the crystal lattice. The hot spots are formed during defect mediated structural relaxation which converts the localised strain energy into heat. The amount of heating produced depends upon the quantity of strain energy within the crystal and the amount of energy released. Molecular dynamic calculations performed by Strachan *et al* [155] showed that the presence of voids caused localised heating in excess of 1000 K during propagation of a shock wave. Simulations performed by Kuklja and Kunz have [156] shown that a crystal containing defects was approximately 30% more compressible than a defect free crystal. They concluded that the increased compressibility reduced the pressure required for detonation also by 30%. This may explain the relationship observed between the stiffness/elasticity data and the shock sensitivity data from the R⁴ study. Crystals that have many defects are less elastic and may be more prone to form hotspots and ignite when subjected to a shock wave.

5.3.2 b) Discussion of results comparing crystal size

For all RDX samples and crystal size the elasticity decreases as maximum load increases. This is because, with increasing load, the RDX crystal lattice structure becomes less able to elastically deform, i.e. less able to return to its pre-stressed conformation. At higher applied maximum loads, above 100 mN, plastic deformation is predominant, often “pop-ins” occur where the crystal suddenly cracks while the load is applied. This is indicated when the indentation depth suddenly increases. Examination of the nanoindentation data showed that the average minimum load at which pop-ins occurred had some correlation with the quantity of internal defects. RDX samples which had higher internal defect scores exhibited pop-in behaviour at lower loading

levels, compared to samples with few internal defects. Figure 5.20 shows the mean minimum load for pop-in against the internal defect score for each RDX sample.

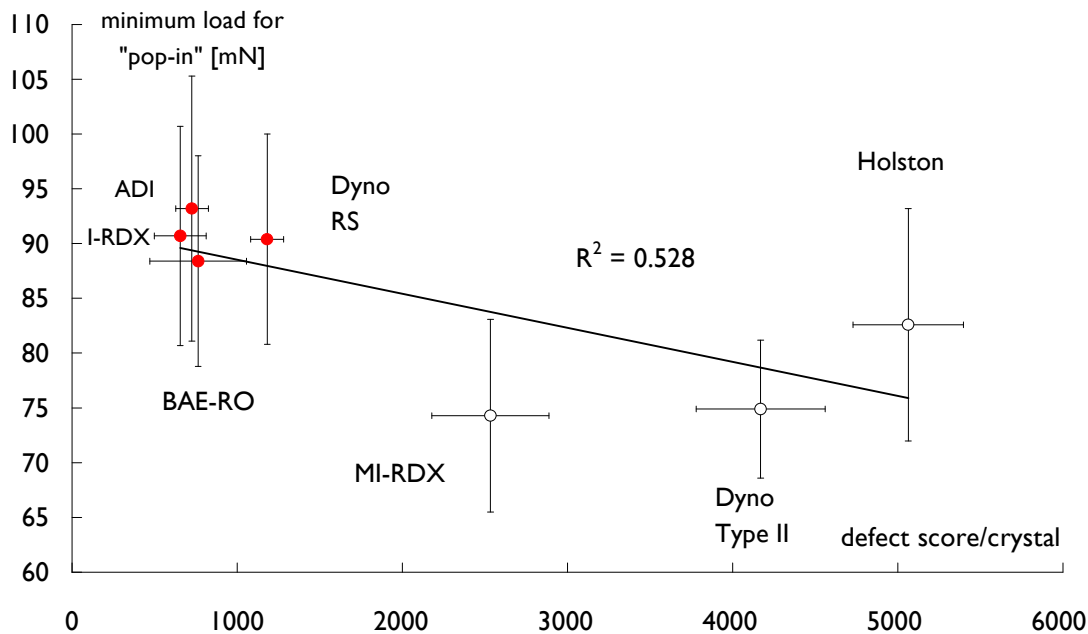


Fig. 5.20 Plot of mean internal defect score per crystal against minimum load for pop-in. Error bars give the 95% confidence intervals. Red circles, low defect samples, white circles high defect samples. Pop-in data was taken from indentations measured at a loading rate of 400 mN/min to a maximum load of 200mN.

The presence of internal voids reduces the resilience of the RDX crystal making plastic deformation more likely, hence the lower loads required for pop-ins to occur in high defect crystals. Average minimum load for pop-in was also plotted against the shock sensitivity data from the R4 study [24], see figure B1 in appendix B. There was a good correlation between shock sensitivity of the RDX samples and the minimum load for pop-in. RDX samples containing crystals which exhibited pop-in behaviour at lower loads had increased sensitivity. Since pop-ins are indicative of fracturing of the crystal during loading, this relationship is easily explained. Fracturing of the crystal creates new surfaces which rub together and so increases hot spot formation. The minimum load required for pop-in was also plotted against the mean number of large and small defects per crystal for each RDX lot and the fraction of crystals that were cloudy/dark, (see figures B2-B4). There was no correlation between the quantity of large defects ($>100 \mu\text{m}$) and minimum load for pop-

in. The best correlation was with the fraction of cloudy crystals. This implies that many very small defects make plastic deformation more likely than isolated large defects. Finally, the minimum load for pop-in was plotted against the elasticity, E_{IT} and proportion of elastic work, η_{IT} (see figures B4 and B5). RDX samples that had a higher elasticity showed pop-in behaviour at higher applied loads. Pop-ins also occurred at higher applied loads for RDX lots which underwent a smaller proportion of elastic work. These correlations also make sense, less elastic crystals would be expected to deform plastically at lower applied loads as they are less able to dissipate stress. Determining when pop-ins occurred was rather subjective however, as it was sometimes difficult to distinguish where the first pop-in was on a load/displacement curve. Further examination of the raw data, perhaps by using a technique that could distinguish between actual pop-in events and background “noise” would remove any subjectivity.

Larger crystals are more elastic than smaller crystals when subjected to a load because the greater volume of material is better able to dissipate the stress and is therefore more able to recover elastically than a smaller crystal. For all RDX samples (irrespective of size and defect quantity), creep increases as the maximum applied load increases. Smaller crystals with many defects undergo more creep during constant load than a large crystal with few defects. The presence of voids within a crystal allows more deformation to occur while the load is applied.

An indentation in a small crystal is proportionally much larger than an indentation produced by the same load in a much larger crystal. The faster decrease in elastic modulus and increase in creep with increasing applied load for smaller crystals is due to this larger indentation volume to bulk crystal volume relationship. Harder crystals undergo less creep than softer crystals, as they tend to be larger and contain fewer defects (figure 5.18). The absence of defects makes them more resistant to deformation. Larger crystals have more material volume to dissipate stress during loading making them harder and creep less. Crystals with intermediate mechanical properties are either large with many defects or small with few defects. A crystal that is large but has many defects would have reduced hardness/elasticity because the defects

would cancel out the benefit of having a larger bulk volume. Conversely, a crystal containing few defects but having only a small bulk volume would have the benefit of having few defects reduced.

5.4 Conclusions

The internal defect assessment using microscopy and scoring system was shown to be semi-quantitative. It was able to distinguish between type A (Woolwich) and type B (Bachmann) RDX samples. This shows that the production method used influences the number of defects present. For example, RDX crystals that have been recrystallised tend to have fewer defects (especially larger ones) because during recrystallisation voids are replaced by recrystallised material. Also, RDX crystals produced by the Woolwich process tend to have less intra-crystalline impurities which can promote formation of internal defects. There was some indication of a correlation between the defect score and shock sensitivity results from the R⁴ study. The defect score for Eurenco MI-RDX was much lower than would be expected from its shock sensitivity. However MI-RDX had many crystals that were cloudy/dark, possibly due to the presence of sub-micron defects or out of focus large defects. This suggests that the score given for a cloudy crystal should be much higher. Nanoindentation has been shown to distinguish between RDX lots containing different quantities of internal defects. The presence of internal defects reduces elastic modulus, hardness and increases creep deformation. It has also shown that the mechanical properties of RDX crystals are linked to shock sensitivity. Crystal size has been shown to contribute to mechanical properties. Crystals that are larger and contain fewer defects have superior mechanical properties than smaller crystals with many defects within them. In contrast to the microscopic assessment of crystal defects, nanoindentation provides a non-subjective and fully quantitative assessment method. Therefore nanoindentation offers a method of determining RDX crystal quality that is superior to optical microscopy as used in the R⁴ programme.

CHAPTER 6

Results and discussion; morphology assessments and rheology analysis

6.1 Morphology assessment results

Frictional forces between contacting RDX crystals is a significant mechanism for the formation of hot spots. It would be expected that crystals that are angular with sharp facet edges and tips would produce more hot spots than smooth crystals. The literature [66,90] discussed in section 2.2 has in fact shown that this can be the case. This chapter will present further work that has been done exploring this relationship.

6.1.1 Rheology analysis results and discussion

Figure 6.1 shows how the viscosity changes as a function of applied shear stress, σ , for each RDX sample. As expected, all the suspensions showed non-Newtonian behaviour, (viscosity dependent upon applied shear stress). This departure from non-Newtonian properties is due to the presence of the RDX crystals in the suspension. Viscous forces between the crystals and the PEG alter the overall rheological properties of the suspension. For all samples there is an initial rise in viscosity which peaks at an applied shear stress between 7 and 12 Pa, after which the viscosity decreases exponentially due to shear thinning. The initial rise in viscosity is due to the suspension resisting flow deformation, as at low shear stress the crystals are closely packed together. At the maximum viscosity the suspension is at a steady state. After the peak in viscosity the shear stress has become high enough to break down the structure in the suspension, allowing flow to occur. The viscosity/shear stress curves show that crystal morphology has an effect on the RDX-PEG suspension viscosity. The suspension containing Dyno Type II RDX (which has very angular/irregular morphology) has the highest mean viscosity at all shear stress values. On the other hand, the suspension made with the very smooth/rounded Dyno RS crystals has the lowest mean viscosity across the shear stress range. RDX suspensions containing crystals of intermediate morphology have intermediate viscosities. The influence of morphology on

viscosity is due to how crystals of different morphology allow flow to occur. Crystals that are very rough/angular are expected to flow less easily as they tend to “jam up” in the suspension. As particle morphology becomes rounder/smoother there is less resistance to flow because the crystals can move against each other more easily, resulting in a lower viscosity. Dexter *et al* have reported that the morphology of RDX crystals affects the viscosity of pre-cured PBX formulations. A formulation made with rounder crystals had a lower viscosity than an equivalent formulation made with angular crystals [157]. A similar result was observed by Sharabi *et al* [158]. They found that HMX that had been spheroidised by using an ultrasonic smoothing technique when formulated into a PBX, flowed much easier compared to a PBX containing rough HMX crystals. Furthermore, the mixing time was halved when preparing the composition with the smooth crystals and its viscosity was only 1.1 kPa.s in contrast to 8.5 kPa.s for the PBX containing rough crystals.

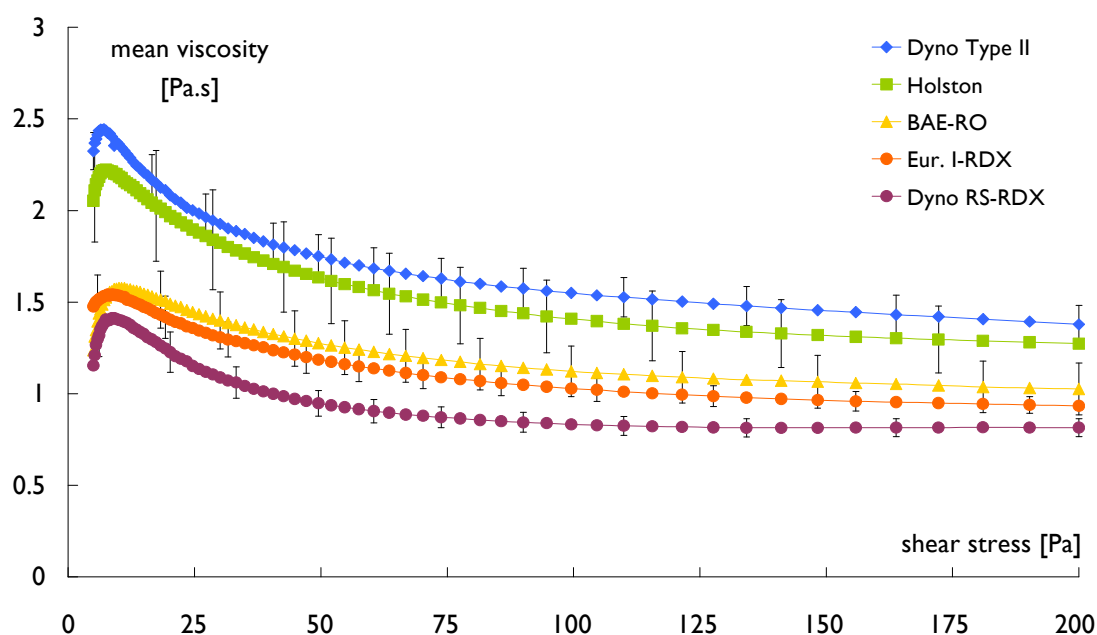


Fig. 6.1 Plots of mean viscosity verses applied shear stress for the RDX-PEG suspensions. Error bars give the 95% confidence intervals.

For all suspensions the shear rate increases linearly with increasing applied shear stress (figure 6.2). Again, crystal morphology is seen to have an effect on the shear rate. The Dyno Type II suspension has the lowest shear rate at all shear stresses measured, whereas the Dyno RS suspension has the highest. The gradient of each line is the viscosity. Dyno Type II has the highest

viscosity and has the steepest gradient, whereas the Dyno RS suspension has the lowest viscosity and shallowest gradient.

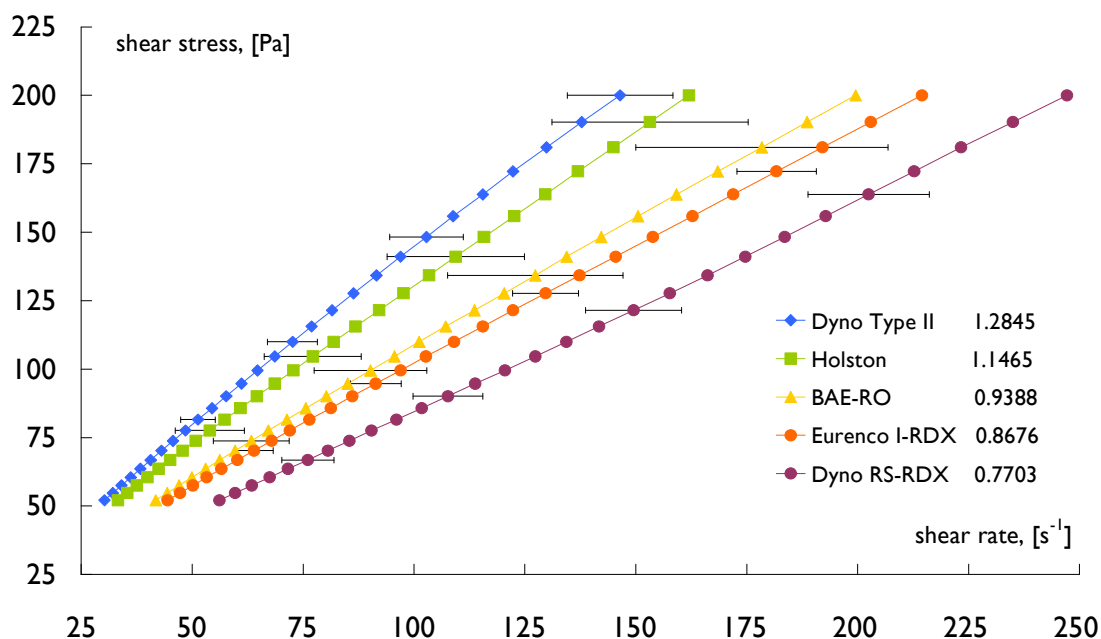


Fig. 6.2 Plots of mean shear rate versus applied shear stress for the RDX-PEG suspensions. Error bars give the 95% confidence intervals, gradients for each line are given in the key.

For all suspensions the viscosity initially increases to a maximum with increasing shear rate, after which there is a smooth reduction in viscosity as the shear rate increases (figure 6.3). The Dyno Type II suspension has the highest viscosity and lowest maximum shear rate, 2.44 Pa.s and 146.5 s⁻¹ respectively. The Dyno RS-RDX suspension, however, has a maximum viscosity of 1.41 Pa.s and maximum shear rate of 247.2 s⁻¹. As crystal morphology changes from angular/rough to smooth, the maximum shear rate increases because viscosity decreases as explained earlier. This allows an increasing rate of shear deformation to occur within the suspension. With increasing crystal smoothness frictional forces between the moving crystals are reduced.

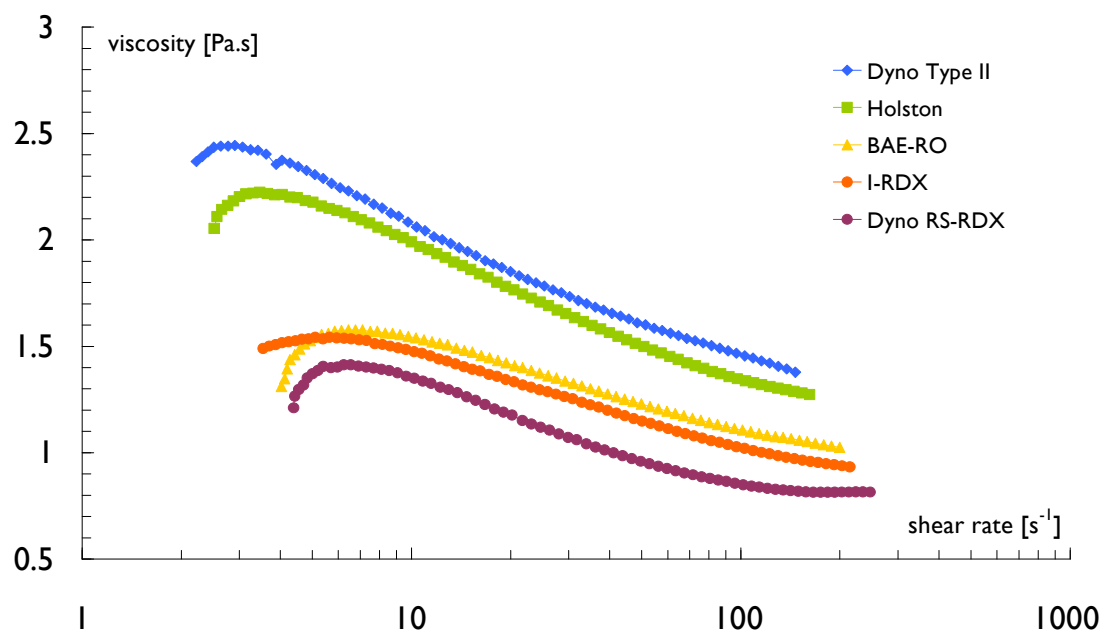


Fig. 6.3 Plots of mean shear rate verses mean viscosity for each RDX-PEG suspension.

With increasing morphology score (figure 6.4) the maximum shear rate decreases. Conversely, as the maximum viscosity increases the morphology score increases. Initially, the maximum shear rate and maximum viscosity changes rapidly as morphology score increases (Moving from Dyno RS to intermediate morphology), but when crystal morphology becomes more angular it decreases at a slower rate. This implies that the rheological properties of the RDX-PEG suspensions are very sensitive to changes in morphology of the smooth crystals. A change from medium to very angular/rough morphology has only a small effect. The strong correlation between the morphology scores and the parameters measured suggests that rheological characterisation of RDX suspensions could provide a non-subjective alternative to matching fluid microscopy for RDX crystal morphology assessment.

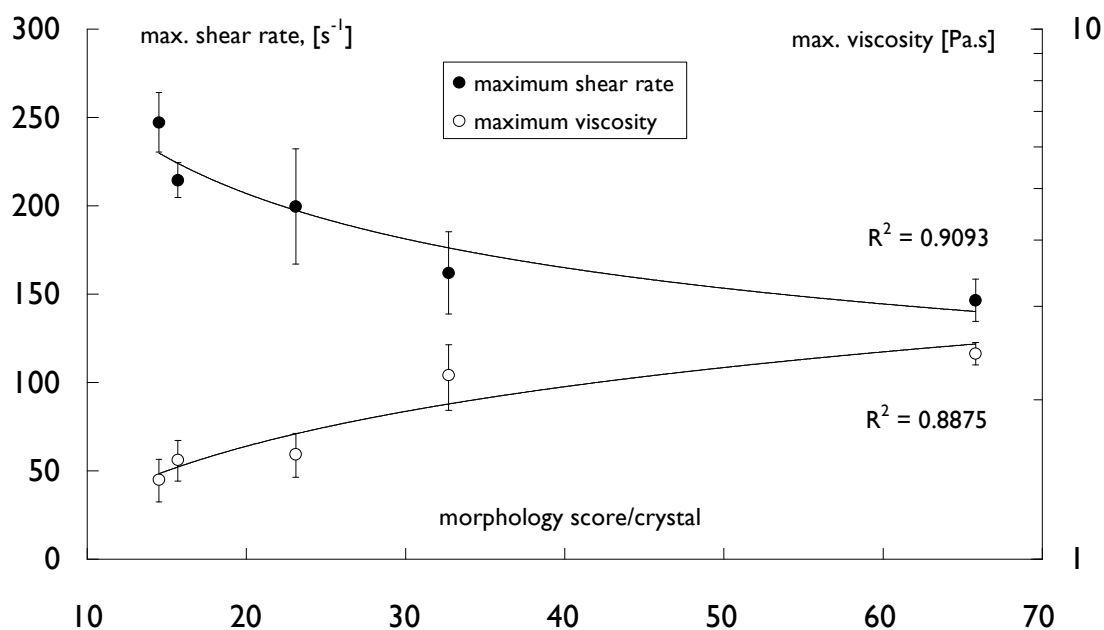


Fig 6.4 Plots of maximum shear rate and maximum viscosity against the mean morphology score of the RDX lots. Error bars give the 95% confidence limits.

Figure 6.5 indicates a strong correlation between crystal morphology and PBX shock sensitivity. As the shock sensitivity decreases, (higher initiation pressure required for 50% probability of initiation), the crystal morphology becomes smoother.

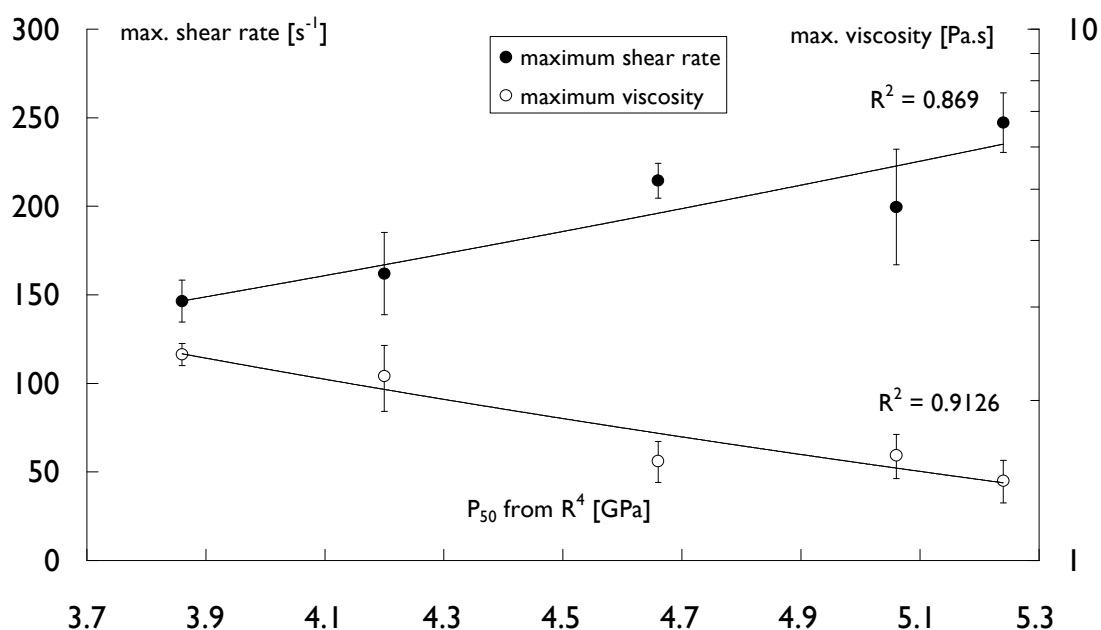


Fig. 6.5 Plots of maximum shear rate and maximum viscosity versus the shock sensitivity results from the R⁴. Error bars give the 95% confidence limits.

Compositions that were made with very angular crystals showed the lowest maximum shear rate and highest maximum viscosity when in suspension and were also the most shock sensitive in the gap test. Angular crystals seem to reduce the ability of the formulation to flow and dissipate regions of concentrated shock energy (hot spots). As the crystals become smoother, the formulation is able to flow better (higher shear rate) allowing hot spots to be dissipated, therefore reducing shock sensitivity. The correlation between shock sensitivity and the rheological properties indicates that measuring the rheological properties of an RDX suspension provides an alternative method of measuring crystal morphology. Rheological measurement has the advantage of being less subjective and time consuming than using optical microscopy. The correlation with the R^4 results may also suggest a link between shock sensitivity and morphology. However the LSGT results are also influenced by other confounding factors such as crystal defects, so a direct causal relationship cannot be easily derived. Further work involving formulation, rheology analysis and shock sensitivity testing of PBX formulations would be needed to verify rheology as a test to predict shock sensitivity.

6.2 Results and discussion of morphology assessment by optical microscopy.

Inspection of the optical micrographs indicated that crystal morphology varies considerably between different RDX lots. The morphology covered a wide range from angular/irregular shaped crystals with sharp edges and corners to smooth almost spherical particles. Figure 6.6 shows the morphology distribution for each RDX lot displayed as the accumulative percentage of crystals that were assigned to each morphology bin. Bin A has the most angular crystals while bin H has smooth and rounded crystals (c.f. table 4.4).

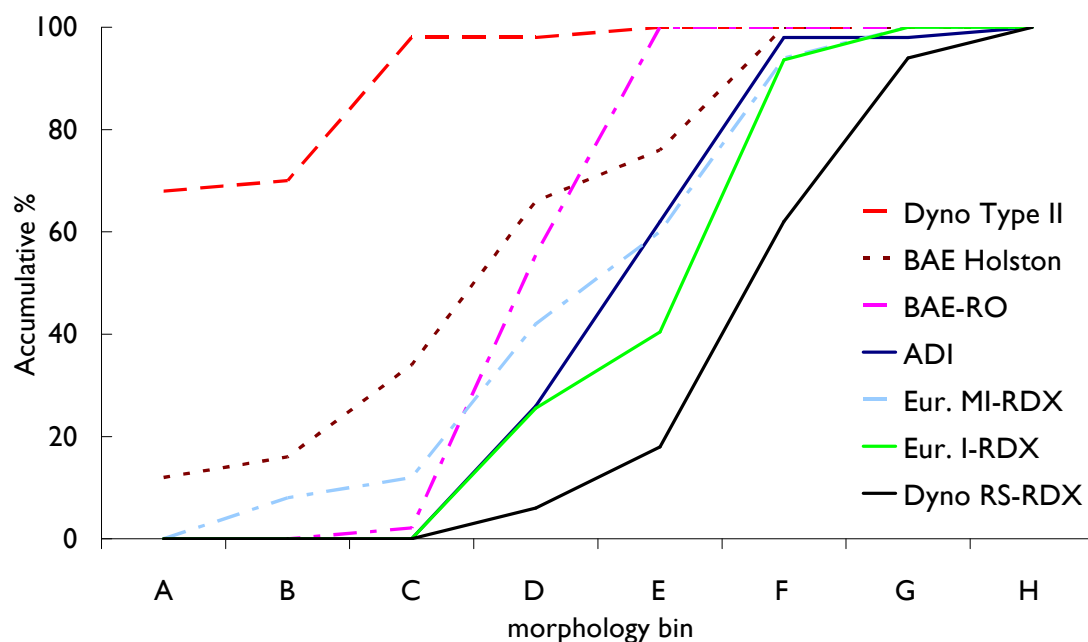


Fig. 6.6 Morphology distributions for the RDX lots examined plotted as an accumulative percentage of crystals assigned to each morphology bin.

For example, 68% of the Dyno Type II crystals (red dashed line in figure 6.1) were assigned to bin A with another 2% being in bin B. The remaining 30% were assigned to bins C and E. Clearly Dyno Type II RDX crystals were the most angular and irregular shaped. Dyno RS-RDX had the most rounded crystals with no crystals in bins A to C, 6% and 12% respectively in bins D and E and the rest in the smoother morphology bins F to H. Table 6.1 gives a description of the general morphology of each RDX lot.

Table 6.1 General description of the morphology of each RDX lot. Listed in order of shock sensitivity.

RDX Lot	Morphology
Eureco MI-RDX	Mostly irregular with smooth surfaces. Some elliptical or elongated, a few rough crystals.
Dyno Type II	Many faceted, angular crystals. Large numbers of very rough and irregular crystals. Lots of very small particles and fragments.
BAE Holston	Morphology like Eureco MI-RDX
Eureco I-RDX	Morphology like Dyno RS-RDX. But fewer elliptical and more irregular crystals.
BAE-RO	Most crystals either have some geometry or much geometry (bins E,F), some crystals appear fused together.
ADI	Morphology very similar to BAE-RO.
Dyno RS-RDX	Most crystals have some geometry (bin F), also many elliptical crystals. Crystals had a “beach pebble” or “potato” shaped appearance.

Figure 6.7 shows the mean morphology scores for each of the R⁴ RDX lots plotted against their shock sensitivities obtained during the R⁴ study [24]. The upper and lower 95% confidence limits are also plotted to give an indication of the reliability of each score. Dyno Nobel type II RDX has by far the highest morphology score, thereby suggesting that they are the roughest, most angular crystals. BAE Holston RDX also has a mean score that is higher than most of the other RDX lots. Both BAE Holston and Dyno type II have wider confidence limits than the other RDX lots, indicating that there is greater variability in their overall morphology. The other RDX lots have morphology scores that are similar to each other, with Dyno RS-RDX having a slightly lower score. Crystal morphology is strongly dependent upon the method of production and recrystallisation. RDX lots produced by the Woolwich process or that have been recrystallised using cyclohexanone (Dyno RS-RDX, empty circles on figure 6.7) are smoother than the unprocessed Bachmann RDX lots (red circles). During the recrystallisation process, the crystals are effectively polished to remove any rough surfaces [22], although the main purpose of recrystallisation is to remove or reduce the number of internal defects.

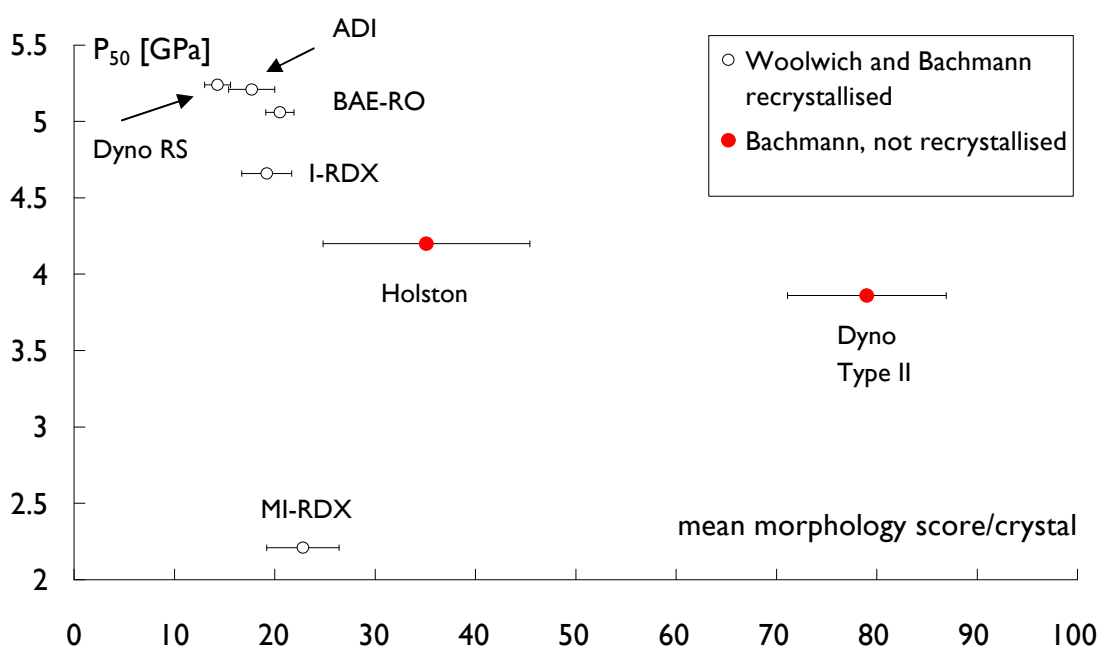


Fig. 6.7 Mean morphology scores of the R⁴ RDX lots plotted against shock sensitivity. Error bars give 95% confidence intervals of the mean values.

The plot of shock sensitivity against morphology score suggests that rougher/angular crystals are more sensitive than smoother crystals. However, the morphology score for MI-RDX is much lower than would be anticipated given that it is the most sensitive lot. Sensitivity is influenced by other factors as well as crystal morphology. Other parameters such as internal/surface defects or surface roughness are involved. This assumption is supported by Matsuzuki *et al.* [84] who found that a greater reduction in shock sensitivity was obtained by reducing crystal surface defects (cracks and pores) rather than making crystals smoother. They obtained an increase of required initiation shock pressure from 2.2 to 5.0 GPa when surface defects were removed but only an increase from 5.0 to 5.6 GPa when the crystals had been spheroidised.

This assessment method is highly subjective. Assigning crystals to the morphology bins is dependent upon human judgement. Sometimes it is not easy to assign a crystal to a specific bin which can lead to selection bias where crystals that are easy to assign are selected whilst other crystals that have ambiguous morphology are not. Reproducibility is therefore an issue. The number of points assigned for each morphology bin is also subjective. This method is time consuming and tedious which further reduces the reliability of this assessment. The observations from the R⁴ study are in general agreement with the results obtained here. The R⁴ results showed that type II materials were more angular and irregular whereas the type I lots were smoother and more rounded.

To improve the reliability of the results obtained from the morphology assessment, the same micrograph images assessed by the author were supplied to staff and students at Cranfield University. There was a very good agreement between the morphology scores from the assessment by the author and mean multi-person assessment scores. This shows that the assessment method used was reproducible. Figure 6.8 illustrates the very close agreement between the mean morphology scores from the author's and the multi-person assessment. The morphology distribution was very similar to the original assessment and is shown in figure 6.9. Again, Dyno Type II RDX (red dashed line) has the most (and is mostly comprised of), crystals that are angular or rough/irregular (bins "A" and "B").

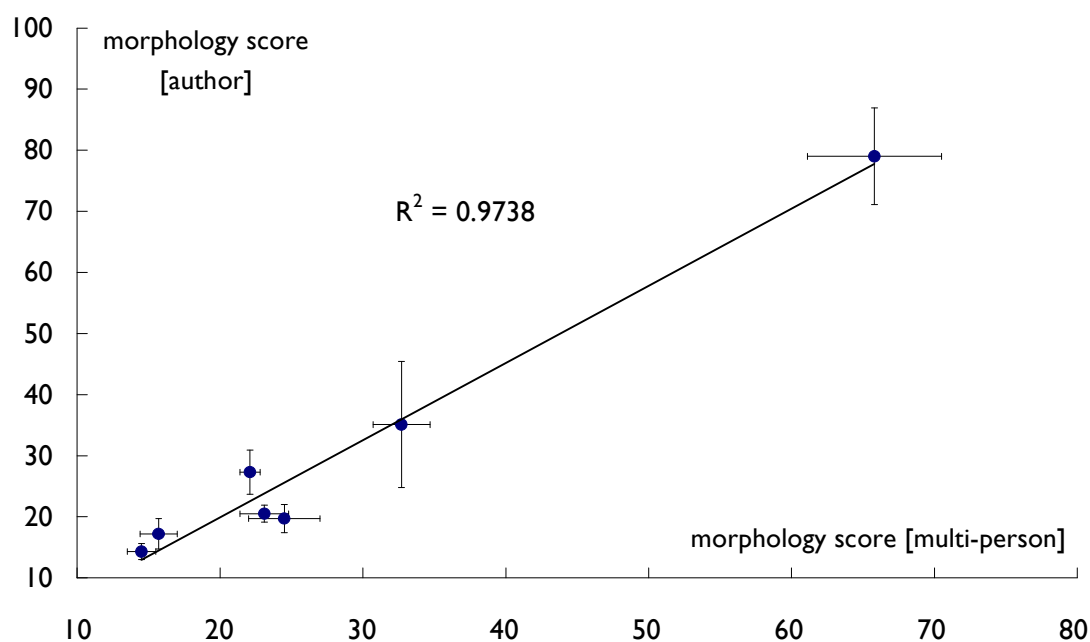


Fig. 6.8 Plot showing the agreement between the mean morphology scores from the author's assessment and the multi-person assessment. Error bars give 95% confidence intervals of the mean values.

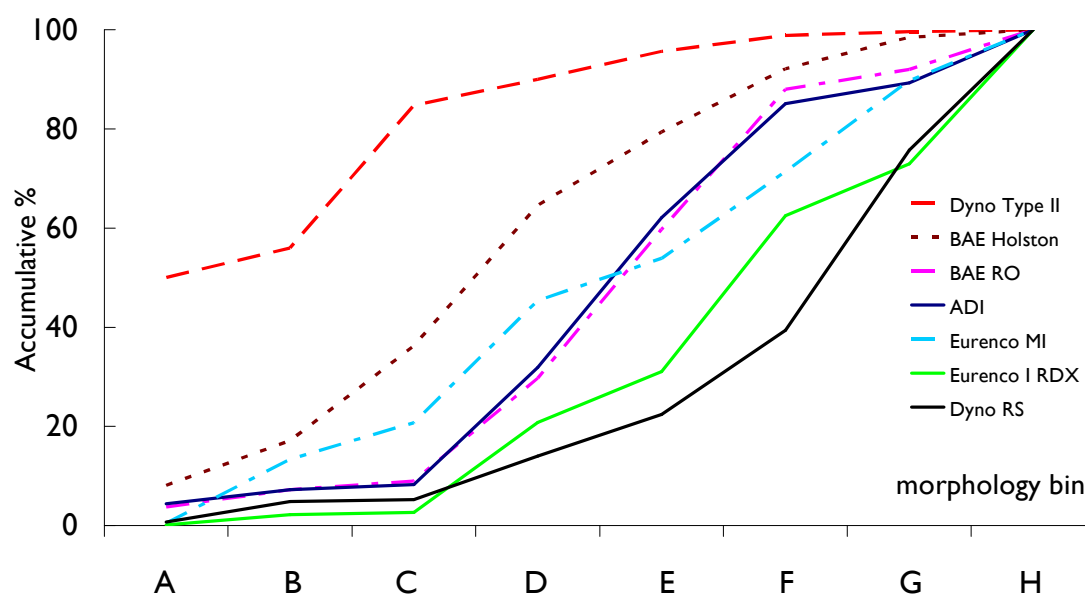


Fig. 6.9 Morphology distributions of the RDX lots from the multi-person assessment.

Mean morphology scores were also well associated with the method of production. The larger variation in the mean scores for Dyno type II is possibly due to ambiguity between morphology bins “A” and “E”. Both

classifications contain crystals with a strongly geometric shape, but bin “A” crystals have sharp corners whereas bin “E” crystals have rounded corners. In some cases crystals could be assigned to either bin “A” or “E”. Since there is a considerable difference between the scores assigned to these bins (100 points for “A” and only 20 points for “E”), this could introduce large discrepancies between overall scores for different assessors. There was also potential for confusion between bins “A” and “C”. Both bins have crystals that have sharp angular features, but bin “C” only has short jagged edges whereas bin “A” has longer edges. Again there is a large difference in scores between the two bins (65 points). For the bins describing the smoother crystal morphologies there is also some possibility of ambiguity. However, the point differences between them are much smaller.

The overall good agreement between the two assessments is in contrast to the results from the R⁴ study which showed large differences between laboratories. The discrepancies between the laboratories involved were due to many factors. For instance, some laboratories were more careful in getting a representative sample. Some might have selected crystals that were easy to assign whereas other operators might not (selection bias). The assessment by the author and the multi-person assessment used the same micrographs, thereby removing the variation due to different sampling techniques and crystal selection bias. In the R⁴ study, assessors were only given hand drawn outlines to describe bin morphologies and to guide assessment. The multi-person assessment used photomicrographs of crystals exemplifying each morphology bin, see table 4.4.

6.2.1 Simplification of assessment by reducing the number of morphology bins

Some of the morphology bins used in the assessment are somewhat ambiguous. Bins A and E both denote strongly geometric forms, the only difference being the sharpness of the corners and edges of the crystals. To make the assessment less ambiguous and subjective it was decided to merge some of the bins together. New scores were assigned to the new bins based upon the average of the original bin scores. Table 6.2 shows the combined bins and their scores.

Table 6.2 The combined morphology bins and their associated scores.

New combined bin designation	Original bins	Combined bin score
1	A, C, E	50
2	B, D, F,	30
3	G, H	7.5

The same crystal photomicrographs were then assessed by the author using the combined morphology bins. Figure 6.10 Plots the morphology distributions for the RDX lots using the three bins described in table 6.2.

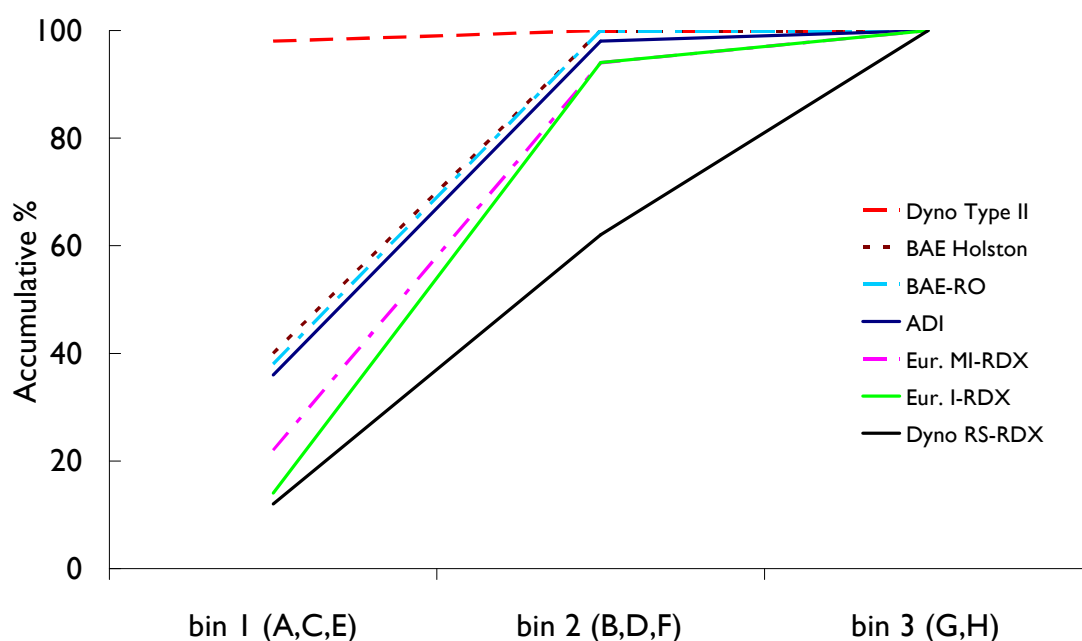


Fig. 6.10 Plot of total morphology scores from the original and combined bins assessment.

There is very little difference in the overall distributions between the original assessment with eight bins and the assessment with the combined morphology bins. This means that reducing the number of bins does not significantly affect the final result. Therefore, reducing the number of bins has the advantage of reducing ambiguity and so making the assessment easier and less subjective.

6.3 Conclusions

The morphology assessments performed by both the author and the multi-person assessment showed that RDX crystal morphology is controlled by the method of manufacture. For both assessments the morphology scores correlated with the R^4 shock sensitivity data, apart from Euroenco MI-RDX which did not fit this trend. Despite having relatively smooth crystals it was the most shock sensitive. This implies that other factors other than morphology are contributing to its high sensitivity. The most likely reason for its anomalous behaviour compared to the other Woolwich RDX lots is the large proportion of crystals that contain very small defects (cloudy regions, see figure 5.6). There is a good agreement between the author's assessment results and the multi-person assessment scores, in contrast to the large discrepancies seen in the R^4 data. This is possibly due to the improved guidelines given to each assessor. It has been also shown that reducing the number of morphology bins does not affect the scores obtained and provides a version of the assessment that is easier to use and less time consuming. The method, however, suffers from being subjective and assesses only a small number of crystals reducing how representative the method is. The point values given to each morphology bin are not based upon empirical evidence. For instance would a crystal assigned to bin A (100 points) be ten times more sensitive than a crystal in bin G (10 points).

From the results obtained from the rheological analysis, it is clear that RDX crystal morphology strongly affects the rheological properties of RDX-PEG suspensions. Therefore, rheological analysis of RDX suspensions may provide a method to assess crystal morphology. A suspension with a higher viscosity indicates that the RDX crystals are angular rather than smooth/rounded. The good correlation between the rheological parameters

and the morphology scores obtained from the microscopic analysis suggest that this method provides results that are just as reliable but non-subjective. The rheology analysis method is also much faster.

Crystal morphology appears to only have a partial influence on the shock sensitivity. Other crystal characteristics are also involved. Shock sensitivity is not influenced by one characteristic but by many acting together.

CHAPTER 7

Results and discussion; other results

This chapter will discuss the results obtained from the SEM microscopy assessment to investigate surface defects, thermal analysis by DSC and shock sensitivity testing of loose packed RDX using the small scale gap test.

7.1 Surface defect assessment results

Surface defects have a similar effect on shock sensitivity as morphology. Crystals that have a rough irregular surface covered with cracks and pores would be more prone to form frictional hot spots. They also have a much higher surface area for surface hot spots to develop. Therefore, the amount of surface defects was assessed to see if there is any relationship between them and sensitivity.

A wide range and variety of surface defects was observed. Dyno RS-RDX crystals had the smoothest crystals with very few defects (figure 7.1). Dyno Type II crystals had a very rough appearance, covered with many cracks and smaller attached particles (figure 7.2). ADI and BAE-RO crystals were generally smooth to medium roughness with some deep cracks (figure 7.3). Holston, Eurenco MI and I-RDX had many crystals of medium roughness with large numbers of holes, depressions and attached particles (figures 7.4).

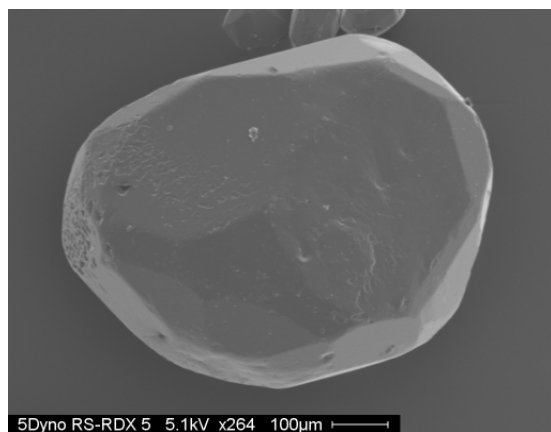


Fig. 7.1 SEM micrograph showing typical surface features of a Dyno RS-RDX crystal.

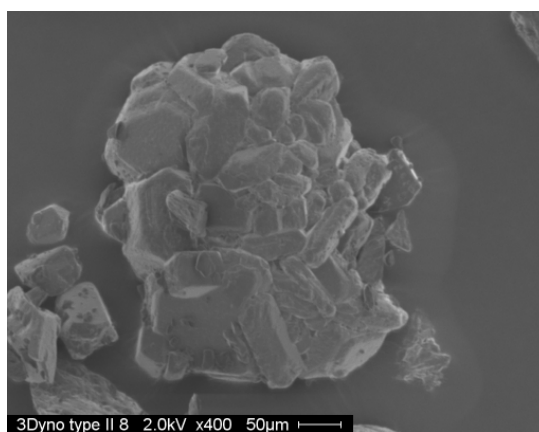


Fig. 7.2 SEM micrograph showing typical surface features of a Dyno Type II RDX crystal.

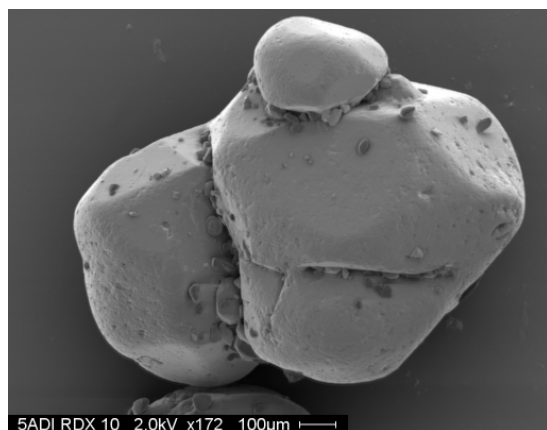


Fig. 7.3 SEM micrograph showing typical surface features of an ADI RDX crystal. BAE-RO crystals had a similar appearance.

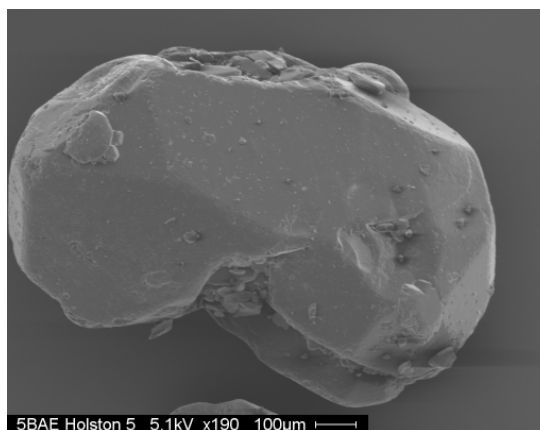


Fig. 7.4 SEM micrograph showing typical surface features of a Holston RDX crystal. Eurenco MI and I-RDX were similar.

Figure 7.5 plots the mean surface defect scores for each RDX lot against their shock sensitivity results from the R⁴ study [24].

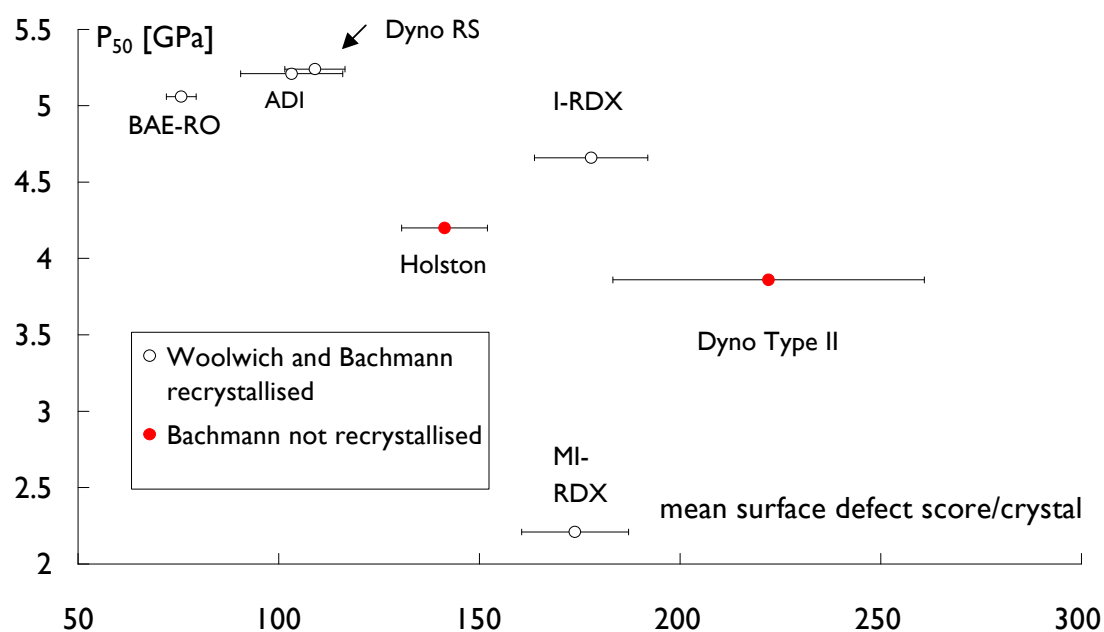


Fig. 7.5 Mean surface defect scores of the R⁴ RDX lots obtained from SEM micrograph images plotted against shock sensitivity data obtained during the R⁴ study. The trend lines illustrate the correlations between surface defect scores and sensitivity, for RDX lots made by Woolwich and Bachmann processes. Error bars give 95% confidence intervals of the mean values.

The plot indicates that generally, as crystal surface roughness increases, shock sensitivity also increases.

Figure 7.6 indicates that there is also a relationship between the overall roughness of a crystal and its sensitivity. Less sensitive crystals had smoother surfaces, whereas more sensitive lots had crystals with rougher surfaces. Only

un-reprocessed type II lots (Dyno type II and BAE Holston) had any crystals judged to be very rough. There is not much correlation between the number of cracks, holes, depressions and knobs, and shock sensitivity (figure 7.7). Certainly, the mean number of cracks per crystal does not vary much between the lots. MI-RDX, the most sensitive RDX, did have the largest mean number of holes and knobs but the middle ranked lot in terms of sensitivity (I-RDX) also had a high mean count for surface defects.

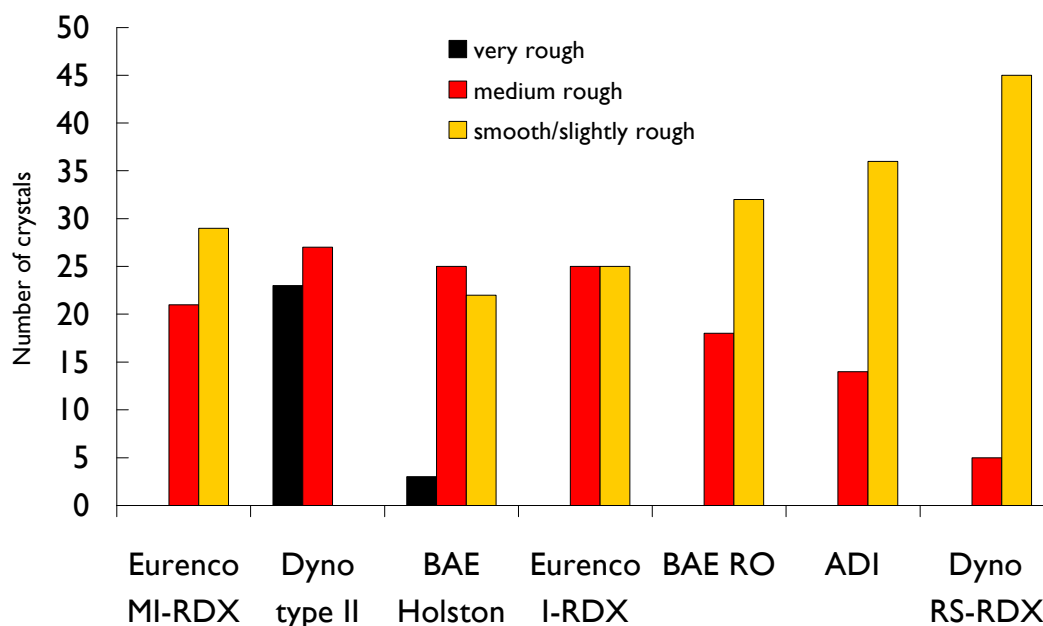


Fig. 7.6 The number of crystals from each RDX lot having either rough, medium rough or smooth surface, sensitivity decreases from left to right.

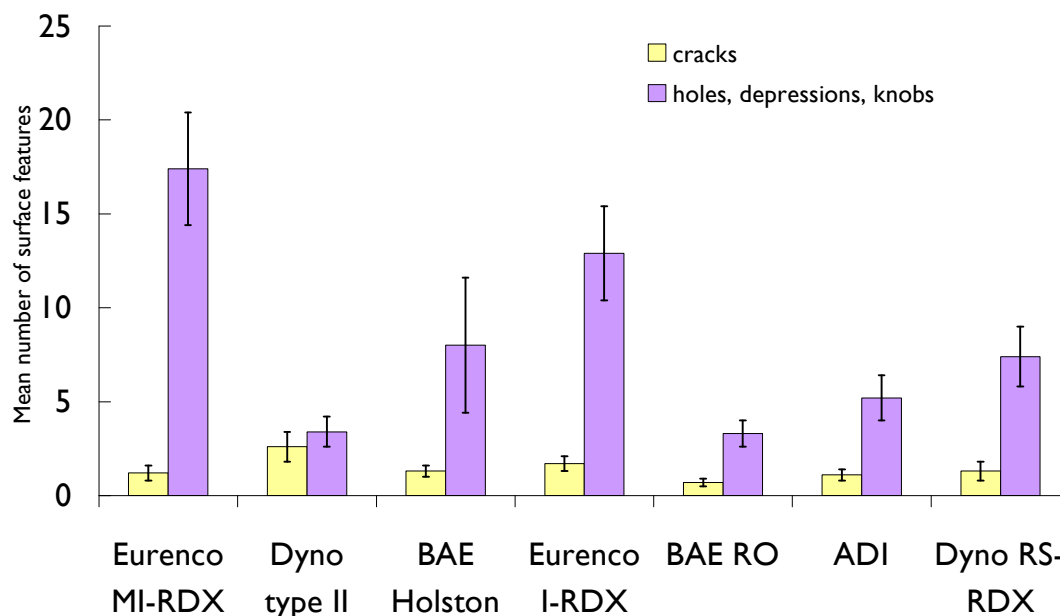


Fig. 7.7 Mean number of cracks, holes, depressions and knobs per crystal from each RDX lot, sensitivity decreases left to right.

7.1.2 Discussion of results from surface defect assessment

Overall analysis of the SEM micrographs shows that RDX lots with more crystals that have medium roughness or are very rough have higher shock sensitivities. Less sensitive RDX lots have crystals that are much smoother (figure 7.6). Only the type II lots have crystals that were judged to be very rough. This is in agreement with the morphology and internal defect results showing that the method of manufacture has a strong effect on these crystal properties. The increase in shock sensitivity with increasing surface roughness is because rougher surfaces increase friction between contacting crystals. Jagged edges and points on crystal surfaces also allow localisation of frictional forces leading to increased hot spot formation [31,88]. It seems that the general surface roughness has a greater influence on sensitivity than the number of specific defects such as holes, cracks and knobs. The number of cracks does not seem to have any influence on sensitivity, and there is only a weak trend between increasing specific defects and sensitivity (figure 7.7). Rougher crystals may also produce poorer quality PBX formulations as their uneven surface makes it harder for the binder to coat them completely. This leads to the formation of pores and voids within the PBX bulk volume which can form hot spots.

The plot of surface defect score against the R^4 study shock sensitivity data (figure 7.5) has a better correlation than the same plots for the morphology and internal defect scores. The data point for MI-RDX fits the general observed trend better than in the plots of internal defect and morphology scores. This implies that surface defects/roughness has a greater influence on shock sensitivity for Eurenco MI-RDX than internal defects or morphology. However, although Eurenco MI-RDX is the most sensitive, it has a very similar surface defect score compared to Eurenco I-RDX which has a much lower sensitivity (mean scores of 1738 and 1778 respectively). The high sensitivity of MI-RDX is possibly not only due to having rougher crystals but also to the presence of many sub-micron internal defects. This suggests that surface defects and roughness are less sensitising than internal defects. The study undertaken by Bellitto *et al* [86,87] highlighted in section 2.2 showed that the average standard deviation of the surface roughness (i.e. the variation of surface roughness) had a greater influence on shock sensitivity. This is demonstrated by figure 7.8 which plots the R^4 shock sensitivity results against the mean standard deviation of the surface roughness for each RDX lot. These values were calculated statistically from the AFM images of each crystal analysed.

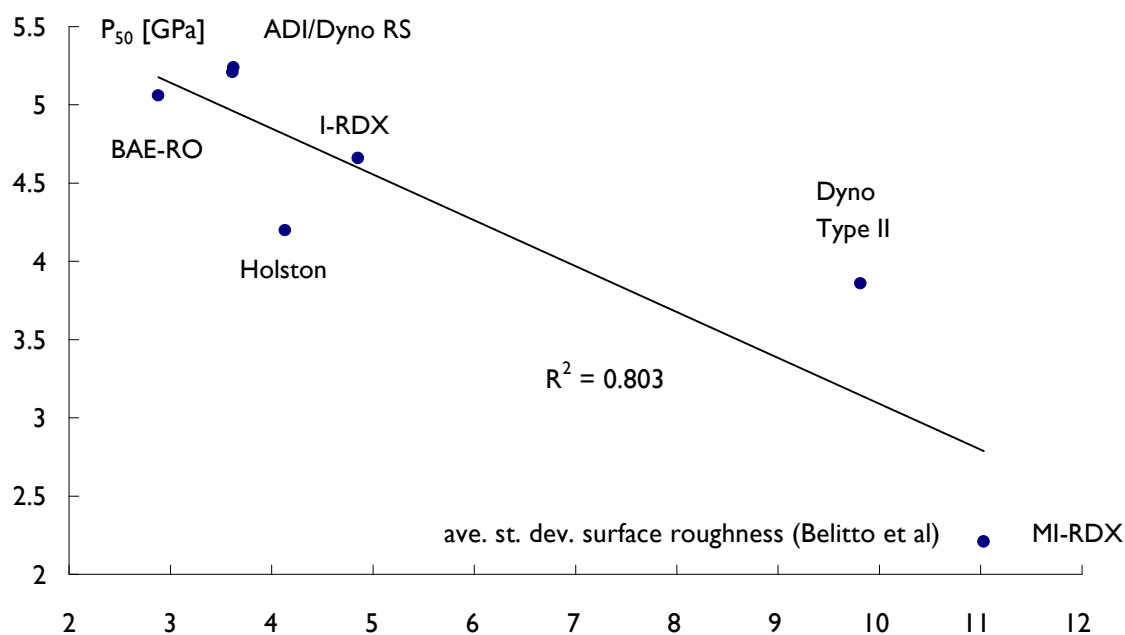


Fig. 7.8 Plot of shock sensitivity results from R^4 against the average standard deviation of the surface roughness calculated by Bellitto *et al*, reference 86,87.

The correlation here is much better ($R^2 = 0.803$) compared to the mean surface defect score plotted against shock sensitivity ($R^2 = 0.3877$). This suggests that the surface defect assessment method does not provide a reliable indication of shock sensitivity. In fact, the surface defect assessment results from the R⁴ study showed wide variation of results from different laboratories even for the same RDX sample. The large variation that is seen in these results is probably due to the highly subjective nature of the method, one laboratory reported twenty times more cracks than another laboratory [147]. This is possibly because multiple branching/forking cracks raise reproducibility problems, e.g. how should they be counted, as one or many? One assessor might count a branching crack as being a single crack while another may assess it as being two or three cracks. The other surface features to be counted (knobs, holes and depressions) also gave wide ranging numbers, one assessor counting fifteen times more of these defects than another. This, therefore, suggests that the guideline descriptions provided [148] are too vague and makes assigning each observed surface feature too dependent upon a “best guess” or approximation. As with the internal defects and morphology assessments, the assessment guidelines need to be more specific. A clearer standardised assessment for counting surface defects would improve the assessments reliability.

7.1.3 Conclusions

There was a wide range of surface defects observed across the samples. Overall surface roughness correlates well with shock sensitivity, which is not surprising since rougher crystals can generate more hot-spots due to frictional forces. Roughness also appears dependent upon how the RDX was produced. RDX lots produced by the Bachmann process being rougher than Woolwich or recrystallised Bachmann products. The number of specific surface defects (cracks, holes, knobs etc) is not well correlated with sensitivity. The poor correlation between the R⁴ results and the author’s results indicates that the method is not reproducible. This was also concluded from the R⁴ study itself. This method is probably more subjective than the morphology assessment. There is more room for confusion in assessing features such as cracks and surface roughness compared to just assessing crystal shape. This, is probably

why there is so much variation between results from the R⁴ laboratories and also between the author's assessment and R⁴ data. Because of this wide discrepancy it is much harder to say if surface defects have an influence on sensitivity. Overall surface roughness could be considered to be linked with morphology as a crystal that is very irregular in shape is likely to have a rougher surface.

7.2 Thermal analysis of the R⁴ RDX lots using DSC

A differential scanning calorimetry method to distinguish between RS and non-RS RDX was reported by Spyckerelle [110,117], however the method was only partially successful [118]. DSC analysis was performed by the author to investigate further Spyckerelle's method and is presented in this chapter. Analysis was performed on the RDX samples alone and on samples in a pseudo-PBX, based upon the formulation used by Spyckerelle to examine how the addition of a binder affects decomposition compared to raw RDX.

7.2.1 Initial analysis of raw RDX

There was no significant difference between the thermograms for all of the raw RDX samples analysed with and without a nitrogen purge. The RDX samples produced by the Woolwich process and Dyno RS-RDX (all containing less than 1% HMX) gave a single endothermic peak at around 206°C. This was from the melting of RDX prior to its thermal decomposition. Subsequently there was a single larger exotherm due to the decomposition of RDX with a peak at approximately 233°C. This exothermic peak tended to be wide. Figure 7.9 shows a typical DSC scan for Woolwich RDX sample.

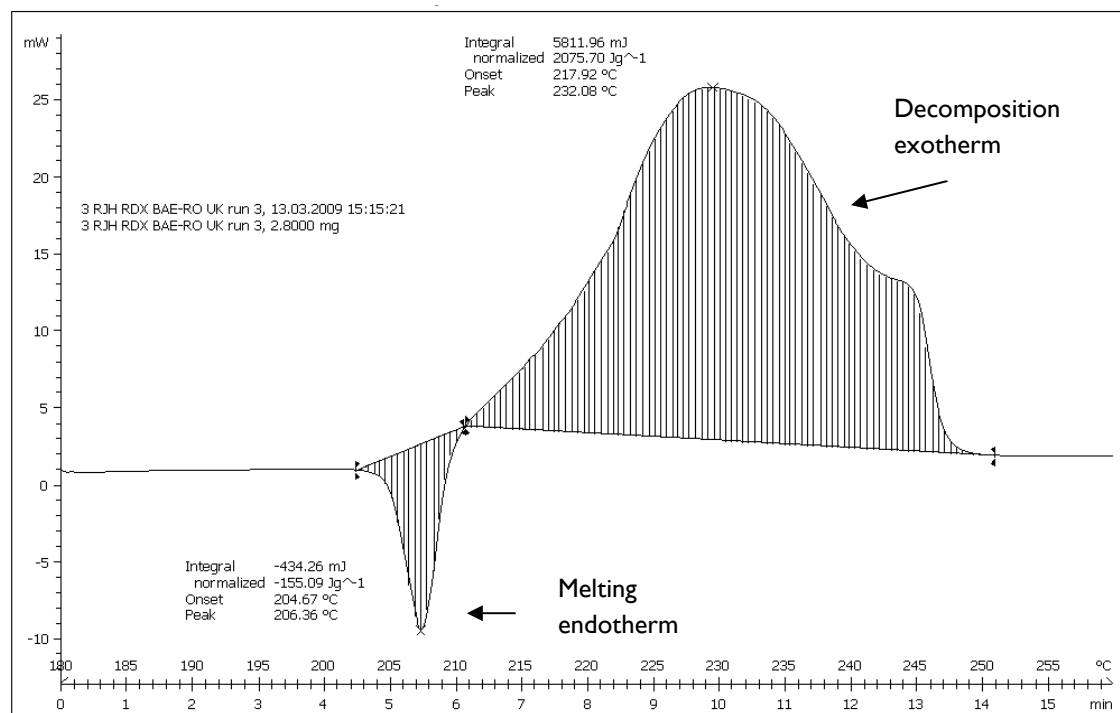


Fig. 7.9 Typical DSC scan of a Woolwich RDX sample, showing the melting endotherm and decomposition exotherm peaks.

For the unrefined Bachmann samples an additional endothermic peak was observed at around 189°C due to the formation of an HMX/RDX eutectic as reported by McKenney and Krawietz [115]. Figure 7.10 demonstrates a typical DSC scan for an unrefined Bachmann RDX sample.

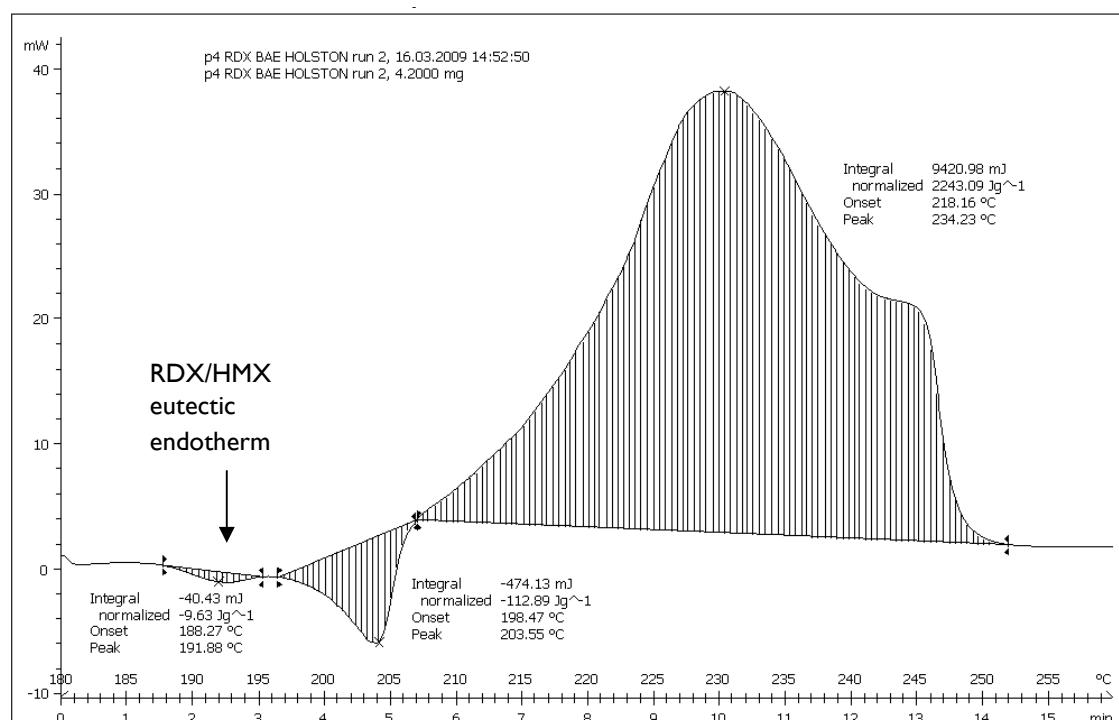


Figure 7.10 Typical DSC scan for an unrefined Bachmann RDX sample, showing the additional endothermic peak arising from the HMX/RDX eutectic.

Tables 7.1 and 7.2 show the mean onset and peak temperatures for the endo/exotherms and the mean energies associated with them for Eurenco I-RDX (type I) and Dyno Nobel (Type II) RDX.

Table 7.1 DSC thermogram data for raw Eurenco I-RDX.

	No nitrogen purge (2x s.d.)	With nitrogen purge (2x s.d.)
Mean melting endotherm	204.86 (0.69)	205.01 (0.19)
Onset, °C		
Mean energy, J g ⁻¹	-150.89 (18.93)	-144.89 (14.40)
Mean decomposition onset, °C	216.17 (3.84)	216.43 (1.93)
Mean decomposition energy, J g ⁻¹	2108.87 (305.56)	2023.93 (267.50)

Table 7.2 DSC thermogram data for raw Dyno Nobel type II RDX.

	No nitrogen purge (2x s.d.)	With nitrogen purge (2x s.d.)
Mean eutectic endotherm onset, °C	189.18 (0.14)	188.52 (0.56)
Mean eutectic endotherm Energy, J g ⁻¹	-31.67 (21.77)	-21.92 (24.99)
Mean melting endotherm Onset, °C	198.36 (1.28)	197.95 (3.05)
Mean melting endotherm Energy, J g ⁻¹	-48.16 (50.76)	-81.80 (73.13)
Mean decomposition Onset, °C	216.52 (5.92)	214.37 (1.78)
Mean decomposition Energy, J g ⁻¹	2147.60 (332.48)	2118.15 (115.42)

7.2.2 Raw RDX spiked with HMX

With no HMX present there was only one endotherm peak observed, just before the decomposition exotherm, due to melting of the RDX. The average onset temperature for the four replicates tested was 205.01 °C (see table 7.1). The energy associated with the melting endotherm was -144.89 J g⁻¹. With increasing amounts of HMX present, the melting endotherm onset point and peak was shifted to lower temperatures and the energy associated with it was reduced. An endotherm at around 189°C was also observed, which is known to arise from the formation of an HMX/RDX eutectic [115]. Oxley *et al* also observed this endotherm for Dyno Nobel RDX spiked with 10% HMX [111]. This endotherm peak was observed to shift to a higher temperature with increasing amounts of HMX in the sample, from 188.77 °C at 4 wt% HMX to 190.46 °C at 16 wt%. The energy associated with the eutectic endotherm also increased from -0.71 to -20.56 J g⁻¹. The decomposition exotherm onset, peak and energy were not changed by increasing HMX levels. Figures 7.11 and 7.12 show how the melting endotherm onset temperature and energy change with wt% HMX.

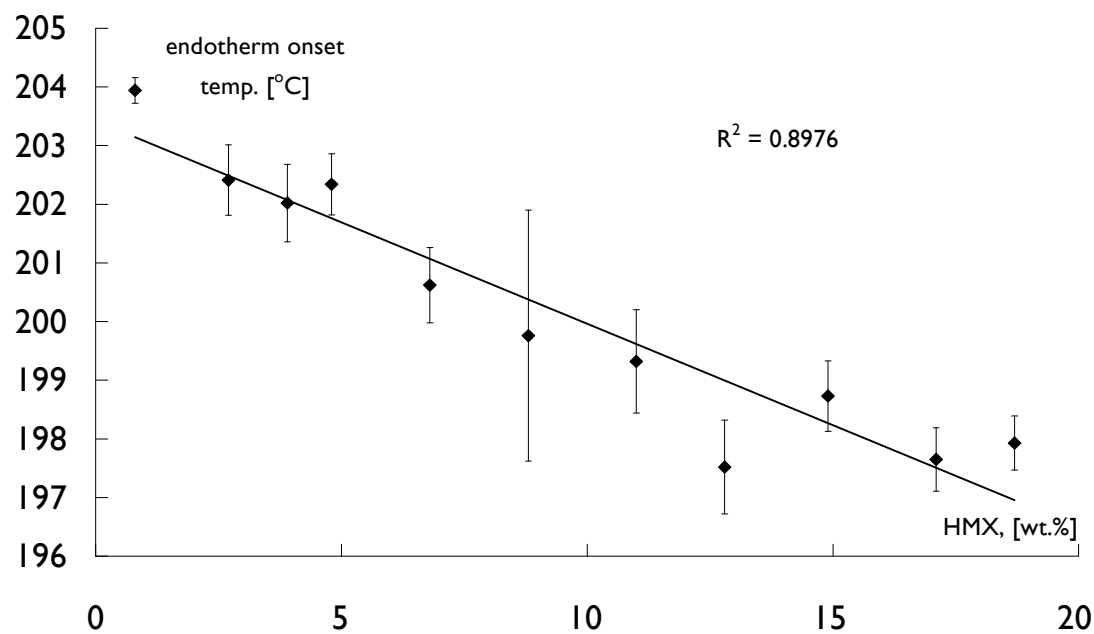


Fig. 7.11 Relationship between wt% HMX in Dyno-RS-RDX and melting endotherm onset temperature. Error bars indicate 95% confidence intervals.

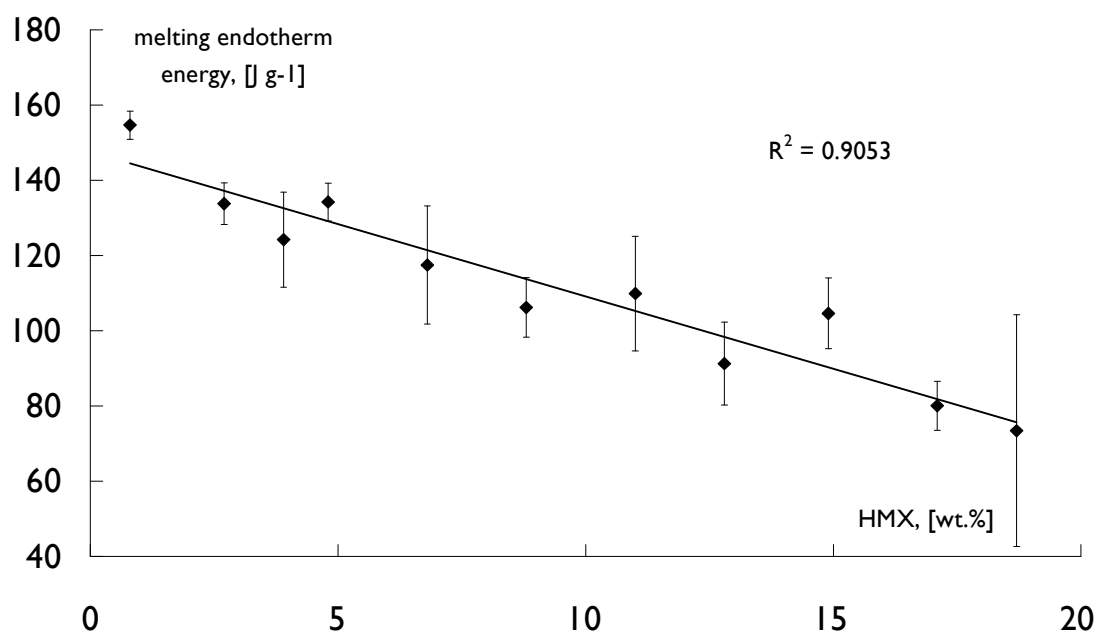


Fig. 7.12 Relationship between wt% HMX in Dyno RS-RDX and the melting endotherm energy. Error bars indicate 95% confidence intervals.

7.2.3 Results from the initial analysis of RDX in pseudo-PBX formulation

Significant differences were seen in the thermograms for type I and type II samples. Thermograms were also affected by using or not using a nitrogen purge. When no nitrogen purge was used, just a single exotherm peak was observed for both type I and type II RDX samples with no other features being seen. When a nitrogen purge was used however, there was a difference between the endotherms of type I and II samples. The Type I samples also gave an endotherm peak between 205°C and 207°C whereas the type II samples did not. Both type I and II samples gave an exotherm peak but it was shifted to a higher temperature compared to when no nitrogen purge was used. Figure 7.13 shows exotherms of type I and II lots without a nitrogen purge. Figure 7.14 shows thermograms for the same lots with a nitrogen purge. Table 7.3 summarises the effects on nitrogen purge on thermal behaviour.

Table 7.3 The effect of RDX type and nitrogen purge on the thermal behaviour.

Sample	N ₂ purge	Thermogram effect
Type I	no	One single exotherm
Type II	no	One single exotherm
Type I	yes	One single exotherm and one single endotherm (205°C-207°C), exothermic peak shifted to higher temperature, between 215 and 220°C.
Type II	yes	One single exotherm, shifted to a higher temperature, between 215 and 220°C.

To determine the cause of the exotherm shift when a nitrogen purge was used further experiments were performed using Dyno type II in the pseudo-PBX formulation. Samples of this pseudo-PBX were analysed using an air purge (50 ml min⁻¹) instead of a nitrogen purge and with no purge. For samples run with an air purge, there was no observed shift in exotherm peak temperature. Figure 7.15 shows DSC scans of the pseudo-PBX with nitrogen purge, air purge and no purge.

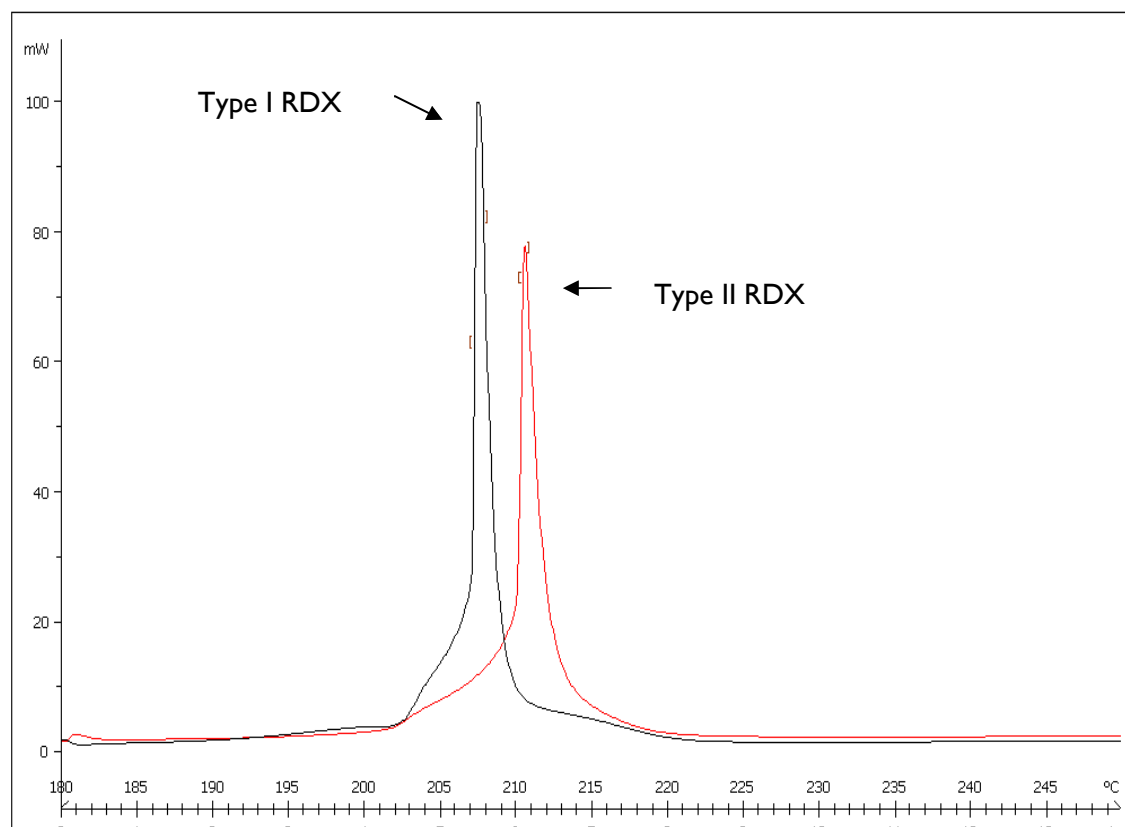


Fig. 7.13 DSC thermograms of BAE-RO (type I) and Holston RDX (type II) in a pseudo-PBX formulation with no nitrogen purge.

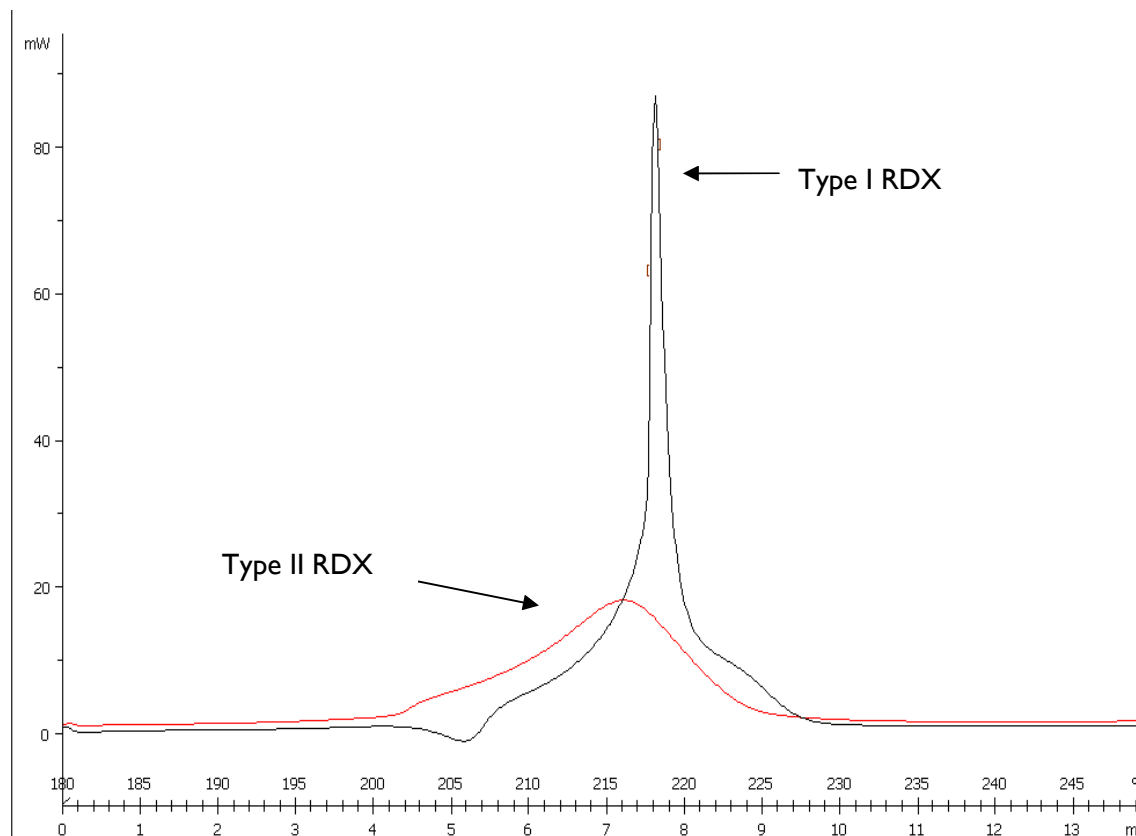


Fig. 7.14 DSC thermograms of BAE-RO (type I) and Holston RDX (type II) in a pseudo-PBX formulation with a nitrogen purge.

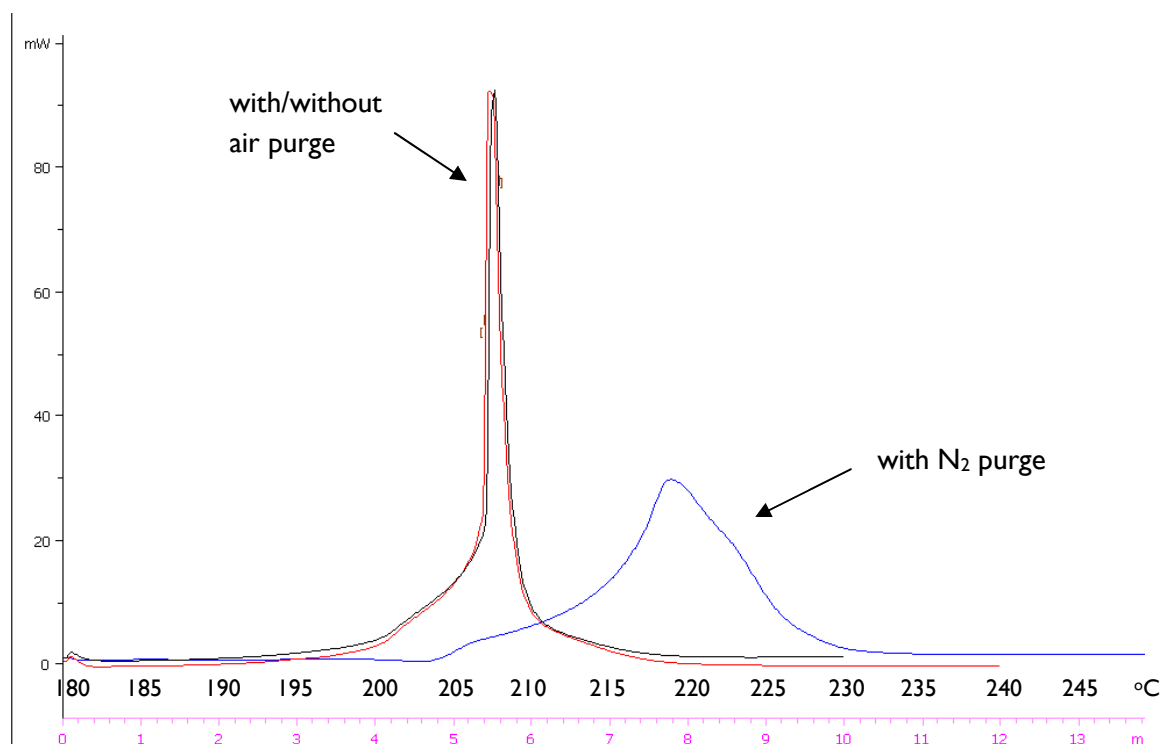


Fig. 7.15 DSC scans of Dyno type II RDX pseudo-PBX analysed without any purge, a nitrogen purge and an air purge.

7.2.4 The effect of RDX Particle size upon pseudo-PBX decomposition

During the analysis of the RDX/HTPB compositions (pseudo-PBX) samples, it was noted that the exotherm peak could be sharp or broad even for the same RDX sample. Therefore a series of analysis was performed using the same RDX sample (Dyno RS-RDX) but using two different RDX crystal sizes in the pseudo-PBX. Dyno RS-RDX was used as it has a low HMX content thereby removing any effect HMX may have. It was thought that a pseudo-PBX containing smaller RDX crystals would have a faster decomposition rate than one made with larger crystals, due to the higher total surface area. The results obtained from the pseudo-PBX samples showed a significant difference in the decomposition peak between compositions made with smaller and larger RDX particle size fractions. For the smaller particle size the exothermic peak was sharp (mean PWHM^{§§§} 1.1°C) for all ten replicates. With the larger particle size pseudo-PBX, the exotherm was much wider (mean PWHM 13.1°C) for eight of the ten replicates, the other two replicates giving sharp peaks (mean PWHM 1.3°C). The onset for decomposition was also earlier for pseudo-PBX samples

^{§§§} PWHM, peak width at half of maximum peak height.

made with RDX particles, between 45 and 125 μm (average onset temperature 200.5°C). For pseudo-PBX samples made with RDX particles between 500 and 1000 μm the average onset temperature for decomposition was 202.5°C (sharp peaks) and 202.8°C (wide peaks). These results are summarised in table 7.4.

Table 7.4 Summary of particle size results, mean peak widths and onset temperatures are shown.

RDX particle size range in PBX (μm)	Wide exotherm peaks	Sharp exotherm peaks	PWHM (wide) °C	PWHM (sharp) °C	Exotherm Onset (wide) °C	Exotherm onset (sharp) °C
500 – 1000	8/10	2/10	13.1	1.3	202.8	202.5
45 – 125	0/10	10/10	-	1.1	-	200.5

Optical micrographs of the fine and coarse RDX crystals in a contrasting medium are shown in figures 7.16 and 7.17.

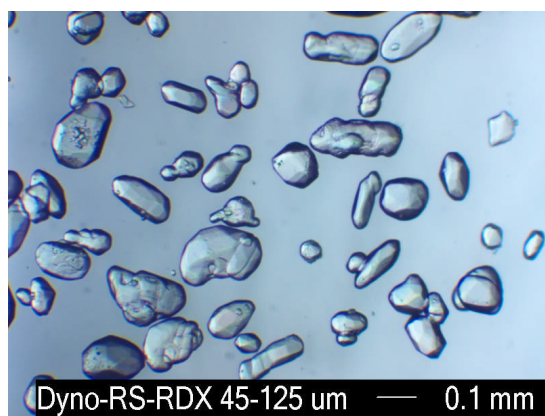


Fig. 7.16 Optical micrograph of RDX crystals from the 45 – 125 μm size fraction of Dyno RS-RDX.

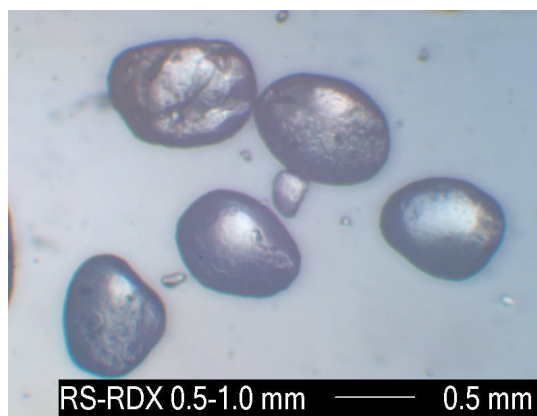


Fig. 7.17 Optical micrograph of RDX crystals from the 500 – 1000 μm size fraction of Dyno RS-RDX.

7.2.5 RDX spiked with HMX in pseudo-PBX formulation

Results from DSC experiments performed on Dyno RS-RDX spiked with HMX in the pseudo-PBX composition are shown in table 7.5. The results shown are averages of the four replicates analysed.

Table 7.5 Melting endotherm data from HMX spiked Dyno RS-RDX samples in the pseudo-PBX composition.

	0 wt% HMX	4 wt% HMX	8 wt% HMX	12 wt% HMX	16 wt% HMX
Mean melting endotherm onset, °C	202.87	202.47	201.44	No peak	No peak
Mean melting endotherm energy, J g ⁻¹	-59.76	-34.61	-15.10	No peak	No peak
Endotherms seen (out of 4 replicates)	4	4	3	0	0

Again, there is an obvious effect on the thermogram with increasing amounts of HMX present. From 0 to 8 wt.% HMX, there is a melting endotherm whose onset and peak temperature are shifted to lower temperatures with increasing HMX content, also there is a large reduction in the mean associated energy. At 12 and 16 wt.% HMX, no endotherms were observed.

7.2.6 Discussion of results from DSC analysis

Thermograms for RS and non-RS RDX samples showed both sharp and broad exothermic decomposition peaks. The reason for the variation of decomposition behaviour was demonstrated to be due to differences in particle size. Pseudo-PBX samples containing particles in the 45-125 µm size range produced sharp exothermic decomposition peaks, indicating a fast rate of combustion. The decomposition of pseudo-PBX samples made with the larger 500-1000 µm crystals, produced much wider decomposition peaks. This indicates a much slower rate of combustion. The effect of particle size on efficiency of heat transfer is shown by the exotherm onset temperatures. For the smaller particles the mean decomposition onset is 200.5°C, for the larger particles though decomposition does not start until 202.5°C (see table 4.3). This shows that the larger crystals have to be raised to a higher temperature to heat the material within them before decomposition can start. These findings are supported by Fathollahi *et al* [159] who observed a reduction of decomposition onset temperature for smaller particles of HMX. They also attributed this to the higher particle surface area, improving the heat absorption of the HMX. The activation energy for decomposition was calculated to be lower for smaller HMX particles. These findings that show particle size is producing the difference in exothermic peak shape, casts some doubt over the method proposed by Spyckerelle [110,117]. This method might

however, provide some indication as to how sensitive a PBX-composition might be, as particle size has an influence on shock sensitivity, as discussed in section 2.3.

The analysis of raw RDX samples in this study has also been able to distinguish between RDX batches with high and low HMX content. RDX lots with high HMX levels show an endotherm peak at around 190°C, arising from the formation of a RDX/HMX eutectic [115]. When HMX was added to RDX, the eutectic endotherm appears and increased in size as the amount of HMX increased. As more HMX was added, a larger eutectic mixture was formed leading to the increased energy observed. The reverse is seen for the second endotherm due to RDX melting. As the proportion of HMX increases, its onset temperature becomes lower and the energy associated with the process smaller. Similar results were obtained by Quintana *et al* [160] who investigated the thermal behaviour of RDX/HMX mixtures using DSC. They also found that as the proportion of HMX increased, the melting endotherm onset was seen earlier and the melting enthalpy was lower. The melting endotherm was attributed to excess RDX not associated with the eutectic. As the proportion of HMX increases there is less excess RDX, so the melting endotherm becomes smaller. These results indicate that DSC is able to detect and possibly give at least a semi-quantitative measure of HMX content in RDX samples. It is not so certain that this method is able to determine RS from non-RS RDX samples.

It was noted that when nitrogen gas flowed through the sample chamber, the maximum of the exothermic peak for all pseudo-PBX samples analysed was shifted to a higher temperature. This was at first thought to be due to the nitrogen gas cooling the samples. Therefore, a higher temperature was reached before decomposition started. However, when an air purge was used there was no significant shift in exotherm peak temperature. This shift is therefore not due to any cooling effects. It is more likely that the nitrogen purge is reducing the amount of oxygen present. Therefore a higher temperature has to be reached before combustion of the PBX can occur. Using a nitrogen purge seems to be able to at least distinguish between samples which contain a high proportion of HMX. Both BAE-OSI Holston and Dyno-Nobel type II RDX which contains a significant proportion of HMX, produced

no endothermic peak, whereas samples which had no or very little HMX content, produced endothermic peaks.

When a low HMX containing RDX was in a pseudo-PBX composition a melting endotherm was seen prior to decomposition during DSC with a nitrogen purge. When a pseudo-PBX formulated with a RDX containing a large amount of HMX was analysed, no endotherm was seen. Pseudo-PBX compositions containing RDX with increasing amounts of added HMX showed that this endotherm was reduced with increasing amount of HMX. With 12 and 16 wt.% HMX present, the melting endotherm was completely absent, the sample therefore behaves like the type II RDX samples. This result is similar to the results from the raw RDX with HMX added samples, although no endotherm peak due to RDX/HMX eutectic formation is present with the PBX samples. This indicates that in the PBX the eutectic is not produced, the presence of HTPB inhibiting its formation.

7.2.7 Conclusions

DSC analysis of RDX indicates the presence and the amount of HMX present. It does not indicate any RS-characteristics itself, instead DSC is detecting the amount of HMX, the presence of which leads to increased sensitivity. DSC could provide a basic indication of sensitivity.

The exotherm decomposition peaks of the RDX/PBX samples could be either sharp or broad for both type I and II RDX batches. The variation is attributed to particle size variation. Some replicate samples containing large RDX crystals produce wide exotherms and smaller crystals produce sharp exothermic peaks.

In summary, DSC could be used to quantitatively assay the amount of RDX/HMX eutectic present, as there seems to be a relationship between the size of the HMX/RDX eutectic endotherm and the amount of HMX in the sample.

7.3 Shock sensitivity testing of loose RDX

Small scale gap tests were performed on loose packed RDX samples. This was to investigate how internal crystal defects, morphology, surface roughness and packing density affect shock sensitivity. To reduce the number of tests required only the RDX samples with significant differences in these characteristics were examined.

7.3.1 Results

Figure 7.18 shows the shock sensitivity results obtained from the five RDX samples tested. The mean gap sizes for the “Go” and “No-Go” response for each sample are given. A larger gap for “Go” and “No-Go” response indicate a more shock sensitive RDX sample.

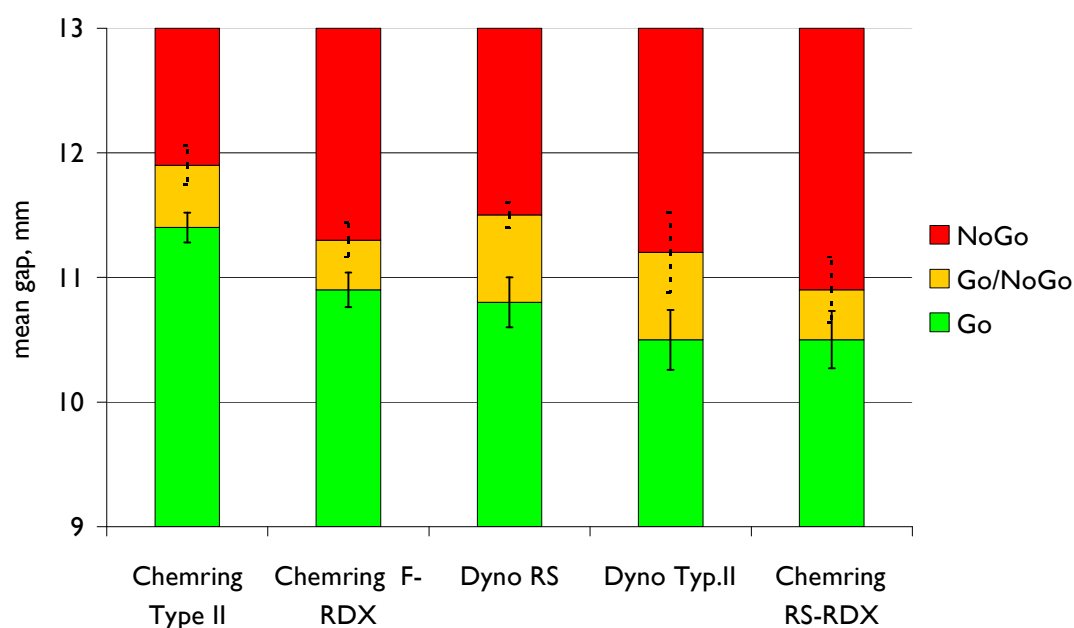


Fig. 7.18 Shock sensitivity results from the small scale gap tests performed, error bars show 95% confidence intervals.

These results show that the Chemring Type II RDX was the most shock sensitive and Chemring RS-RDX the least sensitive. Unexpectedly, given that Dyno RS-RDX has a much smoother morphology and has very few internal defects, it is more sensitive than Dyno Type II. In fact, plotting the mean morphology score per crystal for each of the samples against the mean gap

size for a “Go” shows no correlation (figure A1). There was also very little correlation between the internal defect scores and the gap test results. A somewhat better (although still fairly weak) relationship is seen between the mean surface roughness scores and the sensitivity results. These plots are also shown in appendix A. A good agreement was seen when the mean packing density for each RDX sample was plotted against their shock sensitivities, as shown in figure 7.19. As the mean packing density increased, the shock sensitivity decreased.

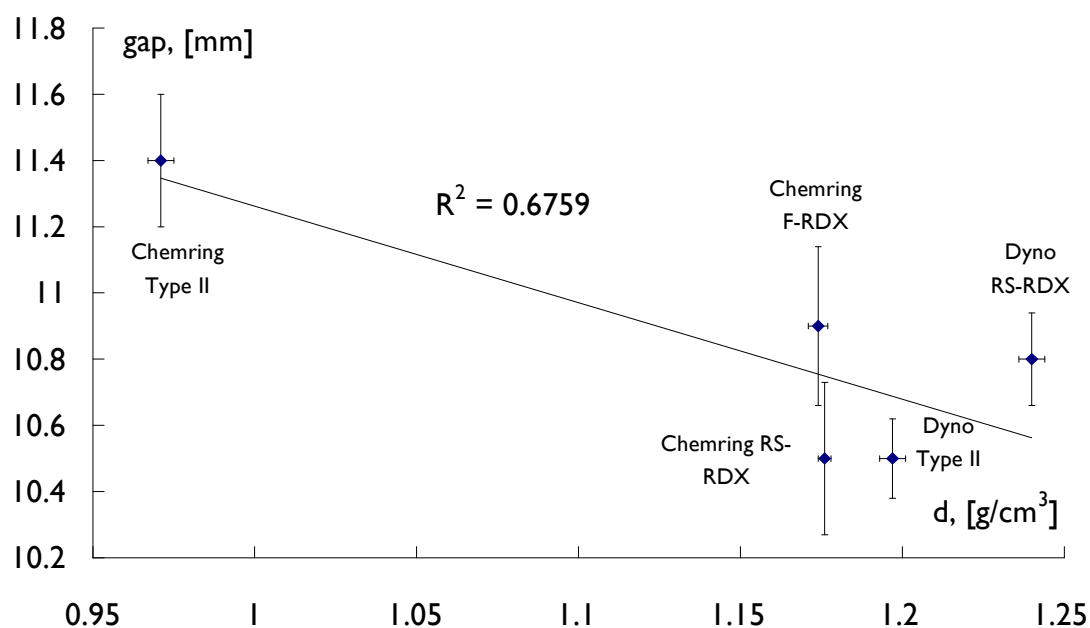


Fig. 7.19 Plot of mean packing density vs. shock sensitivity results from the SSGTs.

7.3.2 Discussion

The results show that, for the samples tested, crystal morphology and internal defects have little or no influence upon RDX shock sensitivity, when in a compacted powder, (see figures 1 and 2 in the appendix). Instead, the packing density has a dominant effect, the shock sensitivity of each sample decreasing as their packing density increases. This suggests that in loose packed RDX powders, intergranular voids are forming hotspots as they are compressed by the shock front passing through them. Also frictional forces between contacting crystals will generate surface hot spots, especially for rough crystals. This can be deduced from the relationship between surface roughness score and the gap test results (figure A3 in the appendix). However, this correlation is only moderate compared to the packing density/shock

sensitivity, which suggests that formation of hot spots by inter-crystal frictional forces is secondary to formation of hot-spots by inter-crystal void compression. RDX samples that have lower packing densities have a larger total intergranular void volume. Therefore, more hotspots can be formed leading to increased shock sensitivity. In a loose packed powder, internal crystal defects are unable to form critical hot spots as efficiently as the air filled intergranular voids. This is because intergranular voids provide more mechanisms for hot spot formation. In addition to void compression, at intergranular voids, crystals impact and grind against each other generating hot spots via frictional forces and plastic deformation. Also, in a packed powder with a large intergranular void volume, thermal conductivity is reduced as there is less contact between crystals. This allows more localisation of heat promoting hot spots [88]. This would explain the lack of correlation between the internal defect score and shock sensitivity. A similar result was seen by Czerski and Proud [82,83], who found that in loose powder charges, internal defects did not contribute to shock sensitivity. Instead, they found that for smaller crystals between 10 and 30 μm , surface defects/roughness was the principle origin for hot spots. Sensitivity in larger crystals (100-300 μm) was seen to be influenced by morphology, angular crystals having a higher sensitivity than smoother crystals. Formation of hot spots was considered to be mostly caused by contact between sharp crystal corners, leading to viscoplastic heating. Frictional forces were thought to be less important as the melting point of RDX is below its decomposition temperature, any hot spots being formed would be quenched before reaching ignition temperature. In contrast, in a PBX composition internal defects become dominant over intergranular voids [60-63,65]. In a formulated explosive, the binder fills the intergranular spaces reducing the total void volume that can produce hotspots, thereby permitting internal defects to become the dominant mechanism of ignition. The absence (or low) intergranular void volume in a PBX would also allow crystal morphology to have a greater effect compared to when in a loose packed powder charge.

7.3.3 Conclusions

The shock sensitivity of RDX packed powders and RDX in a PBX composition is influenced by different factors. In a packed powder, sensitivity is controlled predominantly by intergranular voids as a source of hotspot formation. At Intergranular voids there are more ways that hot spots can be generated as well as compression, friction and plastic deformation also occur, therefore enhancing sensitivity.

In a PBX, intergranular voids are eliminated so internal defects and crystal morphology become important in determining shock sensitivity. Therefore, to obtain a clear understanding of how crystal parameters such as internal defects and morphology have on sensitivity, it would be advantageous to perform gap tests on PBX compositions rather than loose packed powders. Further shock sensitivity testing was not done on loose packed powders as it was considered that the results would be predominantly influenced by packing density, masking the contribution of internal defects and crystal morphology.

CHAPTER 8

Final conclusions and recommendations

8.1 Final conclusions

This thesis has developed two novel diagnostic techniques that are an advancement upon current methods [148] used to determine the quantity of internal defects and crystal morphology. Nanoindentation has shown that the quantity of internal defects is strongly linked to RDX mechanical properties and shock sensitivity. The rheological properties of RDX suspensions have been demonstrated to be correlated well to crystal morphology and shock sensitivity. These findings are supported by data from the literature which indicates that shock sensitivity increases as the number of internal defects increases [59-65,70,72] and crystal morphology becomes rougher/angular [66,67,84,89]. With further studies to validate these methods, they may be proven as suitable testing techniques for a revised STANAG.

The results obtained from this study and from previous investigations discussed in the literature review have shown that the shock sensitivity of RDX is dependent upon the influence of many interacting factors as follows:

- Crystal size:

In monomodal compositions; larger crystals are more sensitive at lower shock pressures. With increasing shock pressure smaller crystals show increased sensitivity. For example, the study by Moulard [93] showed that large crystals (428 μm) were most sensitive at shock pressures of 4.4 GPa whereas at 12 GPa fine crystals (6 μm) were most sensitive.

In bimodal compositions; Keeping the relative sizes of the small crystals and large crystals unchanged but increasing the proportion of smaller crystals, increases the shock sensitivity. Shock sensitivity is also increased by reducing the size of the smaller crystals whilst maintaining the proportion of small and large crystals.

Two stage initiation process; The shock to detonation process is controlled by initial formation of hot spots by the shock wave and then growth of the reaction front by hot spot coalescence [94]. Hot spots formed within larger crystals are more efficient in initiating a reaction as they have a larger surrounding volume of material to dissipate heat into. Once the reaction has started, smaller crystals are more efficient in propagation and growth of the reaction front due to their combined high surface area.

Analysis by DSC has shown that thermal decomposition behaviour is affected by crystal size. Smaller crystals decompose faster and at a lower temperature than larger crystals, again due to their larger combined surface area.

- **Crystal morphology:**

Morphology is strongly influenced by the method of production (Woolwich or Bachmann process), solvent used for crystallisation (cyclohexanone, acetone or γ -butyrolactone) and the crystallisation process. Crystals that have an angular/rough morphology tend to have increased sensitivity compared to smooth/rounded crystals. Increased sensitivity is due to friction between angular crystals, also, facet edges and tips promote shock focusing leading to hot spot formation. During PBX formulation the binder may not coat rougher crystals completely producing air gaps between the binder and RDX crystals which can be compressed forming hot spots.

The optical microscopy method was able to distinguish between RDX made by different processes but suffered from being very subjective. Measuring the rheological properties of RDX suspensions was shown to provide an objective method for determining morphology. Rheological analysis will provide a suitable alternative procedure in the future.

- **Internal defects:**

Internal defects form during crystallisation due to presence of impurities and crystal lattice defects. Internal defects become hot spots

as they are collapsed by a shock wave due to adiabatic heating of trapped air/crystallisation solvent. Jetting across voids can also occur, the impact of the jet upon the void wall causing further heating [34,35]. Shock sensitivity is enhanced as amount of defects increases. Defect size is also an important factor determining shock sensitivity. Larger defects are more compressible than smaller defects and are more efficient in forming hot spots at low shock pressures. At higher pressures, small defects become predominant over large defects [59,61]. Therefore the overall sensitivity is influenced by the size range and size distribution of internal defects within the crystals.

The optical microscopy and scoring method to quantify internal defects was able to discriminate between Bachmann and Woolwich RDX. This technique is, however, time consuming and suffers from operator subjectivity. Using nanoindentation to measure the mechanical properties of RDX crystals provides an empirical test to determine defect content. Nanoindentation should be a suitable alternative method for determining RDX crystal quality.

- Surface defects:

Surface roughness is linked to the method of production. RDX crystals produced by the Bachmann process tend to be rougher than those made by the Woolwich process. RDX produced by the Bachmann process contains more impurities, which when incorporated within the RDX crystal (co-crystallisation) causes disruption of crystal structure. This can produce a rough crystal surface. Cracks, holes and general surface roughness cause increased sensitisation by the formation of frictional hot spots. General surface roughness is better correlated to sensitivity than the number of holes or cracks. The SEM method and scoring system used to quantify the amount of surface defects is very subjective.

- HMX content:

In smaller amounts (less than approximately 1 to 4 wt.% [109,110]) HMX as a bi-product does not have a significant effect on sensitivity. Under this circumstance morphology and defects have a greater influence. At higher quantities it increases sensitivity. Co-crystallised HMX within RDX crystals may also be sensitising as the HMX inclusions strain and distort the crystal structure [112]. HMX inclusions can therefore promote the formation of internal defects.

DSC analysis showed that the amount of HMX present in a RDX sample was negatively correlated to the melting endotherm onset temperature and associated energy. DSC can, therefore, potentially be used as another method to determine the amount of HMX present within a RDX sample. DSC though cannot give a definitive indication of sensitivity as other factors are involved as well as HMX content.

In summary, this work has shown that RDX shock sensitivity is controlled by a combination of factors and these are influenced by the production process and recrystallisation method employed. In a PBX, internal crystal defects are probably the most dominant factor in influencing shock sensitivity. Crystal morphology has also a strong influence, angular/faceted crystals enhancing sensitivity due to shock focusing effects [90]. Surface roughness is less significant as the binder will prevent/reduce contact between crystals therefore limiting hot spot formation by frictional forces. Although rough crystals may not be coated as efficiently as smoother crystals, leading to voids being formed between the binder and crystal surface. These voids can form hot spots and increase sensitivity. HMX content only has a sensitising effect when present in larger quantities as found in non-recrystallised type II RDX.

8.2 Recommendations

Results obtained during this work have all been compared to the shock sensitivity data obtained from the R⁴ programme which used the complex PBXN-109 formulation. It would be useful to obtain new gap test data for the samples tested using a simplified “pseudo-PBX” perhaps one using only PEG

as used in the rheology experiments. This would remove any confounding factors that might be present with PBXN-109 and allow a clearer understanding of how different crystal properties affect shock sensitivity. Ionisation probes could also be inserted into the acceptor charge to investigate the shock wave behaviour through the sample. This would provide information such as run-to-detonation distance, shock wave peak pressure and shock wave duration rather than just a GO or NO-GO result.

Since shock sensitivity is determined by a combination of factors, there are some issues with the R⁴ samples. For instance, Dyno Type II has crystals that contain many defects *and* also have a very angular morphology. It would be a useful exercise to perform shock sensitivity tests on different RDX samples that have different quantities of internal defects but very similar morphology (preferably smooth), or samples with a range of morphologies with similar quantities of defects (preferably few defects). This would separate the effects of morphology and internal defect quantity and give a better indication of how these characteristics influence sensitivity.

Recrystallisation experiments could be performed, perhaps using different rates of cooling to obtain samples with different morphologies and internal defect content. Holston RDX would be a good sample to re-crystallise as its crystals contain a large number of defects. Nano-indentation could be performed on the re-crystallised materials to see if any change in mechanical properties has occurred due to the different crystallisation methods.

Further experiments investigating nanoindentation should be undertaken to verify that measuring the micromechanical properties of RDX crystals is a reliable testing method. This could be done using a different set of samples to the R⁴ lots, thereby giving an indication of the reproducibility/repeatability of the technique.

Appendix A

Extra data from loose powder gap tests

The following figures show the plots of the gap test results from chapter 7 against the mean morphology, internal defect and surface defect scores.

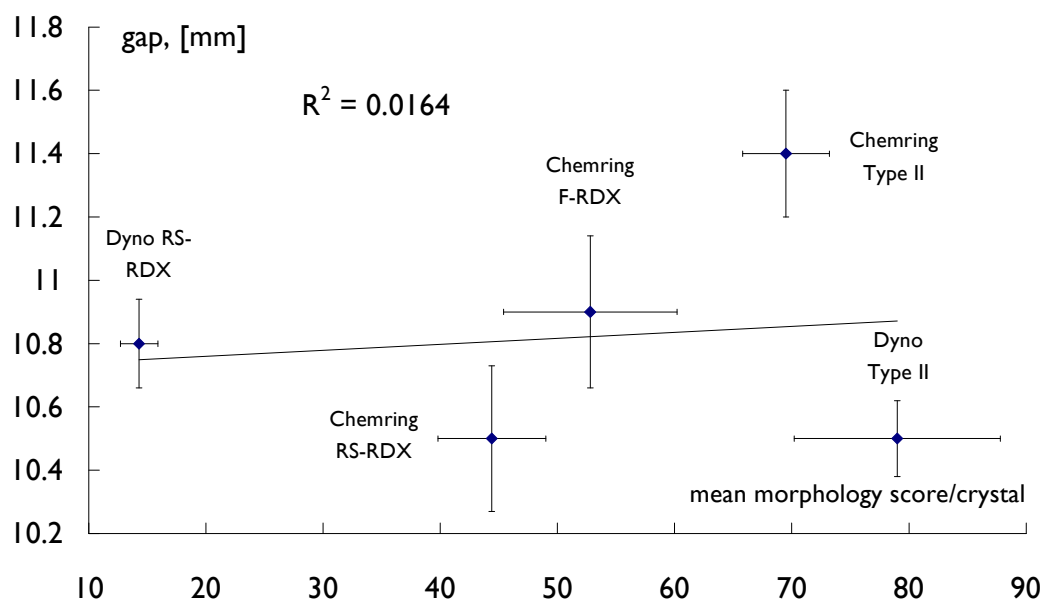


Fig. A1 Plot of mean morphology score per crystal vs. shock sensitivity results from the SSGTs.

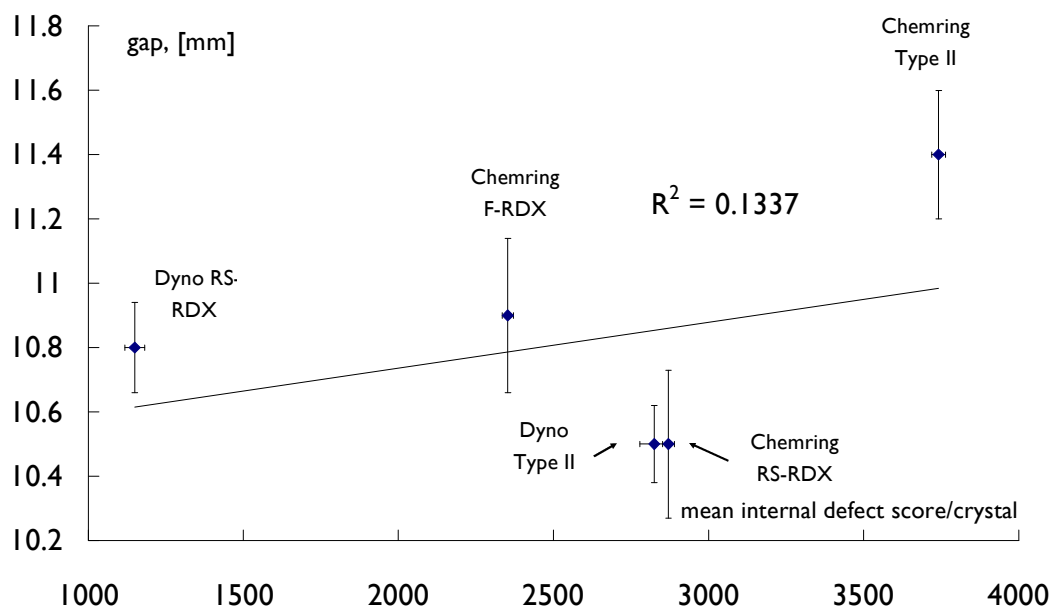


Fig A2 Plot of mean internal defect score per crystal vs. shock sensitivity results from the SSGTs.

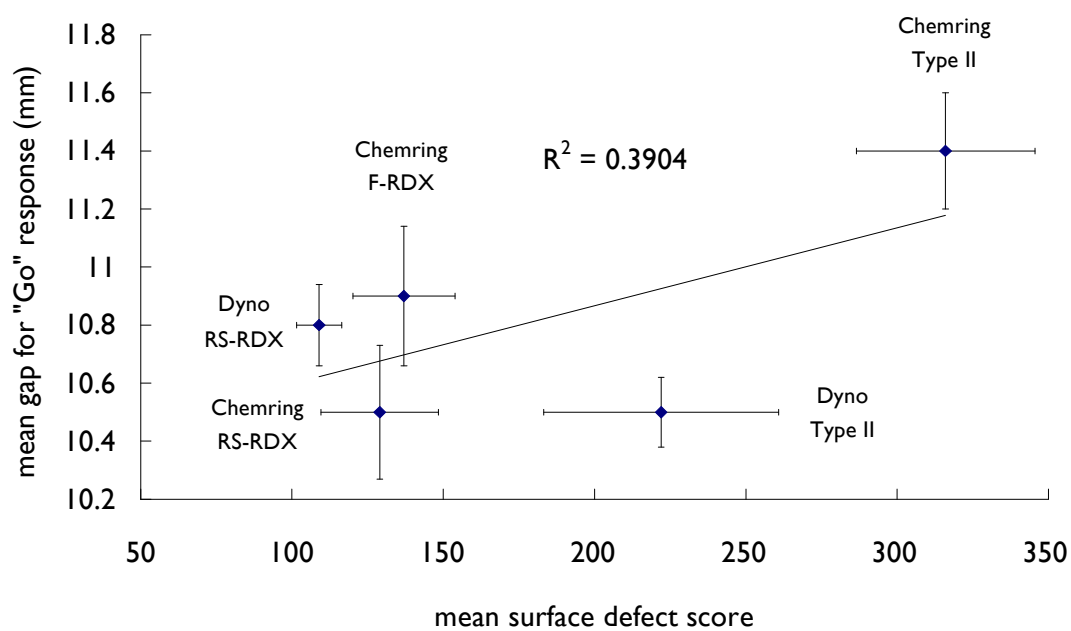


Fig. A3 Plot of mean surface defect score per crystal vs. shock sensitivity results from the SSGTs.

Appendix B

Extra data from nanoindentation experiments

The following plots show how pop-in behaviour (plastic deformation) is linked to shock sensitivity. The dependence of defect size and quantity upon pop-in is also illustrated. All pop-in data is from indentation measurements at a loading rate of 400 mN/min, with a maximum load of 200 mN.

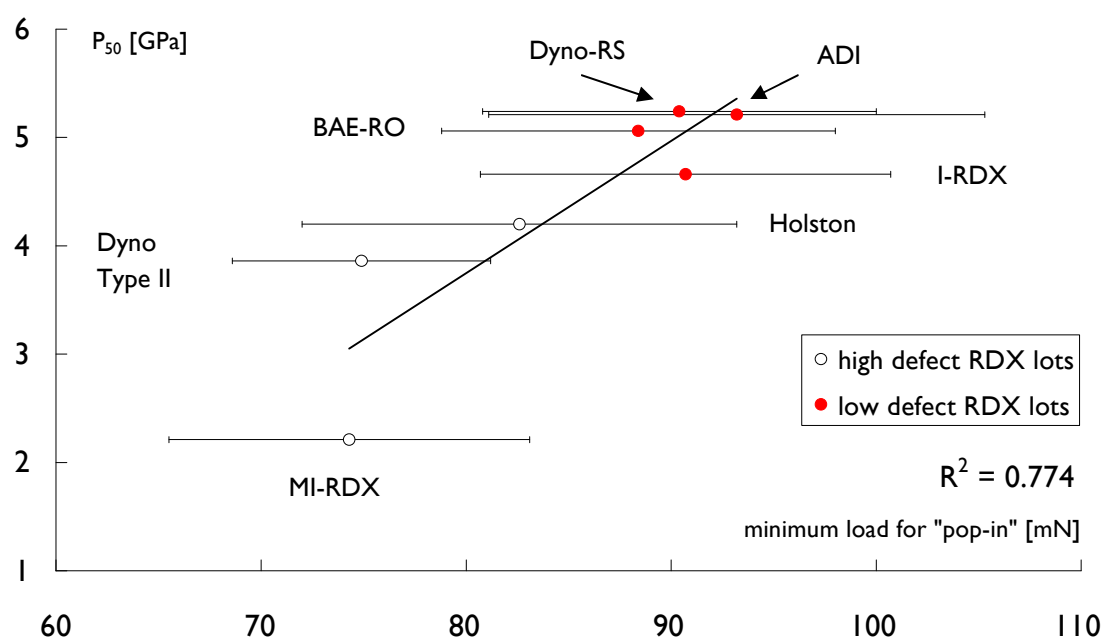


Fig. B1 Plot of minimum load required for pop-in to occur versus the shock sensitivity (LSGT) results from the R^4 study. Error bars give 95% confidence intervals of the mean load required for pop-in.

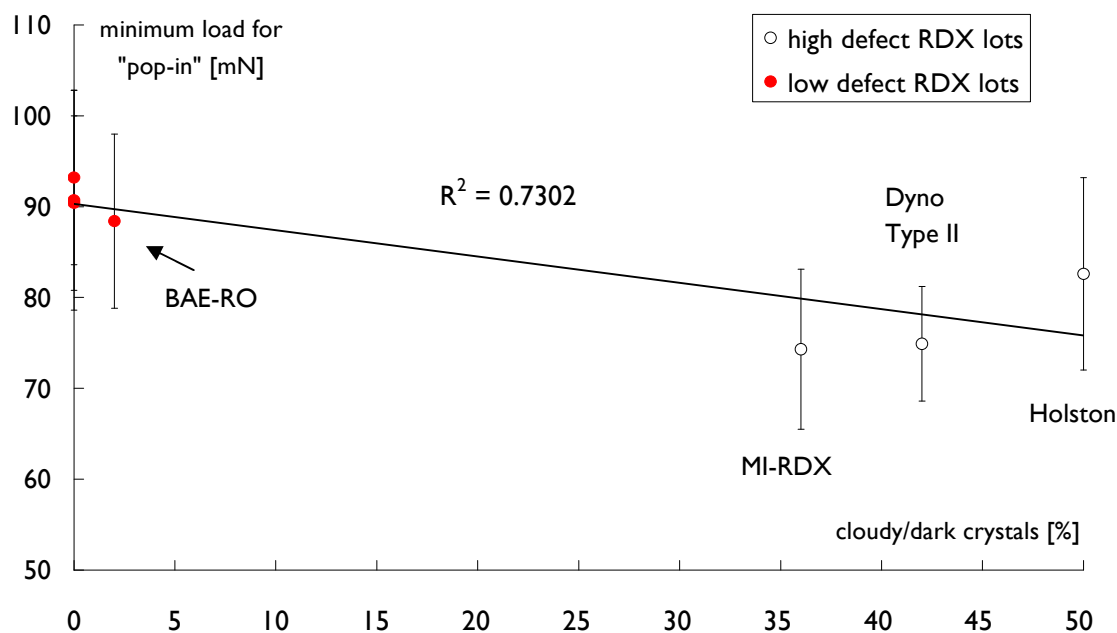


Fig. B2 Plot of fraction of dark/cloudy crystals versus minimum load for pop-in. Error bars give 95% confidence intervals of the mean load required for pop-in. ADI, I-RDX and Dyno RS-RDX had no cloudy/dark crystals, c.f. fig. 5.6.

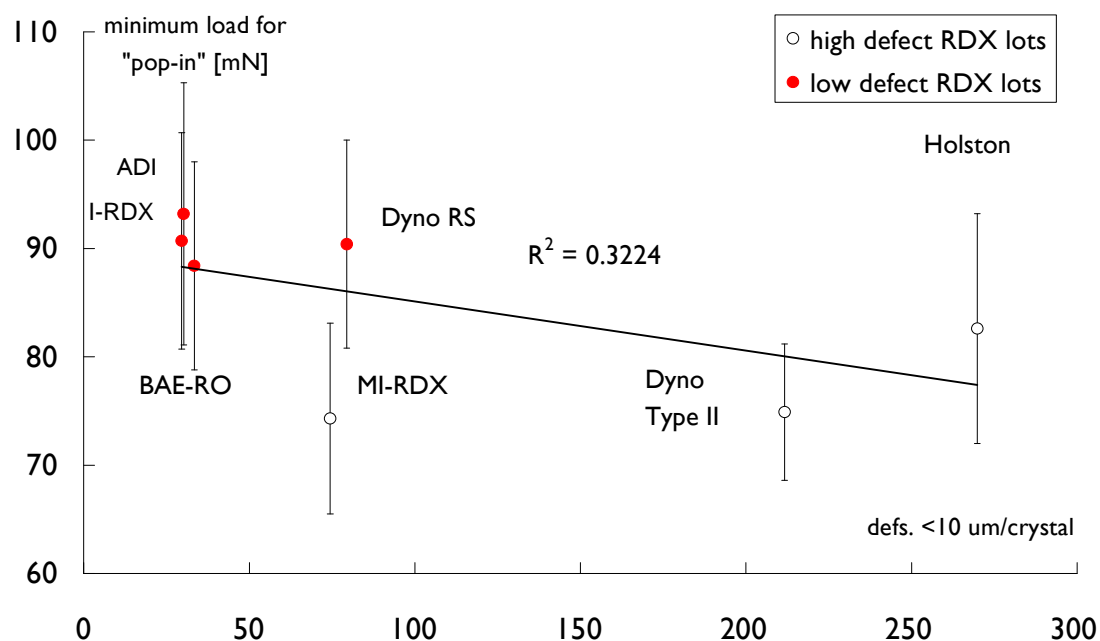


Fig. B3 Plot of mean number of internal defects less than 10 μm in size per crystal versus minimum load for pop-in. Error bars give 95% confidence intervals of the mean load required for pop-in.

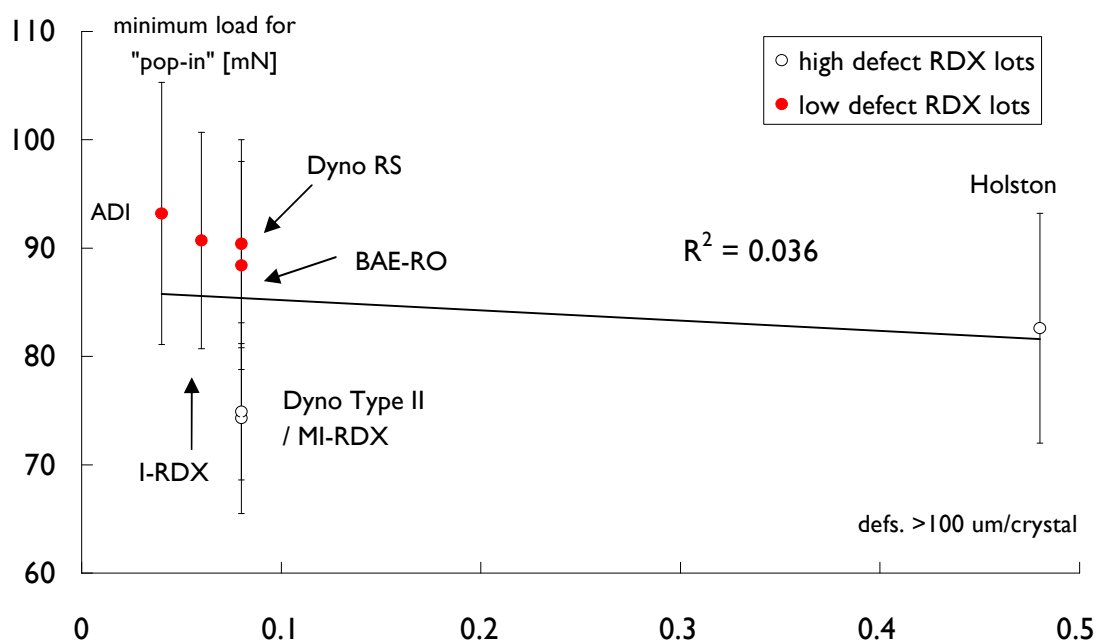


Fig. B4 Plot of mean number of internal defects greater than 100 μm per crystal versus minimum load for pop-in. Error bars give 95% confidence intervals of the mean.

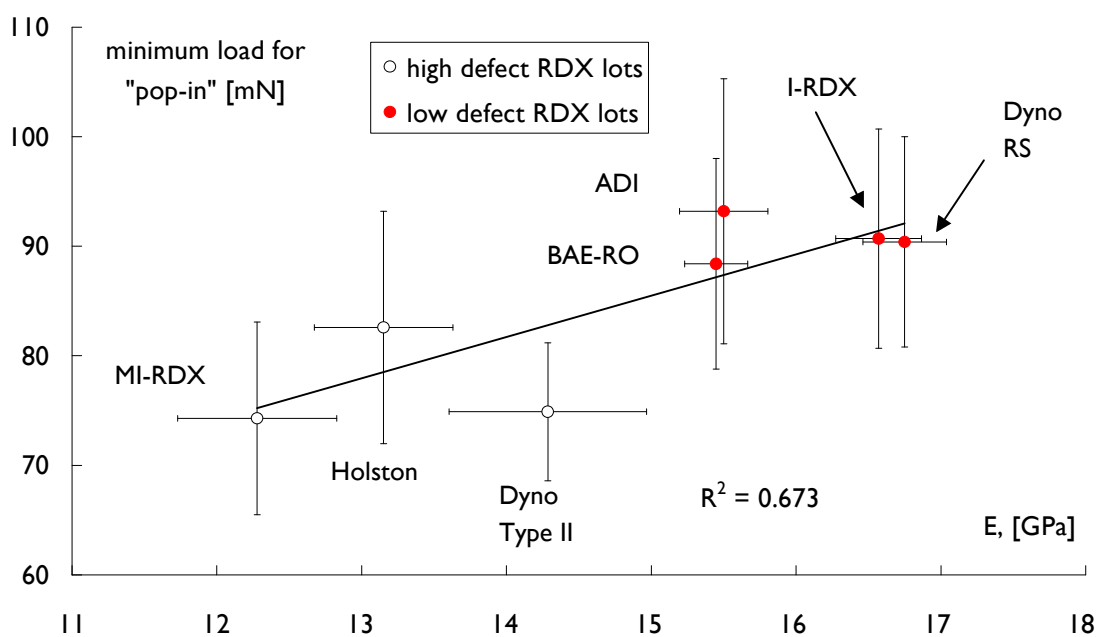


Fig. B5 Plot of mean elasticity of the RDX samples against the mean minimum load required for pop-in. Error bars give 95% confidence intervals of the mean.

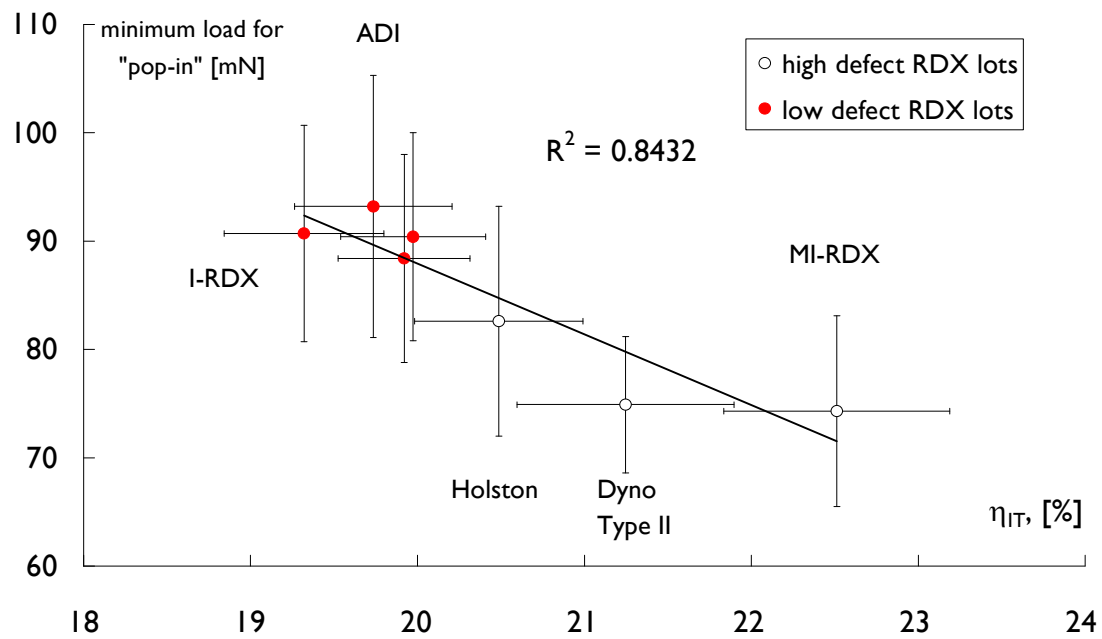


Fig. B6 Plot of proportion of elastic work against the mean minimum load required for pop-in. Error bars give 95% confidence intervals of the mean.

Appendix C

Angle of repose measurements

The angle of repose is the maximum angle reached between the slope of a conical pile of granular material and the surface on which it rests. Granular materials which have more jagged particles can form a pile with steeper sides (higher angle of repose) than materials with smoother particles. It therefore can provide a quantitative measure of particle morphology.

The angle of repose of the RDX samples that were tested in the loose powder gap test (section 7.3), was measured. This was carried out by pouring RDX through a funnel onto a flat plastic surface. When the pile reached the maximum slope angle before slipping of material occurred, a photograph of the pile was taken. The angle of repose was then found by measuring the height and base width of the pile from the photograph, figure C1. For each RDX sample, 7-12 replicate measurements were taken.

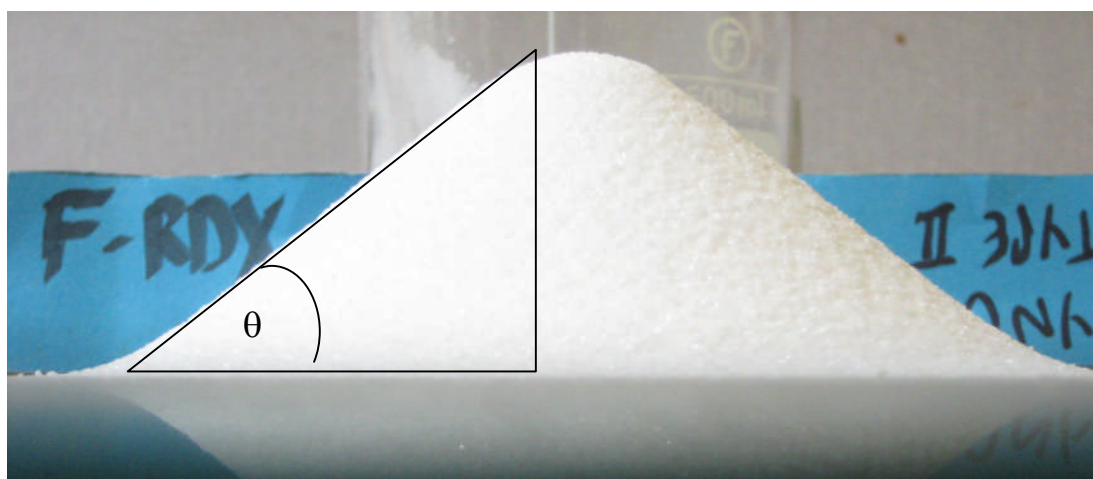


Fig. C1 Measurement of the angle of repose, θ of a conical pile of RDX.

It was found that the mean angle of repose for the samples did not have any correlation with the morphology scores obtained from the optical microscopy study, figure C2. This therefore indicates that measuring the angle of repose does not provide a useful indication of the morphology of the RDX samples being tested here.

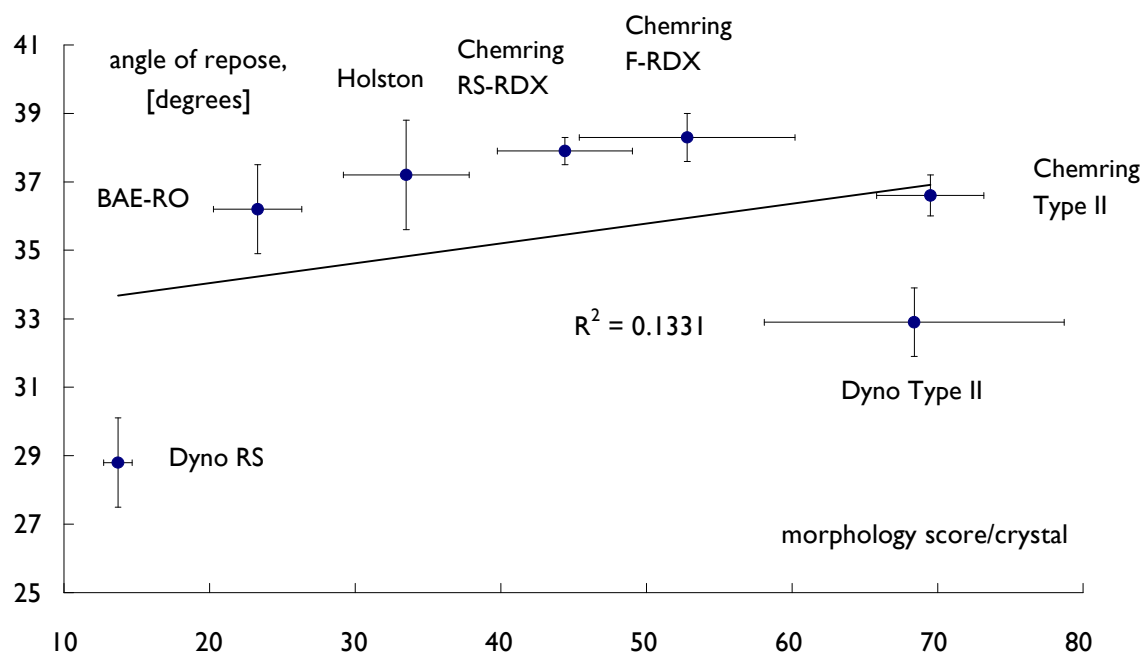


Fig. C2 Plot of mean morphology score against mean angle of repose. Error bars give the 95% confidence intervals.

The surface roughness of particles can also influence the angle of repose. However, plotting the surface defect score against the angle of repose for the samples tested, again showed no correlation, figure C3.

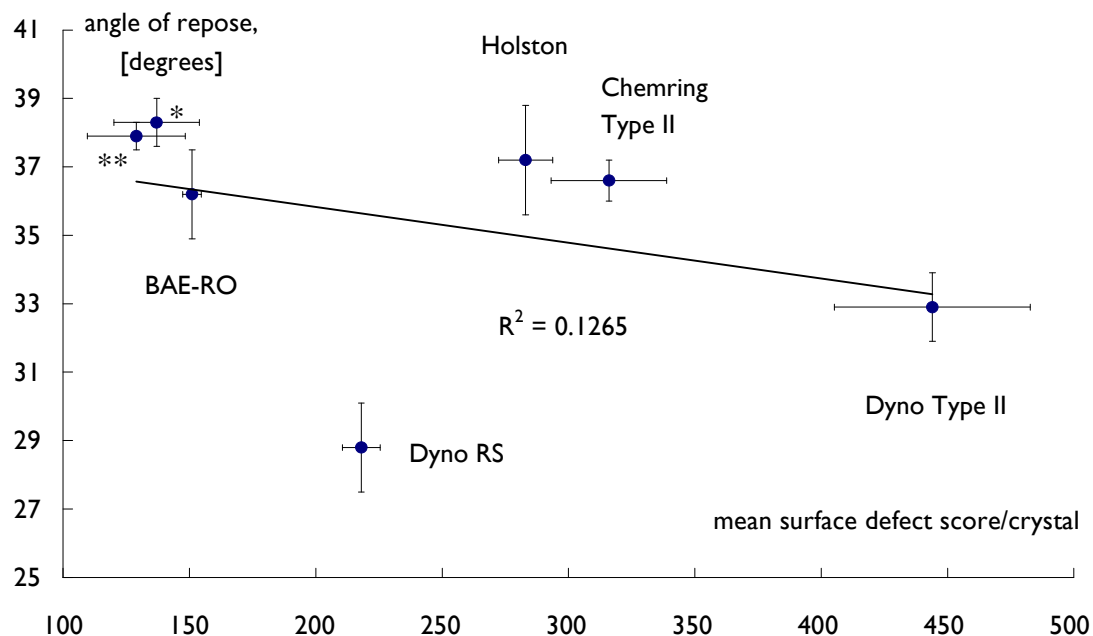


Fig. C3 Plot of mean surface defect score against mean angle of repose. Error bars give the 95% confidence intervals. * Chemring F-RDX, ** Chemring RS-RDX.

Finally, the shock sensitivity results from the loose powder gap tests are plotted against the angle of repose (figure C4), as with the morphology and surface defect scores, there was no correlation. Czerski *et al* [161] also found no relationship between their shock sensitivity results from loose packed RDX and the angle of repose.

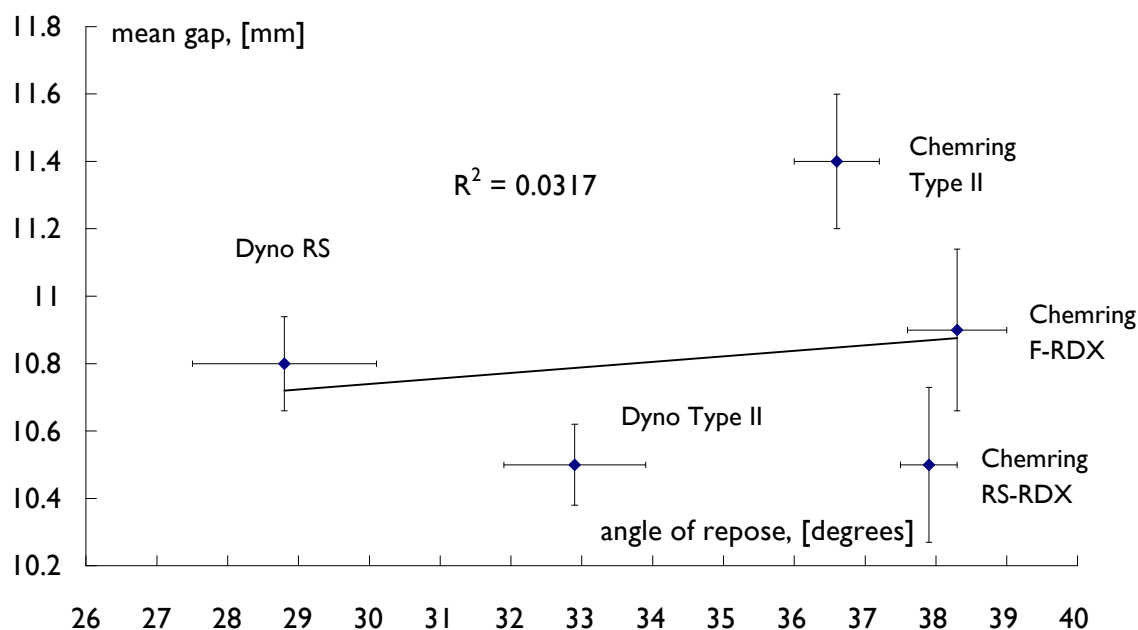


Fig. C4 Plot of angle of repose against the shock sensitivity from the loose powder gap tests. Error bars give the 95% confidence intervals.

In conclusion, measuring the angle of repose does not seem to provide any indication about RDX crystal morphology or shock sensitivity.

References

1. A. Bailey, S.G. Murray Explosives, Propellants and Pyrotechnics p. 34, Vol. 2, Brassey's, London and Oxford, **(1989)**.
2. T. Urbanski Chemistry and Technology of Explosives, Vol. 3, p. 77, Pergamon Press, Oxford, **(1988)**.
3. D. I. A. Millar, I. D. H Oswald, D. J. Francis, W. G. Marshall, C. R. Pulham, A. S. Cumming. *Chemical Communications* **(2009)**, p. 562-564.
4. J Akhavan The Chemistry of Explosives, p. 63, RSC Paperbacks, Cambridge, **(1998)**.
5. *Ibid.* Reference #4, p. 39.
6. *Ibid.* Reference #1 p. 15.
7. *Ibid.* Reference #1 p. 19.
8. G. F. Henning, German patent 104280, **(1899)**.
9. G. C. V. Herz, British patent 145793, (1921), U. S. patent 1402693 **(1922)**.
10. *Ibid.* Reference #4 p. 10.
11. J. Yinon, S. Zitrin. Modern Methods and Applications in Analysis of Explosives. p.6, Wiley, U.K. **(1993)**.
12. W. E. Bachmann, J. C. Sheehan. *Journal of the American Chemical Society*. **(1949)**, vol. 71, p. 1842-1845.
13. NATO, Explosives specification for RDX (Hexogene), STANAG 4022, draft 6 edition 4.
14. Detail Specification – RDX (Cyclotrimethylenetrinitramine), MIL-DTL 398D, Dec. 1966.
15. *Ibid.* Reference #2 p. 88.
16. A. H. Vroom, C. A. Winkler. *Canadian Journal of Research*. **(1950)**, vol. 28 B, p. 701
17. J. Vaughan, L. Phillips, *Journal of the Chemical Society*. **(1949)**, p. 2741.
18. A. H. Lamberton, *Quarterly Review*. **(1951)**, vol. 5, p. 75.
19. G. F. Wright, *Gilman's Organic Chemistry*. Vol. 4, p. 983, Wiley, New York, **(1953)**.

-
20. W. J. Chute, D. C. Downing, A. F. McKay, G. S. Myers, G. F. Wright. *Canadian. Journal of Research*. **(1949)**, vol. 27 B, p. 218.
21. K. Singh, *J. Sci. Ind. Research (India)*, **(1956)**, vol. A 15, p. 450.
22. A. E. D. M. van der Heijden, R. H. Bouma. *Crystal Growth and Design*, **(2004)**, vol. 4, p. 999-1007.
23. A. E. D. M. van der Heijden, Y. L. M. Creighton, E. Marino, R. H. Bouma, G. J. H. G. Scholtes, W. Duvalois. *Propellants Explosives Pyrotechnics*, **(2008)**, vol. 33, p. 25-32.
24. R. M. Doherty, D. S. Watt. *Propellants Explosives and Pyrotechnics*, **(2008)**, vol. 33, p. 4-13.
25. *Ibid.* Reference #2, p. 113.
26. J. H. ter Horst, R. M. Geertman, A. E. van der Heijden, G. M. van Rosmalen. *Journal of Crystal Growth*, **(1999)**, vol. 198, p. 773-779.
27. J. H. ter Horst, R. M. Geertman, A. E. van der Heijden, G. M. van Rosmalen *Proceedings of the 27th annual International Conference of the ICT*, **(1996)**, p. 126(1)-126(13).
28. J. E. Field, *Acc. Chem. Res.* **(1992)**, vol. 25. p. 489-496.
29. J. E. Field, N. K. Bourne, S. J. P. Palmer, S. M. Walley. *Phil. Trans. Royal Society of London A*. **(1992)**, vol. 339, p. 269-283.
30. S. M. Walley, J. E. Field, M. W. Greenaway. *Materials Science and Technology*. **(2006)**, vol. 22, p. 402-413.
31. F. W. Bowden, Y. D. Yoffe. *Initiation and growth of explosion in liquids and solids*. **(1952)**, Cambridge, Cambridge University Press.
32. K. Yano, Y. Horie, D. Greening. *Impact Engineering and Application*. **(2001)**, p. 201-206.
33. J. E. Field, *hot spot ignition of explosives*. Presentation, Fracture group, Cavendish Laboratory, Cambridge.
34. M. M. Chaudhri, J. E. Field. *Proceedings Royal Society London, A*. **(1974)**, vol. 340, p. 113-128.
35. N. K. Bourne, J. E. Field. *Proceedings Royal Society London, A*. **(1991)**, vol. 435, p. 423-435.
36. J. P. Dear, J. E. Field. *Journal of Fluid Mechanics*. **(1988)**, vol. 190, p. 409-425.

-
37. J. P. Dear, J. E. Field, A. J. Walton. *Nature*. **(1988)**, vol. 332, p. 505-508.
38. M. M. Chaudhri. *Nature*. **(1976)**, vol. 263, p. 121-122.
39. R. E. Winter, J. E. Field. *Proceedings Royal Society London, A*. **(1975)**, vol. 343, p. 399-413.
40. J. E. Field, M. A. Parry, S. J. P. Palmer, J. H. Huntley. *Proceeding of the 9th Symposium (International) on Detonation*. **(1989)**, p. 886.
41. K. N. G. Fuller, P. G. Fox, J. E. Field. *Proceedings Royal Society London, A*. **(1975)**, vol. 341, p. 537-557.
42. P. G. Fox, J. Soria-Ruiz. *Proceedings Royal Society London, A*. **(1970)**, vol. 317, p. 79-90.
43. M. M. Chaudhri, *Combustion and Flame*. **(1972)**, vol. 19, p. 419-425.
44. M. M. Chaudhri, *Proceeding of the 9th Symposium (International) on Detonation*. **(1989)**, p. 857.
51. F. G. Katsamanis, C. G. Delides. *Journal of Physics D: Applied Physics*. **(1988)**, vol 21, p. 79-86.
46. J. E. Field, G. M. Swallowe, S. N. Heavens. *Proceedings Royal Society London, A*. **(1982)**, vol. 382, p. 231-244.
47. C. S. Coffey. *Physical Review B*. **(1981)**, vol. 24, p. 6984-6990.
48. V. Krishna-Mohan, J. E. Field, G. M. Swallowe. *Proceeding of the 9th Symposium (International) on Detonation*. **(1989)**, p. 1276.
49. *Ibid.* Reference #1, p. 21-25.
50. *Ibid.* Reference #4, p. 44-55.
51. <http://www.cordin.com/images.html>, 20th May 2009. Naval Air Weapons Centre, China Lake, USA.
- 52 J. H. ter Horst, R. M. Geertman, A. E. van der Heijden, G. M. van Rosmalen. *Proceedings of the 30th annual International Conference of the ICT*, **(1999)**, p. 42(1)-42(15).
53. J. Garside, M. A. Larson. *Journal of Crystal Growth*. **(1978)**, vol. 43, p. 694-704.
54. H. Miki, T. Terashima, Y. Asakuma, K. Maeda, K. Fukui. *Separation and Purification Technology*. **(2005)**, vol. 43, p. 71-76.
55. N. Saito, M. Yokota, T. Fujiwara, N. Kubota. *Chemical Engineering Journal*. **(2001)**, vol. 84, p. 573-575.

-
56. K. A. Gross. *Journal of Crystal Growth*. **(1970)**, vol. 6, p. 210-212.
57. S. Amelinckx, W. Maenhout-Van der Vorst, W. Dekeyser. *Acta Metallurgica*. **(1959)**, vol. 7, p. 8-17.
58. J-W. Kim, J-K. Kim, H-S. Kim, K. K. Koo. *Proceedings of the 12th seminar of New Trends in Research of Energetic Materials, Czech Republic*, **(2009)**, p. 575-578.
59. I. B. Mishra, L. J. Vande-Kieft. *Proceedings of the 19th International Conference of the ICT*. **(1988)**, p. 25/1-25/21.
60. F. Balliou, J. M. Dartyge, C. Spyckerelle, J. Mala. *Proceedings of the 10th International Symposium on Detonation*. **(1993)**, p. 816-823.
61. L. Borne. *Proceedings of the 10th International Symposium on Detonation*. **(1993)**, p. 286-293.
62. L. Borne. *Proceedings of the 11th International Symposium on Detonation*. **(1998)**, p. 657-663.
63. L. Borne, A. Beaucamp. *Proceedings of the 12th International Detonation Symposium*. **(2002)**. p. 35.
64. L. Borne, J-C. Patedoye, C. Spykerelle. *Propellants, Explosives, Pyrotechnics*. **(1999)**, vol. 24, p. 255-259.
65. L. Borne, J. Mory, F. Schlessier. *Propellants, Explosives, Pyrotechnics*. **(2008)**, vol. 33(1), p. 37-43.
66. A. C. van der Steen, H. J. Verbeek, J. J. Meulenbrugge. *Proceedings of the 9th International Symposium on Detonation*. **(1989)**, p. 83-88.
67. N. H. A. van Ham, A. C. van der Steen, J. J. Meulenbrugge. *AGARD Conference Proceedings*. **(1991)**, p. 9/1-9/7.
68. L. N. Erofeev, Yu. P. Tarasov, Yu. B. Kalmykov, Y. Shu, V. V. Dubikhin, G. M. Nazin. *Russian Chemical Bulletin, International Edition*. **(2001)**, vol. 50. No. 6, p. 1000-1002.
69. M. L. Buess, S. M. Caulder. *Applied Magnetic Resonance*. **(2004)**, vol. 25, p. 383-393.
70. M. L. Buess, S. M. Caulder, A. N. Garroway, P. J. Miller. *Proceedings of the 8th International Pyrotechnical Congress*, **(2003)**, p. 29-35.
71. J. T. Mang, C. B. Skidmore, P. M. Howe, R. P. Hjelm, T. P. Rieker. *Shock Compression of Condensed Matter*. **(1999)**, p. 699-702.

-
72. C. A. Stoltz, B. P. Mason, J. Hooper. *Journal of Applied Physics*. **(2010)**, vol.107, p. 103527/1- 103527/6.
73. J-W. Kim, J-K. Kim, H-S. Kim, K-K. Koo. *Crystal Growth and Design*. **(2009)**, vol. 9(6), p. 2700-2706.
74. D-Y. Kim K-J. Kim. *Chemical Engineering Research and Design*. **(2010)**, vol. 88, p. 1461-1466.
75. C. W. Roberts, S. M. Hira, B. P. Mason, G. F. Strouse, C. A. Stoltz. *Crystal Engineering Communications*. **(2011)**, vol. 13, p. 1074-1076.
76. R. H. B. Bouma, A. G. Boluijt, H. J. Verbeek, A. E. van der Heijden. *Journal of Applied Physics*. **(2008)**, vol. 103, p. 093517.
77. A. E. van der Heijden, Y. L. M. Creighton, E. Marino, R. H. B. Bouma, G. J. H. G. Scholtes, W. Duvalois, M. C. P. M. Rowlands. *Propellants, Explosives, Pyrotechnics*. **(2008)**, vol. 33(1), p. 25-32.
78. L. Ming, H. Ming, K. Bin, W. Maoping, L. Hongzhen, X. Rong. *Propellants, Explosives, Pyrotechnics*. **(2007)**, vol. 32(5), p. 401-405.
79. X. Yang, T. Zhou, C. Chen. *Computational Materials Science*, **(2007)**, vol. 40, p. 51-56.
80. J. T. Hagan, M. M. Chaudhri. *Journal of Materials Science*. **(1977)**, vol. 12, p. 1055-1058.
81. M. Li, W-J. Tan, B. Kang, R-J. Xu, W. Tang. *Propellants, Explosives, Pyrotechnics*. **(2010)**, vol. 35, p. 379-383.
82. H Czerski, W. G. Proud. *Journal of Applied Physics*. **(2007)**, vol. 102, p. 113515/1-113515/8.
83. H. Czerski, M. W. Greenaway, W.G. Proud J. E. Field, *Shock Compression of Condensed Matter*, **(2005)**, p. 1053-1056.
84. S. Matsuzaki, E. Yano, S. Suzuki, Y. Suzuki, T. Hasegawa, Y. Kato. *Proceedings of the 38th annual International Conference of the ICT*. **(2007)**, p. 130/1-130/10.
85. S. Lecume, C. Boutry, C. Spyckerelle. *Proceedings of the 35th International Conference of the ICT*. **(2004)**, p. 2/1-2/14.
86. V. J. Bellitto. M. I. Melnik. *Applied Surface Science*. **(2010)**, vol. 256, p. 3478-3481.

-
- 87.** V. J. Bellitto, M. I. Melnik. *Journal of Thermal Analytical Calorimetry*. **(2010)**, vol. 102, p. 557-562.
- 88.** X. Song, F. Li, Y. Wang, C. An, J. Wang, J. Zhang. *Journal of Energetic Materials*. **(2012)**, vol. 30, p. 1-29.
- 89.** K. Min-Jun, J. Won-Bok, C. Joo-Seung. *Proceedings of the 14th seminar of New Trends in Research of Energetic Materials, Czech Republic*, **(2011)**, part II, p. 718-722.
- 90.** Y. Shi, D. W. Brenner. *Journal of Physical Chemistry B*. **(2008)**, vol. 112, p. 14898-14904.
- 91.** H. Moulard, J. W. Kury, A. Declos. *Proceedings of the 8th International Symposium on Detonation*. **(1985)**, p. 902-913.
- 92.** C. Belanger, P. Pelletier, J. F. Droulet. *Proceedings of the 8th International Symposium on Detonation*. **(1985)**, p. 361-371.
- 93.** H. Moulard. *Proceedings of the 9th International Symposium on Detonation*. **(1989)**, p. 18-24.
- 94.** E. L. Lee, C. M. Tarver. *Physics of Fluids*. **(1980)**, vol. 23, p. 2362-2372.
- 95.** F. Schledbauer, A. Kretschmer. *Proceedings of the 10th International Symposium on Detonation*. **(1993)**, p. 876-880.
- 96.** A. C. van der Steen. *Journal de Physique IV*. **(1995)**, vol. 5, p. C4/107-C4/108.
- 97.** R. H. B. Bouma, A. C. Hordijk, A. C. van der Steen. *Insensitive Munitions and Energetic Materials Symposium*. **(2001)**, p. 454-465.
- 98.** Z. Wang, Y. Liu, J. Zhang. *5th International Symposium on Test and Measurement*. **(2003)**, p. 849-852.
- 99.** S. M. Caulder, P. J. Miller, K. D. Gibson, J. M. Kelly. Effect of Particle Size, Particle Morphology, and Crystal Quality on the Critical Shock Initiation Pressures of Cast RDX/HTPB compositions. **(2006)**, Naval Surface Warfare Centre, Indian Head, USA.
- 100.** M. Herrmann. *Particle and Particle Systems Characterisation*, **(2005)**, vol. 22, p. 401-406.
- 101.** M. Herrmann, P. M. Kempa, S. Doyle. *Zeitschrift Kristallographie Suppl.* **(2007)**, vol. 26, p. 557-562.

-
- 102.** H Qiu, V. Stepanov, A. R. Di Stasio, T. Chou, W. Y. Lee. *Journal of Hazardous Materials*. **(2011)**, vo. 185, p. 489-493.
- 103.** J. E. Balzer, J. E. Field, M. J. Gifford, W. G. Proud, S. M. Walley. *Combustion and Flame*. **(2002)**, vol. 130, p. 298-306.
- 104.** V. Stepanov, V. Anglade, W. A. Balas-Hummers, A. V. Bezmelnitsyn, L. N. Krasnoperov. *Propellants Explosives, Pyrotechnics*. **(2011)**, vol. 36, p. 240-246.
- 105.** A. Chakravarty, M. J. Gifford, M. W. Greenaway, W.G. Proud, J.E. Field. *Shock Compression of Condensed Matter*. **(2001)**, p. 1007-1010.
- 106.** M. W. Greenaway, M. J. Gifford, W. G. Proud, J. E. Field, S. G. Goveas. *Shock Compression of Condensed Matter*. **(2001)**, p. 1035-1038.
- 107.** *Ibid.* Reference #4, p.64.
- 108.** P. Gerber, I. Fuhr, I. Mikonsaari, A. Kretschmer. *Proceedings of the 36th International Conference of the ICT*. **(2005)**, p. 139/1-139/10.
- 109.** L. Borne, H. Ritter. *Propellants, Explosives, Pyrotechnics*. **(2006)**, vol. 31(6), p. 482-489.
- 110.** C. Spyckerelle, G. Eck, P. Sjöberg, A-M. Amnéus. *Propellants, Explosives, Pyrotechnics*. **(2008)**, vol. 33(1), p. 14-19.
- 111.** J. Oxley, J. Smith, R. Bucu, J. Huang. *Journal of Energetic Materials*. **(2007)**, vol. 25, p. 141-160.
- 112.** M. Herrmann, P. B. Kempa, U. Förter-Barth. *Proceedings of the 41st International Conference of the ICT*. **(2010)**, p. 81/1-81/9.
- 113.** V. M. Boddu, A. Krishnaiah, R. Damavarapu. *Proceedings of the 12th seminar of New Trends in Research of Energetic Materials, Czech Republic*, **(2009)**, p. 62-68.
- 114.** C. Spyckerelle, A. Freche, G. Eck, C. Boutry. *Proceedings of the 35th International Conference of the ICT*. **(2004)**, p. 38/1-38/10.
- 115.** R. L. McKenney Jr. T. R. Kraweitz. *Journal of Energetic Materials*, **(2003)**, vol. 21, p. 141-166.
- 116.** D. S. Watt, M. Doherty, L. Nock. *RS-RDX Round Robin (R4) Preliminary Results Analysis*, MSAIC **(2006)**.
- 117.** C. Spyckerelle, A. Freche, G. Eck. *Insensitive Munitions and Energetic Materials Symposium*. **(2006)**.

-
- 118.** R. M. Doherty, D. S. Watt. *Minutes of the RS-RDX Round Robin (R4) Technical Meeting (ICT 2006)*, MSAIC (**2006**)
- 119.** Patant pending. *Instit National de Protection Industrielle*, number 0755501.
- 120.** Ø. H. Johansen, J. D. Kristiansen, R. Gjersoe, A. Berg, T. Halvorsen, K-T. Smith. *Propellants, Explosives, Pyrotechnics*. (**2008**), vol. 33(1), p. 20-24.
- 121.** T. Halvorsen, J. D. Kristiansen, Ø. H. Johansen, K-T. Smith, A. Berg, R. Gjersoe, M. Christensen, G. Nevstad. *Proceedings of the 36th International Conference of the ICT*. (**2005**), p. 36/1-36/12.
- 122.** NATO, Explosives, shock sensitivity tests, STANAG 4488, edition 1, (**2002**).
- 123.** D. Watt, F. Peugeot, R. Doherty, M. Sharp, D. Topler, D. Tucker. *Proceedings of the 35th Conference (international) of the ICT*, (**2004**), 9/1 - 9/12.
- 124.** A. Freche, J. Aviles, L. Donno, C. Spyckerelle. *Insensitive Munitions and Energetic Materials Symposium*, (**2000**).
- 125.** F. Trimborn, R. Wild. *Propellants Explosives and Pyrotechnics*, (**1982**), vol. 7, p. 87-90.
- 126.** F. Peugeot. *The NIMIC Excel Worksheets on Gap Tests*. NIMIC/NATO document O-089, August 2004.
- 127.** G. Bocksteiner, M. G. Wolfson, D. J. Whelan. *The critical diameter, detonation velocity and shock sensitivity of Australian PBXW-115*. (**1994**), DSTO-TR-0076, DSTO.
- 128.** B. L. Hamshire. *Australian Reduced Sensitivity RDX and its use in polymer bonded explosives*. Reduced sensitivity RDX technical meeting, WTD91, Meppen, Germany, (**2003**).
- 129.** P. Sjöberg, H. Hytti, R. Strandberg, A. Kariniemi, M. Muilu. *Proceedings of the 33rd international conference of the ICT*, (**2003**), p. 16/1 – 16/12.
- 130.** S. Lecume, P. Chabin, P. Brunet. *Two RDX qualities for PBXN-109 formulations sensitivity comparison, Insensitive Munitions and Energetic Materials Technology Symposium*. (**2001**).

-
- 131.** I. J. Lochert, M. D. Franson, B. L. Hamshire. *Reduced Sensitivity RDX (RS-RDX) Part I: Literature Review and DSTO Evaluation*. DSTO-TR-1447, **(2003)**.
- 132.** P. Gerber, I. Fuhr, I. Mikonsaari, A. Kretschmer. *Proceedings of the 36th International Conference of the ICT*. **(2005)**, p. 139/1-139/10.
- 133.** A. Freche. *Insensitive nitramines, Insensitive Munitions and Energetic Materials Technology Symposium*, **(2003)**.
- 134.** MSIAC report, L-103, RS-RDX technical meeting report. **(2004)**.
- 135.** W. C. Oliver, G. M. Pharr. *Journal of Materials Research*, **(2004)**, vol. 19(1), p. 3-19.
- 136.** <http://www.microstartech.com/index/NANOINDENTERS.pdf>, 13 April 2012.
- 137.** <http://www.engineering.unl.edu/research/bm3/Nanoindenter.shtml#details>, 17 April 2012.
- 138.** CSM Instruments, *Indentation Software User's Guide*, version 3.0, p. 111.
- 139.** CSM Instruments, *Applications Bulletin*, number 18 September, **2002**
- 140.** D. L. Logan, *Mechanics of Materials*, p.50, Harper Collins, **(1991)**.
- 141.** H. A. Barnes, J. F. Hutton, K Walters. *An Introduction to Rheology*, p. 1, Elsevier, **(1989)**.
- 142.** P. W. Cleary. *Powder Technology*. **(2008)**, vol. 179, p. 144-163.
- 143.** F. Podczek, Y. Miah. *International Journal of Pharmaceutics*. **(1996)**. vol. 144, p. 187-194.
- 144.** M. K. Stanford, C. DellaCorte. D. Eylon. *NASA Technical Memorandum TM-2002-211206*. **(2002)**.
- 145.** S. T. Erdogan, N. S. Martys, C. F. Ferraris, D. W. Fowler. *Cement and Concrete Composites*. **(2008)**, vol. 30, p. 393-402.
- 146.** U. Teipel (ed.) *Energetic Materials, Particle Processing and Characterisation*. **(2005)**, p. 433-434, Wiley-VCH, Germany.
- 147.** D. S. Watt, R. M. Doherty, L. Nock. *RS-RDX Round Robin (R4) Preliminary Results Analysis*, MSAIC, **(2006)**.
- 148.** NATO/NIMIC, Testing methods for the RS-RDX Round Robin (R4) Program.

-
- 149.** *Ibid.* Reference #131 p. 2.
- 150.** R. B. Frey. *Proceedings of the 8th Symposium on Detonation*, **(1985)**, p. 68-80.
- 151.** K. J. Ramos, D.F. Bahr, D.E. Hooks. *Philosophical Magazine*. **(2011)**, vol. 91, p. 1276-1285.
- 152.** D. H. Tsai, R. W. Armstrong, *J. of Physical Chemistry*, **(1994)**, vol. 98(43), p. 10997-11000.
- 153.** R. W. Armstrong, H. L. Ammon, W. L. Elban, D. H. Tsai, *Thermochimica Acta*, **(2002)**, vol. 384, p 303-313.
- 154.** D. H. Tsai, *J. of Chemical Physics*, **(1991)**, vol. 95(10), p. 7497-7503.
- 155.** A. Strachan, A. C. T. van Duin, W. A. Goddard. *Shock compression of Condensed Matter*. **(2003)**, p. 895-898.
- 156.** M. M. Kuklja, A. B. Kunz. *Journal of Applied Physics*, **(1999)**, vol. 86(8), p. 4428-4434.
- 157.** R. M. Dexter, B. L. Hamshire, I. J. Lochert. Evaluation of an alternative grade of CXM-7 for use in PBXN-109, the explosive fill for the Penguin ASM warhead. DSTO-TN-0441, **(2002)**.
- 158.** D. Sharabi, T. Kaully, C.-A. Yael, C. Nativ, D. Shaham, T. Tenanbaum, *Proceedings of the 39th International Conference of the ICT*. **(2008)**, p. 9/1-9/13.
- 159.** M. Fathollahi, S. M. Pourmortazavi, S. G. Hosseini. *Journal of Energetic Materials*. **(2008)**, vol. 26, p. 52-69.
- 160.** J. R. Quintana, J. A. Ciller, F. J. Serna. *Propellants, Explosives, Pyrotechnics*. **(1992)**, vol. 17, p. 106-109.
- 161.** H. Czerski, W. G. Proud, J. E. Field. *Central European Journal of Energetic Materials*. **(2006)**, vol. 3(3), p. 3-13.